

Neuroscience Bulletin

The Official Journal of The Chinese Neuroscience Society

神经科学通报

Volume 37
Number 7
July 2021

“Dual-switch” Function of TRPV4



TRPV4

NMDA

NLRP3



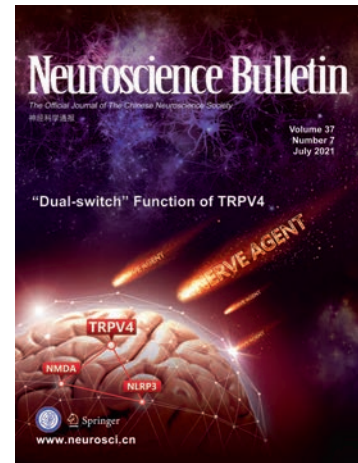
Springer

www.neurosci.cn

About the Cover

Nerve agents are among the deadliest poisons known to man. In this issue, Wang *et al.* demonstrate the “dual-switch” function of TRPV4 in the treatment of nerve agent intoxication. TRPV4 is a key target of soman poisoning due to its modulation of NMDA-mediated excitotoxicity in the early stage of poisoning and NLRP3-mediated neuroinflammation in the late stage. As shown in this cover image, the brain is attacked by the nerve agent soman, and a defensive line formed by blocking TRPV4 and its downstream NMDAR and NLRP3 pathways can effectively protect the brain against the nerve agent. See pages 905–920. (Cover image designed by Shuai Wang).

Volume 37 Number 7
July 2021



Original Articles

905 TRPV4 Regulates Soman-Induced Status Epilepticus and Secondary Brain Injury *via* NMDA Receptor and NLRP3 Inflammasome

Shuai Wang · Huanhuan He · Jianhai Long · Xin Sui · Jun Yang · Guodong Lin · Qian Wang · Yongan Wang · Yuan Luo

921 CCL2/CCR2 Contributes to the Altered Excitatory-inhibitory Synaptic Balance in the Nucleus Accumbens Shell Following Peripheral Nerve Injury-induced Neuropathic Pain

Xiao-Bo Wu · Qian Zhu · Yong-Jing Gao

934 Lateral Hypothalamic Area Glutamatergic Neurons and Their Projections to the Lateral Habenula Modulate the Anesthetic Potency of Isoflurane in Mice

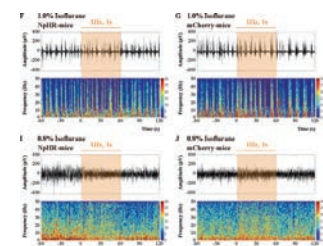
Shiyi Zhao · Rui Li · Huiming Li · Sa Wang · Xinxin Zhang · Dan Wang · Juan Guo · Huihui Li · Ao Li · Tingting Tong · Haixing Zhong · Qianzi Yang · Hailong Dong

947 Rac1 Signaling in Amygdala Astrocytes Regulates Fear Memory Acquisition and Retrieval

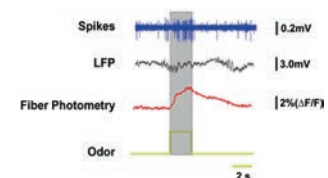
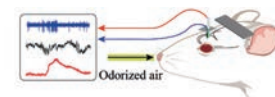
Xiao-Cen Fan · Chao-Nan Ma · Jia-Chen Song · Zhao-Hui Liao · Nan Huang · Xing Liu · Lan Ma

959 Distinct Characteristics of Odor-evoked Calcium and Electrophysiological Signals in Mitral/Tufted Cells in the Mouse Olfactory Bulb

Han Xu · Chi Geng · Xinzhong Hua · Penglai Liu · Jinshan Xu · Anan Li



p 943



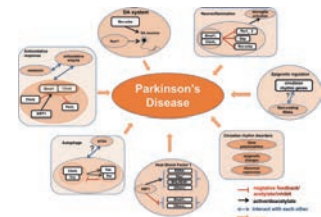
p 963

973 Dysregulated *CRMP* Mediates Circadian Deficits in a *Drosophila* Model of Fragile X Syndrome

Juan Zhao · Jin Xue · Tengfei Zhu · Hua He · Huaixing Kang · Xuan Jiang · Wen Huang · Ranhui Duan

985 Homeobox Gene *Six3* is Required for the Differentiation of D2-Type Medium Spiny Neurons

Xiaolei Song · Haotian Chen · Zicong Shang · Heng Du · Zhenmeiyu Li · Yan Wen · Guoping Liu · Dashi Qi · Yan You · Zhengang Yang · Zhuangzhi Zhang · Zhejun Xu



p 1017

Letters to the Editor

999 CRH Neurons in the Laterodorsal Tegmentum Mediate Acute Stress-induced Anxiety

Wenqi Tang · Danqing Zhou · Siyu Wang · Sijia Hao · Xiaomeng Wang · Mohamed Helmy · Junming Zhu · Hao Wang

1005 Restricted Feeding Resets Endogenous Circadian Rhythm in Female Mice Under Constant Darkness

Yue Mei · Huajing Teng · Zhigang Li · Cheng Zeng · Yuanyuan Li · Wei Song · Kaifan Zhang · Zhong Sheng Sun · Yan Wang

Reviews

1010 Recent Progress in Non-motor Features of Parkinson's Disease with a Focus on Circadian Rhythm Dysregulation

Yufei Liu · Long Niu · Xinyao Liu · Cheng Cheng · Weidong Le

1025 Comprehensive Management of Daily Living Activities, behavioral and Psychological Symptoms, and Cognitive Function in Patients with Alzheimer's Disease: A Chinese Consensus on the Comprehensive Management of Alzheimer's Disease

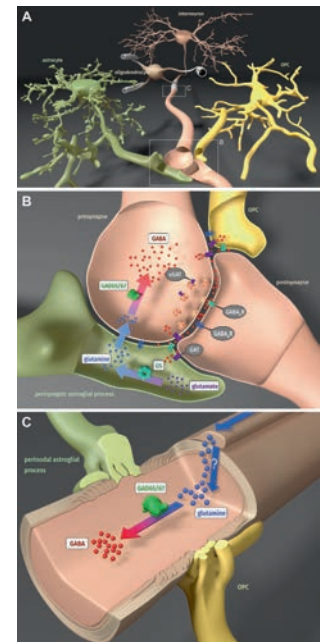
Jianjun Jia · Jun Xu · Jun Liu · Yongjun Wang · Yanjiang Wang · Yunpeng Cao · Qihao Guo · Qiuming Qu · Cuibai Wei · Wenshi Wei · Junjian Zhang · Enyan Yu

1039 Oligodendroglial GABAergic Signaling: More Than Inhibition!

Xianshu Bai · Frank Kirchhoff · Anja Scheller

1051 Structural, Functional, and Molecular Imaging of Autism Spectrum Disorder

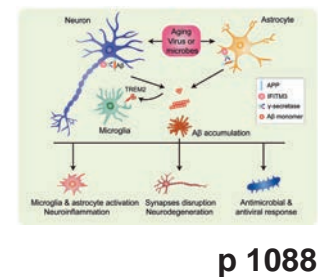
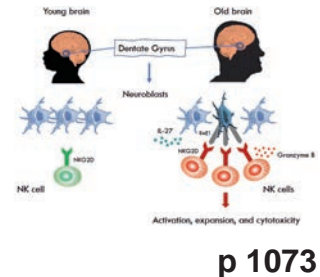
Xiaoyi Li · Kai Zhang · Xiao He · Jinyun Zhou · Chentao Jin · Lesang Shen · Yuanxue Gao · Mei Tian · Hong Zhang



p 1040

Research Highlights

- 1072 Activated Natural Killer Cells Hit Neurogenesis in the Aging Brain**
 Angelica Cuapio · Hans-Gustaf Ljunggren
- 1075 STING-ing Pain: How Can Pro-inflammatory Signaling Attenuate Pain?**
 Wolfgang Liedtke
- 1079 The Parabrachial Nucleus as a Key Regulator of Neuropathic Pain**
 Zilong Wang · Zhen-Zhong Xu
- 1082 Combination of Biomedical Techniques and Paradigms to Improve Prognostications for Disorders of Consciousness**
 Ming Song · Jianghong He · Yi Yang · Tianzi Jiang
- 1085 Autologous Transplantation for Parkinson's Disease Patients: Feasibility and Challenge**
 Qi Zhang · Yanlin Wang · Yukai Wang · Han Liu · Huifang Sun · Zhuoya Wang · Changhe Shi · Jing Yang · Yuming Xu
- 1087 Breakthrough in Structural and Functional Dissection of the Hypothalamo-Neurohypophysial System**
 Ying Wang · Huamin Xu · Xia Zhang





TRPV4 Regulates Soman-Induced Status Epilepticus and Secondary Brain Injury *via* NMDA Receptor and NLRP3 Inflammasome

Shuai Wang¹ · Huanhuan He¹ · Jianhai Long¹ · Xin Sui¹ · Jun Yang¹ · Guodong Lin¹ · Qian Wang¹ · Yongan Wang¹ · Yuan Luo¹

Received: 14 June 2020 / Accepted: 6 December 2020 / Published online: 24 March 2021
© Center for Excellence in Brain Science and Intelligence Technology, CAS 2021

Abstract Nerve agents are used in civil wars and terrorist attacks, posing a threat to public safety. Acute exposure to nerve agents such as soman (GD) causes serious brain damage, leading to death due to intense seizures induced by acetylcholinesterase inhibition and neuronal injury resulting from increased excitatory amino-acid levels and neuroinflammation. However, data on the anticonvulsant and neuroprotective efficacies of currently-used countermeasures are limited. Here, we evaluated the potential effects of transient receptor vanilloid 4 (TRPV4) in the treatment of soman-induced status epilepticus (SE) and secondary brain injury. We demonstrated that TRPV4 expression was markedly up-regulated in rat hippocampus after soman-induced seizures. Administration of the TRPV4 antagonist GSK2193874 prior to soman exposure significantly decreased the mortality rate in rats and reduced SE intensity. TRPV4-knockout mice also showed lower incidence of seizures and higher survival rates than wild-type mice following soman exposure. Further *in vivo* and *in vitro* experiments demonstrated that blocking TRPV4 prevented NMDA receptor-mediated glutamate excitotoxicity. The protein levels of the NLRP3 inflammasome complex and its downstream cytokines IL-1 β and IL-

18 increased in soman-exposed rat hippocampus. However, TRPV4 inhibition or deletion markedly reversed the activation of the NLRP3 inflammasome pathway. In conclusion, our study suggests that the blockade of TRPV4 protects against soman exposure and reduces brain injury following SE by decreasing NMDA receptor-mediated excitotoxicity and NLRP3-mediated neuroinflammation. To our knowledge, this is the first study regarding the “dual-switch” function of TRPV4 in the treatment of soman intoxication.

Keywords Nerve agents · Soman · TRPV4 · NMDA receptor · NLRP3 inflammasome

Introduction

With the disturbing effects of sarin attacks against civilians in Syria in August 2013, important questions regarding the level of preparedness and the adequacy of existing medical responses against exposure to such nerve agents have been raised [1]. The appearance of Novichok, or “newcomer”, which was used in the attack on a Russian dissident and his daughter in 2018 highlights the importance of protection against the potentially lethal effects of nerve agents [2]. The primary effect of exposure to organophosphorus nerve agents is a decrease in acetylcholinesterase (AChE) activity and a concurrent rise in acetylcholine (ACh) levels, which are considered to be the decisive events that initiate epileptiform activity. The over-elevation of ACh levels mainly activates muscarinic receptors, and, in the cholinergic phase, the administration of receptor antagonists can halt the development of seizures and status epilepticus (SE), but only when they are administered as pretreatments or shortly after the onset of seizures (within 5 min). The

Electronic supplementary material The online version of this article (<https://doi.org/10.1007/s12264-021-00662-3>) contains supplementary material, which is available to authorized users.

✉ Yongan Wang
yonganw@126.com

✉ Yuan Luo
luoyuan2006@163.com

¹ State Key Laboratory of Toxicology and Medical Countermeasures, Institute of Pharmacology and Toxicology, Academy of Military Medical Sciences, Beijing 100850, China

anticonvulsant potential of most anticholinergics, such as atropine, is gradually lost when the administration is delayed beyond 20 min, and they completely lose their anticonvulsant potential when administered 40 min after seizure onset [3]. These narrow time windows limit their application. Nevertheless, some anticholinergics such as biperiden and procyclidine can exert anticonvulsant activity even with a 40-min delay in treatment; this is because they have anti-NMDA (N-methyl-D-aspartate) properties to some extent [4], suggesting that seizures are sustained and reinforced by glutamatergic rather than cholinergic hyperexcitation [5, 6]. As seizure activity progresses, non-cholinergic excitatory activity gradually takes control over the seizure independent of the initiating cholinergic drive [3]. This phenomenon is critical for the development of drugs that target the non-cholinergic phase. Several studies have demonstrated that in the case of nerve agent seizures, intense activation of NMDA receptors (NMDARs) would allow additional entry of Ca^{2+} into neurons, leading to neurotoxicity and subsequent neuropathology [7, 8]. Braitman and Sparenborg (1989) first reported that pretreatment with the NMDA antagonist MK-801 terminates nerve agent-induced SE. Meanwhile, after a period of epileptiform activity, a lower dose of MK-801 is still able to terminate SE [9]. All this evidence indicates that the NMDAR has predominant control over nerve agent-induced seizure activity at the later stages [10–12].

Several studies have reported that exposure to nerve agents is associated with a cellular inflammatory response in the form of astrocytic and microglial activation [13]. Neuroinflammatory genes, such as *IL-1 β* , *TNF- α* , and *IL-6*, are widely described to be implicated in nerve agent-induced seizures [14–17]. Unfortunately, since most studies are limited to the downstream factors of the inflammatory response, the biochemical processes remain unclear and the inflammatory mechanism induced by nerve agents needs to be further clarified. Here we attempted, at least to some extent, to identify the intracellular signaling mechanisms of inflammatory responses following soman-induced seizures and key factors in the process.

Transient receptor potential vanilloid 4 (TRPV4), a member of the TRPV ion channel family, is sensitive to various types of stimuli, including hypotonic environments, mechanical forces, arachidonic acid metabolites, and exogenous chemical ligands [18, 19]. Activation of TRPV4 induces Ca^{2+} influx, thus increasing the intracellular free Ca^{2+} concentration ($[\text{Ca}^{2+}]_i$). It has been reported that TRPV4 plays a pivotal role in central nervous system disorders and injuries such as Alzheimer's disease [20], ischemic stroke [21], traumatic brain injury [22], and seizures [23]. An interesting finding is that the activation of TRPV4 during cerebral ischemia injury increases NMDAR function, which indicates that closing TRPV4 may be

neuroprotective against NMDAR-mediated glutamate excitotoxicity [24]. Furthermore, a study on febrile seizures suggests that TRPV4 channels and NMDARs both play a role in hyperthermia-induced seizures [25]; these results indicate that there may be an association between TRPV4 and NMDARs during epilepsy, and this is supported by a study showing that the activation of TRPV4 depolarizes the resting membrane potential of cultured hippocampal neurons and relieves the blockade of NMDARs by Mg^{2+} [26]. Recent research has pointed out that the TRPV4 agonist GSK1016790A increases the expression levels of inflammasome components of the NLRP3 pathway and downstream pro-inflammatory cytokines. The increased protein levels of NLRP3-related pro-inflammatory cytokines are blocked by the use of a TRPV4 antagonist, which markedly increases the number of surviving cells in a pilocarpine model of temporal lobe epilepsy in mice [27]. Furthermore, in a previous study, we conducted preliminary assessment of the expression changes of various TRP subtypes (TRPM2, TRPV1, TRPV4, TRPM7, TRPC3, and TRPC6) in a variety of models organophosphorus compound poisoning (including soman), and found that the expression of TRPV4 was significantly increased in all of them.

Taking into account the involvement of NMDAR-mediated excitotoxicity and neuroinflammation in soman-induced seizures and secondary neuronal injury, with the possible triggering of NMDAR function by TRPV4 activation, we hypothesized that TRPV4 could be a key target involved in the seizures and neuronal injury caused by soman exposure. Here, we used a wide range of methods to determine the effects of soman on the function of TRPV4 channels. This included behavioral studies in rats and corresponding histopathology, as well as immunofluorescence, biochemistry, electrophysiological recordings, and Ca^{2+} imaging *in vitro*.

Materials and Methods

Chemicals and Agents

Soman (pinacolyl methylphosphonofluoridate) was obtained from the Institute of Nuclear, Biological, and Chemical Defence (Beijing, China), and was only used for the purposes of the current study. Soman was diluted in cold saline. HI-6 was synthesized by the Institute of Pharmacology and Toxicology, Academy of Military Medical Science (Beijing, China) and was dissolved in saline. GSK2193874 (GSK) was from Selleck Chemicals (S8367, Houston, USA). GSK2193874 was dissolved in DMSO (Sinopharm, Shanghai, China), then diluted with Neurobasal medium immediately prior to use in cells

(0.05% DMSO) or with sterilized water for use in rats (1% DMSO).

Animals and Experimental Groups

Adult male Sprague-Dawley rats (7–8 weeks old, 180–220 g) and adult male C57BL/6J mice (6–8 weeks old, 18–20 g) were from Vital River Laboratory Animal Technology Co., Ltd (Beijing, China). TRPV4-knockout (TRPV4-KO) mice were bred in-house from heterozygous breeding pairs originally derived from a colony generated by GemPharmatech Co., Ltd (Nanjing, China). All animals were treated humanely and maintained in a temperature-controlled room ($22 \pm 2^\circ\text{C}$) with a 12-h light/dark cycle (lights on at 07:00 and off at 19:00), with food and water available *ad libitum*. All animal experiments were conducted in accordance with national legislation and approved by the Institutional Animal Care and Use Committee (IACUC number: IACUC-2018-075, IACUC-2018-098, National Beijing Center for Animal Drug Safety Evaluation and Research, Beijing, China).

Soman was diluted in cold saline and administered *via* a single subcutaneous injection ($160 \mu\text{g}/\text{kg}$, $1.4 \times \text{LD}_{50}$). To block peripheral effects and increase the survival rate of rats, the oxime HI-6 ($125 \text{ mg}/\text{kg}$, i.p.) was administered 30 min prior to soman exposure. HI-6 is a bispyridinium oxime that reactivates inhibited AChE primarily in the periphery to control the peripheral effects of soman and prevent death from respiratory suppression [3, 28]. Also, HI-6 does not prevent the brain injury caused by soman poisoning because it is unable to cross the blood-brain barrier [29]. The rats were randomly divided into three groups: (1) Control: (HI-6 $125 \text{ mg}/\text{kg}$, i.p., 1% DMSO, i.v., $n = 10$); (2) Soman: HI-6 ($125 \text{ mg}/\text{kg}$, i.p.) and solvent (1% DMSO, i.v.) administered 30 min prior to soman ($160 \mu\text{g}/\text{kg}$, s.c.), $n = 42$; (3) GSK2193874 + soman: TRPV4 antagonist GSK2193874 ($1 \text{ mg}/\text{kg}$, i.v.) and HI-6 ($125 \text{ mg}/\text{kg}$, i.p.), administered 30 min prior to soman ($160 \mu\text{g}/\text{kg}$, s.c.), $n = 39$. To evaluate TRPV4-KO intervention, the mice were divided into three groups ($n = 10$ per group): (1) WT (wild-type): WT mice treated with HI-6 ($125 \text{ mg}/\text{kg}$, i.p.); (2) WT + soman: WT mice treated with HI-6 ($125 \text{ mg}/\text{kg}$, i.p.) 30 min prior to soman ($125 \mu\text{g}/\text{kg}$, s.c.); (3) TRPV4-KO + soman: TRPV4-KO mice treated with HI-6 ($125 \text{ mg}/\text{kg}$, i.p.) 30 min prior to soman ($125 \mu\text{g}/\text{kg}$, s.c.). The mortality rate was calculated as the number of deceased rats or mice (24 h after soman exposure) divided by the total number of rats or mice.

NMDA was diluted in cold 0.9% NaCl and administered *via* a single intraperitoneal injection ($100 \text{ mg}/\text{kg}$). Memantine, an NMDA antagonist, was used as a positive control. The rats were divided randomly into three groups ($n = 20$ per group): (1) NMDA: rats treated with solvent (1%

DMSO) 30 min before NMDA ($100 \text{ mg}/\text{kg}$, i.p.); (2) Memantine + NMDA: rats treated with memantine ($20 \text{ mg}/\text{kg}$, i.p.) and solvent (1% DMSO) 30 min before NMDA ($100 \text{ mg}/\text{kg}$, i.p.); (3) GSK2193874 + NMDA: rats treated with the TRPV4 antagonist GSK2193874 ($1 \text{ mg}/\text{kg}$, i.v.) 30 min before NMDA ($100 \text{ mg}/\text{kg}$, i.p.). The mortality rate was calculated as the number of deceased rats (24 h after NMDA exposure) divided by the total number of rats.

Behavioral Assessment

Seizures were classified according to the Racine scale with the following minor modifications: stage 0, no abnormality; stage 1, facial movements, chewing; stage 2, rhythmic head nodding; stage 3, forelimb clonus plus Straub tail, without rearing; stage 4, forelimb clonus, bilateral forelimb clonus plus rearing; stage 5, rearing and falling [30–33].

Histopathological Examination

Rats and mice were anesthetized with chloral hydrate, and then 0.9% NaCl (4°C) was perfused, followed by a fixative solution made up of 4% formaldehyde in 0.1% mol/L phosphate-buffered saline (PBS, pH 7.4). After cervical dislocation, the brain was removed and fixed for 24 h at 4°C (4% formaldehyde in PBS), processed, and embedded in paraffin. The coronal sections of the CA1 hippocampal area were selected and processed for hematoxylin-eosin (H&E) staining. Three sections from each brain were visualized on an inverted microscope (IX71, Olympus, Japan).

Immunofluorescence Analysis

For immunofluorescence staining, paraffin-embedded sections were microwaved in 0.01 mol/L citrate buffer and washed three times with 0.01 mol/L PBS for 15 min each, and subsequently blocked by 5% bovine serum albumin (BSA) in 0.01 mol/L PBS for 30 min at room temperature ($22 \pm 2^\circ\text{C}$). Then the sections were incubated with anti-TRPV4 antibody (1:200) at 4°C overnight. After washing three times with PBS for 15 min each, Texas Red-conjugated secondary antibodies (1:1000, ZSGB-BIO) were added and incubated for 60 min in the dark. After washing three times with PBS, sections were treated with Hoechst 33342 (1:2000, H3570, Invitrogen) for 5 min. The positive rate was calculated by dividing the number of positive cells (TRPV4⁺/Hoechst⁺) by the total number of cells (Hoechst⁺).

Primary hippocampal neurons were washed three times in PBS following the appropriate treatment, fixed with 4% paraformaldehyde for 15 min and then washed three times with PBS. The cells were permeated with 0.5% Triton

X-100 (solvent in goat serum working reagent) for 10 min on ice and blocked with 1% goat serum working reagent for 1 h. Cells were incubated at room temperature for 5 min with propidium iodide (PI) (1 $\mu\text{g}/\text{mL}$, ab14083, Abcam). After washing three times with PBS, cells were treated with Hoechst 33342 (1:2000, H3570, Invitrogen) for 5 min. The death rate was calculated by dividing the number of dead cells (PI⁺/Hoechst⁺) by the total number of cells (Hoechst⁺).

The positive cells were measured using ImageXpress Micro Confocal (Molecular Devices) and calculated using MetaXpress software (Molecular Devices).

Western Blotting Analysis

Hippocampal tissue was lysed using a membrane protein and cytoplasmic protein extraction kit together with protease and phosphatase inhibitors (KeyGEN Biotech Co., Ltd), and proteins were isolated according to the manufacturer's instructions. Membrane protein and cytoplasmic protein were quantified using a BCA protein reagent kit (KeyGEN Biotech Co., Ltd). The proteins were separated by 8% or 10% SDS-PAGE and transferred to 0.2 μm PVDF membranes (Bio-Rad). Membranes were blocked with 5% BSA in Tris-buffered saline (TBS) with 0.1% Tween-20 for 2 h at $22 \pm 2^\circ\text{C}$ and then incubated at 4°C overnight with the following antibodies: anti-TRPV4 (1:400, PA5-41066, Thermo Fisher), anti-NMDAR2B (1:500, MA1-2014, Thermo Fisher), anti-p-NMDAR2B (1472) (1:500, ab3856, Abcam), anti-NLRP3 (1:400, A14223, Abclonal), anti-ASC (1:500, YT0365, ImmunoWay), anti-caspase-1 (1:400, ab179515, Abcam), anti-IL-1 β (1:1000, A16288, Abclonal), and anti-IL-18 (1:500, A16737, Abclonal). After washing with TBS containing 0.1% Tween-20, blots were incubated in horseradish peroxidase-conjugated secondary antibody (1:2000, ZSGB-BIO) for 1 h at $22 \pm 2^\circ\text{C}$. Bands of proteins bound to antibodies were detected using a chemiluminescence detection system (Pro-light HRP Chemiluminescent Kit, TianGen Biotech). Densitometric analysis was performed using Quantity One software (Bio-Rad). These analyses were normalized to β -actin (1:1000, 4970S, CST).

Cell Culture and Treatment

All experimental protocols were approved by the Institutional Animal Care and Use Committee (IACUC number: IACUC-2018-107, National Beijing Center for Drug Safety Evaluation and Research, Beijing, China). Primary cultures of rat hippocampal neurons were aseptically obtained from the hippocampus of E17–E18 Wistar rat embryos. The hippocampi were treated with 0.25% trypsin in Ca^{2+} - and Mg^{2+} -free Hank's balanced salt solution for 15 min in a

CO_2 incubator, and then washed with 10% fetal bovine serum in Dulbecco's modified Eagle's medium to stop trypsin activity. The samples were then transferred to Neurobasal medium (Thermo Fisher) supplemented with B27 (1:50 dilution, Thermo Fisher) and GlutaMAXTM-1 (1:100, Thermo Fisher). The neurons were plated at $4.0\text{--}6.0 \times 10^5$ cells/well in 96 or 6-well plates, which were pretreated with poly-D-lysine (0.1 mg/mL). The cultures were maintained in a humidified incubator under 5% CO_2 at 37°C . Hippocampal neurons were grown for 7 days in culture plates before being used for experiments. First, they were treated with different concentrations of NMDA (50–500 $\mu\text{mol}/\text{L}$) to determine an appropriate dose (Fig. S1). To explore the protective effect of the TRPV4 antagonist GSK2193874 on primary hippocampal neurons against NMDA-induced cytotoxicity, three comparison groups were studied: the control group, in which neurons were treated with solvent (0.01% DMSO); the NMDA group, in which neurons were treated with NMDA (50–500 $\mu\text{mol}/\text{L}$) for 24 h; and the GSK group, in which neurons were treated with GSK2193874 (50–500 nmol/L) for 24 h before NMDA exposure.

Electrophysiological Recording

Whole-cell patch-clamp recording was performed at $22\text{--}24^\circ\text{C}$. Hippocampal neurons were visualized on an inverted microscope (IX71, Olympus, Japan). Inward current (I_{NMDA}) was recorded using an EPC-10 amplifier (HEKA Elektronik, Lambrecht/Pfalz, Germany). Neurons were continuously perfused with an external solution of the following composition (in mmol/L): NaCl 140, KCl 4.0, CaCl_2 2.0, HEPES 10, and D-glucose 5. The pH was adjusted to 7.4 with NaOH. Glass pipettes (resistance 4–5 M Ω) were pulled from borosilicate glass capillaries on a micropipette puller (P97, Sutter Instruments, USA) and filled with an internal solution of the following composition (in mmol/L): NaCl 10, CsMes 110, MgCl_2 2, HEPES 10, EGTA 10, $\text{Na}_2\text{-ATP}$ 2, and $\text{Na}_2\text{-GTP}$ 0.2. The pH was adjusted to 7.2 with CsOH.

When recording I_{NMDA} , hippocampal neurons were held at -70 mV. First, NMDA (100 $\mu\text{mol}/\text{L}$) and glycine (10 $\mu\text{mol}/\text{L}$) were applied by local pressure perfusion, followed by NMDA, glycine, and GSK2193874 (0.3 and 3 $\mu\text{mol}/\text{L}$). Strychnine (1 $\mu\text{mol}/\text{L}$), bicuculline (10 $\mu\text{mol}/\text{L}$), NBQX (10 $\mu\text{mol}/\text{L}$), and QX314 (10 mmol/L) were added to the solution to block glycine receptors, GABA_A receptors, AMPA receptors, and voltage-gated Na^+ channels, respectively. Data were collected by PatchMaster software (HEKA Elektronik) and analyzed with IGOR-Pro (WaveMetrics Inc.).

Cell Viability Assay

Cells were seeded in 96-well plates at 4.0×10^5 cells/mL. NMDA at 100 $\mu\text{mol/L}$ was chosen as the appropriate dose for experiments, based on its toxicity to cells and to ensure a certain cell survival rate. After treatment, 20 μL 3-(4,5-dimethylthiazol-2-yl)-2,5-diphenyltetrazolium bromide (MTT) (KeyGEN Biotech Co., Ltd) was added to each well, and the cells were incubated for 4 h at 22–24°C. After incubation, MTT was removed and 200 μL DMSO was added to solubilize the formazan crystals that formed in the intact cells. Absorbance was measured at 470 nm with SpectraMax (Molecular Devices). Each group included 8 wells. The results are expressed as the percentage of MTT reduction in the treated cells, assuming taking the absorbance of the control cells as 100%. Cell viability was calculated as $\text{OD}_{470}(\text{treatment})/\text{OD}_{470}(\text{control})$.

Lactate Dehydrogenase Release Assay

Cell death or cytotoxicity is classically evaluated by the quantification of plasma membrane damage. Lactate dehydrogenase (LDH) is a marker of membrane integrity and the amount released into the culture medium was measured using a diagnostic kit (BioVision), according to the manufacturer's instructions. NMDA at 100 $\mu\text{mol/L}$ was used. Each group included 10 wells.

RNA Silencing

Rat primary hippocampal neurons were transfected with a negative control (NC) siRNA (4390843, Thermo Fisher) or TRPV4-siRNA (s134883, Thermo Fisher) using the Lipofectamine RNAiMAX kit (1295300, Thermo Fisher), following the manufacturer's instructions. The siRNA duplex was diluted in Opti-MEM I medium without serum and gently mixed with Lipofectamine RNAiMAX. Then, they were mixed in a 1:1 ratio to form the siRNA duplex/Lipofectamine RNAiMAX complexes. The complexes were incubated for 15 min at 22–24°C. The complexes were then added to the wells at 4×10^5 cells/well to a final siRNA concentration of 10 nmol/L. The contents were mixed gently and cells were incubated for 24 h at 37°C in a CO_2 incubator.

Calcium Imaging

$[\text{Ca}^{2+}]_i$ was measured with Fluo-4/AM Direct Calcium Assay kits (Invitrogen). A total of 50 μL of the $2 \times$ Fluo-4 Direct Ca^{2+} reagent loading solution per well was added to a 96-well plate, 1:1 with Neurobasal medium. The plates were incubated at 37°C for 60 min and then treated with Hoechst 33342. Each group included 6 wells. Fluorescein

isothiocyanate and DAPI fluorescence were measured using the ImageXpress Micro Confocal system (Molecular Devices). The mean of the average cell intensity was calculated using MetaXpress software (Molecular Devices).

Statistical Analysis

Data are expressed as the mean \pm SD. Fisher's exact test was used to compare the survival rates between groups. Comparisons among more than two groups were performed using one-way ANOVA followed by Dunnett's multiple comparisons test. The differences between two treatments for the same sample were compared using the paired *t*-test. The criterion for statistical significance was $P < 0.05$. Results were analyzed using SPSS 20.0 software (SPSS Inc., Chicago, IL, USA).

Results

Effect of GSK2193874 on Soman-Induced Seizures and Histopathological Lesions in Rats

Sprague-Dawley rats were challenged with soman (160 $\mu\text{g/kg}$, s.c., $1.4 \times \text{LD}_{50}$). To increase the survival rate, all animals were administered HI-6 (125 mg/kg, i.p.) 30 min before soman exposure to block peripheral effects [3] such as respiratory depression. A behavioral seizure score of stage 4 was reached within 30–60 min in the soman group, and SE stopped spontaneously within 6–8 h, while behavioral seizures were significantly suppressed by the TRPV4 antagonist GSK2193874 within 60–90 min (Fig. 1A, $P < 0.05$). The mortality rate in the soman-treated rats was 61.9% (42 in total, 26 deaths), while the administration of GSK2193874 markedly decreased this to 25.6% (39 in total, 10 deaths).

Hippocampal tissue was collected from rats for H&E staining 24 h after soman exposure. Histological examination indicated that the CA1 hippocampal neurons of control rats showed structural integrity with distinct and well-characterized round nucleoli (Fig. 1B-I). Compared with the control group, soman exposure caused severe damage in the rat hippocampi, manifested as loose structure, neuronal loss, and nuclear pyknosis (Fig. 1B-II). GSK2193874 significantly reduced the histopathologic lesions caused by soman exposure (Fig. 1B-III).

Effect of GSK2193874 on TRPV4 Expression in Rat Hippocampus after Soman Exposure

To investigate the effect of soman exposure (160 $\mu\text{g/kg}$, s.c.) on the expression levels of TRPV4 in the

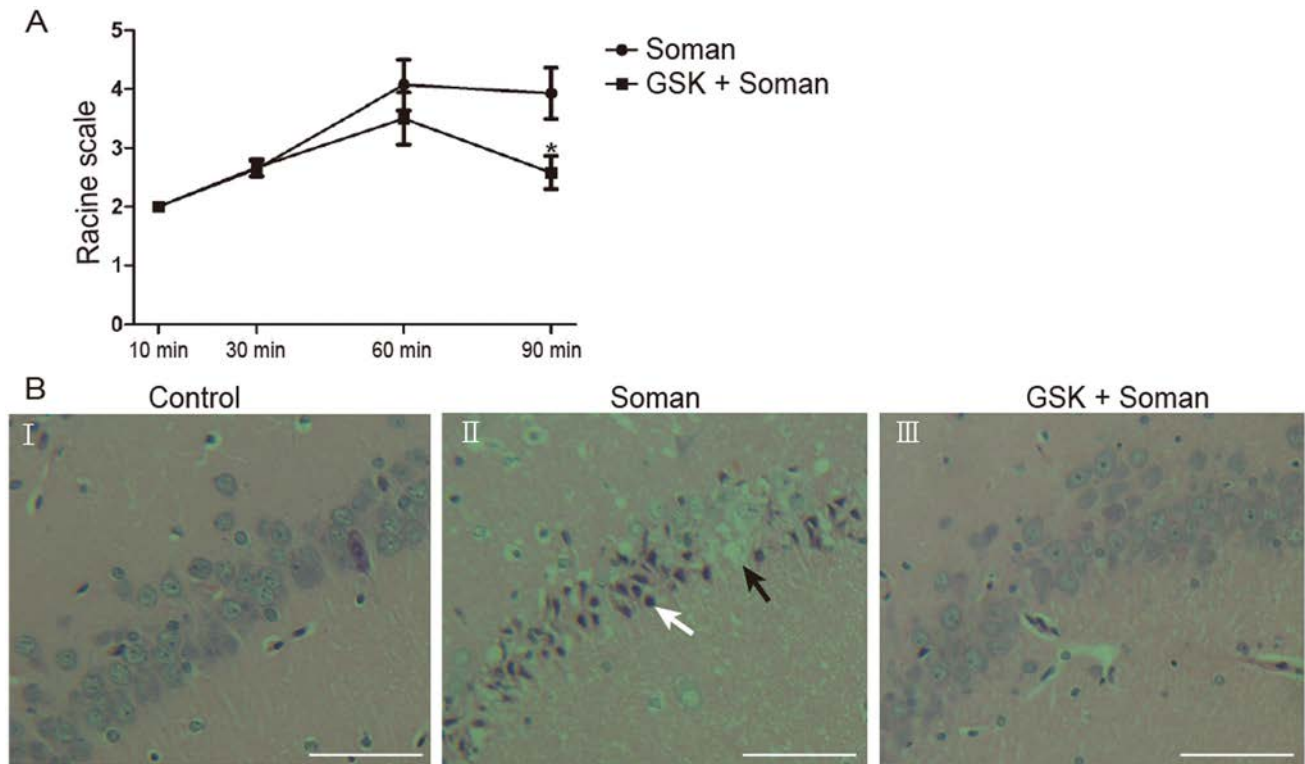


Fig. 1 GSK2193874 inhibits behavioral seizures and the development of histopathological lesions induced by soman. Soman group ($n = 14$): rats were treated with HI-6 (125 mg/kg i.p.) before soman injection (160 $\mu\text{g}/\text{kg}$, s.c.); GSK2193874 (GSK) group ($n = 12$): rats were additionally treated with the TRPV4 antagonist GSK2193874 (1 mg/kg, i.v.) immediately after HI-6 injection and before soman injection. **A** Maximum Racine scale scores (means \pm SD; * $P < 0.05$ vs soman group, one-way ANOVA). **B** Development of soman-

induced histopathological lesions in the CA1 hippocampal area is attenuated by GSK2193874 ($\times 200$, original magnification, scale bars, 50 μm). **B-I** Control group retains the typical appearance of normal neurons with a clear edge and uniform size. **B-II** Soman exposure decreases the volume of neurons and leads to nuclear pyknosis (white arrow) and loss of neurons (black arrow). **B-III** GSK2193874 reduces the histopathologic lesions caused by soman exposure.

hippocampus, Western blot (WB) (Fig. 2A) and immunofluorescence analyses (Fig. 2B) were performed. WB analysis showed that the expression of TRPV4 was up-regulated after soman exposure compared to that in the control group (Fig. 2A, $P < 0.001$); however, GSK2193874 treatment abrogated the TRPV4 expression (Fig. 2A, $P < 0.05$). Immunofluorescence analysis showed that the percentage of TRPV4-positive cells markedly increased from $4.83 \pm 1.03\%$ to $28.18 \pm 3.03\%$ after soman exposure (Fig. 2B, $P < 0.001$); however, GSK2193874 treatment significantly decreased the ratio from $28.18 \pm 3.03\%$ to $13.1 \pm 2.09\%$ (Fig. 2B, $P < 0.05$). These results indicate that TRPV4 expression in the rat hippocampus is significantly increased after soman exposure and this is reversed by GSK2193874.

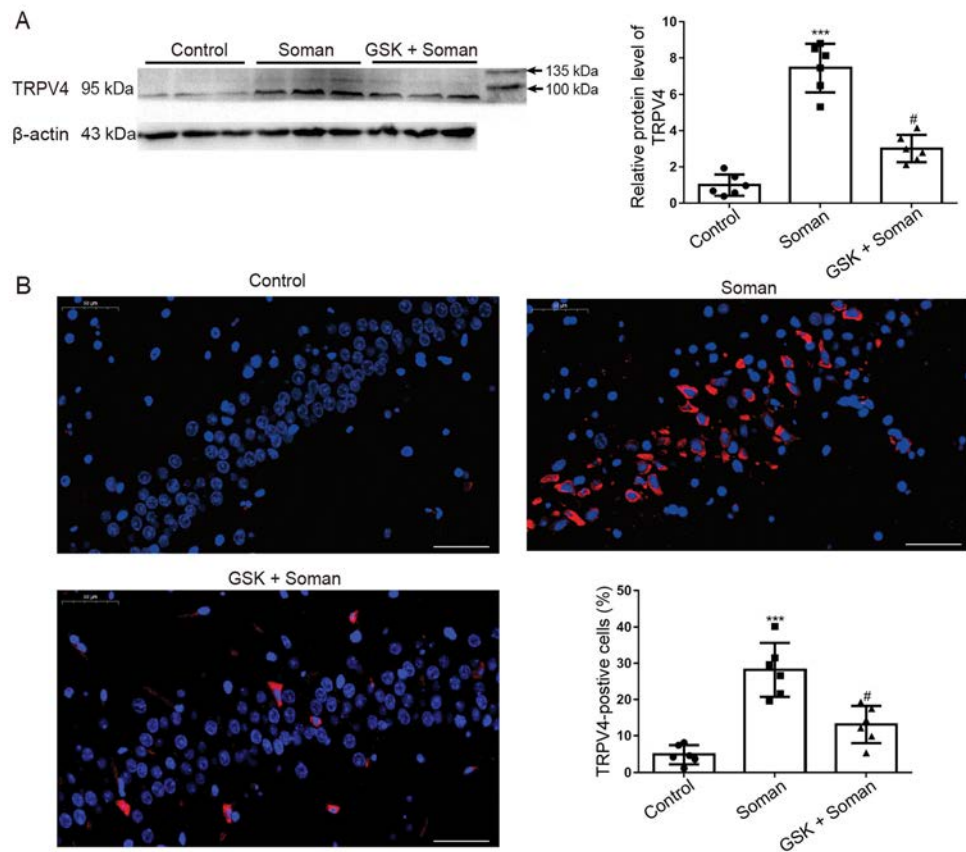
Effect of GSK2193874 on NMDA Receptor Function

To explore the molecular mechanisms by which the TRPV4 channel might be involved in soman-induced excitotoxicity, we tested the effect of a TRPV4 antagonist

on the phosphorylation of the NMDAR 2B subunit (NR2B) protein, a key factor in excitotoxicity [34]. WB analysis showed that NR2B phosphorylation was significantly increased in rat hippocampus after soman exposure compared with the control group, and the phosphorylation was remarkably reversed by GSK2193874 (Fig. 3A, $P < 0.001$).

Patch clamp was used to further explore whether TRPV4 inhibition modulates NMDAR function. After application of NMDA (100 $\mu\text{mol}/\text{L}$) and glycine (10 $\mu\text{mol}/\text{L}$) to primary cultured rat hippocampal neurons, an inward current (I_{NMDA}) was recorded. According to the results, the current was blocked by the specific NMDAR antagonist D-AP5 (100 $\mu\text{mol}/\text{L}$), confirming its mediation by the NMDAR (Fig. 3B). The NMDA-activated current was markedly decreased by $11.13 \pm 2.67\%$ from -619.7 ± 68.15 pA to -557 ± 80.76 pA after application of 0.3 $\mu\text{mol}/\text{L}$ GSK2193874 (Fig. 3B, $n = 6$, paired t -test, $P < 0.01$), and decreased by $19.11 \pm 2.24\%$ from -619.7 ± 68.15 pA to -457.7 ± 89.36 pA after application of 3 $\mu\text{mol}/\text{L}$ GSK2193874 (Fig. 3B, $n = 6$, paired t -test,

Fig. 2 GSK2193874 inhibits TRPV4 expression in the hippocampus of rats exposed to soman. Protein expression of TRPV4 was assessed by (A) Western blotting and (B) immunofluorescence (red, TRPV4; blue, Hoechst; $\times 200$, original magnification; scale bars, 50 μm). TRPV4⁺/Hoechst⁺ cells are TRPV4-positive cells, and Hoechst⁺ cells are total cells. Soman group: rats were treated with HI-6 (125 mg/kg i.p.) before soman injection (160 $\mu\text{g}/\text{kg}$, s.c.); GSK2193874 (GSK) group: rats were additionally treated with the TRPV4 antagonist GSK2193874 (1 mg/kg, i.v.) immediately after HI-6 injection and before soman injection; Control group: rats received HI-6 and solvent instead of antagonist and soman (mean \pm SD, $n = 6$; *** $P < 0.001$ vs control group, # $P < 0.05$ vs soman group, one-way ANOVA and Dunnett's multiple comparison test).



$P < 0.001$). These results imply that blocking TRPV4 inhibits NMDAR function.

Action of GSK2193874 Against NMDA-Induced Excitotoxicity *In Vitro* and *In Vivo*

To determine whether TRPV4 is involved in NMDA-mediated excitotoxicity, we further explored the effect of GSK2193874 (1 mg/kg, i.v.) against NMDA-induced (100 mg/kg, i.p.) seizures and death in rats. Memantine, an NMDAR antagonist, was used as a positive control. As shown in Table 1, memantine (20 mg/kg, i.p.) delayed the onset of seizures and completely prevented rat death (Table 1, $P < 0.05$, < 0.001), but had no effect on tonic-clonic seizure control. Meanwhile, pretreatment with GSK2193874 delayed the onset of seizures and reduced the tonic-clonic seizures and mortality induced by NMDA (Table 1, $P < 0.05$, < 0.001).

To confirm the neuroprotective properties of GSK2193874 on NMDA-induced excitotoxicity *in vitro*, its effects on cytotoxicity induced by NMDA in primary cultured rat hippocampal neurons were evaluated by the MTT and LDH release assays. Cells were pretreated with GSK2193874 for 24 h, then exposed to NMDA (100 $\mu\text{mol}/\text{L}$) for a further 24 h (Fig. 4A). GSK2193874 (50, 100, 200,

and 500 nmol/L) increased the cell viability from 61.41% to 90.05%, 84.18%, 91.04%, and 89.81%, respectively, compared with the GSK 0 nmol/L group (Fig. 4A, $P < 0.05$) while reducing the LDH release from 10.58% to 6.33%, 6.13%, 4.74%, and 4.86%, respectively (Fig. 4B, $P < 0.001$).

Cell death was also assessed using Hoechst/PI dual staining. This showed that the rate of cell death increased from 19.3% to 27.9% after NMDA exposure (100 $\mu\text{mol}/\text{L}$) for 24 h (Fig. 4C, $P < 0.05$), whereas pretreatment with GSK2193874 (200 nmol/L) for 24 h reduced the death rate to 16% (Fig. 4C, $P < 0.001$), compared with the NMDA group.

To assess the effect of GSK2193874 on the $[\text{Ca}^{2+}]_i$ after NMDA exposure, cytoplasmic Ca^{2+} levels were measured by Ca^{2+} -sensitive Fluo-4/AM staining (Fig. 4D). NMDA treatment (100 $\mu\text{mol}/\text{L}$) increased the $[\text{Ca}^{2+}]_i$ compared with that of the control group (Fig. 4D, $P < 0.05$). Pretreatment with GSK2193874 (200 nmol/L) for 24 h attenuated the NMDA-induced Ca^{2+} accumulation compared with that of the NMDA-treated group (Fig. 4D, $P < 0.05$). The above results demonstrated that TRPV4 inhibition attenuates the excitotoxicity induced by NMDA *in vitro* and *in vivo*.

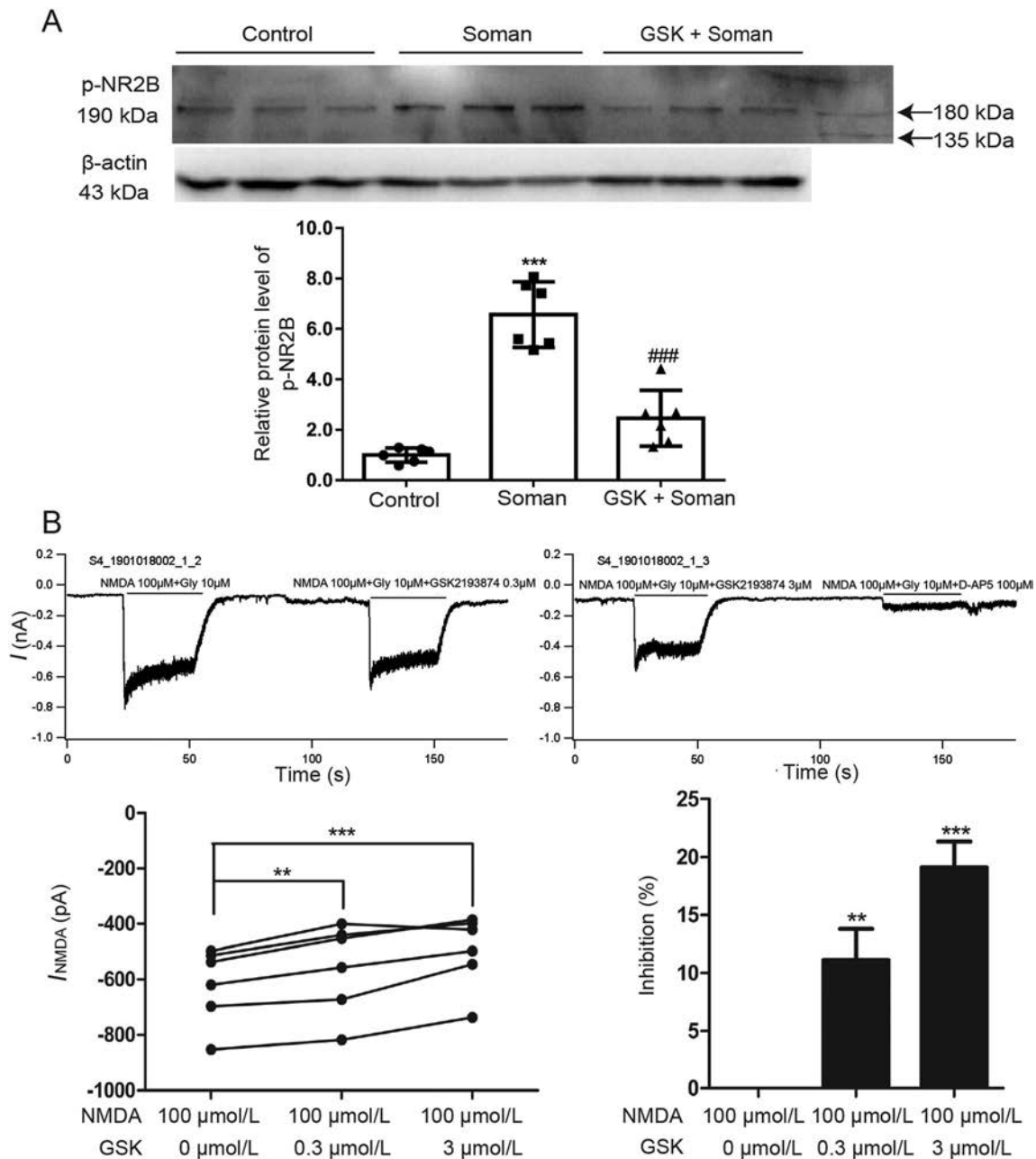


Fig. 3 GSK2193874 inhibits NMDA receptor function. **A** GSK2193874 inhibits NR2B phosphorylation in the hippocampus of rats exposed to soman. Soman group: rats were treated with HI-6 (125 mg/kg i.p.) before soman injection (160 μ g/kg, s.c.); GSK2193874 (GSK) group: rats were additionally treated with the TRPV4 antagonist GSK2193874 (1 mg/kg, i.v.) immediately after HI-6 injection and before soman injection; Control group: rats received HI-6 and solvent instead of the antagonist and soman (mean \pm SD,

$n = 6$; *** $P < 0.001$ vs control group, ### $P < 0.001$ vs soman group, one-way ANOVA and Dunnett's multiple comparison test). **B** GSK2193874 inhibits I_{NMDA} in primary cultured rat hippocampal neurons. In the presence of 0.3 μ mol/L and 3 μ mol/L GSK2193874, I_{NMDA} decreases by $11.13 \pm 2.67\%$ and $19.11 \pm 2.24\%$, respectively ($n = 6$; ** $P < 0.01$, *** $P < 0.001$ vs NMDA 100 μ mol/L group, paired t -test).

Effect of TRPV4 siRNA on Rat Primary Neuron Viability and Intracellular Ca^{2+} Accumulation in NMDA-Induced Excitotoxicity

TRPV4 was knocked down using a specific siRNA (10 nmol/L) and transfected cells were cultured for 24 h with or

without NMDA. Cell viability was reduced after NMDA treatment (100, 200, and 400 μ mol/L) compared with that of the NC siRNA group, while TRPV4 siRNA reversed the decrease in cell viability after NMDA exposure (200 and 400 μ mol/L) (Fig. 5A, $P < 0.05$), similar to the effects of GSK2193874.

Table 1 Effect of GSK2193874 against NMDA-induced seizures and death in rats

	Tonic-clonic seizures	Latency for seizure onset (s)	Mortality
NMDA	95% (19/20)	363.5 ± 173.8	45% (9/20)
Memantine + NMDA	90% (18/20)	627.4 ± 224.1 *	0% (0/20) ***
GSK2193874 + NMDA	65% (13/20) *#	1096.9 ± 558.9 *#	10% (2/20) ***

Data are shown as the mean ± SD, * $P < 0.05$, *** $P < 0.001$ vs NMDA group; # $P < 0.05$ vs Memantine + NMDA group.

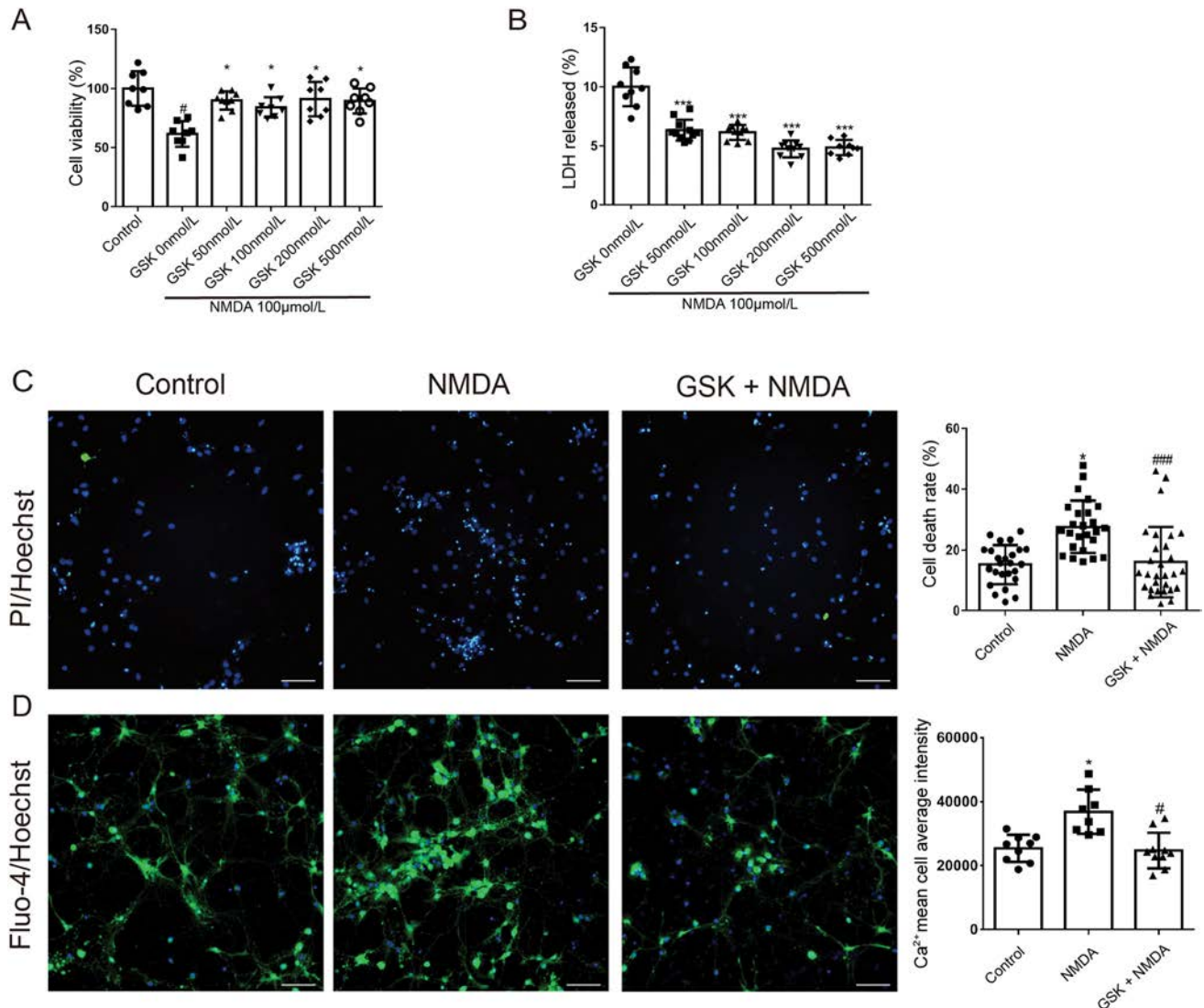


Fig. 4 NMDA-induced cytotoxicity is prevented by GSK2193874. Effect of GSK2193874 against NMDA-induced cytotoxicity assessed by MTT (**A**, $n = 8$) and LDH release (**B**, $n = 10$) assays. Neurons were pretreated with GSK2193874 (50, 100, 200, and 500 nmol/L) for 24 h, and then exposed to NMDA (100 μmol/L) for 24 h [means ± SD; # $P < 0.05$ vs control group, * $P < 0.05$, *** $P < 0.001$ vs GSK2193874 (0 nmol/L) group]. **C** PI⁺/Hoechst⁺ cells are dead cells, and the number of Hoechst⁺ cells indicates the total number of cells (green,

PI; blue, Hoechst; original magnification ×200; scale bars, 50 μm; mean ± SD, $n = 25$; * $P < 0.05$ vs control group, ### $P < 0.001$ vs NMDA group. **D** Intracellular Ca²⁺ concentrations measured with Fluo-4 Direct Calcium Assay kits (green, Fluo-4; blue, Hoechst; original magnification ×200; scale bars, 50 μm; mean ± SD, $n = 8$; * $P < 0.05$ vs control group, # $P < 0.05$ vs NMDA group, one-way ANOVA and Dunnett's multiple comparison test).

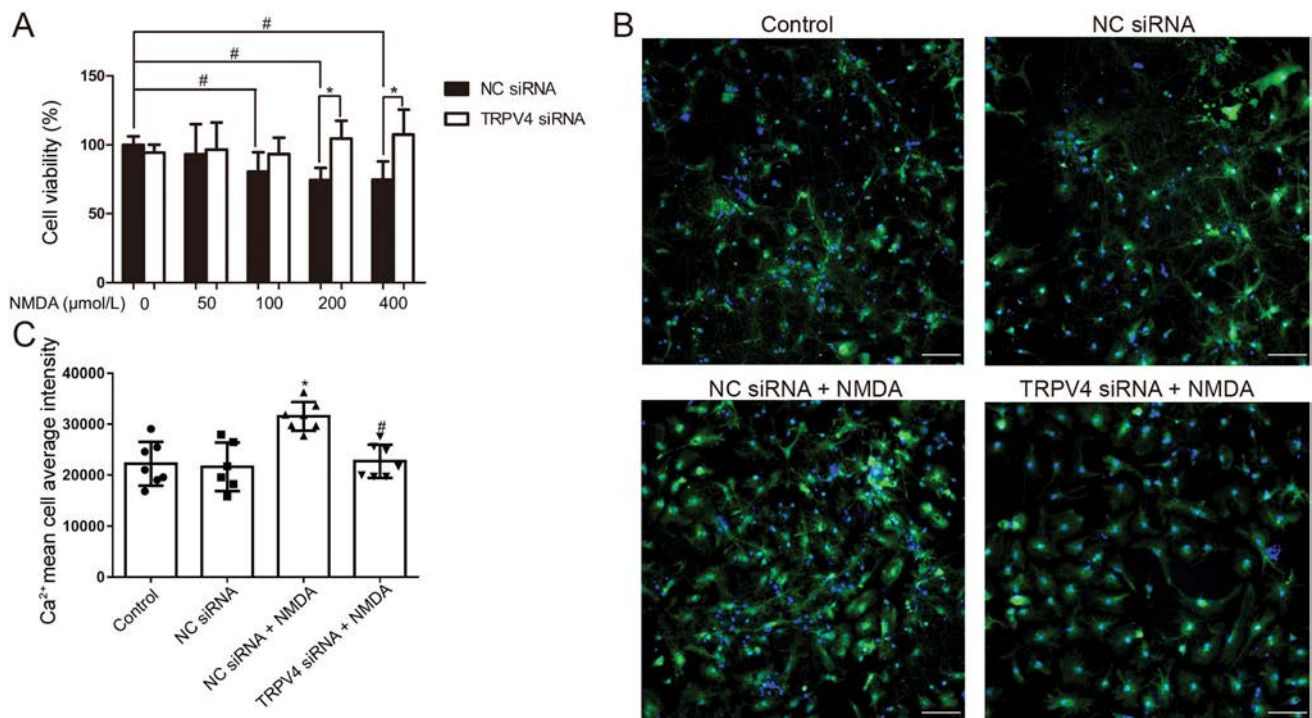


Fig. 5 Knock-down of TRPV4 with siRNA-attenuated NMDA-induced cytotoxicity and calcium accumulation in primary cultured hippocampal neurons. Neurons were pretreated with TRPV4 siRNA (10 nmol/L) for 24 h, and then exposed to NMDA (100 μmol/L) for 24 h. **A** Cell viability evaluated by MTT assays (mean \pm SD, $n = 6$; * $P < 0.05$ vs NC siRNA group, # $P < 0.05$ vs NMDA 0 μmol/L group).

B, C Intracellular Ca²⁺ concentrations measured using Fluo-4 Direct Calcium Assay kits (green, Fluo-4; blue, Hoechst; original magnification $\times 200$; scale bars, 50 μm; mean \pm SD, $n = 7$; * $P < 0.05$ vs negative siRNA group, # $P < 0.05$ vs NMDA group, ANOVA and Dunnett's multiple comparison test).

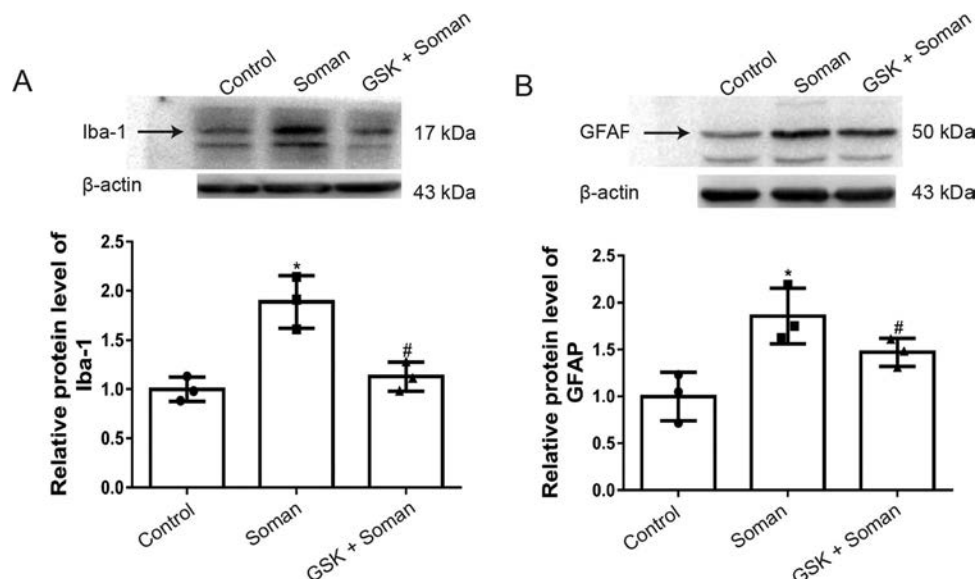


Fig. 6 Activation of astrocytes and microglial cells by soman is attenuated by GSK2193874. Soman group: rats were treated with HI-6 (125 mg/kg i.p.) before soman injection (160 μg/kg, s.c.); GSK2193874 (GSK) group: rats were additionally treated with the TRPV4 antagonist GSK2193874 (1 mg/kg, i.v.) immediately after HI-6 injection and before soman injection; Control group: rats received

HI-6 and solvent instead of the antagonist and soman. Iba-1 and GFAP reflect the activation state of microglial cells and astrocytes, respectively. **A, B** Protein levels of Iba-1 (**A**) and GFAP (**B**) (mean \pm SD, $n = 3$; * $P < 0.05$ vs control group, # $P < 0.05$ vs soman group, one-way ANOVA and Dunnett's multiple comparison test).

Fig. 7 GSK2193874 inhibits NLRP3 inflammasome expression and pro-inflammatory cytokine production in rat hippocampus after soman exposure. Soman group: rats were treated with HI-6 (125 mg/kg i.p.) before soman injection (160 µg/kg, s.c.); GSK2193874 (GSK) group: rats were additionally treated with the TRPV4 antagonist GSK2193874 (1 mg/kg, i.v.) immediately after HI-6 injection and before soman injection; Control group: rats received HI-6 and solvent instead of the antagonist and soman. (A–F) Western blots (A) and analysis of NLRP3 (B), ASC (C), caspase-1 (D), IL-1β (E), IL-18 (F), and β-actin protein levels (mean ± SD, $n = 3$; * $P < 0.05$, *** $P < 0.001$ vs control group, # $P < 0.05$, ### $P < 0.001$ vs soman group, one-way ANOVA and Dunnett's multiple comparison test).

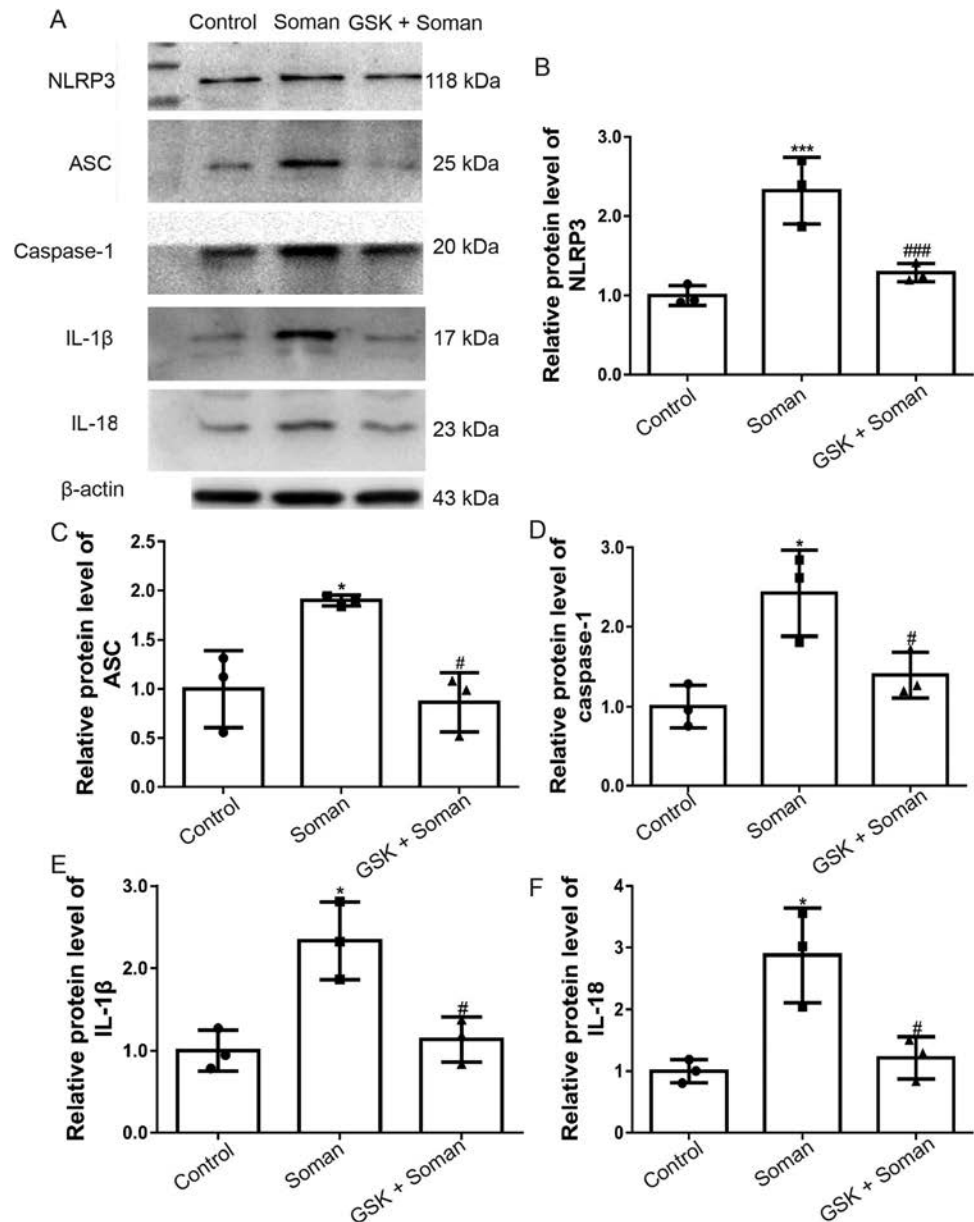


Table 2 Incidence and latency of seizures in WT and TRPV4-KO mice after soman exposure

	Incidence of seizures	Latency for seizure onset (s)
WT	100% (10/10)	419.7 ± 111.5
TRPV4-KO	70% (7/10)*	603.7 ± 212.3*

Data are shown as the mean ± SD, * $P < 0.05$, vs WT.

Moreover, NMDA treatment (100 µmol/L) increased the $[Ca^{2+}]_i$ compared with that in the NC siRNA group, whereas TRPV4 siRNA attenuated the NMDA-induced Ca^{2+} accumulation (Fig. 5B, C; $P < 0.05$).

Effect of GSK2193874 on Microglia and Astrocyte Activation in Rat Hippocampus after Soman Exposure

Glial cells are vital for the initiation of neuroinflammatory responses. In the present study, we explored the effects of a TRPV4 antagonist on soman-induced microglial cell and astrocyte activation. Iba-1 was used as a marker for microglial cells and GFAP (glial fibrillary acidic protein) for astrocytes. The expression level of Iba-1 protein was increased in the rat hippocampus after soman exposure, whereas GSK2193874 abrogated the effects of soman exposure on Iba-1 (Fig. 6A, $P < 0.05$). The expression of GFAP was markedly increased after soman exposure

(Fig. 6B, $P < 0.05$) and attenuated by GSK2193874. These results indicated that soman exposure leads to the activation of microglia cells and astrocytes, while GSK2193874 inhibits it.

Effect of GSK2193874 on NLRP3 Inflammasome Activation and Downstream Pro-inflammatory Cytokine Production in Rat Hippocampus after Soman Exposure

The protein expression levels of NLRP3, ASC, and caspase-1 (Fig. 7A–D) were increased in rat hippocampus after soman exposure compared with the control group ($P < 0.05$, $P < 0.001$). Inflammatory cytokines IL-1 β (Fig. 7A, E) and IL-18 (Fig. 7A, F) were also markedly increased after soman exposure ($P < 0.05$). However, pretreatment with GSK2193874 reversed the effect of soman exposure on NLRP3 inflammasome activation and IL-1 β and IL-18 cytokine expression (Fig. 7A–F, $P < 0.05$). These results indicated that soman promotes NLRP3 inflammasome activation and neuroinflammation, and this is reversed by TRPV4 inhibition.

TRPV4-knockout Protects Against Soman-induced Neurotoxicity by Suppressing NMDAR and NLRP3

To confirm the role of the TRPV4 channel in soman-induced neurotoxicity, we used TRPV4 knockout mice. Wild-type (WT) and TRPV4-KO mice were administered HI-6 (125 mg/kg i.p.) 30 min prior to soman exposure to block peripheral effects, and then were challenged with soman (125 μ g/kg, s.c.). The results showed that, compared with the WT mice, TRPV4-KO mice had fewer seizures, a prolonged seizure latency (Table 2, $P < 0.05$), and a higher survival rate (Fig. 8A, $P < 0.05$). The H&E staining assessment of hippocampal tissue indicated that the neurons of WT control mice were structurally intact with distinct and well-characterized round nucleoli. Soman exposure, however, caused severe pathological injury in the hippocampus of WT mice, with neuronal loss and nuclear pyknosis. Interestingly, assessment of the hippocampal neurons of the TRPV4-KO mice showed reduced histopathological lesions after soman exposure compared with WT mice (Fig. 8B)

To confirm the impact of TRPV4 on soman-induced hyperfunction of NMDARs, NR2B phosphorylation was measured in WT and TRPV4-KO mice by western blot. The results showed that NR2B phosphorylation was higher in the hippocampus of WT mice after soman exposure than in the WT control group, and the phosphorylation was remarkably reversed in the TRPV4-KO group (Fig. 8C, $P < 0.05$).

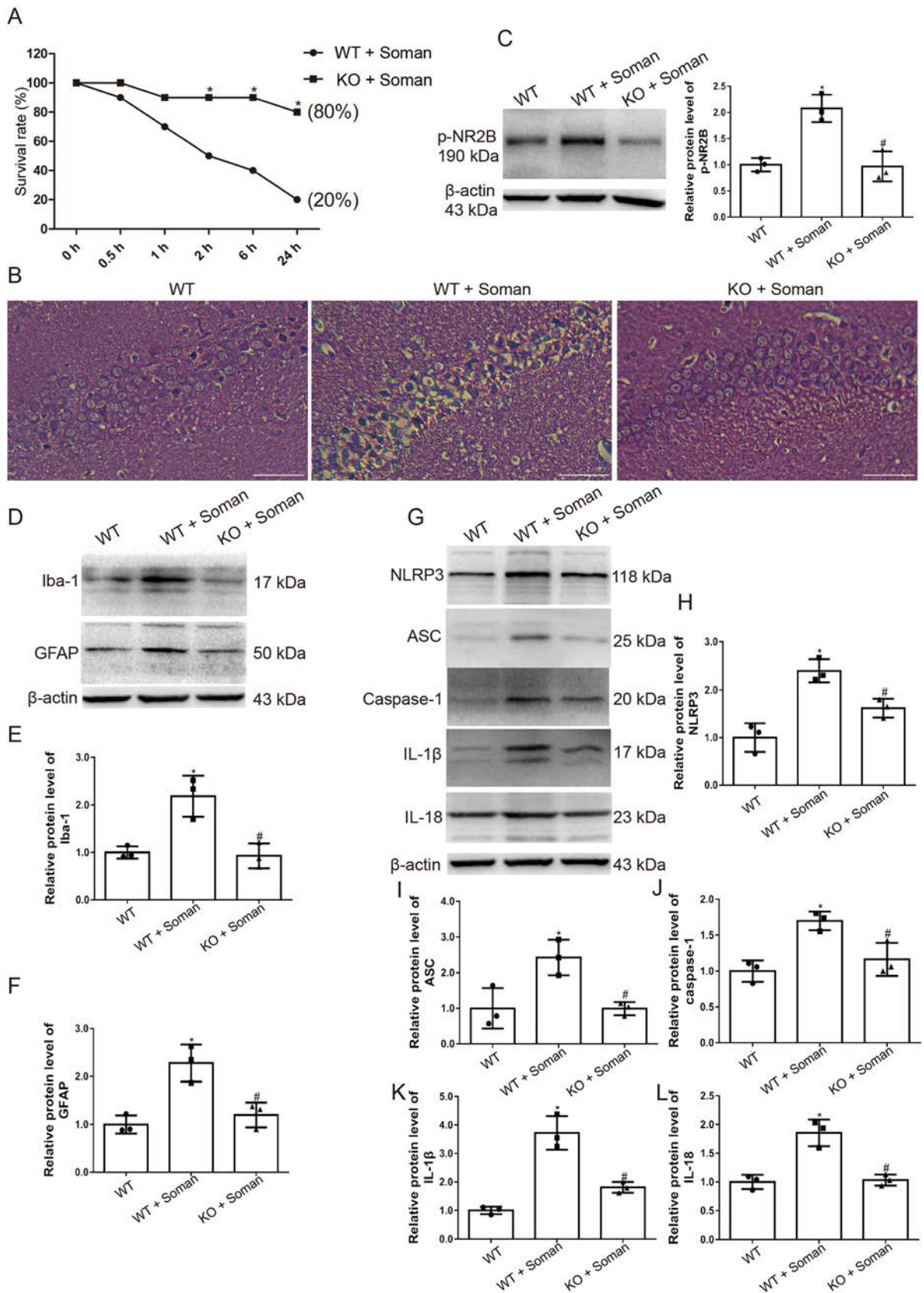
Fig. 8 TRPV4-KO mice are protected against soman exposure. WT mice and TRPV4-KO mice were treated with HI-6 (125 mg/kg i.p.) before soman injection (125 μ g/kg, s.c.). **A** Survival rates calculated as the number of living mice (24 h after soman exposure) divided by the total number of mice ($n = 10$; $*P < 0.05$ vs WT + soman group). **B** Histological assessment showing severe injury, neuron loss, and nuclear pyknosis in the WT + soman group; TRPV4-KO reduces the histopathologic lesions in the hippocampus of mice caused by soman exposure ($\times 200$, original magnification, scale bars, 50 μ m). **C** TRPV4-KO inhibits NR2B phosphorylation in the hippocampus of mice exposed to soman, compared to the WT + soman group (mean \pm SD, $n = 3$; $*P < 0.05$ vs WT group, $^{\#}P < 0.05$ vs WT + soman group). **D, E** Iba-1 reflects the activation state of microglial cells. Activation of astrocytes and microglial cells induced by soman is attenuated by TRPV4-KO (mean \pm SD, $n = 3$; $*P < 0.05$ vs WT group, $^{\#}P < 0.05$ vs WT + soman group). **D, F** GFAP reflects the activation of astrocytes. Activation of astrocytes induced by soman is attenuated by TRPV4-KO (mean \pm SD, $n = 3$; $*P < 0.05$ vs WT group, $^{\#}P < 0.05$ vs WT + soman group). **G–L** Western blots (**G**) and analysis of expression of the NLRP3 inflammasome complex proteins NLRP3 (**H**), ASC (**I**), caspase-1 (**J**), and downstream inflammatory cytokines IL-1 β (**K**), IL-18 (**L**), and β -actin (mean \pm SD, $n = 3$; $*P < 0.05$ vs WT group, $^{\#}P < 0.05$ vs WT + soman group, one-way ANOVA and Dunnett's multiple comparison test).

Then we explored the effects of TRPV4 deletion on soman-induced microglial and astrocyte activation. The protein levels of both Iba-1 and GFAP were increased in WT mice hippocampus after soman exposure, while knocking out TRPV4 abrogated the effects of soman exposure on the activation of microglia and astrocytes (Fig. 8D–F, $P < 0.05$).

The effects of the deletion of TRPV4 on the activation of the NLRP3 inflammasome and the production of downstream pro-inflammatory cytokines in mouse hippocampus after soman exposure were measured by western blot. The expression levels of NLRP3, ASC, and caspase-1 protein were increased in WT hippocampus after soman exposure compared the WT control group ($P < 0.05$) (Fig. 8G–J). Meanwhile, IL-1 β and IL-18 were also clearly increased after soman exposure ($P < 0.05$) (Fig. 8G, K, L). However, the soman-induced NLRP3 inflammasome activation and IL-1 β and IL-18 production were abrogated in the TRPV4-KO mice (Fig. 8G–L, $P < 0.05$). These results indicated that soman promotes NLRP3 inflammasome activation and neuroinflammation, which can be reversed by deleting TRPV4.

Discussion

Several studies have focused on the role of TRPV4 in modulating nervous system functions due to its widespread expression and Ca²⁺ permeability. Reports have demonstrated that the neurotoxicity caused by TRPV4 over-activation is an important factor in intracerebral



hemorrhage and cerebral ischemic injury [35, 36]. Seizure-related neural activity triggered by an increase in brain temperature is blocked by a TRPV4 antagonist in larval zebrafish [25]. Furthermore, TRPV4 expression is significantly increased in cortical tubers of the tuberous sclerosis complex, a known form of therapy-refractory epilepsy [37]. Taken together, these data imply that TRPV4 is involved in the pathogenesis of epilepsy. In this study, we demonstrated that TRPV4 blockade or deletion was protective against soman-induced SE and neuroinflammation. Its mechanisms of action included a decrease in NMDAR-mediated excitotoxicity and suppression of the NLRP3-mediated neuroinflammatory response.

Our data showed that exposure to soman led to an increase of TRPV4 protein levels in rat hippocampal cells, while treatment with the TRPV4 antagonist GSK2193874 protected the cells against soman poisoning, as reflected by improved survival rates and suppressed behavioral seizures. Unlike anticholinergics, GSK2193874 did not block the onset of soman-induced seizures in rats, but did relieve and terminate seizures, similar to the effect of NMDA antagonists [10]. The reason for this phenomenon is that the seizures after soman exposure are initiated by an increase in ACh levels following the irreversible inhibition of brain AChE by soman. Once initiated, non-cholinergic neurotransmitter systems, especially the NMDARs of the glutamatergic excitatory amino-acid system, are rapidly perturbed by the excitatory activity of the seizure itself, and as it progresses, non-cholinergic excitatory activity gradually gains control over the seizure independent of the initiating cholinergic drive [3]. Activation of NMDARs sustains seizure activity and increases the excessive levels of $[Ca^{2+}]_i$, which launches biochemical reactions that lead to neuronal death. Previous studies have suggested that the NR2B subunit of NMDARs is the major factor in excitotoxicity, with the phosphorylation of tyrosine 1472 (Tyr1472) site of NR2B considered as the vital pathway for excitotoxicity [34, 38]. In our study, soman exposure led to NMDAR activation *via* up-regulation of NR2B phosphorylation (Tyr1472) in the rat hippocampus, which was reversed by GSK2193874 or TRPV4-KO. Moreover, our *in vitro* experiments showed that NMDA-induced I_{NMDA} was markedly attenuated by a TRPV4 antagonist indicating that TRPV4 inhibition impedes activation of NMDARs and their mediated I_{NMDA} . Furthermore, NMDA-induced neurotoxicity was significantly increased in rat primary cultured hippocampal neurons, and pretreatment with GSK2193874 or TRPV4 siRNA reduced the cytotoxicity after NMDA exposure, as reflected in increased cell viability and reduced LDH release. Furthermore, NMDA-induced Ca^{2+} accumulation was also inhibited by GSK2193874 or TRPV4 siRNA. Therefore, our findings strongly suggest that TRPV4 activation induces NMDAR-

mediated excitotoxicity, resulting in seizures and secondary brain injury after soman exposure. This is supported by a previous study using a cerebral ischemia model, which indicated that activation of TRPV4 facilitates and prolongs the glutamate excitotoxicity by potentiating the NMDAR response [24]. In addition, there are limitations in the clinical applications of NMDA antagonists due to their side-effects [39–42]; blocking the TRP channel appears to inhibit NMDAR function by diminishing membrane depolarization and not by directly blocking NMDARs [43, 44], suggesting that TRPV4 is a promising novel target for treatment. However, more evidence is required, and the specific mechanisms of action need to be elucidated in future work.

TRPV4 is strongly expressed in rat hippocampal astrocytes and microglial cells that have been reported to be involved in neuronal injury induced by neuroinflammation. More specifically, TRPV4 is responsible for amyloid β -induced neuronal and astrocytic damage [20] and, in its closed state, inhibits the influx of Ca^{2+}_i and decreases the levels of IL-1 β and TNF- α in lipopolysaccharide-activated microglial cells [45]. A recent study showed that the TRPV4 agonist GSK1016790A initiates the NLRP3-related inflammatory process by activating astrocytes and microglia [27]. The NLRP3 inflammasome, an integral part of the innate immune system, is a cytoplasmic complex in which NLRP3 interacts with the adaptor protein ASC to enable the recruitment and activation of caspase-1, leading to the maturation of IL-1 β and IL-18. In our study, astrocytes and microglial cells were activated in the hippocampus of rats and mice after soman exposure and were attenuated by GSK2193874. Furthermore, blocking or deletion of TRPV4 inhibited the up-regulation of NLRP3, ASC, caspase-1, and the downstream IL-1 β and IL-18 protein levels induced by soman. Our results suggest that TRPV4 is involved in the activation of astrocytes and microglia induced by soman and we provide the first evidence that NLRP3 is involved in the inflammatory response after soman exposure, which may be regulated by the TRPV4 channel.

In conclusion, we demonstrated that the “dual-switch” function of TRPV4 mediating Ca^{2+} influx causes changes in downstream pathways, leading to seizures and secondary brain injury when exposed to soman. Once we turned off the switch by blocking or deleting the TRPV4 channel, a marked protective effect against soman-induced SE and neuroinflammation occurred, *via* decreased NMDAR-mediated excitotoxicity and reduction in the NLRP3-mediated neuroinflammatory response. The present study provides useful data for future research, particularly for the treatment of casualties caused by exposure to nerve agents or organophosphorus pesticides.

Acknowledgements This work was supported by the Special Fund for Military Medical Science (AWS15J007 and BWS16J007) and the National Natural Science Foundation of China (81703505).

Conflict of interest The authors claim that there are no conflicts of interest.

References

- Dolgin E. Syrian gas attack reinforces need for better anti-sarin drugs. *Nat Med* 2013, 19: 1194–1195.
- Chai PR, Hayes BD, Erickson TB, Boyer EW. Novichok agents: a historical, current, and toxicological perspective. *Toxicol Commun* 2018, 2: 45–48.
- McDonough JH Jr, Shih TM. Neuropharmacological mechanisms of nerve agent-induced seizure and neuropathology. *Neurosci Biobehav Rev* 1997, 21: 559–579.
- McDonough JH Jr, Shih TM. A study of the N-methyl-D-aspartate antagonistic properties of anticholinergic drugs. *Pharmacol Biochem Behav* 1995, 51: 249–253.
- Shih T, McDonough JH Jr, Koplovitz I. Anticonvulsants for soman-induced seizure activity. *J Biomed Sci* 1999, 6: 86–96.
- Skovira JW, McDonough JH, Shih TM. Protection against sarin-induced seizures in rats by direct brain microinjection of scopolamine, midazolam or MK-801. *J Mol Neurosci* 2010, 40: 56–62.
- Olney JW, Collins RC, Sloviter RS. Excitotoxic mechanisms of epileptic brain damage. *Adv Neurol* 1986, 44: 857–877.
- Sloviter RS, Dempster DW. “Epileptic” brain damage is replicated qualitatively in the rat hippocampus by central injection of glutamate or aspartate but not by GABA or acetylcholine. *Brain Res Bull* 1985, 15: 39–60.
- Braitman DJ, Sparenborg S. MK-801 protects against seizures induced by the cholinesterase inhibitor soman. *Brain Res Bull* 1989, 23: 145–148.
- Carpentier P, Foquin-Tarricone A, Bodjarian N, Rondouin G, Lerner-Natoli M, Kamenka JM. Anticonvulsant and antilethal effects of the phencyclidine derivative TCP in soman poisoning. *Neurotoxicology* 1994, 15: 837–851.
- Shih TM, Koenig JA, Acon Chen C. Comparative effects of scopolamine and phencyclone on organophosphorus nerve agent-induced seizure activity, neuropathology and lethality. *Toxicol Mech Methods* 2019, 29: 322–333.
- Sparenborg S, Brennecke LH, Jaax NK, Braitman DJ. Dizocilpine (MK-801) arrests status epilepticus and prevents brain damage induced by soman. *Neuropharmacology* 1992, 31: 357–368.
- Zimmer LA, Ennis M, Shipley MT. Soman-induced seizures rapidly activate astrocytes and microglia in discrete brain regions. *J Comp Neurol* 1997, 378: 482–492.
- Ferrara-Bowen TM, Chandler JK, Guignet MA, Irwin JF, Laitypay K, Palmer DD, *et al.* Neuropathological and behavioral sequelae in IL-1R1 and IL-1Ra gene knockout mice after soman (GD) exposure. *Neurotoxicology* 2017, 63: 43–56.
- Johnson EA, Guignet MA, Dao TL, Hamilton TA, Kan RK. Interleukin-18 expression increases in response to neurovascular damage following soman-induced status epilepticus in rats. *J Inflamm (Lond)* 2015, 12: 43.
- Svensson I, Waara L, Johansson L, Bucht A, Cassel G. Soman-induced interleukin-1 beta mRNA and protein in rat brain. *Neurotoxicology* 2001, 22: 355–362.
- Williams AJ, Berti R, Yao C, Price RA, Velarde LC, Koplovitz I, *et al.* Central neuro-inflammatory gene response following soman exposure in the rat. *Neurosci Lett* 2003, 349: 147–150.
- Shibasaki K. TRPV4 ion channel as important cell sensors. *J Anesth* 2016, 30: 1014–1019.
- Moore C, Gupta R, Jordt SE, Chen Y, Liedtke WB. Regulation of pain and itch by TRP Channels. *Neurosci Bull* 2018, 34: 120–142.
- Bai JZ, Lipski J. Involvement of TRPV4 channels in A β ₄₀-induced hippocampal cell death and astrocytic Ca²⁺ signalling. *Neurotoxicology* 2014, 41: 64–72.
- Jie P, Hong Z, Tian Y, Li Y, Lin L, Zhou L, *et al.* Activation of transient receptor potential vanilloid 4 induces apoptosis in hippocampus through downregulating PI3K/Akt and upregulating p38 MAPK signaling pathways. *Cell Death Dis* 2015, 6: e1775.
- Lu KT, Huang TC, Tsai YH, Yang YL. Transient receptor potential vanilloid type 4 channels mediate Na-K-Cl-co-transporter-induced brain edema after traumatic brain injury. *J Neurochem* 2017, 140: 718–727.
- Men C, Wang Z, Zhou L, Qi M, An D, Xu W, *et al.* Transient receptor potential vanilloid 4 is involved in the upregulation of connexin expression following pilocarpine-induced status epilepticus in mice. *Brain Res Bull* 2019, 152: 128–133.
- Li L, Qu W, Zhou L, Lu Z, Jie P, Chen L, *et al.* Activation of transient receptor potential vanilloid 4 increases NMDA-activated current in hippocampal pyramidal neurons. *Front Cell Neurosci* 2013, 7: 17.
- Hunt RF, Hortopan GA, Gillespie A, Baraban SC. A novel zebrafish model of hyperthermia-induced seizures reveals a role for TRPV4 channels and NMDA-type glutamate receptors. *Exp Neurol* 2012, 237: 199–206.
- Shibasaki K, Suzuki M, Mizuno A, Tominaga M. Effects of body temperature on neural activity in the hippocampus: regulation of resting membrane potentials by transient receptor potential vanilloid 4. *J Neurosci* 2007, 27: 1566–1575.
- Wang Z, Zhou L, An D, Xu W, Wu C, Sha S, *et al.* TRPV4-induced inflammatory response is involved in neuronal death in pilocarpine model of temporal lobe epilepsy in mice. *Cell Death Dis* 2019, 10: 386.
- Wang YA, Zhou WX, Li JX, Liu YQ, Yue YJ, Zheng JQ, *et al.* Anticonvulsant effects of phencyclone hydrochloride and other anticholinergic drugs in soman poisoning: neurochemical mechanisms. *Life Sci* 2005, 78: 210–223.
- Yang J, Fan L, Wang F, Luo Y, Sui X, Li W, *et al.* Rapid-releasing of HI-6 via brain-targeted mesoporous silica nanoparticles for nerve agent detoxification. *Nanoscale* 2016, 8: 9537–9547.
- Racine RJ. Modification of seizure activity by electrical stimulation. II. Motor seizure. *Electroencephalogr Clin Neurophysiol* 1972, 32: 281–294.
- Apland JP, Aroniadou-Anderjaska V, Figueiredo TH, Green CE, Swezey R, Yang C, *et al.* Efficacy of the GluK1/AMPA receptor antagonist LY293558 against seizures and neuropathology in a soman-exposure model without pretreatment and its pharmacokinetics after intramuscular administration. *J Pharmacol Exp Ther* 2013, 344: 133–140.
- Prager EM, Figueiredo TH, Long RP 2nd, Aroniadou-Anderjaska V, Apland JP, Braga MF. LY293558 prevents soman-induced pathophysiological alterations in the basolateral amygdala and the development of anxiety. *Neuropharmacology* 2015, 89: 11–18.
- Bohnert S, van den Berg RM, Mikler J, Klaassen SD, Joosen MJA. Pharmacokinetics of three oximes in a guinea pig model and efficacy of combined oxime therapy. *Toxicol Lett* 2020, 324: 86–94.

34. Li Y, Sun W, Han S, Li J, Ding S, Wang W, *et al.* IGF-1-involved negative feedback of NR2B NMDA subunits protects cultured hippocampal neurons against NMDA-induced excitotoxicity. *Mol Neurobiol* 2017, 54: 684–696.
35. Jie P, Lu Z, Hong Z, Li L, Zhou L, Li Y, *et al.* Activation of transient receptor potential vanilloid 4 is involved in neuronal injury in middle cerebral artery occlusion in mice. *Mol Neurobiol* 2016, 53: 8–17.
36. Zhao H, Zhang K, Tang R, Meng H, Zou Y, Wu P, *et al.* TRPV4 blockade preserves the blood-brain barrier by inhibiting stress fiber formation in a rat model of intracerebral hemorrhage. *Front Mol Neurosci* 2018, 11: 97.
37. Chen X, Yang M, Sun F, Liang C, Wei Y, Wang L, *et al.* Expression and cellular distribution of transient receptor potential vanilloid 4 in cortical tubers of the tuberous sclerosis complex. *Brain Res* 2016, 1636: 183–192.
38. Xu XX, Luo JH. Mutations of N-methyl-D-aspartate receptor subunits in epilepsy. *Neurosci Bull* 2018, 34: 549–565.
39. Olney JW, Labruyere J, Price MT. Pathological changes induced in cerebrocortical neurons by phencyclidine and related drugs. *Science* 1989, 244: 1360–1362.
40. Olney JW, Labruyere J, Wang G, Wozniak DF, Price MT, Sesma MA. NMDA antagonist neurotoxicity: mechanism and prevention. *Science* 1991, 254: 1515–1518.
41. Allen HL, Iversen LL. Phencyclidine, dizocilpine, and cerebrocortical neurons. *Science* 1990, 247: 221.
42. Fix AS, Horn JW, Wightman KA, Johnson CA, Long GG, Storts RW, *et al.* Neuronal vacuolization and necrosis induced by the noncompetitive N-methyl-D-aspartate (NMDA) antagonist MK(+)-801 (dizocilpine maleate): a light and electron microscopic evaluation of the rat retrosplenial cortex. *Exp Neurol* 1993, 123: 204–215.
43. Chen J, Li Z, Hatcher JT, Chen QH, Chen L, Wurster RD, *et al.* Deletion of TRPC6 attenuates NMDA receptor-mediated Ca^{2+} entry and Ca^{2+} -Induced neurotoxicity following cerebral ischemia and oxygen-glucose deprivation. *Front Neurosci* 2017, 11: 138.
44. Menigoz A, Ahmed T, Sabanov V, Philippaert K, Pinto S, Kerselaers S, *et al.* TRPM4-dependent post-synaptic depolarization is essential for the induction of NMDA receptor-dependent LTP in CA1 hippocampal neurons. *Pflugers Arch* 2016, 468: 593–607.
45. Liu M, Liu X, Wang L, Wang Y, Dong F, Wu J, *et al.* TRPV4 inhibition improved myelination and reduced glia reactivity and inflammation in a cuprizone-induced mouse model of demyelination. *Front Cell Neurosci* 2018, 12: 392.



CCL2/CCR2 Contributes to the Altered Excitatory-inhibitory Synaptic Balance in the Nucleus Accumbens Shell Following Peripheral Nerve Injury-induced Neuropathic Pain

Xiao-Bo Wu¹ · Qian Zhu¹ · Yong-Jing Gao^{1,2}

Received: 17 July 2020 / Accepted: 10 February 2021 / Published online: 18 May 2021

© Center for Excellence in Brain Science and Intelligence Technology, Chinese Academy of Sciences 2021

Abstract The medium spiny neurons (MSNs) in the nucleus accumbens (NAc) integrate excitatory and inhibitory synaptic inputs and gate motivational and emotional behavior output. Here we report that the relative intensity of excitatory and inhibitory synaptic inputs to MSNs of the NAc shell was decreased in mice with neuropathic pain induced by spinal nerve ligation (SNL). SNL increased the frequency, but not the amplitude of spontaneous inhibitory postsynaptic currents (sIPSCs), and decreased both the frequency and amplitude of spontaneous excitatory postsynaptic currents (sEPSCs) in the MSNs. SNL also decreased the paired-pulse ratio (PPR) of evoked IPSCs but increased the PPR of evoked EPSCs. Moreover, acute bath application of C–C motif chemokine ligand 2 (CCL2) increased the frequency and amplitude of sIPSCs and sEPSCs in the MSNs, and especially strengthened the amplitude of N-methyl-D-aspartate receptor (NMDAR)-mediated miniature EPSCs. Further *Ccl2* overexpression in the NAc *in vivo* decreased the peak amplitude of the sEPSC/sIPSC ratio. Finally, *Ccr2* knock-down improved the impaired induction of NMDAR-dependent long-term depression (LTD) in the NAc after SNL. These results suggest that CCL2/CCR2 signaling plays a role in the integration of excitatory/inhibitory synaptic transmission

and leads to an increase of the LTD induction threshold at the synapses of MSNs during neuropathic pain.

Keywords E/I balance · Synaptic transmission · LTD · CCL2 · CCR2 · Nucleus accumbens · Neuropathic pain

Introduction

The nucleus accumbens (NAc) plays a critical role in mediating reward, motivation, depression, and chronic pain. Medium spiny neurons (MSNs), the main projection neurons in the NAc, are involved in a decrease of motivation under chronic pain conditions [1], as well as an increase of pain sensitivity and the induction of depression after nerve injury [2, 3]. Interrupting the activity of the MSNs in the medial shell of the NAc relieves peripheral nerve injury-induced neuropathic pain in rats [4]. Electrophysiological studies have shown that nerve injury changes the excitatory glutamatergic transmission at synapses of MSNs in the NAc [1, 2], manifested as a decreased ratio of α -amino-3-hydroxy-5-methyl-4-isoxazolepropionic acid receptor (AMPA)- to N-methyl-D-aspartate receptor (NMDAR)-mediated currents [1] and changes in the function of specific AMPAR and NMDAR subunits [1, 5]. Accordingly, the expression levels of the GluA1 subunit of the AMPAR and the GluN2B subunit of the NMDAR are increased on the postsynaptic membrane surface in MSNs of the NAc under neuropathic pain conditions [1, 5–7]. Although chronic pain-induced neural adaptations at excitatory glutamatergic synapses have been investigated, little is known about how inhibitory synaptic input to MSNs of the NAc is affected during neuropathic pain.

✉ Xiao-Bo Wu
xbwu1983@ntu.edu.cn

✉ Yong-Jing Gao
gaoyongjing@ntu.edu.cn; gaoyongjing@hotmail.com

¹ Institute of Pain Medicine and Special Environmental Medicine, Nantong University, Nantong 226019, China

² Co-innovation Center of Neuroregeneration, Nantong University, Nantong 226001, China

The MSNs integrate GABAergic inhibitory synaptic inputs from intrinsic and extrinsic sources [8, 9]. Finely-tuned excitatory and inhibitory synaptic transmission to a neuron regulates the functional state for action potential discharge and gates synaptic plasticity [10–12]. It has been demonstrated that impaired excitatory/inhibitory (E/I) balance in the spinal cord contributes to central sensitization and chronic pain [12]. In the brain, disruption of the E/I balance in the somatosensory cortex is linked to large-scale neuronal plasticity and pain sensitivity in mice with multiple sclerosis [13]. More recent evidence has shown that nerve injury attenuates the overall E/I balance of basolateral amygdala inputs to prefrontal cortex neurons [14]. The NAc shell plays an important role in mediating neuropathic pain [2, 15]. Whether the E/I synaptic balance in the MSNs of NAc shell is altered under neuropathic pain condition deserves investigation.

Chemokine CCL2 (also called monocyte chemoattractant protein 1) and its receptor CCR2 are involved in the pathogenesis of neuropathic pain *via* increasing glutamatergic synaptic transmission in the spinal cord [16]. In addition, our recent study showed that peripheral nerve injury increases the expression of CCL2 and CCR2 in the MSNs of the NAc shell. Importantly, inhibition of CCR2 in the NAc shell by shRNA or an antagonist attenuates spinal nerve ligation (SNL)-induced neuropathic pain and the associated depressive behaviors in mice [3]. Consistent with this, overexpression of CCL2 in the NAc induces pain hypersensitivity and depression-like behaviors [3]. In addition, CCL2/CCR2 increases NMDAR-mediated currents in the cells *via* activating extracellular signaling-regulated kinase (ERK) [3, 17]. It has been reported that the enhanced function of NMDARs modulates the magnitude of long-term depression (LTD) induced by low-frequency stimulation (LFS) at MSN synapses in the NAc [18, 19]. Moreover, nerve injury- or inflammation-induced chronic pain attenuates and even impairs the induction of LTD in the anterior cingulate cortex [20, 21]. Whether CCL2/CCR2 signaling in the NAc shell regulates neuropathic pain and depression [3] *via* modulation of the E/I balance and NMDAR-mediated LTD remains unknown.

In the current study, we first assessed the impact of SNL on the excitatory-inhibitory current ratio at MSN synapses in the NAc shell and confirmed that the E/I balance was disrupted under SNL-induced neuropathic pain conditions. We also found that the increased CCL2/CCR2 in the NAc after SNL contributed to the disrupted E/I balance and NMDAR-mediated LTD in the NAc shell.

Materials and Methods

Animals and Surgery

Male ICR mice (8–12 weeks) were purchased from the Experimental Animal Center of Nantong University and housed in the Animal Facility of Nantong University. The SNL model was created as previously described [22]. Briefly, mice were anesthetized with 2% isoflurane and the bilateral L5 spinal nerves were exposed and ligated. For sham operation, the L5 spinal nerves were exposed but not ligated. All the procedures were approved by the Animal Care and Use Committee of Nantong University and performed in accordance with the institutional guidelines for the International Association for the Study of Pain.

Lentiviral Vector Construction and Intra-NAc Injection

The *Ccl2*-overexpression lentivirus (LV-*Ccl2*) and negative control lentivirus (LV-NC) were generated as described in our previous study [3]. In brief, recombinant lentivirus expressing *Ccl2* vector was designed by using the pGV365 lentiviral expression vector to generate pLV-Ubi-Ccl2-3FLAG-CMVEGFP (LV-*Ccl2*). A lentiviral vector that expressed GFP alone (LV-NC) was produced as control. In addition, shRNAs targeting the mice *Ccr2* and negative control (NC) were also designed as described previously [3]. The recombinant lentivirus shRNA-expressing vectors containing NC (LV-NC, scramble-shRNA) or *Ccr2* (LV-*Ccr2* shRNA, 5'-TGC ATT AAT CCT GTC ATT T-3') were constructed using pGCSIL-GFP vector by Shanghai GeneChem. To inject the lentivirus, mice were anesthetized using isoflurane. The head was fixed in a stereotaxic apparatus. Two holes were drilled on the skull (anteroposterior: bregma +1.53 mm, lateral: ± 0.8 mm, depth: 4.82 mm). The lentivirus (0.25 μ L per side) was injected into the NAc through a 32G needle (Hamilton) within 10 min. After the injection, the needle remained in the position for 5–6 min, and the scalp was sutured.

NAc Slice Preparation

NAc slices were prepared and patch-clamp recordings were made as previously described [3]. Briefly, each mouse was deeply anesthetized with 5% isoflurane and sacrificed 14 to 21 days after SNL or sham operation. The brain was quickly removed, and sagittal slices (300 μ m) containing the NAc and prefrontal cortex were cut on a Vibratome (VT1000S; Leica, Germany) in sucrose-rich ice-cold artificial cerebrospinal fluid (aCSF) containing (in mmol/

L): 235 sucrose, 25 NaHCO₃, 2.5 KCl, 1.2 CaCl₂, 1.25 NaH₂PO₄, 2.5 MgCl₂, and 10 glucose (pH 7.2–7.4 when bubbled with 95% O₂ and 5% CO₂). Slices were incubated in normal aCSF (oxygenated with 95% O₂ and 5% CO₂) containing (in mmol/L): 125 NaCl, 1.25 NaH₂PO₄, 3 KCl, 1.2 MgCl₂, 2.4 CaCl₂, 26 NaHCO₃, and 11 glucose for 30 min at 34°C and subsequently kept at room temperature until transfer to the recording chamber.

Patch-clamp Recording from NAc Shell Slices

MSNs within the NAc shell were visualized under a BX51WI infrared-differential interference contrast microscope (Olympus, Japan). Patch-clamp recordings of inhibitory or excitatory postsynaptic currents (IPSC/EPSC) at synapses of NAc shell neurons were conducted with a patch-clamp amplifier (Multiclamp 700B; Axon Instruments, Burlingame, CA). Currents were filtered at 2 kHz and sampled at 10 kHz with a digitizer (DigiData 1440A; Axon Instruments). All recordings were analyzed using Clampfit 10.4 software (Molecular Devices, Sunnyvale, CA). MSNs in the NAc slice were identified by their small size (< 20 μm) and hyperpolarized resting membrane potential (–75 to –85 mV). The tip of the electrode was 4–8 MΩ when filled with patch pipette internal solution containing (in mmol/L): 120 CsMeSO₃, 2 NaCl, 20 HEPES, 5 tetraethylammonium-Cl, 2.5 Na₂ATP, 0.4 EGTA 0.3 GTP-Tris, and 2.5 mmol/L QX-314 (pH 7.2–7.4, adjusted with CsOH). A concentric bipolar electrode was placed at the border between the prefrontal cortex (PFC) and NAc, which mainly stimulated the PFC-synaptic transmission input to the MSNs [23]. Synaptic afferents were stimulated at 0.1 Hz (100-μs pulses) by a programmable stimulator (Master-8, A.M.P.I., Jerusalem, Israel). The stimulation intensity that evoked a half-maximum synaptic response was used in the experiments. Input resistance was monitored online with a depolarizing step voltage (+5 mV, 200 ms) following each afferent stimulus, and the data were discarded if the resistance changed by > 25%. Total evoked postsynaptic currents of NAc shell MSNs containing AMPAR-mediated EPSCs and GABA_A-receptor-mediated IPSCs were recorded at a holding voltage of –70 mV in normal aCSF. After recording a stable total postsynaptic current baseline, the AMPAR-mediated EPSC was isolated by perfusing with the GABA_A receptor antagonist picrotoxin (PTX, 100 μmol/L), and digital subtraction of the AMPAR-mediated EPSC from the total postsynaptic current in the same neuron yielded the GABA_A-receptor-mediated IPSC. For sEPSC recording, the membrane voltage was held at –70 mV and the cells were perfused by aCSF with 100 μmol/L PTX and 1 μmol/L strychnine. The sIPSCs were recorded with the voltage held at 0 mV (because the reversal

potential for EPSCs was near 0 mV), and 1 μmol/L strychnine was added to the aCSF to block glycine receptor-mediated IPSCs. To calculate ratios of sEPSC/sIPSC peak amplitude and frequency, the sIPSCs and sEPSCs were recorded from the same neuron. Traces for the analyzed ratios were averaged from 80–100 consecutive sIPSCs or sEPSCs. To determine the paired-pulse ratio (PPR), which reflects the transmitter release probability at presynaptic sites, two IPSCs or EPSCs were evoked at an inter-stimulus-interval of 50 ms or 200 ms. The PPR value was calculated by dividing the amplitude of the second event by that of the first event. LTD was induced by low-frequency stimulation (LFS, pulse duration 100 μs, 1 Hz, 900 pulses). The stimulating electrode was positioned at the same location as that in the evoked EPSCs and IPSCs recording.

The total spontaneous miniature EPSCs (mEPSCs) that contain both NMDAR- and AMPAR-mediated components were recorded in the presence of tetrodotoxin (1 μmol/L) and PTX (100 μmol/L) and patch-clamped at –60 mV with Mg²⁺-free aCSF perfusion. The AMPAR- and NMDAR-mediated mEPSCs were isolated by perfusing with the NMDAR antagonist AP-5 (50 μmol/L). AMPAR- and NMDAR-mEPSC components were analyzed as previously described [23]. NMDA-induced currents were recorded by puff application of NMDA (20 μmol/L; Sigma-Aldrich) at a holding potential of –45 mV.

Data Analysis and Statistics

Results are expressed as the mean ± SEM. Each data set to be tested statistically was first tested for normality by the Shapiro-Wilk test. If data were not normally distributed, we used the non-parametric Mann-Whitney test. Otherwise, the data were analyzed *via* Student's *t*-test, one-way or two-way ANOVA with repeated-measures (RM) or regular ANOVA measures, followed by the LSD *post hoc* test. The inter-event intervals and amplitudes for the distribution of sIPSCs or sEPSCs were measured with Kolmogorov–Smirnov (K–S) analysis and the unpaired Student's *t*-test. The criterion of statistical significance was set at *P* < 0.05.

Results

SNL Decreases the E/I Ratio in MSNs of the NAc Shell

Our previous study has shown that SNL induces persistent pain hypersensitivity and depression-like behaviors [3]. To understand the synaptic mechanism underlying the behavioral changes after SNL, we performed whole-cell patch-

clamp recordings of EPSCs and IPSCs from the same MSNs in the NAc shell. The stimulating electrode was positioned at the border of the PFC and NAc within the brain slice to elicit a compound postsynaptic current, which contains both EPSCs and IPSCs. After recording a stable total current, we perfused the slice with PTX to selectively inhibit IPSCs, then subtracted the PTX-insensitive current to get the IPSC component (Fig. 1A). We found that the EPSC/IPSC ratio was markedly reduced in mice with SNL ($P < 0.01$, Student's t -test, Fig. 1B, C). To identify the effect of SNL on the strength of the excitatory and inhibitory synaptic transmission, we examined the

input-output (I–O) curves from the glutamatergic and the GABAergic synapse-mediated currents. Compared with the sham group, SNL significantly suppressed the amplitude of the evoked EPSCs ($F_{1,30} = 8.065$, $P < 0.01$, two-way ANOVA with repeated-measures, Fig. 1D), and markedly increased the amplitude of the evoked IPSCs in MSNs ($F_{1,20} = 8.179$, $P < 0.05$, two-way ANOVA with repeated-measures, Fig. 1E). These data suggest that the E/I balance in MSNs of the NAc shell is disrupted after SNL.

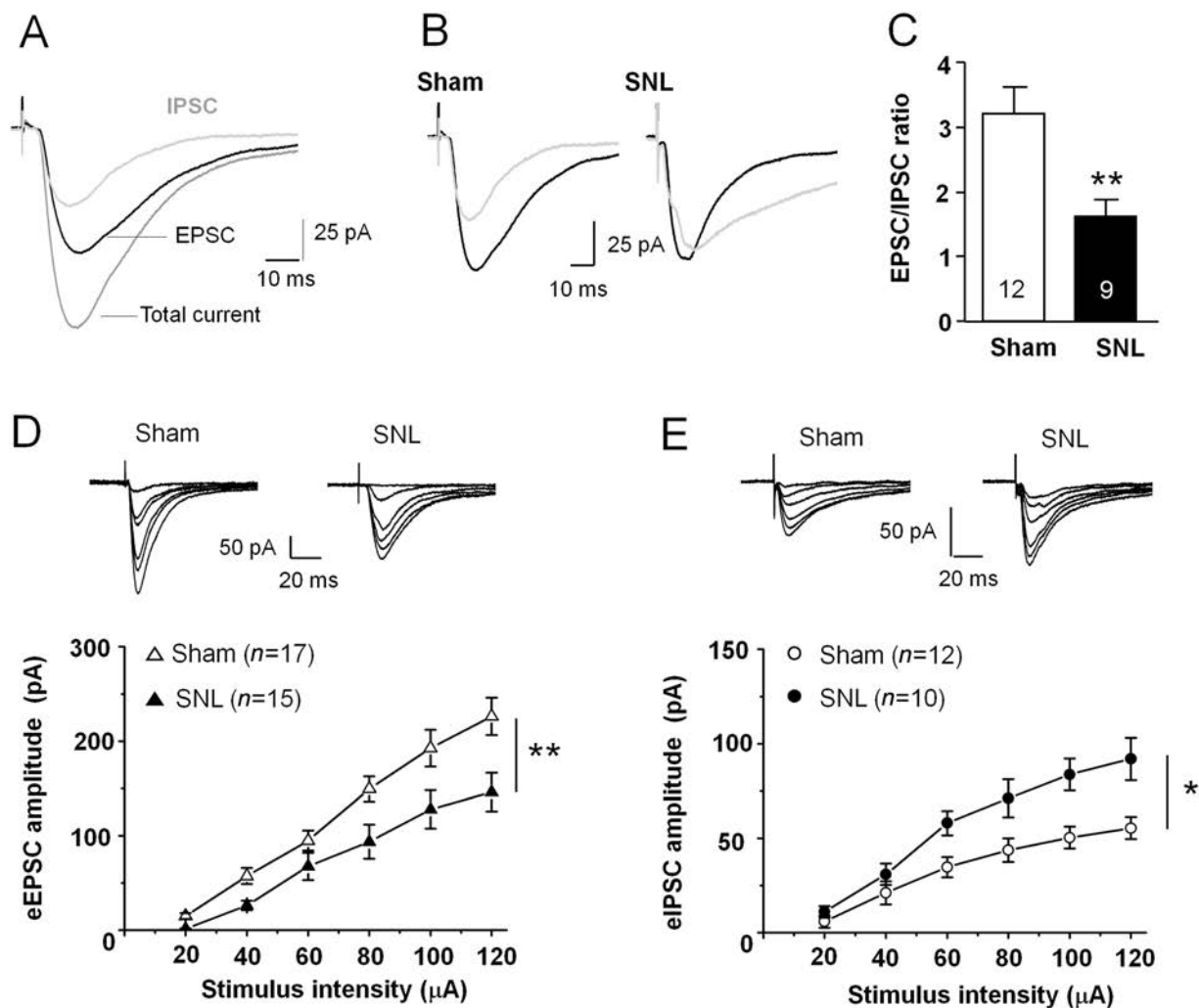


Fig. 1 SNL disrupts the excitatory/inhibitory (E/I) balance at MSN synapses in the NAc shell. **A** Sample traces showing total current, an EPSC, and an IPSC in the same MSN. **B** Sample traces showing EPSCs (black traces) and IPSCs (grey traces) in the same MSN from sham- and SNL-operated mice. **C** The mean EPSC/IPSC ratio is decreased in SNL-operated mice (** $P < 0.01$, Student's t -test). **D** Upper panel, sample traces of EPSCs evoked by stimulation intensity from 20 μ A to 120 μ A. Each trace is averaged from 6–10 EPSCs at the same stimulus intensity. Lower panel, summary data showing that SNL decreases the input-output response of eEPSCs

(15–17 neurons from 4–5 mice, ** $P < 0.01$, two-way ANOVA with repeated-measures). **E** Upper panel, sample traces of GABAergic receptor-mediated IPSCs evoked by stimulation intensity from 20 μ A to 120 μ A from sham- and SNL-operated mice. Each trace is averaged from 6–10 IPSCs at the same stimulus intensity. SNL increases the input-output response of eIPSCs in NAc shell MSNs (10–12 neurons from 4–5 mice, * $P < 0.05$, two-way ANOVA with repeated-measures). Both EPSCs and IPSCs are shown at the peak of the current responses.

SNL Increases Inhibitory Synaptic Transmission in MSNs

To study the detailed changes of inhibitory and excitatory synaptic transmission in MSNs of the NAc shell after SNL, we first examined the inhibitory synaptic component. The sIPSCs were recorded in MSNs from the sham- or SNL-operated mice by holding the membrane potential at 0 mV (Fig. 2A). We analyzed the cumulative probability distributions of inter-event intervals of sIPSCs and found that the cumulative fraction was significantly shifted to the left in SNL mice compared with sham-operated mice ($P < 0.01$, K-S test, Fig. 2B). The mean frequency of sIPSCs was significantly increased in SNL animals ($P < 0.01$, Mann-Whitney test, Fig. 2C). There was no significant difference in the amplitude of sIPSCs between

sham and SNL-operated mice ($P > 0.05$, Mann-Whitney test, Fig. 2D, E).

SNL Decreases Excitatory Synaptic Transmission in MSNs

To determine whether the disrupted balance was affected by excitatory synaptic transmission in SNL animals, we directly measured the sEPSCs by holding the membrane potential at -70 mV in MSNs of NAc slices from sham- or SNL-operated mice in the presence of PTX ($100 \mu\text{mol/L}$) and strychnine ($1 \mu\text{mol/L}$) to exclude GABA_A receptor- and glycine receptor-mediated inhibitory synaptic inputs (Fig. 3A). The cumulative probability distribution of inter-event intervals of sEPSCs shifted to the right after SNL ($P < 0.01$, K-S test, Fig. 3B). The mean frequency of

Fig. 2 SNL enhances the sIPSC frequency in MSNs in the NAc shell. **A** Sample traces of sIPSCs recorded from MSNs in sham- and SNL-operated mice. **B** Cumulative probability distribution of sIPSC inter-event intervals is shifted to the left after SNL ($P < 0.01$, K-S test). **C** The mean sIPSCs frequency is increased in MSNs after SNL ($**P < 0.01$, Mann-Whitney test). **D** Cumulative probability distribution for sIPSC amplitude is not significantly different in sham- and SNL-operated animals ($P > 0.05$, K-S test). **E** The mean sIPSC amplitude is comparable in the two groups ($P > 0.05$, n.s., not significant, Mann-Whitney test).

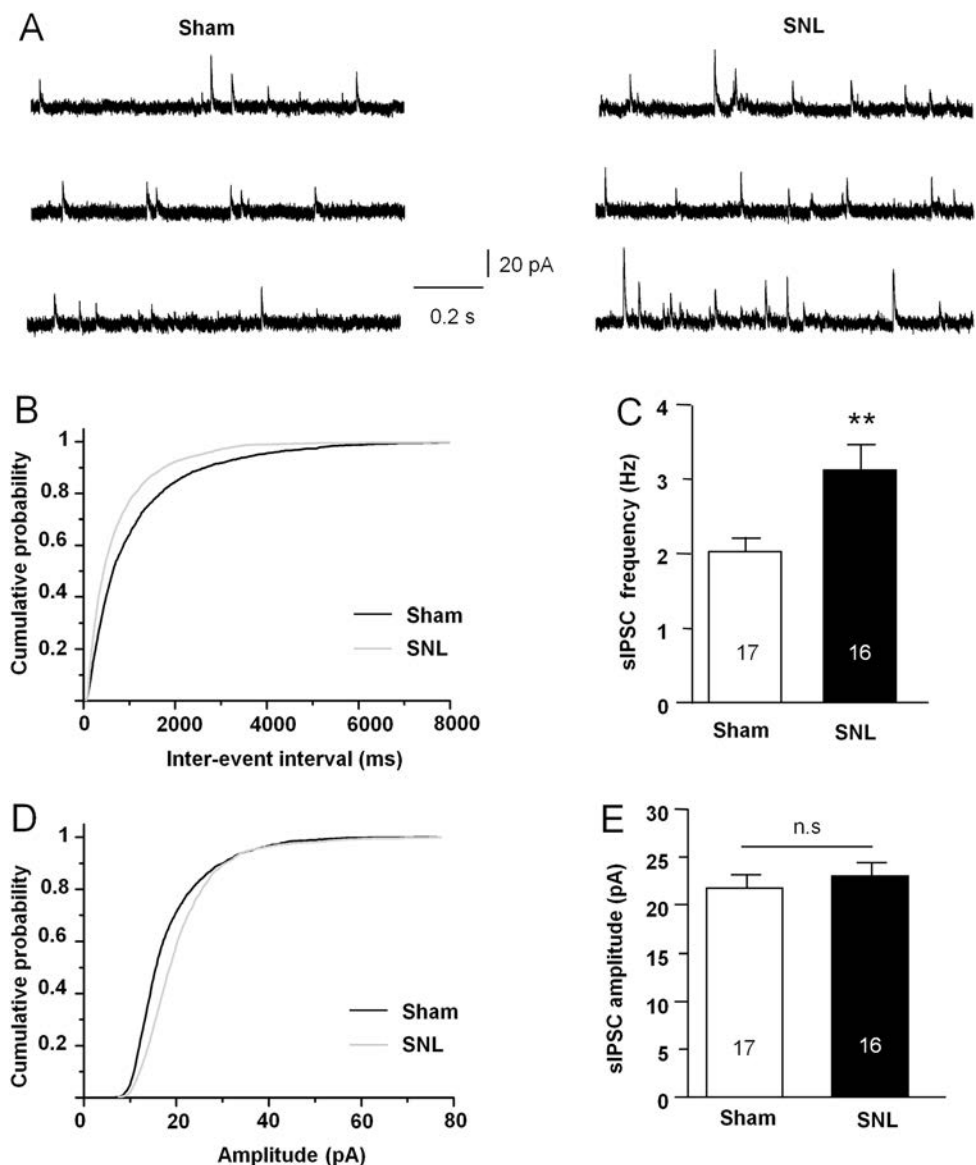
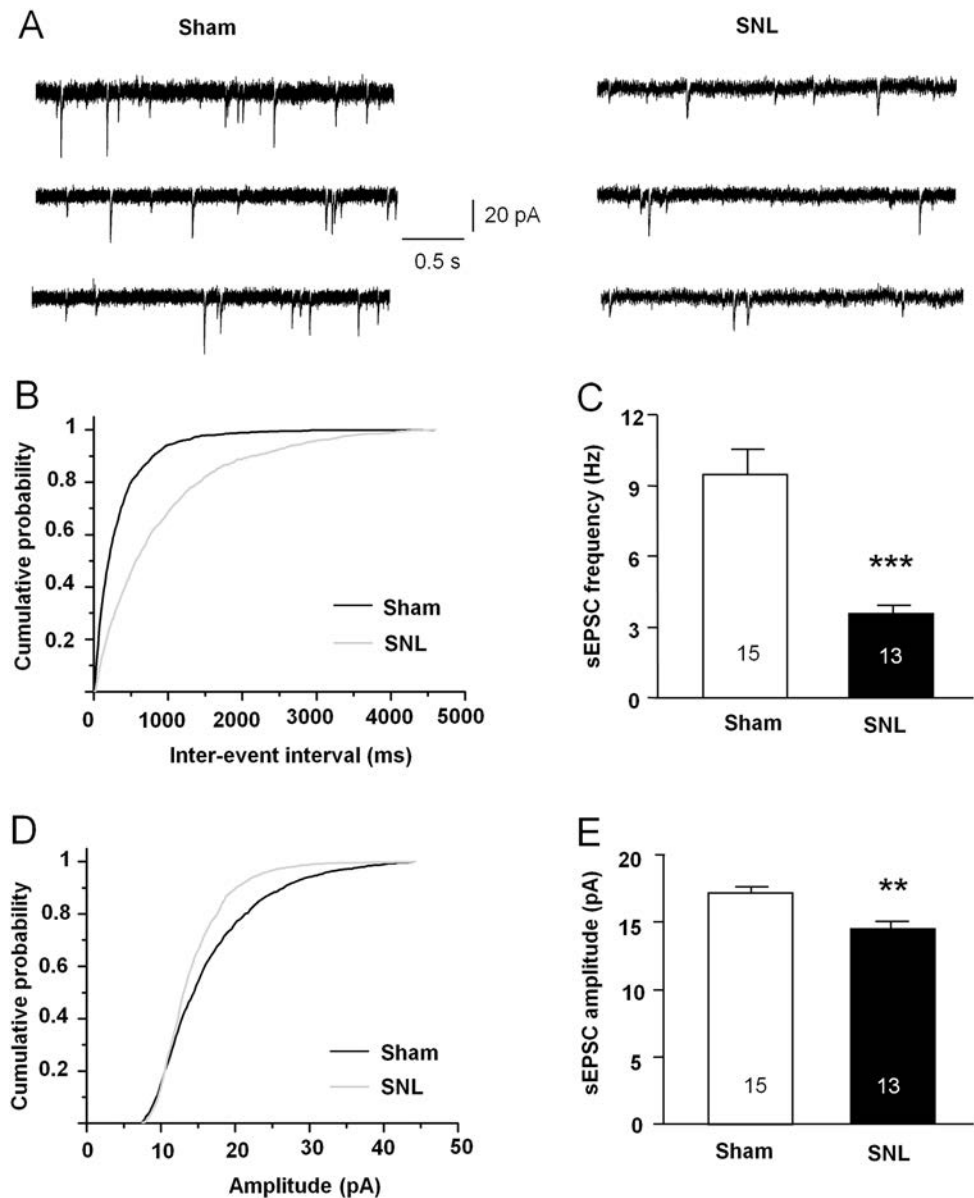


Fig. 3 SNL suppresses the sEPSC frequency and amplitude in MSNs in the NAc shell.

A Sample traces of sEPSCs recorded from NAc shell MSNs in sham- and SNL-operated mice. **B** Cumulative probability distribution of sEPSC inter-event intervals is shifted to the right after SNL ($P < 0.01$, K–S test). **C** The mean sEPSC frequency is decreased in MSNs after SNL ($***P < 0.001$, Student's *t*-test). **D** Cumulative probability distribution for sEPSC amplitude in MSNs from SNL-operated mice is shifted to the left relative to the sham-treated group ($P < 0.01$, K–S test). **E** Mean sEPSC amplitude is decreased in MSNs after SNL ($**P < 0.01$, Mann-Whitney test).



sEPSCs was significantly decreased in SNL-operated animals ($P < 0.001$, Student's *t*-test, Fig. 3C). The distribution of sEPSCs amplitudes shifted to the left after SNL ($P < 0.05$, K–S test, Fig. 3D). The mean amplitude of sEPSCs was decreased in SNL-operated animals ($P < 0.01$, Mann-Whitney test, Fig. 3E).

SNL Leads to Different Changes in the PPR of eIPSCs and eEPSCs in MSNs

To further determine the change of presynaptic GABA and glutamate release, we compared the paired-pulse ratio (PPR) in NAc slices from sham- and SNL-operated mice. The PPR of eIPSCs was elicited by two pulses at 50-ms or 200-ms inter-pulse intervals in the presence of the AMPAR

antagonist DNQX and the NMDAR antagonist AP-5. The PPR of eIPSCs was significantly lower in SNL mice than in sham-operated mice with the 50-ms inter-pulse interval, but no such change was found with the 200-ms inter-pulse interval (50 ms, $P < 0.01$; 200 ms, $P > 0.05$, Student's *t*-test, Fig. 4A, B). The same was found in the eEPSC PPR, which was elicited in the presence of the GABA_A receptor antagonist PTX and the glycine receptor antagonist strychnine. In contrast, the PPR of eEPSCs was significantly higher in the SNL group than in the sham group at the 50-ms inter-pulse interval; no difference was found at the 200-ms inter-pulse interval (50 ms, $P < 0.01$; 200 ms, $P > 0.05$, Student's *t*-test, Fig. 4C, D).

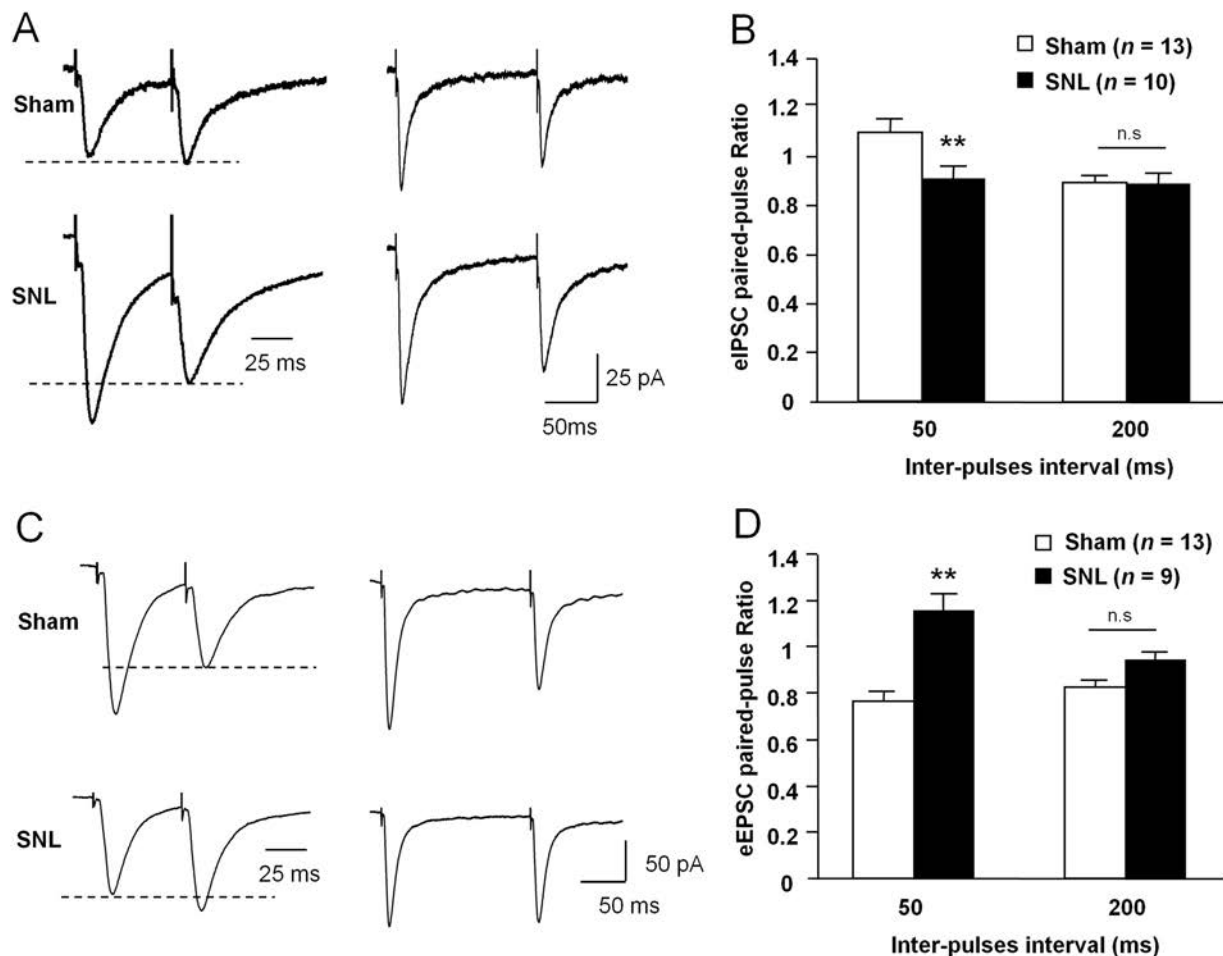


Fig. 4 SNL differentially changes the PPR of eIPSCs and eEPSCs in MSNs in the NAc shell. **A** Sample traces of IPSCs evoked by paired-pulse stimulation with inter-pulse intervals of 50 ms (left) and 200 ms (right) in MSNs from sham- and SNL-operated mice. **B** The mean PPR of eIPSCs is decreased after SNL at inter-pulse intervals of 50 ms (** $P < 0.01$, Student's t -test), but not at inter-pulse intervals of

200 ms. **C** Sample traces of EPSCs evoked by paired-pulse stimulation with inter-pulse intervals of 50 ms (left) and 200 ms (right) in MSNs from sham- and SNL-operated mice. **D** The mean PPR of eEPSCs is increased after SNL at inter-pulse intervals of 50 ms (** $P < 0.01$, n.s., not significant, Student's t -test), but not at 200 ms.

CCL2/CCR2 Signaling Regulates Inhibitory and Excitatory Synaptic Inputs in MSNs of the NAc Shell

To explore the molecular mechanisms underlying the disruption of E/I balance after SNL, we tested the role of CCL2/CCR2 in synaptic transmission in MSNs, as CCL2 and CCR2 are markedly increased in the NAc shell after SNL [3]. We first determined whether CCL2 affects inhibitory GABAergic synaptic transmission and found that the frequency and amplitude of sIPSCs were significantly increased by acute CCL2 perfusion compared with baseline (frequency, $149.9\% \pm 13.7\%$, $P < 0.05$; amplitude, $134.5\% \pm 9.9\%$, $P < 0.05$, paired Student's t -test, Fig. 5A and B). Similarly, bath application of CCL2 also increased the frequency and amplitude of sEPSCs (frequency, $144.3\% \pm 8.1\%$, $P < 0.001$; amplitude, $110.5\% \pm$

4.2% , $P < 0.05$, paired Student's t -test, Fig. 5C, D). As SNL persistently increased CCL2 expression in the NAc shell [3], we further investigated how chronic activation of CCL2/CCR2 signaling regulates E/I input to NAc shell MSNs. The *Ccl2*-overexpressing lentivirus (LV-*Ccl2*) or LV-NC was microinjected into the NAc shell. Ten days later, we recorded the sEPSCs and sIPSCs from the same MSN, and then calculated their mean peak amplitudes. Compared with the LV-NC-treated mice, LV-*Ccl2* moderately weakened the sEPSC/sIPSC frequency ratio and significantly decreased the peak amplitude ratio in NAc shell MSNs ($P < 0.05$, Student's t -test, Fig. 5G), similar to the results from SNL-operated mice.

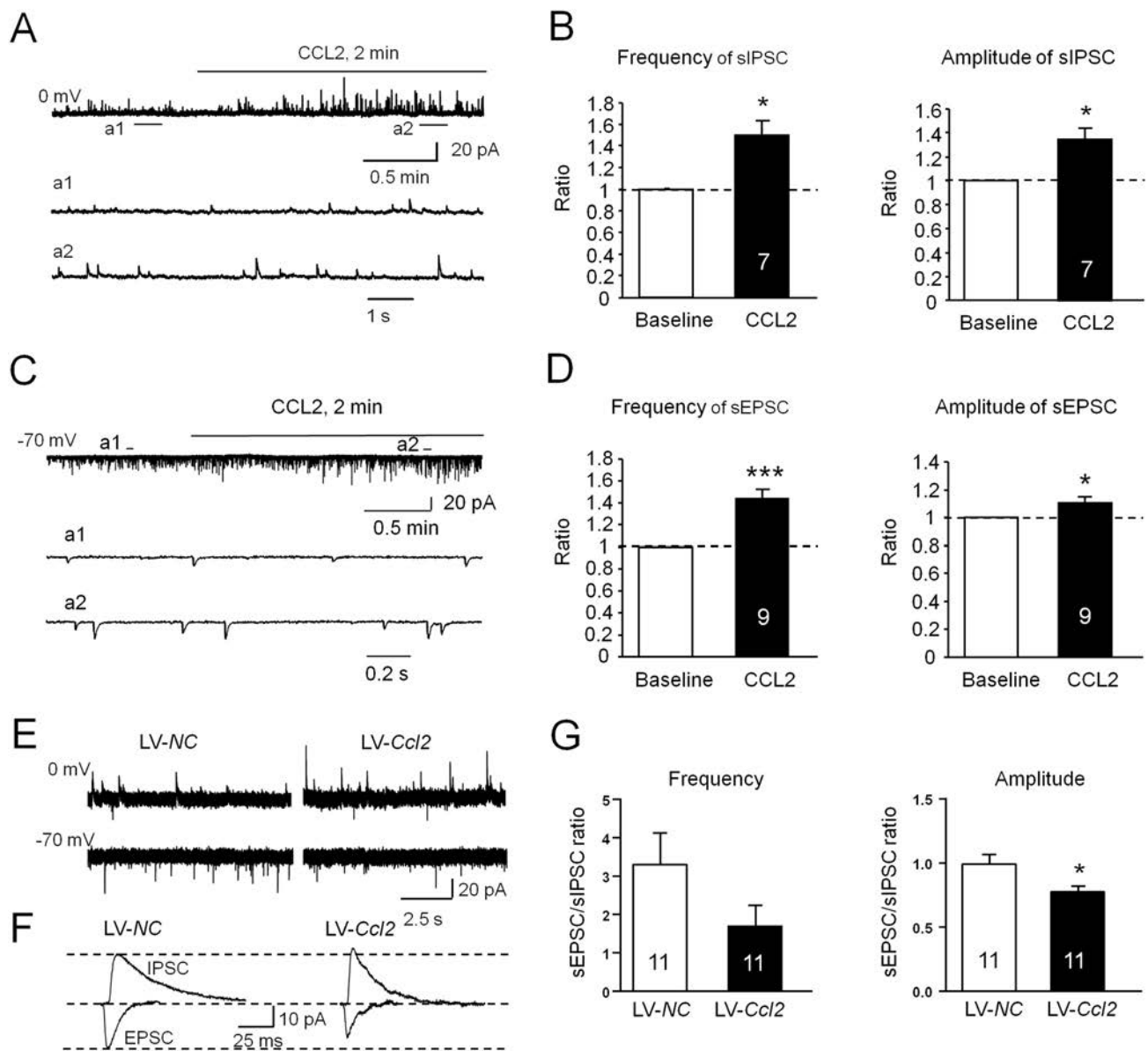


Fig. 5 Effects of CCR2 activation on the sIPSC/sEPSC ratio in MSNs in the NAc shell. **A** Sample traces of sIPSCs from NAc shell MSNs in naive mice after CCL2 (100 nmol/L) application. **a1**, **a2** Expanded traces of sIPSCs recorded in the absence (**a1**) and presence (**a2**) of CCL2. **B** sIPSC frequency and amplitude is increased by CCL2 application ($*P < 0.05$, paired Student's *t*-test). **C** Sample traces of sEPSCs from NAc shell MSNs in naive mice after CCL2 (100 nmol/L) bath application. **a1**, **a2** Expanded sEPSC traces recorded in the absence (**a1**) and presence (**a2**) of CCL2. **D** sEPSC

frequency and amplitude are increased by CCL2 application ($*P < 0.05$, $***P < 0.001$, paired Student's *t*-test). **E** Sample traces of sIPSCs (held at 0 mV) and sEPSCs (held at -70 mV) from the same MSN in naive mice pretreated with LV-NC or LV-Ccl2. **F** Representative averaged traces of sIPSCs and sEPSCs from NAc shell MSNs (data from **E**). **G** Histograms of ratios of EPSC/IPSC frequency and amplitude from mice pretreated with LV-NC or LV-Ccl2. (LV-NC vs LV-Ccl2: frequency: $P > 0.05$; amplitude: $*P < 0.05$, Student's *t*-test)

Acute CCR2 Activation Strengthens NMDAR Function in MSNs

Our previous study showed that SNL increases the NMDAR currents in MSNs, and that they are reduced by *Ccr2* shRNA or a CCR2 antagonist [3]. We further assessed the effect of acute activation of CCR2 by CCL2 on NMDAR-mediated EPSCs in the MSNs. The

amplitudes of NMDAR- and AMPAR-mEPSCs were compared in the presence or absence of CCL2 (Fig. 6A, B). The amplitude of NMDAR-mEPSCs was larger in CCL2-incubated neurons than that in vehicle control ($P < 0.05$, paired Student's *t*-test, Fig. 6C), but no statistical difference was found in the mean amplitude of AMPAR-mEPSCs between the two conditions ($P > 0.05$, paired Student's *t*-test, Fig. 6C). In addition, the amplitude

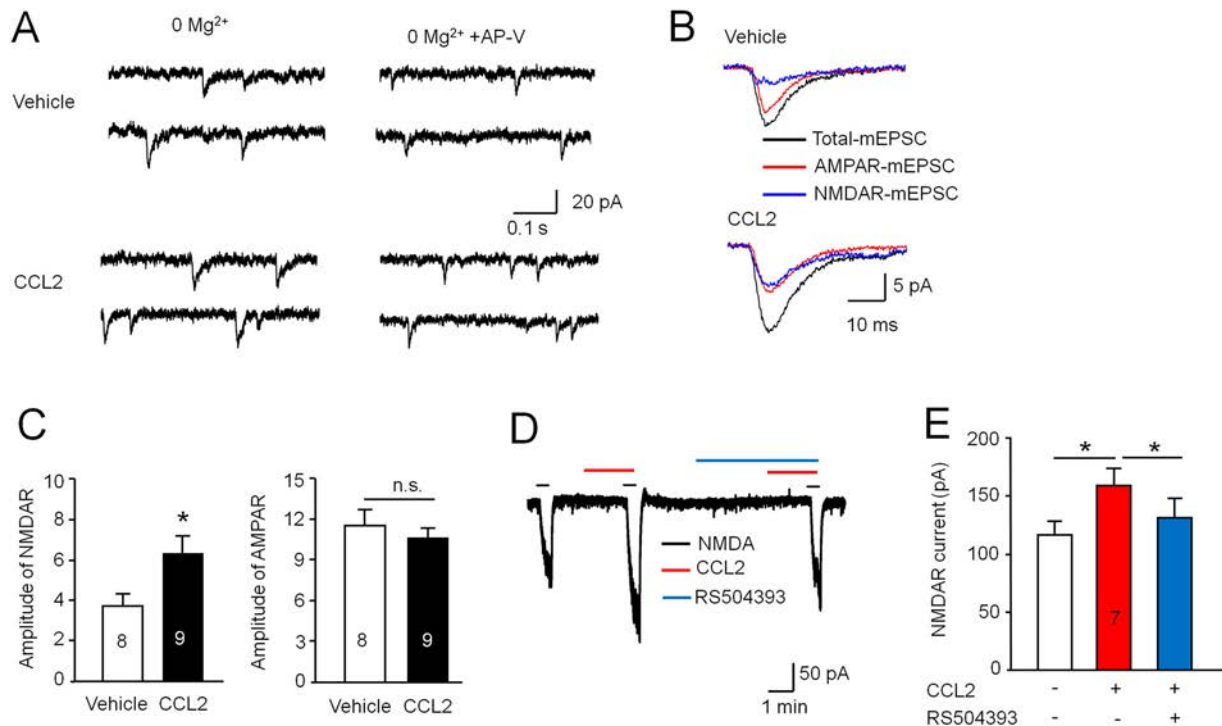


Fig. 6 Activation of CCL2/CCR2 signaling strengthens NMDAR-mediated EPSCs in NAc shell MSNs. **A** Sample traces of mEPSCs from NAc shell MSNs patch-clamped at -60 mV in Mg^{2+} -free aCSF. Total mEPSCs (left) include both NMDAR- and AMPAR-mediated components. AMPAR-mediated mEPSCs (right) were isolated by perfusing with the NMDAR antagonist AP-V ($50 \mu\text{mol/L}$) in the absence and presence of CCL2. **B** Average traces of total mEPSCs, AMPAR-mEPSCs, and NMDAR-mEPSCs from MSNs in the absence and presence of CCL2. **C** Histograms of AMPAR- and NMDAR-

mEPSC amplitude in the absence (vehicle) and presence of CCL2 in aCSF ($*P < 0.05$, Student's *t*-test). **D** Sample trace of NMDA ($20 \mu\text{mol/L}$, 30 s)-induced current recorded in Mg^{2+} -free aCSF solution; this is enhanced in the presence of CCL2 and prevented by RS504393 ($10 \mu\text{mol/L}$), a selective antagonist of CCR2. **E** Histograms of the amplitude of NMDA-induced currents with or without CCL2 incubation and pre-incubation with RS504393 in the aCSF ($*P < 0.05$, paired Student's *t*-test).

of inward current evoked by $20 \mu\text{mol/L}$ NMDA was markedly increased by CCL2 application, and this effect was prevented by the CCR2 antagonist RS504393 ($P < 0.05$, paired Student's *t*-test, Fig. 6D, E). These data suggest that CCL2/CCR2 contributes to the imbalance of inhibitory and excitatory synaptic transmission on MSNs *via* regulating NMDAR function after SNL.

CCR2 Knock-down Improves the Impaired NMDAR-dependent LTD Induction in the NAc Shell after SNL

To determine whether LTD occurs *in vivo* at MSN glutamatergic synapses after SNL, we used LFS (1 Hz, 900 pulses) to evoke LTD in NAc slices. Robust LTD was evoked ($45.8\% \pm 4.8\%$ of baseline, $P < 0.001$ vs baseline, Student's *t*-test) at MSN synapses in the naive mice. This LTD was attenuated by the GluN2B-containing NMDAR-selective antagonist Ro 25-6981 ($85.2\% \pm 7.3\%$ of baseline), but was unaffected by the GluN2A-containing NMDAR-selective antagonist TCN-201 ($55.5\% \pm 10.3\%$ of baseline, $P < 0.05$ vs baseline, Student's *t*-test). The

magnitude of LTD was different in the control and Ro 25-6981-treated groups ($F_{2,19} = 9.66$, $P < 0.01$, one-way ANOVA followed by LSD test, Fig. 7A, B). We then examined the LTD induction in the sham and SNL-operated groups. The magnitude of LTD was lower in the SNL group ($73.3\% \pm 6.4\%$ of baseline, $P < 0.01$ vs baseline, Student's *t*-test) than that in the sham group ($47.9\% \pm 3.2\%$ of baseline, $P < 0.001$ vs baseline; Sham vs SNL, $P < 0.01$, Student's *t*-test, Fig. 7C, D). To determine whether CCR2 in the NAc was involved in the impairment of NMDAR-dependent LTD induction after SNL, we injected *Ccr2* shRNA lentivirus (LV-*Ccr2* shRNA) into the NAc shell 7 days before SNL. Compared with control lentivirus treatment, LV-*Ccr2* shRNA prevented the decrease in the magnitude of NMDAR-dependent LTD induction after SNL (LV-NC-SNL: $79.9\% \pm 8.9\%$ of baseline; LV-*Ccr2*-SNL: $59.8\% \pm 4.1\%$ of baseline, $P < 0.01$ vs baseline, LV-NC vs LV-*Ccr2*-SNL, $P = 0.06$, Student's *t*-test, Fig. 7E, F). These results indicate that the reduction of the magnitude of NMDAR-dependent LTD in the NAc was rescued by the knock-down of *Ccr2* in SNL animals.

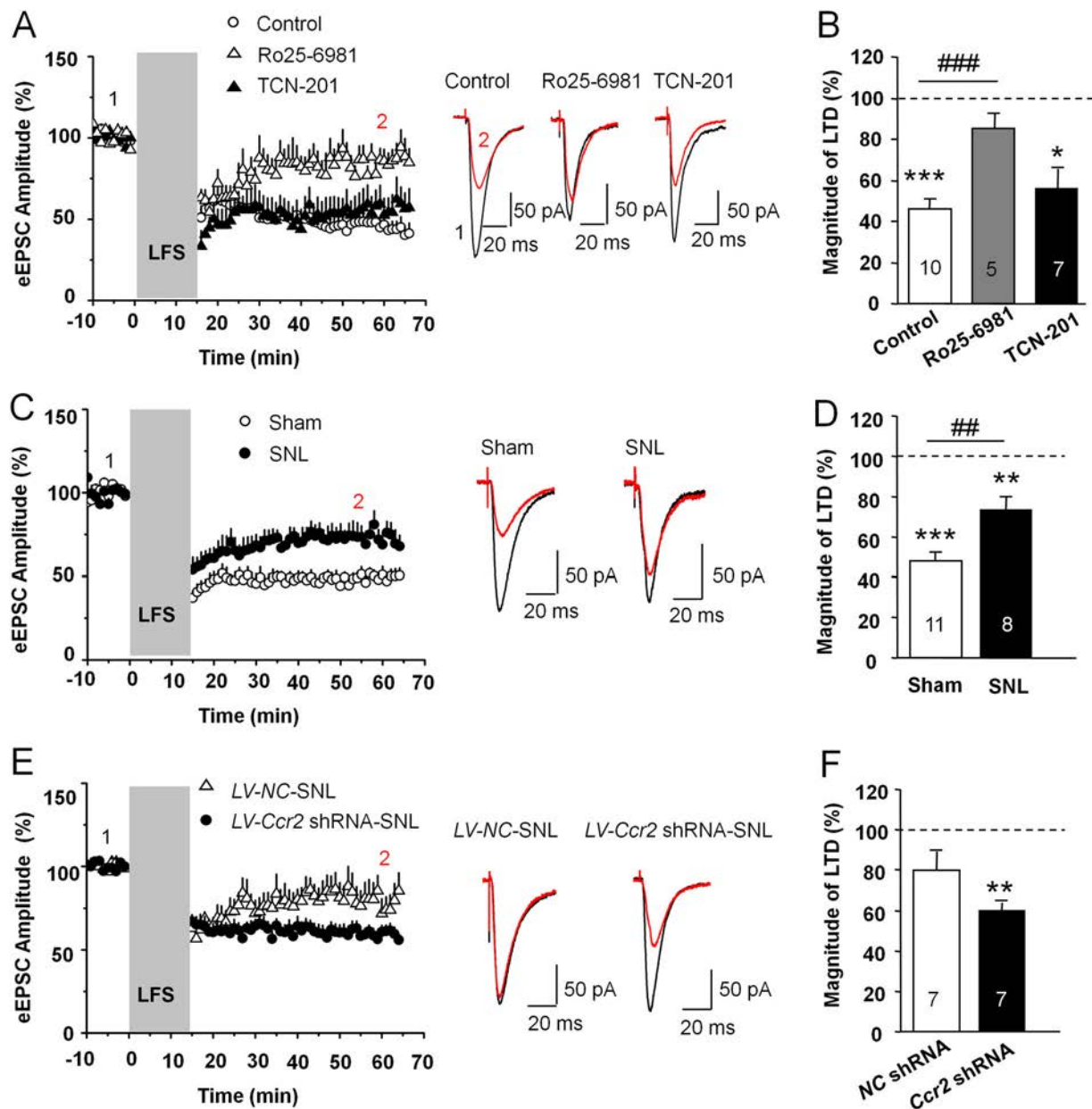


Fig. 7 CCR2 knock-down improves the attenuated NMDAR-dependent LTD in MSNs of the NAc shell after SNL. **A** Left panel, normalized values of evoked EPSCs amplitude showing long-term synaptic plasticity [grey band, LFS duration (1 Hz; 900 pulses)]. LFS decreases eEPSC amplitude in the NAc shell under control condition. LTD induction is impaired by Ro 25-6981 (3 $\mu\text{mol/L}$), but is not changed by TCN-201 (1 $\mu\text{mol/L}$). Right panel, sample eEPSCs before and 30 min after LTD induction in control and Ro 25-6981- or TCN-201-treated slices. **B** Normalized mean magnitude of LTD measured 30 min after LFS stimulation in control, Ro 25-6981-perfused, or TCN-201-perfused slices ($*P < 0.05$, $***P < 0.001$, vs baseline, Student's *t*-test. $### P < 0.001$, vs control, one-way ANOVA

followed by LSD test). **C** Left panel, LFS induced-LTD is reduced in SNL-operated mice. Right panel, sample eEPSCs before and 30 min after LTD induction in sham- and SNL-operated mice. **D** Normalized mean magnitude of LTD measured 30 min after LFS stimulation in sham and SNL mice ($**P < 0.01$, $***P < 0.001$, vs baseline. $## P < 0.01$, vs sham, Student's *t*-test). **E** SNL leads to impaired NMDAR-LTD in LV-NC-injected mice, and this is rescued by LV-Ccr2-shRNA injection. Right panel, sample traces before and 30 min after LTD induction in SNL mice. **F** Normalized mean magnitude of LTD measured 30 min after LFS stimulation in LV-NC or LV-Ccr2-shRNA injected mice ($**P < 0.01$, vs baseline, Student's *t*-test).

Discussion

In the current study, we for the first time showed that CCL2/CCR2 contributed to the altered excitatory and inhibitory balance in the MSNs of NAc shell. The NAc plays a crucial role in the transition from acute to chronic pain [24, 25], and is involved in the affective component during a chronic pain state [15]. As an important area in pain regulation, the output dynamics of the NAc depends on the intrinsic neuronal excitability and overall balance of excitatory and inhibitory synaptic inputs. Recent work has indicated that peripheral nerve injury increases the intrinsic excitability of NAc shell MSNs [2]. Furthermore, inactivating these cells reverses the pain sensitivity, and exciting these cells exacerbates tactile allodynia [2]. Blocking NMDARs in the NAc alleviates nociceptive behaviors and the related affect [3]. Here we found that the EPSC/IPSC ratio was decreased in the SNL-induced neuropathic pain model, and this was partly caused by reduced excitatory synaptic strength. Consistent with this, a previous study showed that the AMPAR/NMDAR current ratio, which reflects basal synaptic transmission strength [23], is decreased in the NAc MSNs of mice with spinal nerve injury [1]. NAc neurons mainly receive excitatory glutamatergic synaptic inputs from the PFC, ventral hippocampus, and basal lateral amygdala [26], and integrate inhibitory GABAergic synaptic inputs from local neurons and the PFC [27, 28]. Spinal nerve injury strengthens the AMPAR/NMDAR current ratio at ventral hippocampus-NAc synapses in dopamine D2 receptor-positive MSNs, but decreases this ratio at PFC-NAc synapses in these MSNs [2]. Similarly, we found a significant reduction in the I-O curves of PFC-NAc excitatory glutamatergic synaptic inputs after SNL. In addition, the reduced EPSC/IPSC ratio may also be caused by increased inhibitory synaptic strength. We also found that SNL increased the I-O curves of inhibitory GABAergic synaptic inputs to the MSNs. In the NAc, synaptic inhibition is mainly mediated by local GABAergic interneurons, which also express parvalbumin or somatostatin [29]. MSNs, as GABAergic projection neurons, can regulate local circuitry by lateral inhibition [28, 29]. Thus, the origin of the changed synaptic inputs to MSNs needs further study.

Our data also showed that the frequency of sIPSCs in NAc MSNs was significantly increased, while the sIPSCs amplitude was not changed, suggesting enhanced presynaptic GABAergic transmitter release at the synapses of NAc MSNs after SNL. Scaling of GABAergic transmission can be triggered by postsynaptic NMDAR-mediated calcium increase, which subsequently enhances GABA release through retrograde activation of the presynaptic NMDARs of interneurons [30]. It has been reported that

brain-derived neurotrophic factor (BDNF) increases inhibitory GABAergic synaptic efficacy in the hippocampus and cortex [31, 32]. BDNF is increased in the NAc during neuropathic pain [33, 34]. Thus, BDNF in the NAc might play a role in regulating inhibitory GABAergic synaptic efficacy on MSNs through presynaptic TrkB signaling in the GABAergic interneurons [35, 36]. In contrast to the inhibitory synapse, we found a reduction of excitatory synaptic inputs which may be caused by decreased presynaptic glutamate release or a decrease in the activity of postsynaptic glutamatergic receptors after SNL. It has been reported that the decreased postsynaptic AMPAR-mediated currents after SNL may contribute to the attenuation of glutamatergic synaptic transmission in neuropathic pain [1, 2]. SNL also led to differential changes in the PPR of eIPSCs and eEPSCs, further indicating that a presynaptic mechanism plays a role in the disruption of E/I balance in NAc MSNs, which may contribute to neuropathic pain and depression.

Our recent study showed that the expression of CCL2 and CCR2 are persistently increased in the NAc shell after SNL, and CCL2/CCR2 signaling is involved in the regulation of SNL-induced neuropathic pain and depressive-like behaviors [3]. Bath application of CCL2 increased the frequency and amplitude of sIPSCs in NAc shell MSNs, suggesting that CCL2/CCR2 signaling increases the presynaptic transmitter release from GABAergic synapses and increases the activity of GABA_A receptors. However, previous studies have reported that the frequency, not the amplitude of sEPSCs is increased in dorsal horn neurons [37] and hippocampus neurons [17] after CCR2 activation, suggesting that CCL2/CCR2 signaling has a presynaptic site of action in the spinal cord and hippocampus. We also found that bath application of CCL2 caused an increase of sEPSCs, suggesting that acute activation of CCR2 potentially leads to transient homeostatic synaptic plasticity to maintain the balance of excitatory and inhibitory inputs to the MSNs [38]. In contrast, persistent activation of CCR2 by LV-*Ccl2* decreased the E/I ratio in the MSNs in the NAc, similar to the changes after SNL, suggesting that persistent CCL2/CCR2 upregulation contributes to resetting of E/I ratio under chronic pain conditions. It has been reported that resetting the E/I balance may increase NMDAR activation and further regulate the long-term form of glutamatergic synaptic plasticity [38]. Indeed, SNL-induced CCR2 activation amplifies the NMDAR-mediated currents in NAc MSNs [3]. We found that the amplitude of NMDAR-mEPSCs, but not of AMPAR-mEPSCs was increased after CCR2 activation. Direct perfusion of the NAc slice with CCL2 increased the NMDA-induced inward current in MSNs, and this was suppressed in the presence of the CCR2 antagonist RS504393. Similarly, bath application of CCL2 enhances

both NR2A- and NR2B-subunit-containing NMDAR EPSCs in hippocampal neurons [17]. Moreover, overexpression of CCL2 by intra-NAc injection of *Ccl2*-expressing lentivirus increased the protein level of phosphorylated NR2B *via* the mitogen-activated protein kinase signaling pathway in the NAc [3]. Overall, these results suggest that CCR2 may regulate the strength of synaptic transmission *via* both presynaptic and postsynaptic effects in the NAc.

Abnormalities of excitatory synaptic function in chronic pain include changes in the frequency and amplitude of sEPSC and the input-output of evoked EPSCs, as well as impairments in the threshold for LTD/LTP induction [39]. Here, LTD was induced at synapses of NAc MSNs with LFS [40, 41]; it was blocked by the selective GluN2B antagonist Ro 25-6981, but was not affected by the GluN2A-containing NMDAR antagonist TCN-201. The enhancement of GluN2B-containing NMDAR at postsynaptic sites might be required for the synaptic depression [42]. Recent investigation indicated that spinal nerve injury induces a significant increase in NMDAR-mediated currents, and impairs LFS-induced LTD at synapses on NAc dopamine D2-positive MSNs [1]. Here, knockdown of *Ccr2* rescued the impaired LTD induction after SNL. In addition, knockdown of *Ccr2* expression in the NAc relieved SNL-induced neuropathic pain and depression *via* suppressing NMDAR function [3]. Thus, CCL2 and CCR2 may contribute to the disruption of E/I input to the MSNs, which further caused the damage of LTD induction in SNL. The forms of synaptic transmission abnormalities may be different in different brain regions and cell types, or under different experiment conditions, and these abnormalities may contribute to the sensory and affective behavior adaptations during chronic pain [43, 44].

In summary, the current study showed that SNL disrupted the E-I balance at the synapses of NAc shell MSNs. This maladaptation was related to changes in both excitatory glutamatergic synaptic transmission and inhibitory GABAergic inhibitory synaptic transmission. The enhancement of inhibitory synaptic inputs may be due to an increase of presynaptic GABAergic transmitter and the suppression of excitatory glutamatergic synaptic inputs. CCL2/CCR2 signaling may contribute to the excitatory and inhibitory synaptic adaptations which potentially modulate LTD induction at the synapses of NAc MSNs during chronic pain.

Acknowledgements This work was supported by Grants from the National Natural Science Foundation of China (32030048, 31871064, and 31671091).

Conflict of interest The authors declare that they have no conflict of interest.

References

- Schwartz N, Temkin P, Jurado S, Lim BK, Heifets BD, Polepalli JS, *et al.* Chronic pain. Decreased motivation during chronic pain requires long-term depression in the nucleus accumbens. *Science* 2014, 345: 535–542.
- Ren W, Centeno MV, Berger S, Wu Y, Na X, Liu X. The indirect pathway of the nucleus accumbens shell amplifies neuropathic pain. *Nat Neurosci* 2016, 19: 220–222.
- Wu XB, Jing PB, Zhang ZJ, Cao DL, Gao MH, Jiang BC, *et al.* Chemokine receptor CCR2 contributes to neuropathic pain and the associated depression *via* increasing NR2B-mediated currents in both D1 and D2 dopamine receptor-containing medium spiny neurons in the nucleus accumbens shell. *Neuropsychopharmacology* 2018, 43: 2320–2330.
- Chang PC, Pollema-Mays SL, Centeno MV, Procissi D, Contini M, Baria AT, *et al.* Role of nucleus accumbens in neuropathic pain: linked multi-scale evidence in the rat transitioning to neuropathic pain. *Pain* 2014, 155: 1128–1139.
- Goffer Y, Xu D, Eberle SE, D'Amour J, Lee M, Tukey D, *et al.* Calcium-permeable AMPA receptors in the nucleus accumbens regulate depression-like behaviors in the chronic neuropathic pain state. *J Neurosci* 2013, 33: 19034–19044.
- Xu D, Su C, Lin HY, Manders T, Wang J. Persistent neuropathic pain increases synaptic GluA1 subunit levels in core and shell subregions of the nucleus accumbens. *Neurosci Lett* 2015, 609: 176–181.
- Su C, D'Amour J, Lee M, Lin HY, Manders T, Xu D, *et al.* Persistent pain alters AMPA receptor subunit levels in the nucleus accumbens. *Mol Brain* 2015, 8: 46.
- Nisenbaum ES, Grace AA, Berger TW. Functionally distinct subpopulations of striatal neurons are differentially regulated by GABAergic and dopaminergic inputs—II. *in vitro* analysis. *Neuroscience* 1992, 48: 579–593.
- Russo SJ, Mazei-Robison MS, Ables JL, Nestler EJ. Neurotrophic factors and structural plasticity in addiction. *Neuropharmacology* 2009, 56(Suppl 1): 73–82.
- Wilson CJ, Kawaguchi Y. The origins of two-state spontaneous membrane potential fluctuations of neostriatal spiny neurons. *J Neurosci* 1996, 16: 2397–2410.
- O'Donnell P, Grace AA. Synaptic interactions among excitatory afferents to nucleus accumbens neurons: hippocampal gating of prefrontal cortical input. *J Neurosci* 1995, 15: 3622–3639.
- Castillo PE, Chiu CQ, Carroll RC. Long-term plasticity at inhibitory synapses. *Curr Opin Neurobiol* 2011, 21: 328–338.
- Potter LE, Paylor JW, Suh JS, Tenorio G, Caliaperumal J, Colbourne F, *et al.* Altered excitatory-inhibitory balance within somatosensory cortex is associated with enhanced plasticity and pain sensitivity in a mouse model of multiple sclerosis. *J Neuroinflammation* 2016, 13: 142.
- Cheriyian J, Sheets PL. Peripheral nerve injury reduces the excitation-inhibition balance of basolateral amygdala inputs to prelimbic pyramidal neurons projecting to the periaqueductal gray. *Mol Brain* 2020, 13: 100.
- Massaly N, Copits BA, Wilson-Poe AR, Hipolito L, Markovic T, Yoon HJ, *et al.* Pain-induced negative affect is mediated *via* recruitment of the nucleus accumbens kappa opioid system. *Neuron* 2019, 102(564–573): e566.
- Gao YJ, Zhang L, Samad OA, Suter MR, Yasuhiko K, Xu ZZ, *et al.* JNK-induced MCP-1 production in spinal cord astrocytes contributes to central sensitization and neuropathic pain. *J Neurosci* 2009, 29: 4096–4108.
- Zhou Y, Tang H, Xiong H. Chemokine CCL2 enhances NMDA receptor-mediated excitatory postsynaptic current in rat

- hippocampal slices—a potential mechanism for HIV-1-associated neuropathy?. *J Neuroimmune Pharmacol* 2016, 11: 306–315.
18. Luscher C, Malenka RC. NMDA receptor-dependent long-term potentiation and long-term depression (LTP/LTD). *Cold Spring Harb Perspect Biol* 2012, 4.
 19. Spiga S, Talani G, Mulas G, Licheri V, Fois GR, Muggironi G, *et al.* Hampered long-term depression and thin spine loss in the nucleus accumbens of ethanol-dependent rats. *Proc Natl Acad Sci U S A* 2014, 111: E3745–3754.
 20. Chiou CS, Huang CC, Liang YC, Tsai YC, Hsu KS. Impairment of long-term depression in the anterior cingulate cortex of mice with bone cancer pain. *Pain* 2012, 153: 2097–2108.
 21. Wei F, Li P, Zhuo M. Loss of synaptic depression in mammalian anterior cingulate cortex after amputation. *J Neurosci* 1999, 19: 9346–9354.
 22. Zhang ZJ, Cao DL, Zhang X, Ji RR, Gao YJ. Chemokine contribution to neuropathic pain: respective induction of CXCL1 and CXCR2 in spinal cord astrocytes and neurons. *Pain* 2013, 154: 2185–2197.
 23. Thomas MJ, Beurrier C, Bonci A, Malenka RC. Long-term depression in the nucleus accumbens: a neural correlate of behavioral sensitization to cocaine. *Nat Neurosci* 2001, 4: 1217–1223.
 24. Baliki MN, Petre B, Torbey S, Herrmann KM, Huang L, Schnitzer TJ, *et al.* Corticostriatal functional connectivity predicts transition to chronic back pain. *Nat Neurosci* 2012, 15: 1117–1119.
 25. Makary MM, Polosecki P, Cecchi GA, DeAraujo IE, Barron DS, Constable TR, *et al.* Loss of nucleus accumbens low-frequency fluctuations is a signature of chronic pain. *Proc Natl Acad Sci U S A* 2020, 117: 10015–10023.
 26. Britt JP, Benaliouad F, McDevitt RA, Stuber GD, Wise RA, Bonci A. Synaptic and behavioral profile of multiple glutamatergic inputs to the nucleus accumbens. *Neuron* 2012, 76: 790–803.
 27. Lee AT, Vogt D, Rubenstein JL, Sohal VS. A class of GABAergic neurons in the prefrontal cortex sends long-range projections to the nucleus accumbens and elicits acute avoidance behavior. *J Neurosci* 2014, 34: 11519–11525.
 28. Taverna S, van Dongen YC, Groenewegen HJ, Pennartz CM. Direct physiological evidence for synaptic connectivity between medium-sized spiny neurons in rat nucleus accumbens *in situ*. *J Neurophysiol* 2004, 91: 1111–1121.
 29. Burke DA, Rotstein HG, Alvarez VA. Striatal local circuitry: a new framework for lateral inhibition. *Neuron* 2017, 96: 267–284.
 30. Duguid IC, Smart TG. Retrograde activation of presynaptic NMDA receptors enhances GABA release at cerebellar interneuron-Purkinje cell synapses. *Nat Neurosci* 2004, 7: 525–533.
 31. Gubellini P, Ben-Ari Y, Gaiarsa JL. Endogenous neurotrophins are required for the induction of GABAergic long-term potentiation in the neonatal rat hippocampus. *J Neurosci* 2005, 25: 5796–5802.
 32. Sivakumaran S, Mohajerani MH, Cherubini E. At immature mossy-fiber-CA3 synapses, correlated presynaptic and postsynaptic activity persistently enhances GABA release and network excitability *via* BDNF and cAMP-dependent PKA. *J Neurosci* 2009, 29: 2637–2647.
 33. Liu D, Tang QQ, Yin C, Song Y, Liu Y, Yang JX, *et al.* Brain-derived neurotrophic factor-mediated projection-specific regulation of depressive-like and nociceptive behaviors in the mesolimbic reward circuitry. *Pain* 2018, 159: 175.
 34. Zhang H, Qian YL, Li C, Liu D, Wang L, Wang XY, *et al.* Brain-derived neurotrophic factor in the mesolimbic reward circuitry mediates nociception in chronic neuropathic pain. *Biol Psychiatry* 2017, 82: 608–618.
 35. Liu Y, Zhang LI, Tao HW. Heterosynaptic scaling of developing GABAergic synapses: dependence on glutamatergic input and developmental stage. *J Neurosci* 2007, 27: 5301–5312.
 36. Chiu CQ, Martenson JS, Yamazaki M, Natsume R, Sakimura K, Tomita S, *et al.* Input-specific nmdar-dependent potentiation of dendritic gabaergic inhibition. *Neuron* 2018, 97(368–377): e363.
 37. Spicarova D, Adamek P, Kalynovska N, Mrozkova P, Palecek J. TRPV1 receptor inhibition decreases CCL2-induced hyperalgesia. *Neuropharmacology* 2014, 81: 75–84.
 38. D'Amour JA, Froemke RC. Inhibitory and excitatory spike-timing-dependent plasticity in the auditory cortex. *Neuron* 2015, 86: 514–528.
 39. Luo C, Kuner T, Kuner R. Synaptic plasticity in pathological pain. *Trends Neurosci* 2014, 37: 343–355.
 40. Deng PY, Lei S. Long-term depression in identified stellate neurons of juvenile rat entorhinal cortex. *J Neurophysiol* 2007, 97: 727–737.
 41. Thomas MJ, Malenka RC, Bonci A. Modulation of long-term depression by dopamine in the mesolimbic system. *J Neurosci* 2000, 20: 5581–5586.
 42. Liu L, Wong TP, Pozza MF, Lingenhoehl K, Wang Y, Sheng M, *et al.* Role of NMDA receptor subtypes in governing the direction of hippocampal synaptic plasticity. *Science* 2004, 304: 1021–1024.
 43. Bie B, Brown DL, Naguib M. Synaptic plasticity and pain aversion. *Eur J Pharmacol* 2011, 667: 26–31.
 44. Bliss TV, Collingridge GL, Kaang BK, Zhuo M. Synaptic plasticity in the anterior cingulate cortex in acute and chronic pain. *Nat Rev Neurosci* 2016, 17: 485–496.



Rac1 Signaling in Amygdala Astrocytes Regulates Fear Memory Acquisition and Retrieval

Xiao-Cen Fan¹ · Chao-Nan Ma¹ · Jia-Chen Song¹ · Zhao-Hui Liao¹ ·
Nan Huang¹ · Xing Liu¹ · Lan Ma¹

Received: 11 August 2020 / Accepted: 9 October 2020 / Published online: 28 April 2021
© Center for Excellence in Brain Science and Intelligence Technology, CAS 2021

Abstract The importance of astrocytes in behavior control is increasingly appreciated, but little is known about the effects of their dynamic activity in regulating learning and memory. In the present study, we constructed AAVs of photoactivatable and photoinactivatable Ras-related C3 botulinum toxin substrate 1 (Rac1) under the *mGFAP* promoter, which enabled the manipulation of Rac1 activity in astrocytes by optical stimulation in free-moving mice. We found that both up-regulation and down-regulation of astrocytic Rac1 activity in the basolateral amygdala (BLA) attenuated memory acquisition in a fear conditioning mouse model. Meanwhile, neuronal activation in the BLA induced by memory acquisition was inhibited under both the up- and down-regulation of astrocytic Rac1 activity during training. In terms of the impact on fear memory retrieval, we found both up- and down-regulation of BLA astrocytic Rac1 activity impaired memory retrieval of fear conditioning and memory retrieval-induced neuronal activation. Notably, the effect of astrocytic Rac1 on memory retrieval was reversible. Our results demonstrate that the normal activity of astrocytic Rac1 is necessary for the activation of neurons and memory formation. Both activation and inactivation of astrocytic Rac1 activity in

the BLA reduced the excitability of neurons, and thereby impaired fear memory acquisition and retrieval.

Keywords Rac1 · Astrocyte · Neuron · BLA · Fear memory

Introduction

Astrocytes are the most numerous glial cells, occupying 25%–50% of brain volume [1]. As believed conventionally, astrocytes are considered to provide structural support for the brain, form the blood-brain barrier, and supply energy for neurons [2]. With the proposal of the ‘tripartite synapse’ theory, many studies focused on their roles in synaptic plasticity, such as secreting signaling molecules to mediate the occurrence, maturation, and deletion of synapses, to maintain their structural plasticity [3, 4]. Besides, astrocytes secrete a variety of glial transmitters, such as glutamate, ATP, and GABA, to regulate the long-term potentiation or depression of synapses and participate in regulating their functional plasticity [5–9]. Furthermore, astrocytes maintain the ion and transmitter homeostasis in synaptic clefts of neurons by recycling potassium ions and glutamate, thus affecting neuronal activity and synaptic plasticity [10]. It has been suggested that the activity of astrocytes is vital for the normal function of neurons and the maintenance of brain homeostasis.

The amygdala is a key area in the control of fear memory, mainly including the basolateral amygdala (BLA) and the central amygdala (CeA) [11]. It is generally believed that the BLA is responsible for receiving information from the cortex, hippocampus, and other brain areas, integrating and then transferring the dominant information to the CeA [11, 12]. The neuronal activity in

Xiao-Cen Fan and Chao-Nan Ma contributed equally to this work.

✉ Xing Liu
xingliu@fudan.edu.cn

✉ Lan Ma
lanma@fudan.edu.cn

¹ Department of Neurosurgery, Huashan Hospital, State Key Laboratory of Medical Neurobiology and MOE Frontiers Center for Brain Science, School of Basic Medical Sciences, Institutes of Brain Science, Fudan University, Shanghai 200032, China

the BLA is essentially involved in the process of learning and memory. Lesions or functional inhibition of the BLA disrupt the formation and expression of conditional fear memory [13, 14]. Astrocytes play important roles in regulating synaptic plasticity, which is considered to be the basis of learning and memory [15]. Most of the current research is focused on the energy metabolism of astrocytes, the glutamate cycle, and the glial transmitters in learning and memory [16]. The traditional interventions in astrocyte activity are usually irreversible, which may trigger compensatory responses [17, 18]. However, the role of astrocytes in associative learning and memory, such as fear conditioning, is unclear. Whether the real-time structural changes of astrocytes in the BLA regulate fear memory acquisition and expression remains unknown.

Ras-related C3 botulinum toxin substrate 1 (Rac1), is a critical small Rho GTPase for cytoskeletal remodeling [19]. Thus, Rac1 is an important molecule in shaping the morphology of astrocytes. It has been shown that activation of Rac1 *in vitro* induces astrocytosis, while Rac1 knockout or inhibition of Rac1 activity shrinks astrocytes [20]. Other studies have shown that the skeletal structure of astrocytes changes dynamically during the formation of fear memory, as a result in changes of the activity of Rac1 [21, 22].

Above all, we hypothesized that the activity of BLA astrocytic Rac1 regulates conditioned fear memory formation and retrieval by modulating BLA neuronal functions. To test this hypothesis, we constructed associated adenovirus (AAV) of photoactivatable Rac1 (*Rac1-PA*) and photoinactivatable Rac1 (*Rac1-DN/PA*) under the *mGFAP* promoter to manipulate the structure of astrocytes in real time, to avoid compensatory reactions [23]. By this means, we found that the temporary changes of astrocytic Rac1 activity decreased neuronal activation and impaired fear memory acquisition and retrieval.

Materials and Methods

Animals

Adult C57BL/6 male mice were purchased from Shanghai Laboratory Animal Center, Chinese Academy of Sciences. Animals were housed 4 per cage under a 12-h alternating light/dark cycle, with food and water available *ad libitum*. Two- to three-month-old mice were used for the experiments. All procedures were approved by the Animal Care and Use Committee of the Shanghai Medical College of Fudan University and were performed according to the National Institutes of Health Guide for the Care and Use of Laboratory Animals.

Preparation of AAVs

The plasmids of *Rac1-PA*, *Rac1-DN/PA*, photoinsensitive Rac1 (*Rac1-C450A*), and pAAV-mGFAP-HA-rM3D(Gs)-IRES-mCherry were from Addgene (Plasmid #22027, #22029, #22028, and #50472). *Rac1-PA*, *Rac1-DN/PA*, or *Rac1-C450A* was inserted into AAV-mGFAP-mCherry as previously described [21]. AAV_{2/9}-mGFAP-Rac1-PA-mCherry, AAV_{2/9}-mGFAP-Rac1-DN/PA-mCherry, and AAV_{2/9}-mGFAP-Rac1-C450A-mCherry were packaged by Obio Technology (Shanghai, China). AAVs at a titer of 2×10^{12} viral genomes/mL were used for the following experiments.

Stereotaxic Surgery

To perform virus injection and optical fiber implantation, mice were anesthetized with 1.5%–2% isoflurane and positioned in a stereotaxic frame (RWD, Shenzhen, China) [24]. AAVs were bilaterally injected into the BLA in a 0.5 μ L volume at 0.1 μ L/min. The coordinates of the BLA were AP, -1.5 mm; ML, ± 3.3 mm; DV, -4.8 mm, referenced to bregma. The needle was left for 5 min after injection and pulled out very slowly to avoid leakage. Ceramic optical fiber cannulas (diameter, 200 μ m; numerical aperture, 0.37; Anilab Software & Instruments, Ningbo, China) were bilaterally implanted in the BLA at AP, -1.5 mm; ML, ± 3.3 mm; DV, -4.6 mm, referenced to bregma. Dental cement was used to fix the optical fibers on the skull. After surgery, the mice were allowed 3 weeks to recover. The locations of virus expression and the cannulas were checked after behavioral tests. Mice with inaccurate virus expression or fiber implantation were excluded.

Conditioned Fear Memory

For fear conditioning, the mice received 5 trials with conditioned (CS) and unconditioned stimulus (US) pairing in the conditioning chamber (MED Associates, VT, USA). One CS (tone, 2800 Hz, 85 dB, 30 s) was paired with one US (footshock, 0.5 mA, 1 s) and the footshock was delivered at the end of the 30-s tone. There was a 2-min interval between each trial. The contextual and cued memory-retention tests were performed 24 h and 48 h after conditioning, respectively. In the contextual memory-retention test, we placed each mouse in the conditioning chamber for 3 min. In the cued memory-retention test, we placed each mouse in a novel chamber (defined as Pre-cue), with a 3-min tone delivered later (defined as Cue). The freezing percentage was scored manually and double-blinded. To measure memory acquisition, the freezing levels were calculated during each tone period. For the

contextual and cued memory-retention tests, the freezing levels were calculated during context and cue presentation.

In Vivo Photostimulation

We connected a 473-nm laser (Shanghai Dream Lasers Technology, Shanghai, China) to a patch cord through a specific omni-directional wheel (Doric Lenses, Quebec, Canada), allowing the fiber to rotate freely. The patch cord was then connected to the implanted ceramic fiber optic cannulas [25]. Sustained 15-mW laser light was delivered. The photostimulation was delivered 5 min before and throughout the conditioning, or 15 min before and during the memory retention tests.

Western Blotting

After 15-min of laser (473 nm) stimulation, mice were anesthetized with 1% pentobarbital sodium. The bilateral BLAs were dissected and the proteins were extracted by RIPA (P0013B, Beyotime Biotechnology, Shanghai, China). The proteins were separated on 12% SDS-PAGE gels and transferred onto nitrocellulose membranes. The membranes were incubated with rabbit anti-cofilin (1:1000, 5175, Cell Signaling Technology, Boston, USA), anti-p-cofilin (1:500, 3313, Cell Signaling Technology), or anti-GAPDH (1:2000, 2118, Cell Signaling Technology) at 4°C for 12 h, and then with anti-rabbit IRDye 800CW secondary antibody (Rockland, PA, USA) at room temperature for 90 min. The Western blot results were analyzed with ImageJ software.

Immunofluorescence

Mice were anesthetized and transcardially perfused with saline followed by 4% paraformaldehyde (PFA, in 0.1 mol/L PB, pH 7.4) [26]. We immersed the brain in 4% PFA at 4°C for 12 h for post-fixation. The brain was then dehydrated in 20% and 30% sucrose. The BLA was cut into 30- μ m coronal sections on a cryostat microtome (Leica Instrument Co., Ltd., Germany). We washed the sections in phosphate-buffered saline (0.01 mol/L PBS), and then blocked them with 5% donkey serum (in 0.01 mol/L PBST) at room temperature for 90 min. The sections were incubated with rabbit anti-c-Fos antibody (1:1000, sc-52, Santa Cruz), or mouse anti-NeuN antibody (1:1000, ab104224, Abcam, Cambridge, UK) at 4°C for 24 h. After washing in PBST, the sections were incubated with the secondary antibody Alexa Fluor 488 goat anti-rabbit IgG (1:1000, 111-545-144, Jackson ImmunoResearch, PA, USA), or Alexa Fluor 488 goat anti-mouse IgG (1:1000, 111-545-166, Jackson ImmunoResearch) at room temperature for 90 min. For further imaging and preservation, the

sections were mounted with an anti-bleaching mounting medium (Thermo Fisher Scientific). Images were captured under a confocal microscope (Nikon A1, Japan).

Cell Counting

To characterize the activation of cells in the BLA induced by fear memory acquisition and retrieval, mice were transcardially perfused 90 min after fear conditioning or the context test [24]. The number of c-Fos⁺ or NeuN⁺ neurons in the BLA was calculated automatically by Image-Pro Plus 6.0 software. A threshold for background fluorescence was applied for cell counting. An average number of 3 sections per mouse was calculated to avoid errors. The counting process was performed double-blinded.

Statistical Analyses

Data are presented as the mean \pm SEM and plotted by GraphPad Prism v.7 software. Student's *t*-test was used to compare two groups. One-way ANOVA, followed by *post hoc* Bonferroni's test was used to compare multiple groups. Two-way ANOVA was used to compare two groups at different time points. The differences were calculated with SPSS and the statistical significance was defined as $P < 0.05$.

Results

Manipulating Rac1 Activity in BLA Astrocytes Suppresses Fear Memory Acquisition

To determine whether the Rac1 activity in BLA astrocytes regulates conditioned fear memory acquisition and retrieval, we constructed AAV-mGFAP-Rac1-PA and AAV-mGFAP-Rac1-DN/PA to test the effects of astrocytic Rac1 activity on behaviors at precise times. Previous studies usually overexpressed or knocked out Rac1, which may cause a compensatory reaction. Here, we connected *Rac1-PA* or *Rac1-DN/PA* to the *mGFAP* promoter to optically up-regulate or down-regulate the activity of Rac1 specifically in astrocytes. In detail, Rac1-PA or Rac1-DN/PA are composed of a constitutively active mutant (Q61L) of Rac1 (Rac1-CA) or a dominant-negative mutant (T17N) of Rac1 (Rac1-DN) and a light oxygen voltage (LOV)-J α sequence [23]. The compact conformation of the LOV-J α domain can preclude the combination of effectors with Rac1. Stimulation with 473 nm light unwinds the helix linking LOV to Rac1, which allows the interaction between Rac1 and effectors (Fig. 1A, B). A light-insensitive LOV mutation (C450A) binding to Rac1 (Rac1-C450A) was

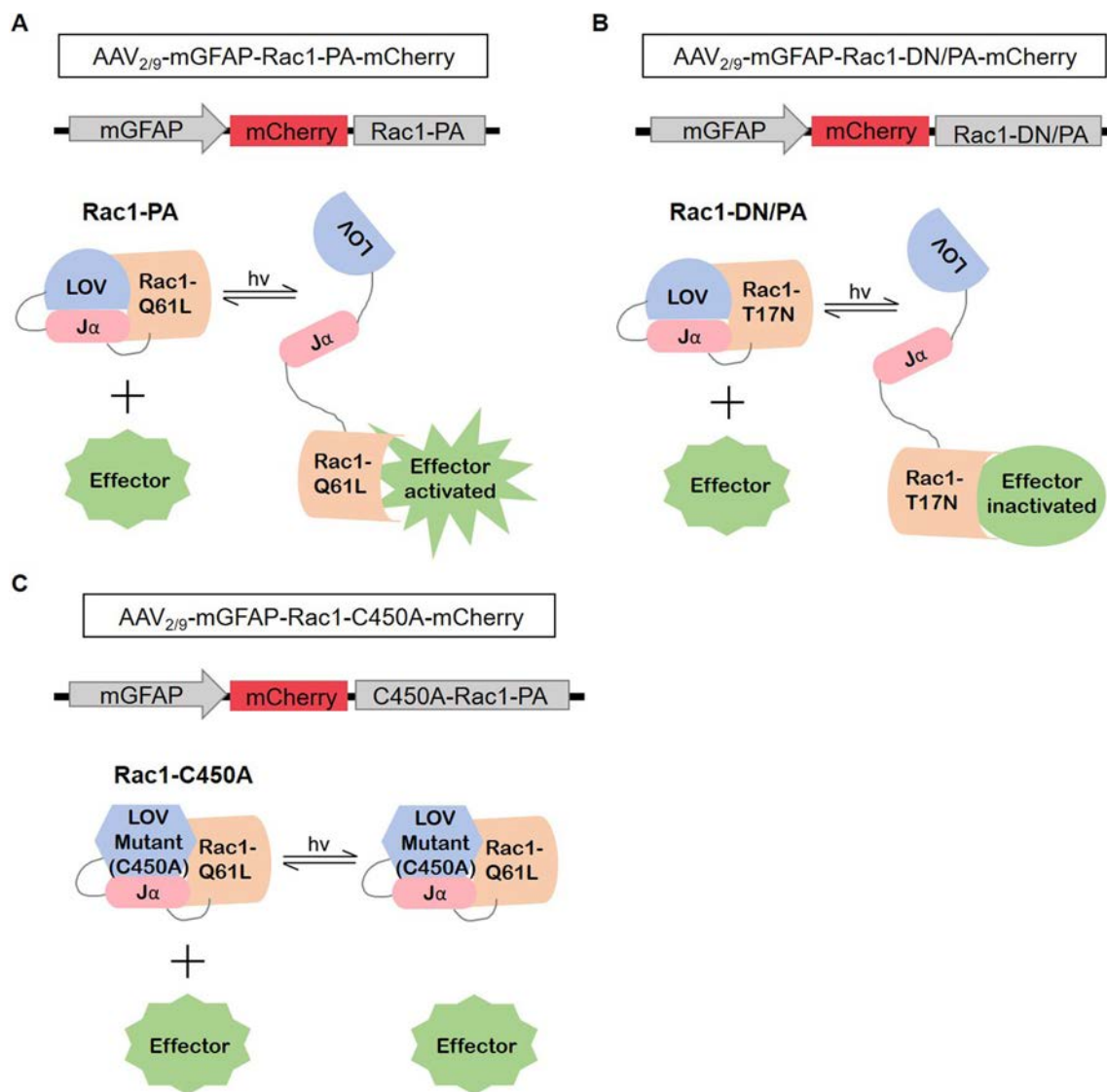


Fig. 1 Constructing recombinant AAVs of *Rac1-PA*, *Rac1-DN/PA*, and *Rac1-C450A* under the *mGFAP* promoter. **A** Cartoon of AAV-*mGFAP-Rac1-PA-mCherry* design. The photoreactive LOV- $J\alpha$ domain blocks the binding of effectors to Rac1-Q61L, and laser stimulation (473 nm) causes the unwinding of the LOV- $J\alpha$ helix, which releases the steric inhibition, and leads to Rac1 and effector

activation. **B** Cartoon of AAV-*mGFAP-Rac1-DN/PA-mCherry* design. Similar to the above, laser stimulation leads to releasing the steric inhibition of Rac1-T17N, and results in Rac1 and effector inactivation. **C** Cartoon of AAV-*mGFAP-Rac1-C450A-mCherry* design. The amino acid substitution in the LOV domain (C450A) leads to the insensitivity to laser stimulation. hv, irradiation.

used as a photo-insensitive control (Fig. 1C). Three weeks after viral injection, we found that only a small proportion ($2.49\% \pm 0.26\%$) of neurons (NeuN^+ cells) were co-labeled with mCherry (Fig. 2A, B), showing that the expression of LOV-Rac1 was restricted to astrocytes. In order to verify the efficiency of the photostimulation of Rac1, we tested the expression levels of phosphorylated cofilin (p-cofilin), a downstream effector of Rac1, and found that, compared to the Rac1-C450A group, photostimulation of Rac1-PA up-regulated p-cofilin, whereas photostimulation of Rac1-DN/PA down-regulated p-cofilin (Fig. 2C, D; $F_{(2,12)} = 13.16$, $P < 0.05$). As a result, we

succeed in up-regulating (Rac1-PA) or down-regulating (Rac1-DN/PA) the Rac1-activity under 473 nm light stimulation in real-time.

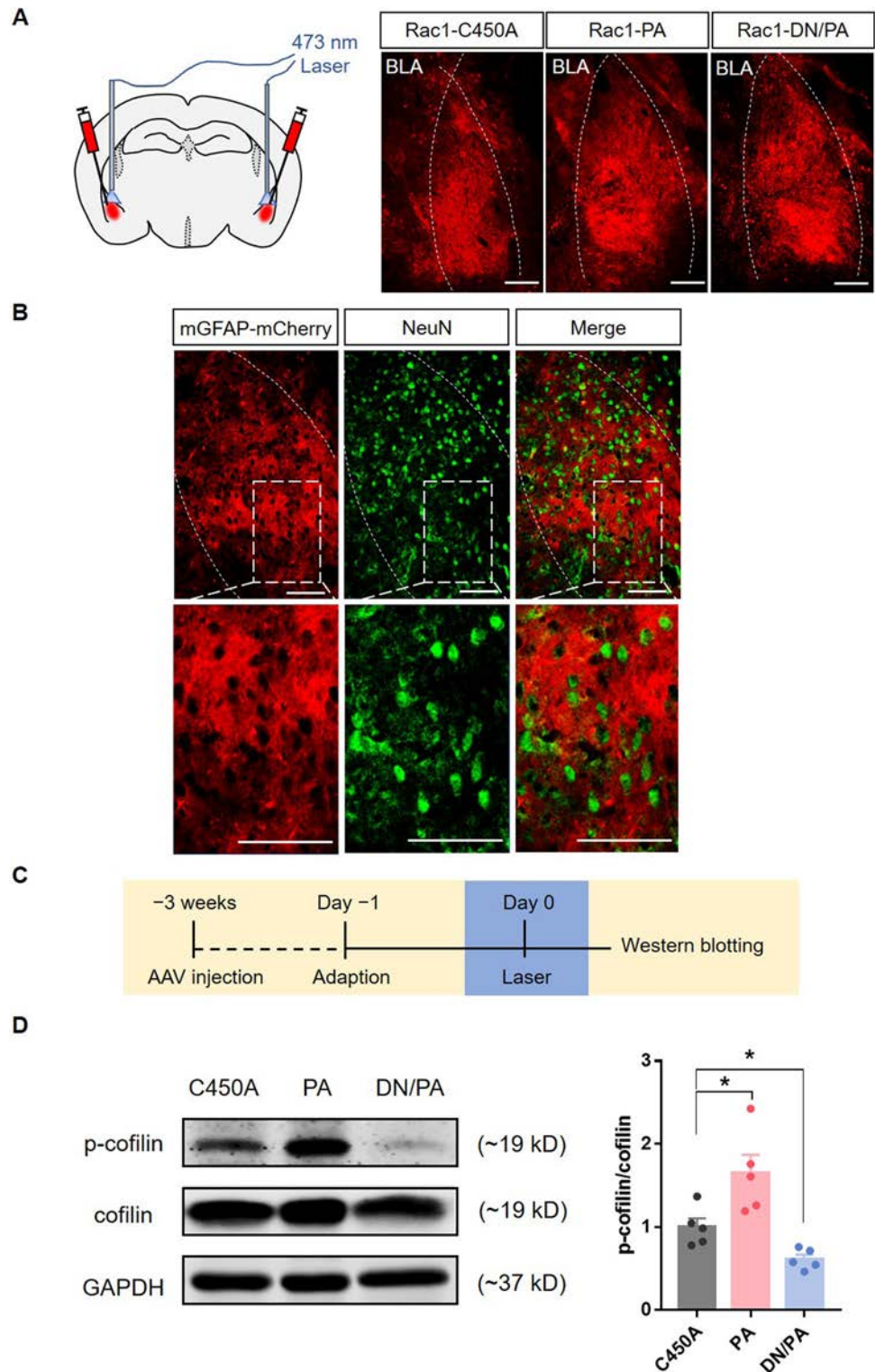
We bilaterally microinjected AAVs encoding *Rac1-PA*, *Rac1-DN/PA*, or *Rac1-C450A* driven by the *mGFAP* promoter into the BLA (Fig. 2A). After 3 weeks for recovery, each mouse was introduced into the conditioning chamber for 5 min without tone or footshock and the basal freezing level in the conditioning context were acquired. One day later, the mice received 5 CS-US pairing trials accompanied by laser stimulation (473 nm) in the bilateral BLA (Fig. 3A). The results showed that, compared to the

Fig. 2 Efficiency tests for *Rac1-PA*, *Rac1-DN/PA*, and *Rac1-C450A*. **A** Schematic of laser stimulation of the bilateral BLA (left) and representative images of *Rac1-C450A*-mCherry, *Rac1-PA*-mCherry, and *Rac1-DN/PA*-mCherry expression in the BLA (right) (dotted lines, location of the BLA; scale bars, 100 μ m).

B Representative immunofluorescence images showing that few ($2.49\% \pm 0.26\%$) neurons (NeuN^+ , green) are co-labeled with AAV-GFAP-mCherry, indicating that the expression of LOV-Rac1 is restricted to astrocytes (scale bars, 100 μ m).

C Diagram of the experiment timeline. Three weeks after virus injection, the mice received 15-min laser (473 nm) stimulation and were anesthetized immediately for Western blotting.

D Laser stimulation of *Rac1-PA* increases the expression levels of p-cofilin, while laser stimulation of *Rac1-DN/PA* decreases its levels (*Rac1-C450A*: $n = 5$, *Rac1-PA*: $n = 5$, *Rac1-DN/PA*: $n = 5$; $*P < 0.05$, C450A vs PA, C450A vs DN/PA, one-way ANOVA).



Rac1-C450A control group, both photoactivation and photoinactivation of astrocytic *Rac1* activity during conditioning attenuated the freezing levels during cue presentation (Fig. 3B; group effect: $F_{(2,57)} = 14.15$, $P < 0.001$; time effect: $F_{(4,228)} = 21.13$, $P < 0.001$; interaction: $F_{(8,228)} =$

2.14 , $P < 0.05$). After conditioning, the contextual and cued memory retention tests were performed in the following days without laser stimulation. The data showed that up-regulation or down-regulation of *Rac1* activity in the BLA significantly decreased the freezing levels in both

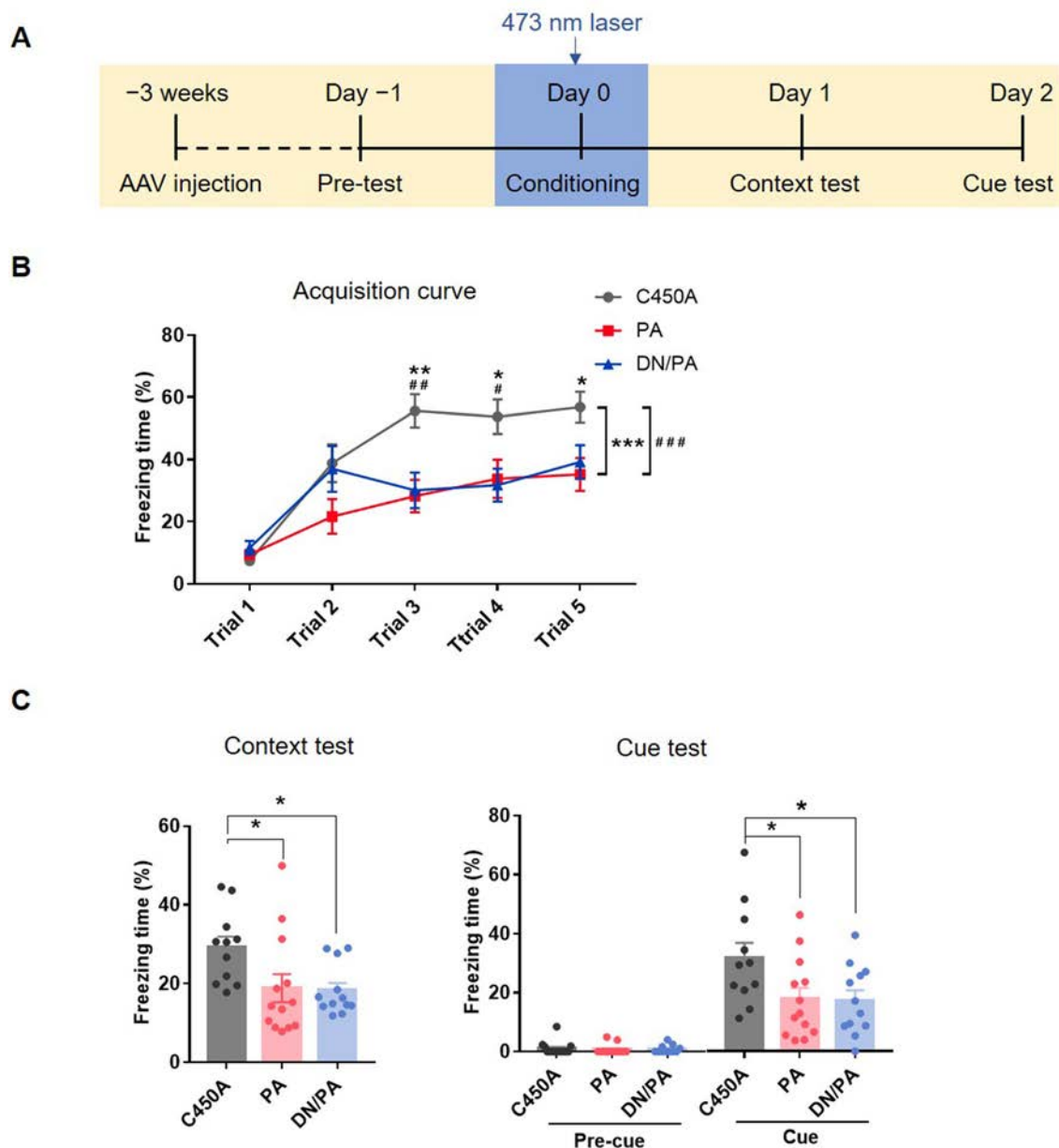


Fig. 3 Increasing or decreasing astrocytic Rac1 activity in the BLA impairs fear memory acquisition. **A** Diagram of the experiment timeline. The AAV was injected 3 weeks before the behavioral tests. The laser stimulation (473 nm) was delivered 5 min before and during the 5 trials of CS-US pairing conditioning, then contextual and cued memory retention were tested 1 and 2 days later. **B** Compared to the Rac1-C450A group, laser activation of Rac1-PA and Rac1-DN/PA both attenuate the fear memory acquisition (Rac1-C450A: $n = 20$,

Rac1-PA: $n = 20$, Rac1-DN/PA: $n = 20$; $*P < 0.05$, $**P < 0.01$, $***P < 0.001$, C450A vs PA, $^{\#}P < 0.05$, $^{\#\#}P < 0.01$, $^{\#\#\#}P < 0.001$, C450A vs DN/PA, ANOVA with repeated measures and Bonferroni's *post hoc* test). **C** Similarly, compared to the Rac1-C450A group, laser activation of Rac1-PA and Rac1-DN/PA both impaired contextual and cued fear memory (Rac1-C450A: $n = 11$, Rac1-PA: $n = 13$, Rac1-DN/PA: $n = 12$; $*P < 0.05$, C450A vs PA, C450A vs DN/PA, one-way ANOVA).

contextual and cued memory retention tests (Fig. 3C; context test: $F_{(2,33)} = 4.31$, $P < 0.05$; cue test: $F_{(2,33)} = 3.85$, $P < 0.05$). The results above suggest that either activation or inhibition of astrocytic Rac1 activity impairs fear memory learning, indicating that the normal activity of astrocytes in BLA is necessary for fear memory acquisition.

Disturbance of Astrocytic Rac1 Activity Decreases Neuronal Activity in the BLA During Fear Memory Acquisition

To explore the interaction between astrocytes and neurons, we tested the activation of BLA neurons after fear conditioning with and without optical stimulation of

astrocytic Rac1 using c-Fos immunostaining (Fig. 4D). Immunofluorescence results showed that fear conditioning increased the c-Fos⁺ cell counts in the BLA (Fig. 4A–C, $t_{(9)} = 5.68$, $P < 0.001$), consistent with previous reports. But after interfering with astrocytic Rac1 activity, the number of c-Fos⁺ neurons in the BLA decreased (Fig. 4E, F; $F_{(2,12)} = 27.15$, $P < 0.001$). These results indicate that

the activity of astrocytic Rac1 is involved in the acquisition of fear memory through the regulation of neuronal activity in the BLA. The abnormal activity of astrocytic Rac1 disrupts the well-balanced function of astrocytes and then impairs neuronal activity and memory acquisition in fear conditioning.

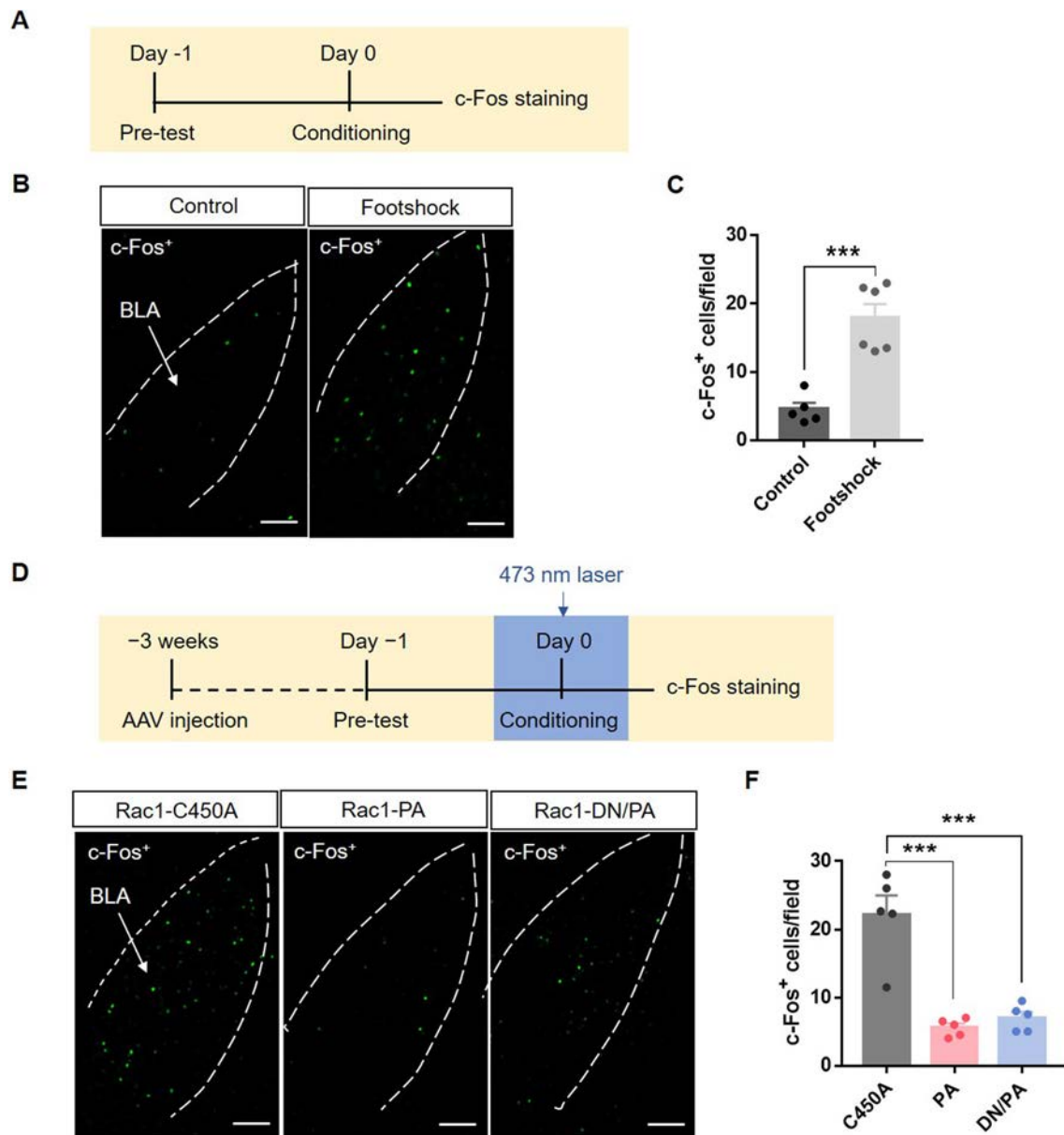


Fig. 4 Optical stimulation of BLA astrocytic Rac1 decreases the neuronal activation induced by fear conditioning. **A** Diagram of the experiment timeline. Mice were put into the behavioral chamber, underwent footshock or not, and were perfused 90 min later. **B** Representative immunofluorescence images of BLA c-Fos⁺ neurons in mice with and without footshock (scale bars, 100 μ m). **C** Quantitative analysis showing that footshock significantly increases c-Fos expression in the BLA (Control: $n = 5$, Footshock: $n = 6$; *** $P < 0.001$, Control vs Footshock, t -test). **D** Diagram of the

experiment timeline. Three weeks after virus injection, the mice underwent 5 trials of CS-US paired conditioning with laser stimulation (473 nm) and were perfused 90 min later. **E** Representative immunofluorescence images showing c-Fos⁺ neurons in the BLA of mice in the Rac1-C450A, Rac1-PA, and Rac1-DN/PA groups (scale bars, 100 μ m). **F** Quantitative analysis showing that laser stimulation of Rac1-PA and Rac1-DN/PA both significantly decrease c-Fos expression in the BLA ($n = 5$ in each group; *** $P < 0.001$, C450A vs PA, C450A vs DN/PA, one-way ANOVA).

Astrocytic Rac1 Activity in the BLA Regulates Fear Memory Retrieval

To determine whether the Rac1 activity of astrocytes in the BLA regulates fear memory retrieval, we bilaterally microinjected AAV-mGFAP-Rac1-PA-mCherry, AAV-mGFAP-Rac1-DN/PA-mCherry, or AAV-mGFAP-Rac1-C450A-mCherry into the BLA. After 3 weeks of recovery, each mouse underwent a 5-min pre-test and 5 CS-US paired conditioning without laser stimulation. For the contextual and cued memory retention tests, each mouse received 473-nm laser stimulation for 15 min before the tests and was put into the chamber immediately after laser delivery (Fig. 5A). Compared to the Rac1-C450A control group, up-regulation or down-regulation of astrocytic Rac1

activity in the BLA decreased the freezing levels induced by context and tone presentation during memory retention tests (Fig. 5B, context test: $F_{(2,36)} = 9.43$, $P < 0.001$; cue test: $F_{(2,36)} = 7.508$, $P < 0.01$), suggesting that astrocytic Rac1 activity in the BLA is critically involved in memory retrieval in fear conditioning.

To investigate whether the effects were transient or permanent, we then performed the contextual and cued memory retention tests again without laser stimulation. The results showed no difference between the Rac1-C450A group and the Rac1-PA group or the Rac1-DN/PA group (Fig. 5C; context test: $F_{(2,36)} = 0.85$, $P = 0.44$; cue test: $F_{(2,36)} = 0.06$, $P = 0.94$), suggesting that astrocytic Rac1 activity in the BLA transiently regulates fear memory retrieval.

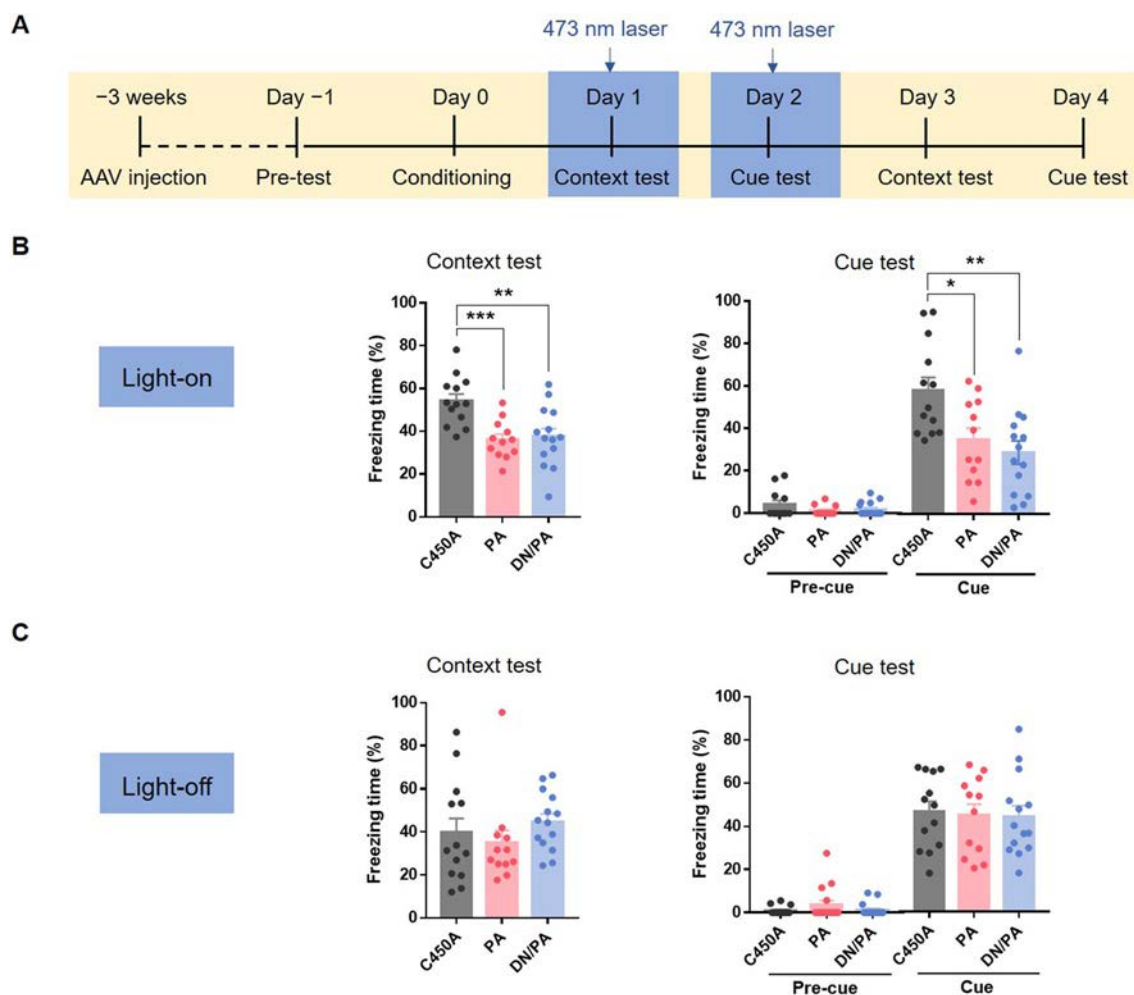


Fig. 5 Increasing or decreasing astrocytic Rac1 activity in the BLA impairs the retrieval of conditioned fear memory. **A** Diagram of the experiment timeline. Mice received 5 trials of CS-US paired conditioning 3 weeks after the AAV injection. Laser stimulation (473 nm) was delivered 15 min before and during the memory retention test, which was repeated without laser stimulation on days 3 and 4. **B** Compared to the Rac1-C450A group, laser stimulation of Rac1-PA and Rac1-DN/PA during tests both impair the contextual

and cued fear memory retrieval (Rac1-C450A: $n = 13$, Rac1-PA: $n = 12$, Rac1-DN/PA: $n = 14$; $*P < 0.05$, $**P < 0.01$, $***P < 0.001$, C450A vs PA, C450A vs DN/PA, one-way ANOVA). **C** Without laser stimulation, the mice in the Rac1-PA and Rac1-DN/PA groups showed no significant changes of freezing levels (Rac1-C450A: $n = 13$, Rac1-PA: $n = 12$, Rac1-DN/PA: $n = 14$; $P > 0.05$, C450A vs PA, C450A vs DN/PA, one-way ANOVA).

These results indicate that both up-regulation and down-regulation of astrocytic Rac1 activity in the BLA affect fear memory retrieval. Moreover, the regulatory effect is transient, and not permanent.

Optical Stimulation of BLA Astrocytic Rac1 Decreases BLA Neuronal activation Induced by Memory Retrieval

To confirm the regulation of neuronal activity by astrocytic Rac1 activity, we performed c-Fos immunostaining 90 min after contextual retrieval (Fig. 6D). Immunofluorescence results showed that the contextual memory retention test increased c-Fos⁺ cell counts in the BLA (Fig. 6A–C; $t_{(10)} = 8.33$, $P < 0.001$), while up-regulation or down-regulation of astrocytic Rac1 activity reduced the number of c-Fos⁺ neurons in the BLA (Fig. 6E, F; $F_{(2,17)} = 19.84$, $P < 0.001$). These results indicate that both up-regulation and down-regulation of astrocytic Rac1 activity in the BLA disrupt the normal function of astrocytes and impair the activation of neurons in BLA, thereby decreasing fear memory retrieval.

Discussion

Our results provide insights into the roles of BLA astrocytes in memory acquisition and retrieval in fear conditioning. Using the photo-stimulation approach, we manipulated astrocytic Rac1 activity in real time and found that both activation and inactivation of Rac1 in astrocytes impaired fear memory acquisition and retrieval, and decreased neuronal activity in the BLA.

Astrocytes, the largest population of neuroglial cells in the brain, have crucial structural, metabolic, and homeostatic functions [27–29]. In the adult brain, astrocytes communicate with neurons by the exocytosis of numerous molecules surrounding synapses. They release glutamate, ATP, GABA, D-serine, or endocannabinoids that regulate synaptic strength, such as long-term potentiation (LTP) and long-term depression (LTD), mechanisms of memory and learning [30]. They also maintain the homeostasis of neurotransmitters by recycling potassium ions and glutamate in the synaptic cleft [31, 32]. Recent studies have shown that the cognitive process requires the coordinated activity of astrocytes and neuron ensembles. Activation of astrocytes in the CeA induces cued fear memory extinction [33]. Chemogenetic activation of astrocytes in CA1 induces LTP, therefore enhancing memory acquisition [34]. Blocking the glutamate uptake into astrocytes in the prefrontal cortex impairs spatial memory [35]. Inhibiting the L-lactate production in astrocytes in the hippocampus suppresses LTP and disrupts the formation of long-term

memory [36]. Here, we showed that both activation and inactivation of Rac1 activity in astrocytes decreased the number of activated neurons in the BLA and impaired fear memory acquisition and retrieval. This phenomenon may be caused by disturbing the balance between astrocytes and neurons: photo-activating Rac1 in astrocytes causes astrocytic expansion [23], and the extensive coverage of astrocytic lamellae might result in more glutamate reuptake into astrocytes [37]. The reduced neurotransmitter availability in synapses, in turn, impairs LTP expression [38]. The curbed function of neurons may lead to reduced responses to stimuli and finally suppress the acquisition and retrieval of conditioned fear memory. On the other hand, photo-inactivating Rac1 in BLA astrocytes causes flattening of astrocytes [23], and the limited coverage of astrocytic lamellae might result in less D-serine and L-lactate reaching synapses [39], which would reduce the activation of N-methyl-D-aspartate receptors and raise the threshold of LTP induction [36, 40]. The curbed function of neurons may also lead to reduced responses to stimuli and suppress the acquisition and retrieval of conditioned fear memory as well. Notably, the activation or inactivation of astrocytic Rac1 activity is not equivalent to activation or inactivation of astrocytic activity by stimulation of Gq-GPCRs or Gi-GPCRs. In conclusion, both up-regulating and down-regulating the activity of Rac1 may disturb the balance between astrocytes and neurons, and disrupt the normal function of neurons in the BLA, thus impairing the acquisition and retrieval of fear memory. Although the behavioral outcomes of the two operations were consistent, the concrete mechanisms may be distinct, which needs further exploration. This research indicates that the well-balanced function of astrocytes in the BLA is the basis of the neuronal activity and the acquisition and expression of fear memory.

Rac1 is a molecular switch of cell signal transduction and is involved in cytoskeletal protein remodeling. It also regulates cell migration, extension, polarity, and other functions [41, 42]. Studies have shown that activating Rac1 promotes spine formation, and inhibiting Rac1 activity decreases the stability of mature spines [43, 44]. In astrocytes, activating Rac1 causes expansion and inhibiting it flattens them [21]. In previous studies, Rac1 activity was usually regulated by permanent interventions, such as knockout, overexpression, sustained activation, and sustained suppression [45–47]. These methods likely lead to compensatory reactions caused by other Rho GTPases and reduce the reliability of experimental results. To optimize them, we constructed *Rac1-PA* and *Rac1-DN/PA* under the *mGFAP* promoter to manipulate the structure of astrocytes in real-time by photostimulation. Previous studies in our lab have shown that Rac1 knockout in BLA astrocytes results in facilitation of the acquisition of fear memory, but

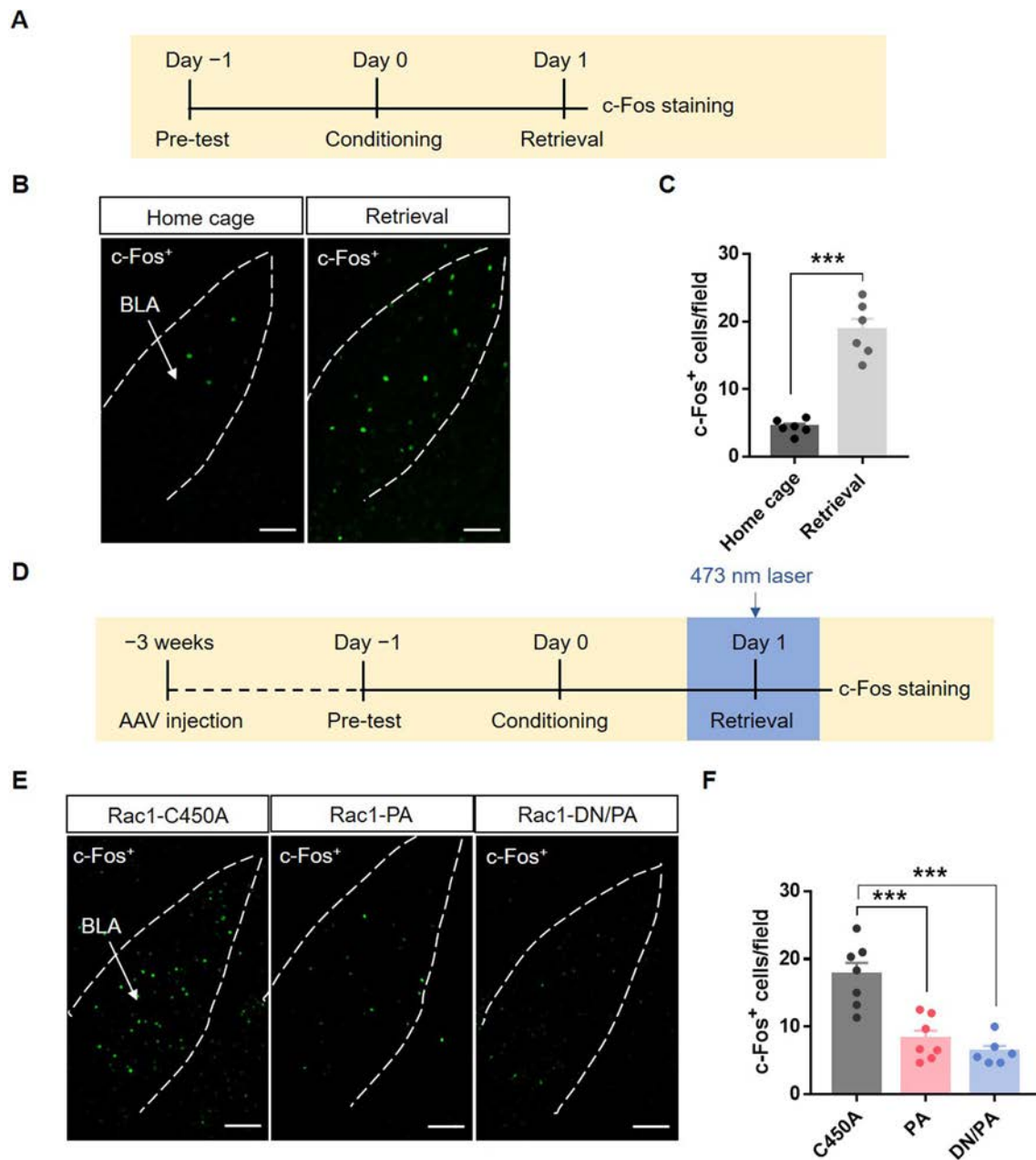


Fig. 6 Optical stimulation of BLA astrocytic Rac1 inhibits neuronal activation induced by memory retrieval. **A** Diagram of the experiment timeline. Mice were placed in the behavior room, underwent contextual retrieval or not, and then were perfused 90 min later. **B** Representative images of c-Fos⁺ neurons in the BLA of mice with and without retrieval (scale bars, 100 μ m). **C** Quantitative analysis showing that contextual retrieval significantly increases c-Fos expression in the BLA (Home cage: $n = 6$, Retrieval: $n = 6$; $***P < 0.001$, Home cage vs Retrieval, t -test). **D** Diagram of the experiment timeline. Three weeks after virus injection, the mice underwent 5

trials of CS-US paired conditioning on day 0. After contextual retrieval with or without laser stimulation; 90 min later, the mice were perfused. **E** Representative images of c-Fos⁺ neurons in the BLA of mice in the Rac1-C450A, Rac1-PA, and Rac1-DN/PA groups (scale bars, 100 μ m). **F** Quantitative analysis showing that laser stimulation of Rac1-PA and Rac1-DN/PA during memory retrieval decreases c-Fos expression in the BLA (Rac1-C450A: $n = 7$, Rac1-PA: $n = 7$, Rac1-DN/PA: $n = 6$; $***P < 0.001$, C450A vs PA, C450A vs DN/PA, one-way ANOVA).

persistent inhibition of astrocytic Rac1 in the BLA has no apparent effect [21]. To explain this phenomenon further, we found that transient inhibition of astrocytic Rac1 activity in the BLA by AAV-Rac1-DN/PA impaired fear

memory acquisition and retrieval. It is possible that diverse interventions lead to different inhibitory effects and permanent interventions may cause compensatory reactions or lead to other radical changes. Photostimulation of Rac1

activity is a good choice for regulating Rac1 activity in real time and avoiding compensatory reactions.

Thanks to the real-time effects of the interventions, we further explored whether the behavioral changes are reversible. We delivered photostimulation before memory retrieval and tested the expression of fear memory without light stimulation two days later. The results showed no significant difference between the Rac1-C450A and Rac1-PA or Rac1-DN/PA groups on fear expression without photostimulation (Fig. 5C), indicating that the inhibitory effect on memory retrieval was temporary. However, photostimulating Rac1 during conditioning not only impaired the acquisition of conditioned fear memory (showed by the decreased freezing level in the learning curve), but also decreased the freezing level in the retrieval of fear memory (Fig. 3C, D). These results suggest that the interventions during fear conditioning inhibit the formation of memory engram cells in the BLA and impair memory acquisition. Nevertheless, temporary stimulation during fear memory retrieval might temporarily suppress the activity of memory engram cells, and not induce permanent changes of the engrams in the BLA.

In conclusion, the present study demonstrates that astrocytic Rac1 activity in the BLA regulates fear memory acquisition and retrieval. Both up-regulation and down-regulation of astrocytic Rac1 activity disrupted the interaction between astrocytes and neurons, inhibited the activation of neurons in the BLA, and finally decreases the acquisition and retrieval of fear memory. The astrocytic Rac1 activity that regulates the balance between astrocytes and neurons might be a promising target for treating memory-related diseases, such as post-traumatic stress disorder.

Acknowledgements This work was supported by Grants from the China Postdoctoral Science Foundation (BX20180070 and 2019M661347), and the National Natural Science Foundation of China (31930046 and 31771176).

Conflict of interest The authors claim that there are no conflicts of interest.

References

- Allen NJ, Barres BA. Neuroscience: Glia - more than just brain glue. *Nature* 2009, 457: 675–677.
- Abbott NJ, Ronnback L, Hansson E. Astrocyte-endothelial interactions at the blood-brain barrier. *Nat Rev Neurosci* 2006, 7: 41–53.
- Araque A, Parpura V, Sanzgiri RP, Haydon PG. Tripartite synapses: glia, the unacknowledged partner. *Trends Neurosci* 1999, 22: 208–215.
- Allen NJ, Eroglu C. Cell biology of astrocyte-synapse interactions. *Neuron* 2017, 96: 697–708.
- Lopez-Bayghen E, Ortega A. Glial glutamate transporters: new actors in brain signaling. *IUBMB Life* 2011, 63: 816–823.
- Pascual O, Casper KB, Kubera C, Zhang J, Revilla-Sanchez R, Sul JY. Astrocytic purinergic signaling coordinates synaptic networks. *Science* 2005, 310: 113–116.
- Araque A, Carmignoto G, Haydon PG, Oliet SH, Robitaille R, Volterra A. Gliotransmitters travel in time and space. *Neuron* 2014, 81: 728–739.
- Savtchouk I, Volterra A. Gliotransmission: beyond black-and-white. *J Neurosci* 2018, 38: 14–25.
- Qin C, Zhou LQ, Ma XT, Hu ZW, Yang S, Chen M, *et al.* Dual functions of microglia in ischemic stroke. *Neurosci Bull* 2019, 35: 921–933.
- Rose CR, Karus C. Two sides of the same coin: sodium homeostasis and signaling in astrocytes under physiological and pathophysiological conditions. *Glia* 2013, 61: 1191–1205.
- Kim JJ, Jung MW. Neural circuits and mechanisms involved in Pavlovian fear conditioning: a critical review. *Neurosci Biobehav Rev* 2006, 30: 188–202.
- Malleret G, Alarcon JM, Martel G, Takizawa S, Vronskaya S, Yin D, *et al.* Bidirectional regulation of hippocampal long-term synaptic plasticity and its influence on opposing forms of memory. *J Neurosci* 2010, 30: 3813–3825.
- Maren S. Synaptic mechanisms of associative memory in the amygdala. *Neuron* 2005, 47: 783–786.
- Rodrigues SM, Schafe GE, LeDoux JE. Molecular mechanisms underlying emotional learning and memory in the lateral amygdala. *Neuron* 2004, 44: 75–91.
- Takeuchi T, Duzskiewicz AJ, Morris RG. The synaptic plasticity and memory hypothesis: encoding, storage and persistence. *Philos Trans R Soc Lond B Biol Sci* 2014, 369: 20130288.
- Alberini CM, Cruz E, Descalzi G, Bessieres B, Gao V. Astrocyte glycogen and lactate: New insights into learning and memory mechanisms. *Glia* 2018, 66: 1244–1262.
- Logan S, Pharaoh GA, Marlin MC, Masser DR, Matsuzaki S, Wronowski B, *et al.* Insulin-like growth factor receptor signaling regulates working memory, mitochondrial metabolism, and amyloid-beta uptake in astrocytes. *Mol Metab* 2018, 9: 141–155.
- Zhang X, Shen X, Dong J, Liu WC, Song M, Sun Y, *et al.* Inhibition of reactive astrocytes with fluorocitrate ameliorates learning and memory impairment through upregulating CRTCL1 and synaptophysin in ischemic stroke rats. *Cell Mol Neurobiol* 2019, 39: 1151–1163.
- Jaffe AB, Hall A. Rho GTPases: biochemistry and biology. *Annu Rev Cell Dev Biol* 2005, 21: 247–269.
- Racchetti G, D'Alessandro R, Meldolesi J. Astrocyte stellation, a process dependent on Rac1 is sustained by the regulated exocytosis of enlargosomes. *Glia* 2012, 60: 465–475.
- Liao Z, Tao Y, Guo X, Cheng D, Wang F, Liu X, *et al.* Fear conditioning downregulates Rac1 activity in the basolateral amygdala astrocytes to facilitate the formation of fear memory. *Front Mol Neurosci* 2017, 10: 396.
- Martinez LA, Klann E, Tejada-Simon MV. Translocation and activation of Rac in the hippocampus during associative contextual fear learning. *Neurobiol Learn Mem* 2007, 88: 104–113.
- Wu YI, Frey D, Lungu OI, Jaehrig A, Schlichting I, Kuhlman B, *et al.* A genetically encoded photoactivatable Rac controls the motility of living cells. *Nature* 2009, 461: 104–108.
- Zhou Y, Zhu H, Liu Z, Chen X, Su X, Ma C, *et al.* A ventral CA1 to nucleus accumbens core engram circuit mediates conditioned place preference for cocaine. *Nat Neurosci* 2019, 22: 1986–1999.
- Couto A, Mack NA, Favia L, Georgiou M. An apicobasal gradient of Rac activity determines protrusion form and position. *Nat Commun* 2017, 8: 15385.
- Fan XC, Fu S, Liu FY, Cui S, Yi M, Wan Y. Hypersensitivity of prelimbic cortex neurons contributes to aggravated nociceptive

- responses in rats with experience of chronic inflammatory pain. *Front Mol Neurosci* 2018, 11: 85.
27. Daneman R, Prat A. The blood-brain barrier. *Cold Spring Harb Perspect Biol* 2015, 7: a020412.
 28. Verkhratsky A, Nedergaard M. Physiology of astroglia. *Physiol Rev* 2018, 98: 239–389.
 29. Ioannou MS, Jackson J, Sheu SH, Chang CL, Weigel AV, Liu H, *et al.* Neuron-astrocyte metabolic coupling protects against activity-induced fatty acid toxicity. *Cell* 2019, 177(1522–1535): e1514.
 30. Chung WS, Allen NJ, Eroglu C. Astrocytes control synapse formation, function, and elimination. *Cold Spring Harb Perspect Biol* 2015, 7: a020370.
 31. Breslin K, Wade JJ, Wong-Lin K, Harkin J, Flanagan B, Van Zalinge H, *et al.* Potassium and sodium microdomains in thin astroglial processes: A computational model study. *PLoS Comput Biol* 2018, 14: e1006151.
 32. Rose CR, Ziemens D, Untiet V, Fahlke C. Molecular and cellular physiology of sodium-dependent glutamate transporters. *Brain Res Bull* 2018, 136: 3–16.
 33. Martin-Fernandez M, Jamison S, Robin LM, Zhao Z, Martin ED, Aguilar J, *et al.* Synapse-specific astrocyte gating of amygdala-related behavior. *Nat Neurosci* 2017, 20: 1540–1548.
 34. Adamsky A, Kol A, Kreisel T, Doron A, Ozeri-Engelhard N, Melcer T, *et al.* Astrocytic activation generates de novo neuronal potentiation and memory enhancement. *Cell* 2018, 174(59–71): e14.
 35. Bechtholt-Gompf AJ, Walther HV, Adams MA, Carlezon WA Jr, Ongur D, Cohen BM. Blockade of astrocytic glutamate uptake in rats induces signs of anhedonia and impaired spatial memory. *Neuropsychopharmacology* 2010, 35: 2049–2059.
 36. Suzuki A, Stern SA, Bozdagi O, Huntley GW, Walker RH, Magistretti PJ, *et al.* Astrocyte-neuron lactate transport is required for long-term memory formation. *Cell* 2011, 144: 810–823.
 37. Pannasch U, Freche D, Dallerac G, Ghezali G, Escartin C, Ezan P, *et al.* Connexin 30 sets synaptic strength by controlling astroglial synapse invasion. *Nat Neurosci* 2014, 17: 549–558.
 38. Poskanzer KE, Yuste R. Astrocytes regulate cortical state switching in vivo. *Proc Natl Acad Sci U S A* 2016, 113: E2675–2684.
 39. Panatier A, Theodosis DT, Mothet JP, Touquet B, Pollegioni L, Poulain DA, *et al.* Glia-derived D-serine controls NMDA receptor activity and synaptic memory. *Cell* 2006, 125: 775–784.
 40. Papouin T, Dunphy JM, Tolman M, Dineley KT, Haydon PG. Septal Cholinergic neuromodulation tunes the astrocyte-dependent gating of hippocampal NMDA receptors to wakefulness. *Neuron* 2017, 94(840–854): e847.
 41. Newey SE, Velamoor V, Govek EE, Van Aelst L. Rho GTPases, dendritic structure, and mental retardation. *J Neurobiol* 2005, 64: 58–74.
 42. Gordon-Weeks PR, Fournier AE. Neuronal cytoskeleton in synaptic plasticity and regeneration. *J Neurochem* 2014, 129: 206–212.
 43. Tashiro A, Minden A, Yuste R. Regulation of dendritic spine morphology by the rho family of small GTPases: antagonistic roles of Rac and Rho. *Cereb Cortex* 2000, 10: 927–938.
 44. Tashiro A, Yuste R. Regulation of dendritic spine motility and stability by Rac1 and Rho kinase: evidence for two forms of spine motility. *Mol Cell Neurosci* 2004, 26: 429–440.
 45. Fan L, Lu Y, Shen X, Shao H, Suo L, Wu Q. Alpha protocadherins and Pyk2 kinase regulate cortical neuron migration and cytoskeletal dynamics via Rac1 GTPase and WAVE complex in mice. *Elife* 2018, 7: e35242.
 46. Vaghi V, Pennucci R, Talpo F, Corbetta S, Montinaro V, Barone C, *et al.* Rac1 and rac3 GTPases control synergistically the development of cortical and hippocampal GABAergic interneurons. *Cereb Cortex* 2014, 24: 1247–1258.
 47. Posada-Duque RA, Lopez-Tobon A, Piedrahita D, Gonzalez-Billault C, Cardona-Gomez GP. p35 and Rac1 underlie the neuroprotection and cognitive improvement induced by CDK5 silencing. *J Neurochem* 2015, 134: 354–370.



Distinct Characteristics of Odor-evoked Calcium and Electrophysiological Signals in Mitral/Tufted Cells in the Mouse Olfactory Bulb

Han Xu¹ · Chi Geng¹ · Xinzhong Hua^{1,2} · Penglai Liu¹ · Jinshan Xu¹ · Anan Li¹

Received: 18 August 2020 / Accepted: 31 December 2020 / Published online: 15 April 2021
© The Author(s) 2021

Abstract Fiber photometry is a recently-developed method that indirectly measures neural activity by monitoring Ca^{2+} signals in genetically-identified neuronal populations. Although fiber photometry is widely used in neuroscience research, the relationship between the recorded Ca^{2+} signals and direct electrophysiological measurements of neural activity remains elusive. Here, we simultaneously recorded odor-evoked Ca^{2+} and electrophysiological signals [single-unit spikes and local field potentials (LFPs)] from mitral/tufted cells in the olfactory bulb of awake, head-fixed mice. Odors evoked responses in all types of signal but the response characteristics (e.g., type of response and time course) differed. The Ca^{2+} signal was correlated most closely with power in the β -band of the LFP. The Ca^{2+} signal performed slightly better at odor classification than high- γ oscillations, worse than single-unit spikes, and similarly to β oscillations. These results provide new information to help researchers select an appropriate method for monitoring neural activity under specific conditions.

Keywords Mitral/tufted cells · Fiber photometry · Electrophysiology · Odor representation · Olfactory bulb

Han Xu, Chi Geng, and Xinzhong Hua have contributed equally to this work.

✉ Anan Li
anan.li@xzhmu.edu.cn

¹ Jiangsu Key Laboratory of Brain Disease and Bioinformatics, Research Center for Biochemistry and Molecular Biology, Xuzhou Medical University, Xuzhou 221004, China

² School of Medical Information and Engineering, Xuzhou Medical University, Xuzhou 221004, China

Introduction

Electrophysiological signals recorded *in vivo* reflect neuronal activity directly with high temporal resolution. Extracellularly-recorded activity ranges from single-unit spikes to neuronal populations [e.g., local field potentials (LFPs)] and has been used extensively in both anesthetized and awake behaving animals [1, 2]. For many years, it has been considered the gold standard for measuring neural activity [2, 3]. Fiber photometry has the ability to record neuronal activity in genetically-defined cell types in specific brain areas, including both cortex and sub-cortical nuclei [4], but monitors the population Ca^{2+} signal; these recordings thus indirectly reflect the activity of a specific population of neurons. Fiber photometry has been widely used to monitor the activity of cell-type-specific populations and to correlate activity with specific behaviors [5–8]. Fiber photometry has several advantages over extracellular electrophysiology, including low noise, low cost, and relatively simple implementation, and has been used extensively in neuroscience studies of sensory processes, motor behavior, learning, memory, and cognition [5].

Olfaction plays a crucial role in survival, helping animals find food and avoid predators, amongst other functions. Olfactory dysfunction has been found in the early stages of several nervous system disorders, including Alzheimer's disease, Parkinson's disease, and depression [9–12]. As the first processing center in the olfactory system, the olfactory bulb (OB) receives input from sensory neurons, processes this information, and then transmits it to higher centers, such as the anterior olfactory nucleus, olfactory tubercle, and piriform cortex [13–16]. The OB also receives feedback from the olfactory cortex and centrifugal innervation from cholinergic, noradrenergic, and serotonergic cells [14, 17, 18]. In the OB, the

mitral/tufted cells (M/Ts) are the main output neurons; M/T activity is regulated by interneurons, including granular cells and juxtglomerular cells [14, 19]. Functionally, M/Ts are critically involved in the representation of odor identity, value, intensity, and timing [20, 21]. Given the complicated networks in the OB and the importance of the M/Ts, efficient methods to sensitively and specifically monitor M/T neural activity are crucial for olfactory research.

In the OB, both spikes and LFP signals recorded from the M/Ts are widely used to investigate its role in the representation of odor information and olfactory learning and memory [22–24]. However, with spike/LFP recording there is no direct genetic evidence to prove that the recorded spikes are from M/Ts rather than other cell types, although indirect evidence can be provided by the firing properties [25–27]. Fiber photometry has been used in the OB and piriform cortex to investigate neural responses to odor stimulation under different brain states [6, 28–30]. In the OB, robust odor-evoked responses are recorded in M/Ts and granule cells [6, 28]. Thus, fiber photometry is emerging as an efficient and popular method to study cell function in the OB. However, because it monitors neural activity indirectly, it is critical to correlate the Ca^{2+} signals recorded *via* fiber photometry with the gold-standard measurement of neural activity.

In this study, we used a mouse model with M/T-specific GCaMP6s expression to simultaneously record odor-evoked Ca^{2+} signals and electrophysiological signals from M/Ts in awake, head-fixed mice. We examined the response characteristics, correlations, and odor-decoding ability of the different types of signal. Our findings show how Ca^{2+} signals recorded by fiber photometry relate to electrophysiological recordings and have implications for the application of fiber photometry throughout the brain.

Materials and Methods

Animals

Eleven male Thy1-cre [FVB/N-Tg(Thy1-cre)1V1n/J] mice aged 8–16 weeks were used in this study. The mice were bred in the animal facilities of Xuzhou Medical University and housed in a vivarium under a 12 h/12 h light/dark cycle, with lights on at 08:00. Experiments were performed during the light cycle. After surgery, the mice were housed individually for at least 10 days before further experiments to allow recovery. Food and water were available *ad libitum*. All experimental procedures were performed in accordance with protocols submitted to and approved by the Xuzhou Medical University Institutional Animal Care and Use Committee.

Fabrication of Opto-tetrodes

The opto-tetrodes included one optical fiber and four tetrodes. The optical fiber (200 μm O.D., NA = 0.37, 18.5 mm long) was coupled with a ferrule (10.5 mm long; 2.5 mm in diameter). Each tetrode consisted of four polyamide-coated nichrome wires (single-wire diameter, 12.7 μm ; coating 1/4 hard PAC; Sandvik, RO-800, item # PF000591) gold-plated to an impedance of 0.2–0.3 $\text{M}\Omega$. The tetrodes and optical fiber together were inserted into tubing (450 μm O.D., 320 μm I.D., 9.0 mm long, A-M Systems), which was glued to an EIB-16 interface board (Neuralynx). The ends of the tetrodes were connected to the interface board with gold pins (large size, Neuralynx); the shafts were glued to the side of the optical fiber and then the tetrodes were cut so that the tetrode tips and the optical fiber tip were at the same level.

Virus Injection

The virus injection procedure was similar to that described in our previous studies [6, 28]. Briefly, in Thy1-cre mice, the mitral cell layer of the OB was injected with AAV-DIO-GCaMP6s virus (PT-0071, AAV2/9, 5.03×10^{12} vg/mL, BrainVTA, Wuhan, China). All injections were made with a glass pipette and the injection volume and velocity were controlled by a microsyringe pump (Quintessential Injector; Stoelting Co.). Virus solutions (300 nL) were injected at 30 nL/min into the mitral cell layer (4.2 mm anterior, 1.0 mm lateral, and 0.8–1.1 mm ventral to bregma). The glass pipette was left in place for an additional 10 min before being slowly withdrawn. After the viral injection, the scalp was sutured. Mice were individually housed for at least three weeks after surgery for recovery and to allow time for the expression of GCaMP6s.

Surgery for Implantation of Opto-tetrodes

Mice were briefly anesthetized with pentobarbital (0.09 mg/g bodyweight, *i.p.*). Depth of anesthesia was verified by toe pinch. Next, each mouse was mounted in a stereotaxic frame and the fur on the surface of the scalp from the midline of the orbits to the midpoint between the ears was removed. A hole was drilled above the right OB for the implantation of opto-tetrodes (4.2 mm anterior from bregma, 1.0 mm lateral from the midline). One screw hole was drilled into the parietal bone to serve as the ground and reference electrode in spike and LFP recordings.

Opto-tetrodes were implanted into the OB with the aim of simultaneously recording Ca^{2+} signals, single-unit spikes, and LFPs. The opto-tetrodes were lowered to the lateral mitral cell layer at an average depth of 1.8–2.0 mm.

Recordings were made during opto-tetrode implantation to ensure optimal placement within the lateral mitral cell layer. The signals recorded from the tetrodes were sent to a headstage, amplified by a 16-channel amplifier (Plexon DigiAmp; bandpass filtered at 1–5000 Hz; 2000× gain), and then sampled at 40 kHz by a Plexon OmniPlex recording system. In order to secure mice in the head-fixed recording system, an aluminum head plate was attached to the skull with stainless steel screws and dental cement.

Odor Presentation

Eight odorants (isoamyl acetate, 2–heptanone, phenyl acetate, benzaldehyde, dimethylbutyric acid, n–heptane acid, n–pentanol, 2–pentanone; from Sinopharm Chemical Reagent Co. and Sigma-Aldrich, USA) were presented by an odor delivery system (Thinkerbiotech, Nanjing, China). All odorants were dissolved in mineral oil at 1% v/v dilution. In the odor delivery period, a stream of nitrogen flowed over the oil at 100 mL/min, and was then diluted to 1/20 by an olfactometer. Odor presentation was synchronously controlled by the data acquisition system *via* a solenoid valve that was driven by the digital-to-analog converter. Air or odorized air was delivered to the nose at a constant rate of 1 L/min to eliminate the effect of airflow. For each odor, 20 trials were presented with an inter-trial interval of 30 s. The duration of each odor presentation was 2 s. Odors were presented passively: mice were head-fixed and awake but were not required to produce any behaviors in response to odor presentation and did not receive any reward.

Histology

To verify viral expression, frozen brain sections were prepared. Mice were anesthetized with pentobarbital (80 mg/Kg bodyweight, i.p.) and transcardially perfused with 20 mL of 0.9% saline, followed by 20 mL of 4% paraformaldehyde (PFA) in PB (0.1 mol/L, pH 7.4). After perfusion, each brain was harvested, postfixed for 24 h in PFA at 4°C, and then cryoprotected with 30% sucrose in PBS until the tissue sank. The brain was then embedded in OCT compound and sectioned at 30 μm on an upright Leica cryostat. Tissue sections were mounted on slides and imaged by a confocal scanning microscope (Zeiss, LSM710).

Calcium Signals, Spikes, and LFP Recordings

Before recording the Ca²⁺ signals, spikes, and LFPs, mice were required to have recovered and be in good condition for 10 days after the surgery. Two horizontal bars (fixed to the head plate by 2 screws) were used to head-fix awake

mice, which were able to maneuver on an air-supported free-floating Styrofoam ball (Thinkerbiotech). After the mice had adapted for a period of time, Ca²⁺ signals, spikes, and LFPs were recorded simultaneously.

A fiber photometry system (ThinkerTech) was used to record fluorescence emissions. A laser beam from a laser tube (488 nm; OBIS 488LS; Coherent) was reflected by a dichroic mirror, focused through a 10× objective lens (NA = 0.3; Olympus) and then coupled to an optical commutator (Doric Lenses). An optical fiber (200 mm O.D., NA: 0.37, 1.5 m long) guided the light between the commutator and the implanted optical fiber. Laser power was modulated to 40–60 μW at the tip of the optical fiber. GCaMP6s fluorescence emission was band-pass filtered (MF525-39, Thorlabs) and detected by a photomultiplier tube (R3896, Hamamatsu). An amplifier (C7319, Hamamatsu) was used to convert the photomultiplier tube current output to voltage, which was further filtered through a low-pass filter (35 Hz cutoff; Brownlee, 440). The analog voltage signals were digitized at 500 Hz and recorded by fiber photometry software.

In vivo electrophysiological data from the tetrodes were sent to the headstage and amplified by a 16-channel amplifier (Plexon DigiAmp; bandpass filtered at 0.1–5000 Hz; 2000× gain) and sampled at 40 kHz by a Plexon OmniPlex recording system. The procedure for spike recordings was similar to that for recordings made during the tetrode implantation described above. The LFP signals were amplified (2000× gain; Plexon DigiAmp), filtered at 0.1–300 Hz, and sampled at 1 kHz. Odor stimulation event markers were recorded alongside the spike/LFP data *via* the Plexon OmniPlex recording system.

Data Analysis and Statistics

Off-line Spike Sorting and Statistics of the Unit Data

Spikes were sorted and identified in Offline Sorter V4 software (Plexon). The separation of different units was performed by principal component analysis. A unit was classified as a single unit if <0.75% of the interspike intervals were <1 ms, as in previous studies [23, 31]. This resulted in unimodal firing rate distributions. The data 2 s before and 6 s after each odor stimulation event were extracted, and the mean firing rate (MFR) was generated by averaging the firing rate in 50-ms bins (Fig. 2B4). The spontaneous firing rate was calculated by averaging across the spikes fired during the 2 s before odor stimulation and the odor-evoked firing rate was calculated by averaging across the spikes fired during the 2 s after the onset of odor stimulation. To test for odor-evoked responses, we compared the area under the receiver operating characteristic curve (auROC) for the baseline firing rate with that for the

odor-evoked firing rate across all trials for each cell–odor pair (Fig. 2C4). See below for details of the ROC and auROC calculations.

Analysis of LFP Signals

MatLab was used to analyze the LFP signals. Similar to previous studies, LFP signals were divided into four frequency bands: theta (2–12 Hz), beta (15–35 Hz), low gamma (36–65 Hz) and high gamma (66–95 Hz) [23, 28]. Since odors usually evoke strong and reliable changes in the power in the beta and high-gamma bands in awake animals [23, 24, 28], we focused on these bands. To assess the odor-evoked beta and high-gamma responses, we analyzed the signals from 4 s before to 6 s after the onset of odor stimulation. The wavelet transform method with the Morlet wavelet was used to compute the signal power spectral density over time (MatLab function ‘cwt’). For each trial, the baseline was normalized to 1; normalized trials were averaged for each odor (Fig. 2B2, B3). As with the spike statistics, we used auROC to estimate whether the odor evoked a significant response (Fig. 2C2, C3).

Analysis of Fiber Photometry Data

Data were exported as MatLab .mat files for further analysis. The data were segmented at the onset of odor stimulation within individual trials. We derived the values of fluorescence change ($\Delta F/F$) by calculating $(F - F_0)/F_0$, where F_0 is the baseline fluorescence signal averaged over a 2-s baseline time window before odor stimulation (Fig. 2A1, lower). $\Delta F/F$ values are presented as heatmaps or average plots. We also used auROC to estimate whether the odor evoked a significant response (Fig. 2B1).

ROC Analysis

ROC analysis was used to assess the responses evoked by odors. ROCs were implemented in MatLab software. The auROC is a nonparametric measure of the discriminability of two distributions. We used auROC to assess the neural responses to 8 odors. The value of auROC was defined as ranging from 0 to 1. A value of 0.5 indicates completely overlapping distributions, whereas a value of 1 indicates perfect discriminability. auROC values <0.25 were defined as inhibitory responses; auROC values >0.75 were defined as excitatory responses; $0.25 < \text{auROC} < 0.75$ were defined as no significant response. The latency of the response onset, the latency of the peak response, and the response duration were calculated from the auROC values (Fig. 3A–C). Onset latency was defined as the time at which the odor-induced response began (auROC <0.25 or >0.75). Peak latency was defined as the time at which the

odor-induced response reached its maximum or minimum point. Response duration was defined as the time from the start to the end of the odor-induced response.

AuROC was also used to calculate the difference between two odor-induced responses. Two responses were randomly selected from 8 odor-induced responses in the same animal. auROC values were positively correlated with the difference in odor-induced responses (Fig. 6A, B).

Logistic Regression Classifier

To assess the discriminability of odor-induced Ca^{2+} and electrophysiological signals, logistic regression classifiers imported from Scikit-learn v0.21.3 were used to measure odor classification accuracy. All odor-induced responses were processed by subtracting the baseline and binned into 50-ms bins over the 0–5s after the onset of odor stimulation. The feature vectors used for training and testing were concatenated sets of binned responses and have been standardized. To evaluate the performance of four types of signal on odor discrimination, two were randomly selected from 8 odor-induced neural responses, and the scores were obtained by the average classification accuracy of 28 odor pairs based on 10-fold cross-validation.

Statistics

Data are expressed as mean \pm standard error (mean \pm SE). The Anderson–Darling test was used to assess the normality of the data. All experimental data were non-normal. The Wilcoxon signed-rank test was used to test for differences between two paired samples. When there were more than two paired samples, the Friedman test was used, and the Tukey method was used for subsequent comparisons. The Kruskal–Wallis test was used for more than two independent samples, and the Tukey method was used for subsequent comparisons. The two-sample Kolmogorov–Smirnov test was used to determine whether data distributions differed between two groups. $P < 0.05$ indicated a statistically significant difference. For correlation analysis, we calculated the absolute value of Pearson’s linear correlation coefficient:

$$\rho(a, b) = \frac{\sum_{i=1}^n (X_{a,i} - \bar{X}_a)(Y_{b,i} - \bar{Y}_b)}{\left\{ \sum_{i=1}^n (X_{a,i} - \bar{X}_a)^2 \sum_{j=1}^n (Y_{b,j} - \bar{Y}_b)^2 \right\}^{1/2}}$$

Results

Odor-evoked Response Characteristics of Calcium Signals and Electrophysiological Signals in M/Ts

To specifically express the Ca^{2+} indicator GCaMP6s in M/Ts, we injected AAV-DIO-GCaMP6s-GFP into the mitral cell layer of the OB in Thy1-Cre mice. As in our previous studies [6, 32], GCaMP6s was specifically and efficiently expressed in M/Ts three weeks after the viral injection (Fig. 1A). To simultaneously record Ca^{2+} signals and electrophysiological signals, we implanted optotetrodes into the mitral cell layer of the OB two weeks after the viral injection. After waiting at least 10 days for recovery, we simultaneously recorded Ca^{2+} signals, single-unit spikes, and LFPs in response to a 2-s odor presentation in awake, head-fixed mice (Fig. 1B).

In the OB, odors usually evoke increased power in LFP beta oscillations and decreased power in high-gamma oscillations [6, 23]. These two types of oscillation are known to play different roles in odor information processing [24, 33]. Thus, we focused on the beta and high-gamma

oscillations in the LFP. Heat maps of the Ca^{2+} signal, beta and high-gamma power, and spike firing rate during 20 odor-stimulation trials to one odor are shown in Fig. 2A (upper), with the averaged traces shown in Fig. 2A (lower). In this example, the odor evoked clear reductions in the Ca^{2+} signal, power in the high-gamma band, and the spike firing rate, but a robust increase in the power in the beta band. To quantitatively assess the odor-evoked responses in the four signal types, we used auROC to define whether the response increased, decreased, or did not change, and to determine the onset latency of the response, the latency to the peak response, and the response duration for significant odor-evoked responses (Fig. 2B; see Materials and Methods for details). For all the animals recorded ($n = 88$ mouse–odor pairs from 11 mice for Ca^{2+} signals and beta and high-gamma oscillations, and $n = 600$ cell–odor pairs from 11 mice for spikes), we found that odor evoked a significant response for all four types of signal (Fig. 2C). However, while both increased and decreased responses were recorded for the Ca^{2+} signals and spike rates (Fig. 2C1, C4), only increased responses were found for the beta oscillations (Fig. 2C2) and only decreased

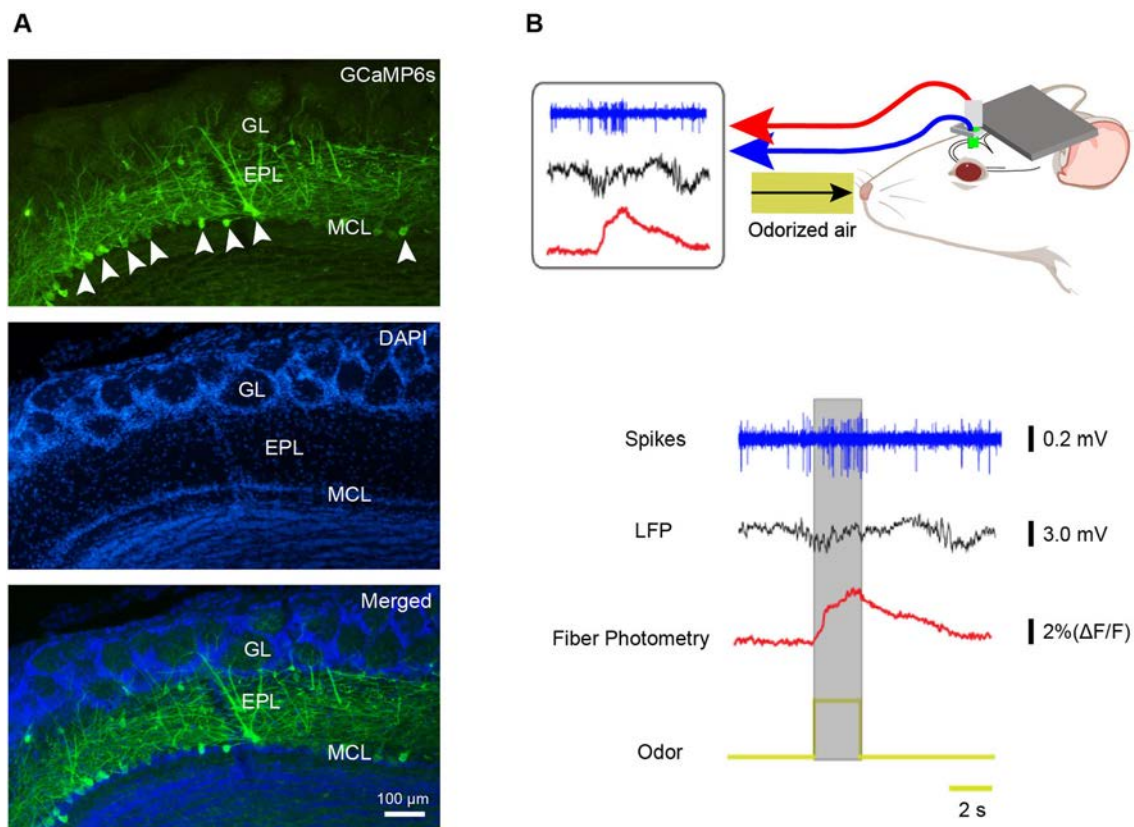


Fig. 1 Simultaneous recording of odor-evoked spikes, LFPs, and population Ca^{2+} signals from M/Ts. **A** Expression of GCaMP6s (green) in M/Ts after injection of Cre-dependent GCaMP6s into the MCL of Thy1-Cre mice (arrowheads, mitral cells expressing

GCaMP6s; GL, glomerular layer; EPL, external plexiform layer; MCL, mitral cell layer; scale bar, 100 μm). **B** Schematic of the recording set-up in awake head-fixed mice and example traces (gray box, 2-s odor-presentation period).

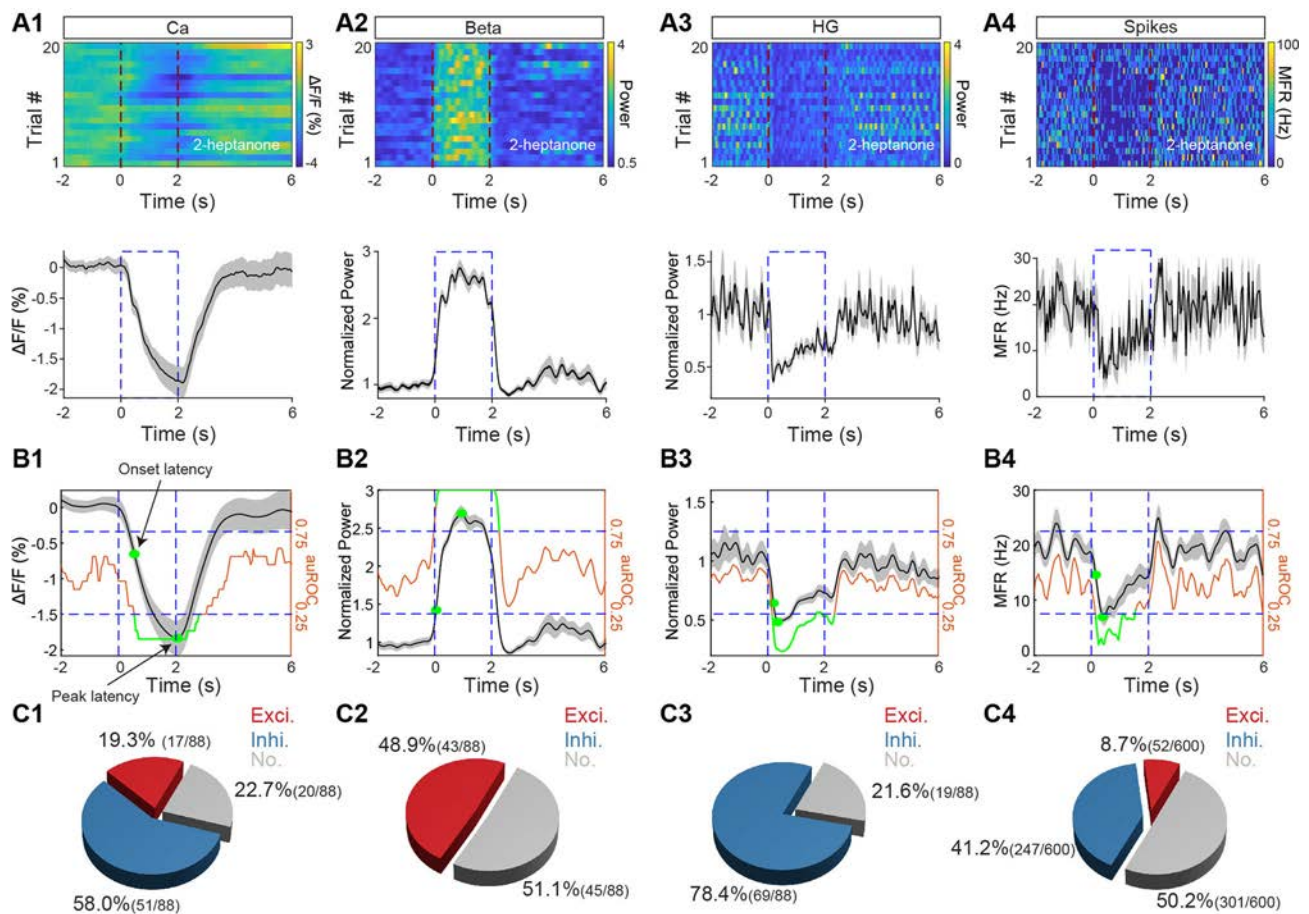


Fig. 2 Odor-evoked Ca²⁺ signals, LFPs, and spikes in M/Ts. **A1–A4** Heat maps (upper panels, 20 trials, each row represents a single trial) and trial-averaged traces (lower panels) for the M/T fiber photometry Ca²⁺ signal, power in the beta and high-gamma LFP bands, and mean spike firing rate (MFR) evoked by one of 8 odors in a representative mouse (Ca, calcium; HG, high gamma). **B1–B4** auROC (brown lines) for $\Delta F/F$, normalized power in the beta and gamma bands, and MFR

(green lines, response duration; green dots, onset and peak latencies; black/gray lines, trial-averaged traces from one mouse/cell–odor pair). **C1–C4** Proportions of mouse/cell–odor pairs producing an excitatory (red), inhibitory (blue), or no (gray) response in the Ca²⁺ and electrophysiological signals ($n = 88$ mouse–odor pairs from 11 mice for Ca²⁺ signals and for beta and high-gamma oscillations, and $n = 600$ cell–odor pairs from 11 mice for spikes).

responses for the high-gamma oscillations (Fig. 2C3). These findings are consistent with results from previous studies in which these signals were recorded separately [6, 23].

Next, to further investigate the odor-evoked temporal characteristics of the four types of signal, we calculated the onset latency, peak latency, and response duration of the significant odor-evoked responses (both increases and decreases) (Fig. 2B) and compared them among the four types of signal (Fig. 3A–C). We found that the order for onset latency was Ca²⁺ signals > spikes > high-gamma oscillations > beta oscillations (Fig. 3D, Kruskal–Wallis test; Ca²⁺ signals vs spikes, $P = 0.001$; spikes vs high-gamma, $P = 0.014$; high-gamma vs beta, $P = 0.014$; $n = 68$, 43, and 69, from 11 mice for calcium signals, beta, and high-gamma, respectively, and $n = 299$ from 11 mice for spikes). The order for peak latency was Ca²⁺ signals > spikes > high-gamma/beta oscillations (Fig. 3E, Kruskal–

Wallis test; Ca²⁺ signals vs spikes, $P = 0.022$; spikes vs high-gamma, $P = 0.007$; $n = 68$, 43, and 69 from 11 mice for Ca²⁺ signals, beta, and high-gamma oscillations, respectively, and $n = 299$ from 11 mice for spikes), with no significant difference in the peak latency for high-gamma and beta oscillations (Fig. 3E, Kruskal–Wallis test; $P > 0.05$; high-gamma: $n = 69$ from 11 mice, beta: $n = 43$ from 11 mice). For response duration, the order was Ca²⁺ signals > high-gamma oscillations > spikes/beta oscillations (Fig. 3F, Kruskal–Wallis test, Ca²⁺ signals vs high-gamma, $P = 0.027$; high-gamma vs spikes, $P = 0.012$; $n = 68$, 43, and 69 from 11 mice for Ca²⁺ signals, beta and high-gamma oscillations, respectively, and $n = 299$ from 11 mice for spikes), with no statistical difference in the response duration for spikes and beta oscillations (Fig. 3F, Kruskal–Wallis test, $P > 0.05$, spikes: $n = 299$ from 11 mice; beta: $n = 43$ from 11 mice). Thus, these findings indicate that the temporal characteristics of odor-evoked

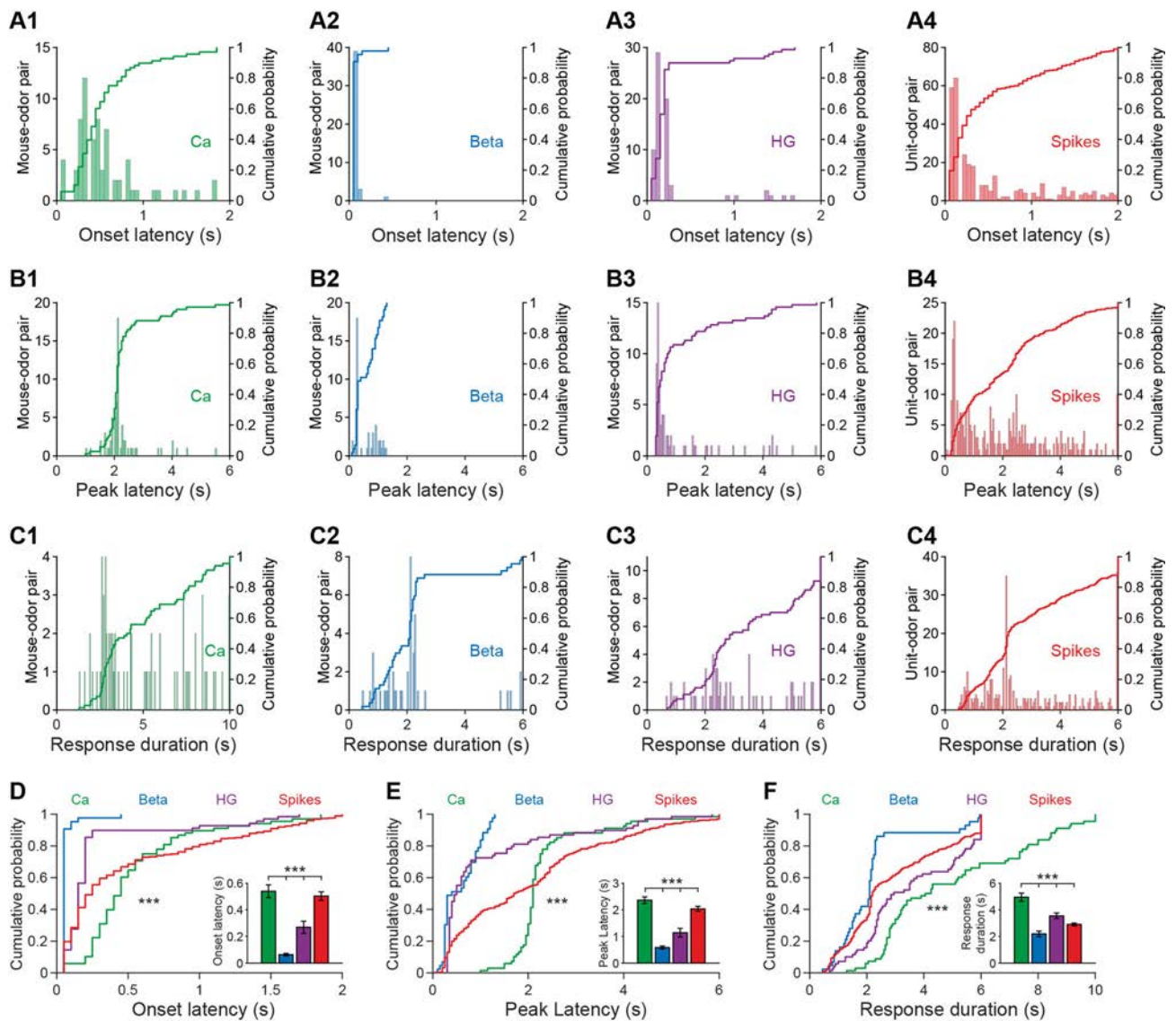


Fig. 3 Odor-evoked temporal characteristics of the Ca²⁺ signals and electrophysiological signals. **A–C** Histograms and cumulative probability for onset latency (**A1–A4**), peak latency (**B1–B4**), and response duration (**C1–C4**) of the Ca²⁺ signal, beta oscillations, high-gamma oscillations, and spikes from all the mouse/cell–odor pairs ($n = 68, 43, 69,$ and 299 for Ca²⁺, beta, high-gamma, and spikes,

respectively). **D–F** Line charts of the cumulative probabilities for onset latency, peak latency, and response duration (two-sample K–S test, $***P < 0.001$). Bar charts (inset) show the mean values for onset latency, peak latency, and response duration (Kruskal–Wallis test, $***P < 0.001$). Ca, calcium; HG, high gamma.

Ca²⁺ signals and electrophysiological signals are largely different, although some similar characteristics were found among the different types of electrophysiological signal.

Correlation Between Calcium Signals and Electrophysiological Signals

Since the Ca²⁺ signals recorded by fiber photometry indirectly reflect neural activity from a population of specific neurons, it is important to assess how they correlate with the spikes and LFPs that directly measure

neural activity, even though there are some differences in response types and time course between Ca²⁺ signals and electrophysiological signals. We analyzed the correlation between Ca²⁺ signals and spikes/beta/high-gamma oscillations using the Pearson correlation coefficient (r). Fig. 4A shows an example of odor-evoked responses measured simultaneously by Ca²⁺ signals, beta oscillations, high-gamma oscillations, and spikes; the correlation between Ca²⁺ and electrophysiological signals is shown in Fig. 4B. The highest correlation was between Ca²⁺ signals and beta oscillations (Fig. 4B). This finding was supported by an

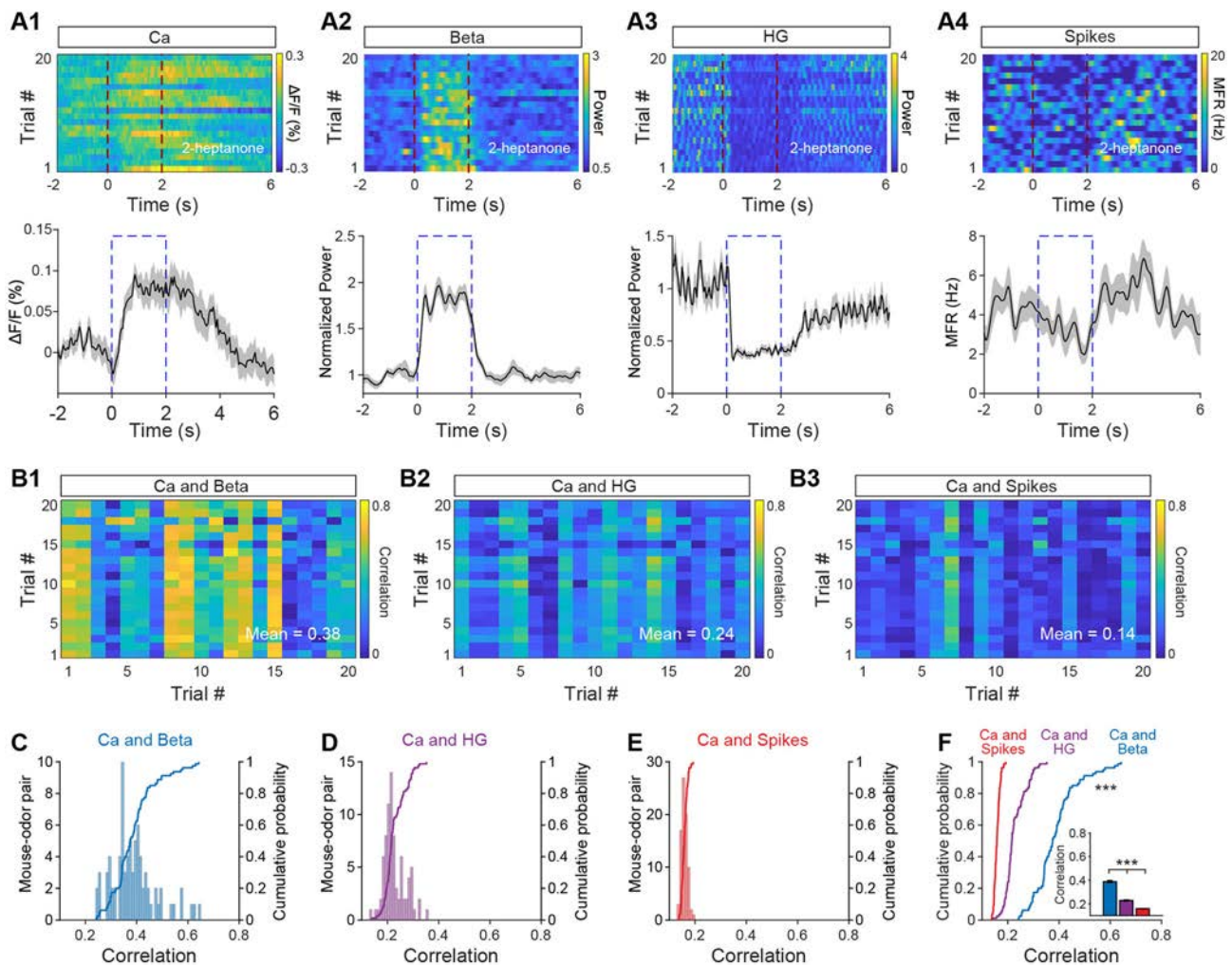


Fig. 4 Correlations between the population Ca^{2+} signals and the electrophysiological signals. **A1–A4** Heat maps (upper panels, 20 trials, each row represents a single trial) and trial-averaged traces (lower panels) for the M/T Ca^{2+} signal, power in the beta and high-gamma LFP bands, and mean spike firing rate evoked by one of 8 odors in a representative mouse (dashed lines, odor-presentation period). **B1–B3** Correlations between the Ca^{2+} and the different electrophysiological signals. The matrices represent the correlation coefficients between the Ca^{2+} and electrophysiological signals

analysis across all animals, in which the strength of the correlation between Ca^{2+} and electrophysiological signals was in the order beta oscillations > high-gamma oscillations > spikes (Fig. 4C–F, Friedman test, beta vs high-gamma, $P < 0.001$; high-gamma vs spikes, $P < 0.001$; $n = 80$ from 11 mice for Ca^{2+} signals, beta, high-gamma oscillations, and spikes). These data therefore indicate that the Ca^{2+} signals recorded by fiber photometry are more closely correlated with power in the LFP beta band than with other electrophysiological signals such as spikes or high-gamma oscillations.

evoked in individual trials by one of the odors (2-heptanone), in a representative mouse. **C–E** Histograms and cumulative probability of the correlation coefficients between the Ca^{2+} signals and the electrophysiological signals from all the mouse/cell–odor pairs ($n = 80$ from 11 mice). **F** Statistical analysis of the correlation coefficients shown in **C**, **D**, and **E** (line charts: two-sample K–S test, $***P < 0.001$; Bar chart: Kruskal–Wallis test, $***P < 0.001$). Ca, calcium; HG, high gamma.

Calcium Signals Show a Reliable Response to the Same Odor but Spikes Perform Best at Discriminating Different Odors

To represent odor information precisely, an individual odor should evoke a reliable neural response, and the neural response should discriminate clearly among different odors. Thus, if a signal recorded from the OB shows high reliability to the same odor on different trials and high variability to different odors, this signal is good at odor representation. To compare the reliability and variability of the Ca^{2+} and electrophysiological signals, we performed a within-odor correlation analysis (correlation between

different trials with the same odor, to assess reliability, Fig. 5A1–D1) and a between-odors correlation analysis (correlation between trials for different odors, Fig. 5A2–D2). Quantitative analyses of the correlation coefficients from all mouse/cell–odor pairs showed that for within-odor correlations, the order of the correlation coefficients for the four signals was Ca^{2+} signals/beta oscillations > high-gamma oscillations > spikes (Fig. 5E, Kruskal–Wallis test,

Ca^{2+} signals vs high-gamma, $P < 0.001$; high-gamma vs spikes, $P < 0.001$; for Ca^{2+} signals, beta, and high-gamma oscillations, $n = 88$ from 11 mice; for spikes: $n = 600$ from 11 mice). There was no statistical difference between the correlation coefficients for the Ca^{2+} signals and beta oscillations (Fig. 5E, Kruskal–Wallis test, $P > 0.05$, $n = 88$ from 11 mice for both Ca^{2+} signals and beta oscillations). For between-odors correlations, the order of the correlation

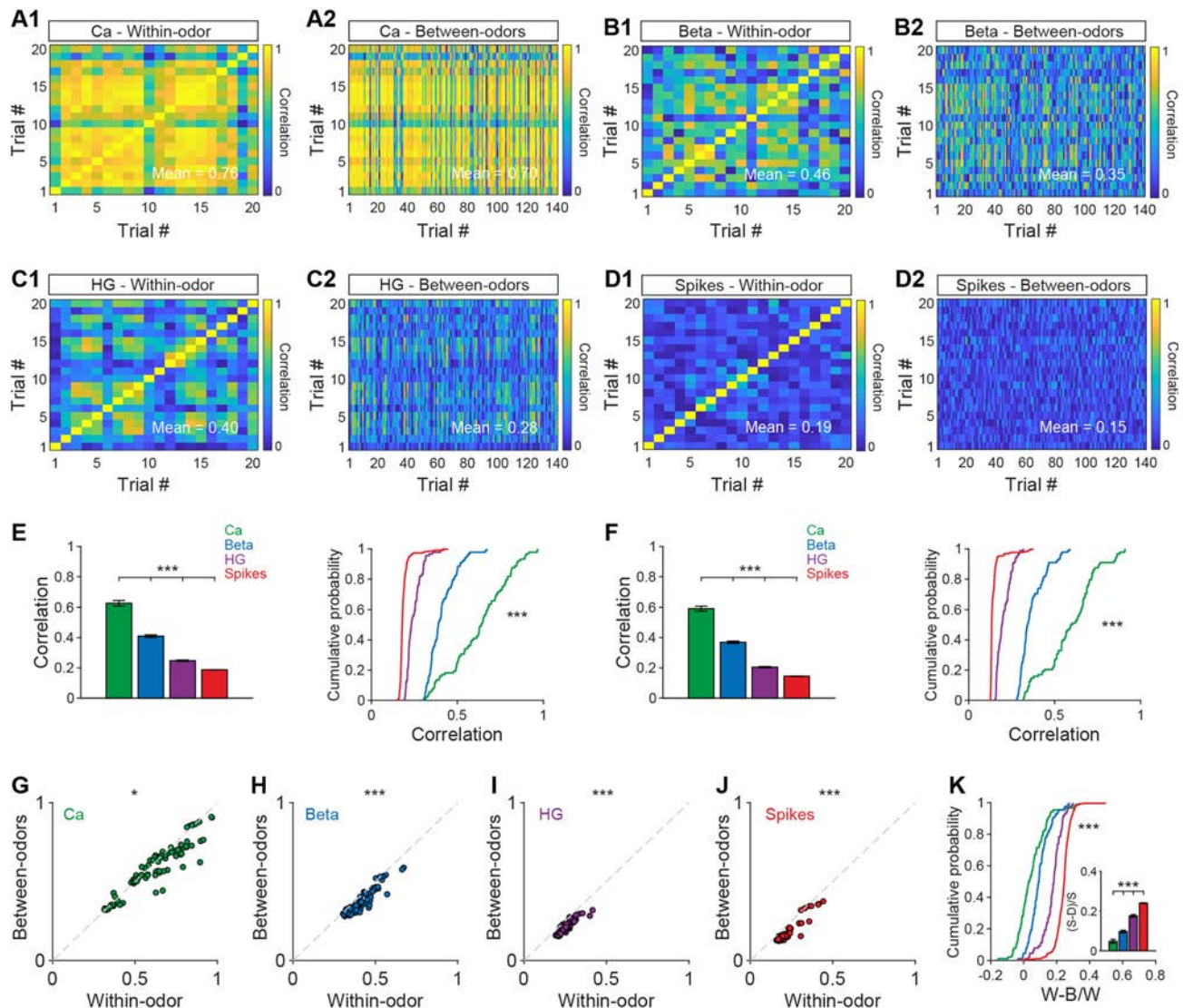


Fig. 5 Within-odor and between-odors correlations for the Ca^{2+} signals, beta oscillations, high-gamma oscillations, and spikes. **A1–D1** Correlation coefficients for within-odor responses in a single mouse/cell–odor pair (20 trials) for the different types of signal. **A2–D2** Correlation coefficients for between-odors responses for the different types of signal. Correlations were calculated between 20 trials from one odor and 140 trials from the other 7 odors. **E, F** Statistical analysis of the correlation coefficients for within-odor (**E**) and between-odors (**F**) responses from all mouse/cell–odor pairs (left, Kruskal–Wallis test, $***P < 0.001$; right, two-sample K–S test, $***P < 0.001$; for Ca^{2+} beta and high-gamma: $n = 88$ from 11 mice; for spikes: $n = 600$ from 11 mice). **G–J** Comparison of the correlation

coefficients for within-odor and between-odors responses from the Ca^{2+} signals (**G**), beta oscillations (**H**), high-gamma oscillations (**I**), and spikes (**J**) (Wilcoxon signed-rank test, Ca^{2+} : $z = 4.619$, $P = 0.010$; beta: $z = 8.064$, $P < 0.001$; high-gamma: $z = 8.147$, $P < 0.001$; spikes: $z = 16.073$, $P < 0.001$; for Ca^{2+} , beta, and high-gamma: $n = 88$ from 11 mice; for spikes: $n = 600$ from 11 mice). The dashed diagonal lines indicate equivalent correlation coefficients in the two conditions. **K** Bar chart (Kruskal–Wallis test, $***P < 0.001$) and cumulative probability (two-sample K–S test, $***P < 0.001$) showing statistical analyses of (within-odor – between-odor)/within-odor. Ca, calcium; HG, high gamma; (W-B)/W, (within-odor – between-odor) / within-odor.

coefficients was Ca^{2+} signals > beta oscillations > high-gamma oscillations > spikes (Fig. 5F, Kruskal–Wallis test, Ca^{2+} signals vs beta, $P = 0.03$; beta vs high-gamma, $P < 0.001$; high-gamma vs spikes, $P < 0.001$; for Ca^{2+} signals, beta, and high-gamma oscillations: $n = 88$ from 11 mice; for spikes: $n = 600$ from 11 mice).

We also found that the within-odor correlation coefficients were higher than the between-odors coefficients for all signals recorded (Fig. 5G–J, Wilcoxon signed-rank test, Ca^{2+} signal: $z = 4.619$, $P = 0.010$; beta: $z = 8.064$, $P < 0.001$; high-gamma: $z = 8.147$, $P < 0.001$; spikes: $z = 16.073$, $P < 0.001$; for Ca^{2+} signals, beta and high-gamma oscillations: $n = 88$ from 11 mice; for spikes: $n = 600$ from 11 mice). This result indicates that all four types of signal responded more reliably to the same odor than to different odors; that is, they all have the ability to represent odor identity. To further assess which signal best discriminates among odors, we analyzed the difference in correlation coefficients from the within-odor and between-odor analyses. If the difference is large, the ability to discriminate odors is better. We found that spikes are the best signal for discriminating among odors, with the order spikes > high-gamma oscillations > Ca^{2+} signals/beta oscillations (Fig. 5K, Kruskal–Wallis test, spike vs high-gamma, $P < 0.001$; high-gamma vs Ca^{2+} signals, $P < 0.001$; for Ca^{2+} signals, beta and high-gamma oscillations, $n = 88$ from 11 mice; for spikes: $n = 600$ from 11 mice). There was no statistical difference between the Ca^{2+} signals and beta oscillations (Fig. 5K, Kruskal–Wallis test, $P > 0.05$; for both Ca^{2+} signals and beta, $n = 88$ from 11 mice). These results indicate that Ca^{2+} signals have the highest reproducibility to odor stimulation in general but that spikes, which have the highest difference in correlation coefficients in the within-odor and between-odor conditions, are potentially the best signal for representing distinct odors.

The analysis above used signal correlation, which only indirectly reflects odor discrimination. To directly analyze which signals best discriminate odors, we performed ROC analysis (Fawcett, 2006) to compare the classification of the responses evoked by odor pairs for the four types of signal. An example is shown in Fig. 6A: both odors in a pair (isoamyl acetate versus n-heptane) evoked robust responses, as measured by the different signals. The auROC, representing the difference in responses to the odor pair, was largest for spikes and smallest for high-gamma oscillations (Fig. 6B). ROC analysis of all animal–odor pairs or cell–odor pairs showed that the auROC values for the four types of signal had the order spikes > Ca^{2+} signals/beta oscillations > high-gamma oscillations (Fig. 6C, D, Kruskal–Wallis test, spikes vs Ca^{2+} signals, $P = 0.047$; Ca^{2+} signals vs high-gamma, $P = 0.002$; for spikes: $n = 1652$ pairs from 11 mice; for Ca^{2+} signals and high-gamma oscillations, $n = 308$ pairs from 11 mice).

There was no statistical difference between Ca^{2+} signals and beta oscillations (Fig. 6C, D, Kruskal–Wallis test, $P > 0.05$; for both Ca^{2+} signals and beta oscillations, $n = 308$ pairs from 11 mice). Therefore, although spikes are the best signals for classifying different odors, the Ca^{2+} signals recorded via fiber photometry can also be used to discriminate odors, and perform better than high-gamma LFP oscillations.

In addition, logistic regression classifiers were used to assess the performance of different types of neural responses in odor pair discrimination. Classification accuracy was calculated from an average of 28 odor pairs. The results were basically consistent with the auROC classification, which was largest for spikes and smallest for high-gamma oscillations. As the concatenated vector sets grew, the order of discrimination showed as spikes > Ca^{2+} signals/beta oscillations/high-gamma oscillations (Fig. 6E, for spikes, sample size = 75 from 11 mice for each of the 8 odors; for Ca^{2+} signals, sample size = 220 from 11 mice for each odor; for beta and high-gamma oscillations, sample size = 200 from 11 mice for each odor). Statistical analyses of the accuracy with all 0–5s vectors after the onset of odor stimulation showed significant differences between the spikes and the other three types of response (Fig. 6F Kruskal–Wallis test, spikes vs Ca^{2+} signals, beta, and high-gamma oscillations, $P < 0.001$; for spikes, sample size = 75 from 11 mice for each of the 8 odors; for Ca^{2+} signals, sample size = 220 from 11 mice for each odor; for beta and high-gamma oscillations, sample size = 200 from 11 mice for each odor). This also confirms that spikes are the best signal for discriminating among odors.

Discussion

Fiber photometry can detect changes in fluorescent signals from a specific neuronal population surrounding the tip of the fiber and is widely used to monitor neural activity from specific brain regions in behaving animals [4–6]. Since the signal it detects is not electrical, it only indirectly reflects neural activity. Thus, understanding the correlation between Ca^{2+} signals recorded from fiber photometry and electrophysiological signals recorded by electrodes is fundamental for interpreting population Ca^{2+} signals and how they relate to neural activity. To our knowledge, this study is the first attempt to correlate population Ca^{2+} signals and electrophysiological signals in the brain. Via simultaneously recording with opto-tetrodes, we identified the response characteristics of Ca^{2+} signals, spikes, and beta and high-gamma LFP oscillations and assessed the ability of each signal to discriminate odors. These findings provide direct evidence of how Ca^{2+} signals recorded by

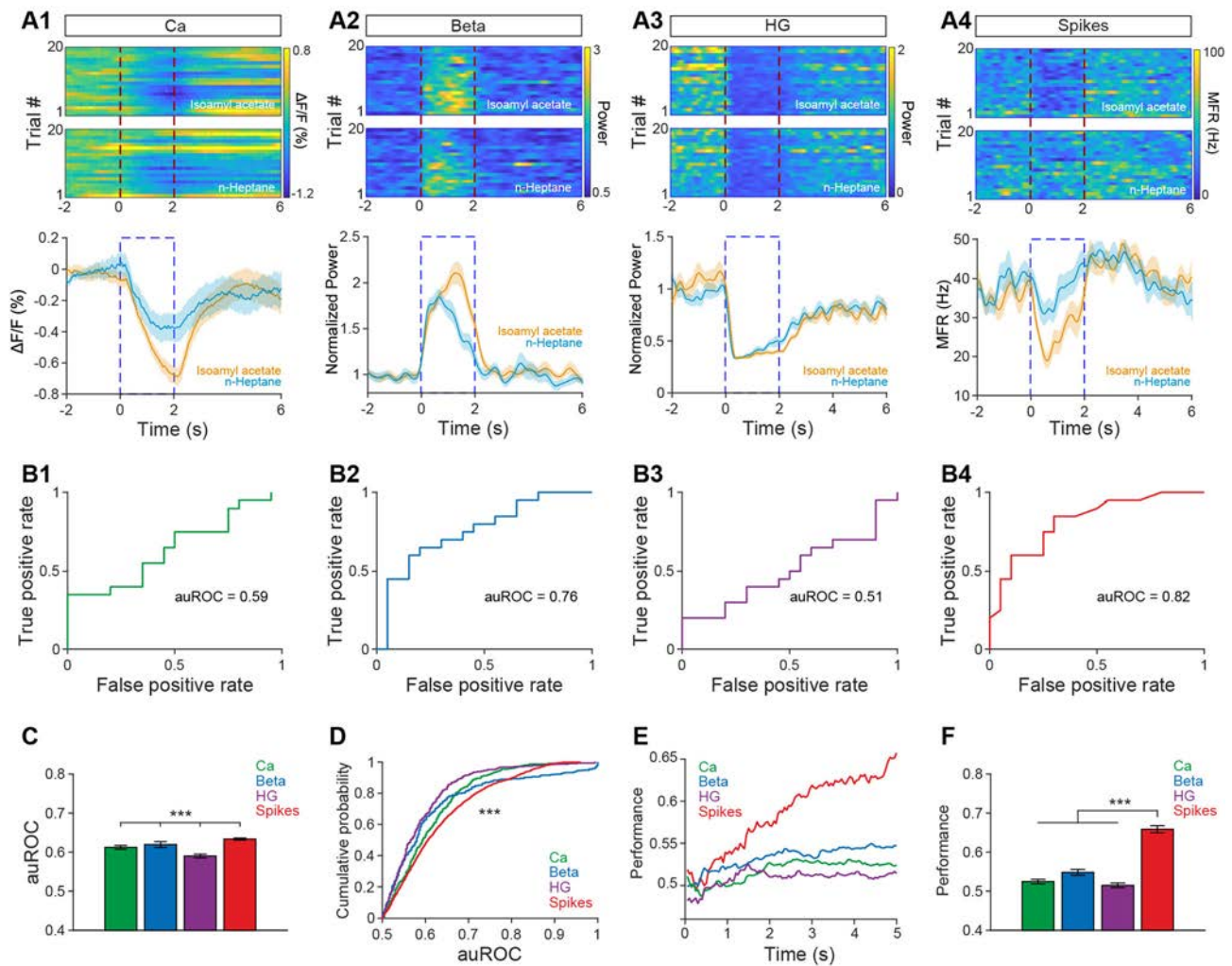


Fig. 6 Decoding ability of the Ca^{2+} and electrophysiological signals. **A1–A4** Heat maps (upper panels, 20 trials) and trial-averaged traces (lower panels) showing the Ca^{2+} signal, power in the beta and high gamma bands, and spikes evoked by a pair of odors (isoamyl acetate vs n-heptane) in a representative mouse. **B** auROC analysis of the difference in $\Delta F/F$, normalized LFP band power, and MFR induced by the two odors shown in **A**. **C**, **D** auROC analysis of all mouse/cell-odor pairs (**C**: Kruskal–Wallis test, $***P < 0.001$; **D**: two-sample K–S test, $***P < 0.001$; for spikes: $n = 1652$ pairs from 11 mice; for Ca^{2+} ,

beta and high-gamma, $n = 308$ pairs from 11 mice). **E** Performance of the logistic regression classifiers on odor-pair discrimination for $\Delta F/F$, normalized LFP band power, and MFR processed by subtracting the baseline. **F** Statistical analyses of the accuracy of all odor pairs when time = 5 s as in **E** (Kruskal–Wallis test, $***P < 0.001$; for spikes, sample size = 75 from 11 mice for each of the 8 odors; for Ca^{2+} signals, sample size = 220 from 11 mice for each odor; for beta and high-gamma oscillations, sample size = 200 from 11 mice for each odor). Ca, calcium; HG, high gamma

fiber photometry correlate with different types of electrophysiological signal.

M/Ts are the main output neurons of the OB. They receive direct input from olfactory sensory neurons and transmit odor information to higher olfactory centers. Within the OB, M/Ts also receive inhibitory input from GABAergic interneurons located in all layers of the OB and dopaminergic interneurons in the glomerular layer [34–36]. The glomerular layer and the external plexiform layer contain two important neural circuits for mediating the M/T odor response [13, 19]. The responses of M/Ts to different odors are complex and dependent on brain state [14]. For example, although odors usually evoke an

increase in single-unit M/T spikes in anesthetized animals, both excitatory and inhibitory responses are recorded in awake, behaving animals, with inhibitory responses more common than excitatory responses [25, 26, 31, 37]. The results from the present study are consistent with those from previous electrophysiological studies: whereas spikes show either inhibitory or excitatory responses depending on the odor and cell recorded, beta oscillations consistently show increases in power to odor presentation and high-gamma oscillations consistently show decreases in power [23, 24]. Moreover, the odor-evoked Ca^{2+} signals recorded *via* fiber photometry are generally consistent with our previous study, with both excitatory and inhibitory

responses detected, although more inhibitory responses were found in the present study and more excitatory responses were found in the previous study [6]. This slight difference is likely due to the recording locations differing slightly in different experiments. Overall, the opto-tetrode method for simultaneously recording electrophysiological signals and Ca^{2+} signals is robust and reliable, and can be widely used in brain areas beyond the OB.

Since Ca^{2+} signals are chemical in nature, it is not surprising that they are much slower than electrical signals. However, direct comparison of the temporal pattern of Ca^{2+} signals and electrophysiological signals is important for interpreting fiber photometry data. Our data indicate that, generally, electrophysiological signals are faster than Ca^{2+} signals, since the former have shorter onset and peak latencies, and have shorter response durations (Fig. 3). Interestingly, although the differences in mean onset and peak latencies between Ca^{2+} signals and spikes were significant, the difference was small in magnitude (Fig. 3, 0.54 s vs 0.50 s for onset latency; 2.36 s vs 2.04 s for peak latency). However, this result does not indicate that the Ca^{2+} signals can be as fast as spikes; rather, this is because the temporal profiles of spike responses to odors were rather variable (Fig. 5). Variability in the M/T spike response to odors in awake animals has been reported extensively [25, 31, 38]. Spikes from a single cell reflect specific properties that vary from cell to cell but Ca^{2+} signals recorded *via* fiber photometry detect the averaged activity from a population of cells and thus do not reflect the properties of any individual cell.

How non-electrical activity correlates with electrical neural activity is a fundamental topic in neuroscience research. The correlations between vascular density, synaptic transmission, metabolism, and neurovascular coupling in optical imaging have been investigated extensively [39, 40]. Furthermore, previous studies have identified that the BOLD signal recorded during fMRI is most closely correlated with low-gamma LFP oscillations in the OB [41]. Our study reveals that the Ca^{2+} signals recorded *via* fiber photometry are most closely correlated with beta LFP oscillations. It is reasonable that the fiber photometry Ca^{2+} signal is better correlated with the LFP than with single-unit spikes since both the fiber photometry signal and the LFP signal reflect activity from a population of cells. It is interesting that the Ca^{2+} signal correlates better with beta oscillations than high-gamma oscillations. In the OB, gamma oscillations arise from interactions in the dendro-dendritic microcircuit between mitral cells and granule cells and reflect local neural network activity [24, 42, 43], whereas beta oscillations reflect activity in the wider olfactory network, including the centrifugal inputs to the OB from higher olfactory centers such as the piriform cortex [42, 44]. Our findings thus indicate that the fiber

photometry Ca^{2+} signal may reflect the activity in global rather than local neural networks. Indeed, the beta oscillations and fiber photometry signals show functional similarities: in both, the odor-evoked responses are significantly modulated by learning in an odor discrimination task [6, 23, 24].

The most important task of the olfactory system is to represent odor information precisely. More and more evidence supports the hypothesis that M/Ts in the OB represent odor identity [14, 15, 20, 45]. Spikes from single M/Ts carry important information about odor identity [45, 46], although spikes that have a sniffing cycle or gamma oscillations as a frame represent odor identity more accurately [22, 47]. Thus, spikes have good features for discriminating odors. For LFP signals, both beta and gamma (especially high-gamma) oscillations are critically involved in the learning process during an odor discrimination task [24, 33, 43], and beta oscillations are thought to carry information on the chemical factors of odors [48]. However, there is no direct evidence that LFPs are a good candidate signal for representing odor identity. The present study is generally consistent with previous findings that spikes perform the best and high-gamma oscillations perform the worst in odor discrimination [6, 23]. Fiber photometry Ca^{2+} signals perform significantly worse than spikes, but can discriminate odors, performing better than gamma oscillations. This is consistent with our previous study in which Ca^{2+} signals could discriminate between a pair of odors, although this discrimination was dependent on task demands [6].

Another interesting finding in our study is that the population Ca^{2+} signal was the most reliable signal when responding to the same odor. This indicates that this signal is a good candidate for detecting odor stimulation even though its ability to discriminate odors is not strong. Since spikes perform well in discriminating odors but are not good at detecting odors, owing to their high variability, combining spike and population Ca^{2+} recordings enables both odor detection and odor discrimination to be precisely monitored. A similar method to simultaneously monitor EEG signals and fiber photometry signals was described in a recent study [49]. Thus, simultaneous recording of neural activity by electrophysiology and fiber photometry, as in the present study, is a powerful technique for studying the functions of single cells and neural circuits underlying sensory processing, cognition, and specific behaviors.

Olfactory dysfunction is closely correlated with many neurodegenerative diseases, such as Alzheimer's disease and Parkinson's disease [12]. The neural activity and odor response in the OB are significantly changed in models of these diseases, in which the function of the OB is impaired. For example, while the spontaneous spike activity is increased and odor-evoked responses in the OB are

decreased in a mouse model of Alzheimer's disease [11, 50], similar findings have also been reported for LFP in the OB in a mouse model of Parkinson's disease. Thus, electrophysiological signals in the OB reflect the functional change of the OB [32]. This raises the question of whether Ca^{2+} signals recorded by fiber photometry also have the ability to reflect functional changes in the OB. This question can be addressed by recording the Ca^{2+} signals and electrophysiological signals simultaneously as in our present study in an OB lesion mouse model. Thus, direct evidence of how Ca^{2+} signals correlate with electrophysiological signals in the impaired OB is needed.

To summarize, in the present study we compared population Ca^{2+} signals with simultaneously recorded electrophysiological signals to fully assess the response characteristics, temporal correlations, and odor identity representations in the different signals. The results provide guidelines for the application of fiber photometry in other areas of neuroscience research and serve as a reminder to be cautious when interpreting Ca^{2+} signals with regard to neural activity.

Acknowledgments This work was supported by the National Natural Science Foundation of China (31872771, 32070995, and 31900713) and the National Demonstration Center for Experimental Basic Medical Science Education (Xuzhou Medical University).

Conflict of interest The authors claim that there are no conflicts of interest.

Open Access This article is licensed under a Creative Commons Attribution 4.0 International License, which permits use, sharing, adaptation, distribution and reproduction in any medium or format, as long as you give appropriate credit to the original author(s) and the source, provide a link to the Creative Commons licence, and indicate if changes were made. The images or other third party material in this article are included in the article's Creative Commons licence, unless indicated otherwise in a credit line to the material. If material is not included in the article's Creative Commons licence and your intended use is not permitted by statutory regulation or exceeds the permitted use, you will need to obtain permission directly from the copyright holder. To view a copy of this licence, visit <http://creativecommons.org/licenses/by/4.0/>.

References

1. Pesaran B, Vinck M, Einevoll GT, Sirota A, Fries P, Siegel M. Investigating large-scale brain dynamics using field potential recordings: analysis and interpretation. *Nat Neurosci* 2018, 21: 903–919.
2. Buzsaki G, Anastassiou CA, Koch C. The origin of extracellular fields and currents—EEG, ECoG, LFP and spikes. *Nat Rev Neurosci* 2012, 13: 407–420.
3. Buzsaki G, Stark E, Berenyi A, Khodagholy D, Kipke DR, Yoon E, *et al.* Tools for probing local circuits: high-density silicon probes combined with optogenetics. *Neuron* 2015, 86: 92–105.
4. Cui G, Jun SB, Jin X, Luo G, Pham MD, Lovinger DM, *et al.* Deep brain optical measurements of cell type-specific neural activity in behaving mice. *Nat Protoc* 2014, 9: 1213–1228.
5. Li Y, Liu Z, Guo Q, Luo M. Long-term fiber photometry for neuroscience studies. *Neurosci Bull* 2019, 35: 425–433.
6. Wang D, Liu P, Mao X, Zhou Z, Cao T, Xu J, *et al.* Task-demand-dependent neural representation of odor information in the olfactory bulb and posterior piriform cortex. *J Neurosci* 2019, 39: 10002–10018.
7. Wu H, Yan X, Tang D, Gu W, Luan Y, Cai H, *et al.* Internal states influence the representation and modulation of food intake by subthalamic neurons. *Neurosci Bull* 2020, 36: 1355–1368.
8. Li Y, Zhong W, Wang D, Feng Q, Liu Z, Zhou J, *et al.* Serotonin neurons in the dorsal raphe nucleus encode reward signals. *Nat Commun* 2016, 7: 10503.
9. Croy I, Hummel T. Olfaction as a marker for depression. *J Neurol* 2017, 264: 631–638.
10. Fullard ME, Morley JF, Duda JE. Olfactory dysfunction as an early biomarker in Parkinson's disease. *Neurosci Bull* 2017, 33: 515–525.
11. Hu B, Geng C, Hou XY. Oligomeric amyloid- β peptide disrupts olfactory information output by impairment of local inhibitory circuits in rat olfactory bulb. *Neurobiol Aging* 2017, 51: 113–121.
12. Doty RL. Olfactory dysfunction in neurodegenerative diseases: is there a common pathological substrate? *Lancet Neurol* 2017, 16: 478–488.
13. Imai T. Construction of functional neuronal circuitry in the olfactory bulb. *Semin Cell Dev Biol* 2014, 35: 180–188.
14. Li A, Rao X, Zhou Y, Restrepo D. Complex neural representation of odour information in the olfactory bulb. *Acta Physiol (Oxf)* 2020, 228: e13333.
15. Uchida N, Poo C, Haddad R. Coding and transformations in the olfactory system. *Annu Rev Neurosci* 2014, 37: 363–385.
16. Wang L, Zhang Z, Chen J, Manyande A, Haddad R, Liu Q, *et al.* Cell-type-specific whole-brain direct inputs to the anterior and posterior piriform cortex. *Front Neural Circuits* 2020, 14: 4.
17. Linster C, Cleland TA. Neuromodulation of olfactory transformations. *Curr Opin Neurobiol* 2016, 40: 170–177.
18. Wen P, Rao X, Xu L, Zhang Z, Jia F, He X, *et al.* Cortical organization of entrifugal afferents to the olfactory bulb: mono- and trans-synaptic tracing with recombinant neurotropic viral tracers. *Neurosci Bull* 2019, 35: 709–723.
19. Nagayama S, Homma R, Imamura F. Neuronal organization of olfactory bulb circuits. *Front Neural Circuits* 2014, 8: 98.
20. Gire DH, Restrepo D, Sejnowski TJ, Greer C, De Carlos JA, Lopez-Mascaraque L. Temporal processing in the olfactory system: can we see a smell? *Neuron* 2013, 78: 416–432.
21. Nunez-Parra A, Li A, Restrepo D. Coding odor identity and odor value in awake rodents. *Prog Brain Res* 2014, 208: 205–222.
22. Li A, Gire DH, Restrepo D. Upsilon spike-field coherence in a population of olfactory bulb neurons differentiates between odors irrespective of associated outcome. *J Neurosci* 2015, 35: 5808–5822.
23. Liu P, Cao T, Xu J, Mao X, Wang D, Li A. Plasticity of sniffing pattern and neural activity in the olfactory bulb of behaving mice during odor sampling, anticipation, and reward. *Neurosci Bull* 2020, 36: 598–610.
24. Martin C, Ravel N. Beta and gamma oscillatory activities associated with olfactory memory tasks: different rhythms for different functional networks? *Front Behav Neurosci* 2014, 8: 218.
25. Rinberg D, Koulakov A, Gelperin A. Sparse odor coding in awake behaving mice. *J Neurosci* 2006, 26: 8857–8865.

26. Doucette W, Gire DH, Whitesell J, Carmean V, Lucero MT, Restrepo D. Associative cortex features in the first olfactory brain relay station. *Neuron* 2011, 69: 1176–1187.
27. Kay LM, Laurent G. Odor- and context-dependent modulation of mitral cell activity in behaving rats. *Nat Neurosci* 1999, 2: 1003–1009.
28. Sun C, Tang K, Wu J, Xu H, Zhang W, Cao T, *et al.* Leptin modulates olfactory discrimination and neural activity in the olfactory bulb. *Acta Physiol (Oxf)* 2019, 227: e13319.
29. Zhou Y, Wang X, Cao T, Xu J, Wang D, Restrepo D, *et al.* Insulin modulates neural activity of pyramidal neurons in the anterior piriform cortex. *Front Cell Neurosci* 2017, 11: 378.
30. Wang D, Wang X, Liu P, Jing S, Du H, Zhang L, *et al.* Serotonergic afferents from the dorsal raphe decrease the excitability of pyramidal neurons in the anterior piriform cortex. *Proc Natl Acad Sci U S A* 2020, 117: 3239–3247.
31. Li A, Guthman EM, Doucette WT, Restrepo D. Behavioral status influences the dependence of odorant-induced change in firing on prestimulus firing rate. *J Neurosci* 2017, 37: 1835–1852.
32. Zhang W, Sun C, Shao Y, Zhou Z, Hou Y, Li A. Partial depletion of dopaminergic neurons in the substantia nigra impairs olfaction and alters neural activity in the olfactory bulb. *Sci Rep* 2019, 9: 254.
33. Frederick DE, Brown A, Brim E, Mehta N, Vujovic M, Kay LM. Gamma and beta oscillations define a sequence of neurocognitive modes present in odor processing. *J Neurosci* 2016, 36: 7750–7767.
34. Vaaga CE, Yorgason JT, Williams JT, Westbrook GL. Presynaptic gain control by endogenous cotransmission of dopamine and GABA in the olfactory bulb. *J Neurophysiol* 2017, 117: 1163–1170.
35. Geramita MA, Burton SD, Urban NN. Distinct lateral inhibitory circuits drive parallel processing of sensory information in the mammalian olfactory bulb. *Elife* 2016, 5.
36. Burton SD. Inhibitory circuits of the mammalian main olfactory bulb. *J Neurophysiol* 2017, 118: 2034–2051.
37. Li A, Gong L, Xu F. Brain-state-independent neural representation of peripheral stimulation in rat olfactory bulb. *Proc Natl Acad Sci U S A* 2011, 108: 5087–5092.
38. Fontanini A, Katz DB. Behavioral states, network states, and sensory response variability. *J Neurophysiol* 2008, 100: 1160–1168.
39. Gurden H, Uchida N, Mainen ZF. Sensory-evoked intrinsic optical signals in the olfactory bulb are coupled to glutamate release and uptake. *Neuron* 2006, 52: 335–345.
40. Petzold GC, Albeanu DF, Sato TF, Murthy VN. Coupling of neural activity to blood flow in olfactory glomeruli is mediated by astrocytic pathways. *Neuron* 2008, 58: 897–910.
41. Li B, Gong L, Wu R, Li A, Xu F. Complex relationship between BOLD-fMRI and electrophysiological signals in different olfactory bulb layers. *Neuroimage* 2014, 95: 29–38.
42. Neville KR, Haberly LB. Beta and gamma oscillations in the olfactory system of the urethane-anesthetized rat. *J Neurophysiol* 2003, 90: 3921–3930.
43. Kay LM, Beshel J, Brea J, Martin C, Rojas-Libano D, Kopell N. Olfactory oscillations: the what, how and what for. *Trends Neurosci* 2009, 32: 207–214.
44. Fukunaga I, Herb JT, Kollo M, Boyden ES, Schaefer AT. Independent control of gamma and theta activity by distinct interneuron networks in the olfactory bulb. *Nat Neurosci* 2014, 17: 1208–1216.
45. Wilson CD, Serrano GO, Koulakov AA, Rinberg D. A primacy code for odor identity. *Nat Commun* 2017, 8: 1477.
46. Chong E, Moroni M, Wilson C, Shoham S, Panzeri S, Rinberg D. Manipulating synthetic optogenetic odors reveals the coding logic of olfactory perception. *Science* 2020, 368: eaba2357.
47. Cury KM, Uchida N. Robust odor coding *via* inhalation-coupled transient activity in the mammalian olfactory bulb. *Neuron* 2010, 68: 570–585.
48. Lowry CA, Kay LM. Chemical factors determine olfactory system beta oscillations in waking rats. *J Neurophysiol* 2007, 98: 394–404.
49. Patel AA, McAlinden N, Mathieson K, Sakata S. Simultaneous electrophysiology and fiber photometry in freely behaving mice. *Front Neurosci* 2020, 14: 148.
50. Doty RL. Olfaction in Parkinson’s disease and related disorders. *Neurobiol Dis* 2012, 46: 527–552.



Dysregulated *CRMP* Mediates Circadian Deficits in a *Drosophila* Model of Fragile X Syndrome

Juan Zhao¹ · Jin Xue¹ · Tengfei Zhu¹ · Hua He¹ · Huaixing Kang¹ ·
Xuan Jiang¹ · Wen Huang^{1,2,3} · Ranhui Duan^{1,2,3}

Received: 23 December 2019 / Accepted: 9 November 2020 / Published online: 15 April 2021
© Center for Excellence in Brain Science and Intelligence Technology, CAS 2021

Abstract Fragile X syndrome (FXS) is the leading inherited cause of intellectual disability, resulting from the lack of functional fragile X mental retardation protein (FMRP), an mRNA binding protein mainly serving as a translational regulator. Loss of FMRP leads to dysregulation of target mRNAs. The *Drosophila* model of FXS shows an abnormal circadian rhythm with disruption of the output pathway downstream of the clock network. Yet the FMRP targets involved in circadian regulation have not been identified. Here, we identified collapsing response mediator protein (CRMP) mRNA as a target of FMRP. Knockdown of pan-neuronal *CRMP* expression ameliorated the circadian defects and abnormal axonal structures of clock neurons (ventral lateral neurons) in *dfmr1* mutant flies. Furthermore, specific reduction of *CRMP* in the downstream output insulin-producing cells attenuated the aberrant circadian behaviors. Molecular analyses revealed that FMRP binds with *CRMP* mRNA and negatively regulates its translation. Our results indicate that *CRMP* is an FMRP

target and establish an essential role for *CRMP* in the circadian output in FXS *Drosophila*.

Keywords Fragile X syndrome · FMRP · *CRMP* · Circadian rhythm

Introduction

Circadian rhythms are present in diverse organisms, characterized by daily rhythmic oscillations in metabolism, physiological processes, cognition, and behaviors [1, 2]. The circadian clock system consists of three fundamental components: a central oscillator that drives endogenous rhythms, an input pathway that conveys environmental cues and entrains the central oscillator, and an output pathway that is governed by the central clock to generate overt rhythms. The circadian clock is driven by the interlocked transcription-translation feedback loops of clock genes, which regulate the expression of clock-controlled genes involved in various biological processes such as metabolism, redox homeostasis, inflammation, hormone secretion, and sleep [1, 3–6]. Evidence from both humans and animal models link circadian rhythms to sleep and normal physiology and behaviors. Circadian rhythms and sleep are tightly linked, and their causal interaction is difficult to delineate. The circadian clock regulates the timing and homeostat of sleep, and alterations in sleep also feed back on the circadian rhythm [7]. Sleep disorders and circadian disruption are commonly reported in neurodevelopmental diseases, including fragile X syndrome (FXS), Prader-Willi syndrome, and Angelman syndrome [8, 9]. Patients have perturbed sleep patterns, usually displaying altered sleep duration and abnormal awakenings at night [10, 11]. Sleep disorders are associated with impaired

Supplementary Information The online version contains supplementary material available at <https://doi.org/10.1007/s12264-021-00682-z>.

✉ Wen Huang
huangwen@sklmg.edu.cn

✉ Ranhui Duan
duanranhui@sklmg.edu.cn

¹ Center for Medical Genetics, School of Life Sciences, Central South University, Changsha 410078, China

² Hunan Key Laboratory of Medical Genetics, Central South University, Changsha 410078, China

³ Hunan Key Laboratory of Animal Models for Human Diseases, Central South University, Changsha 410078, China

circadian clock function, and disrupted expression of circadian genes and deficient rhythms have been documented in patients and animal models of neuropsychiatric diseases [12–17].

FXS is the most common form of inherited autism spectrum disorders and intellectual disability, caused by loss of the fragile X mental retardation protein (FMRP) [18, 19]. FXS patients present cognitive disorders along with symptoms of autism and epilepsy. FXS animal models including mice and *Drosophila* exhibit typical phenotypes mimicking those in FXS patients, such as impaired cognition, social behavioral issues, and neuronal structural deficits as well as excessive protein synthesis and other abnormalities at the molecular level [20, 21]. Sleep disorders in FXS patients can also be well explored in animal models, as impaired sleep patterns and circadian rhythm defects have been reported in FXS mice and *Drosophila*, providing ideal approaches to further explore the underlying mechanisms. Both FXS mice and flies show significantly abnormal sleep profiles and impaired circadian rhythm [22–24]. As early as 2002, a defective locomotor activity rhythm and an aberrant eclosion rhythm have been reported in *dfmr1* mutant flies. FXS flies fail to maintain a circadian locomotor activity rhythm in constant darkness and display an abnormal eclosion pattern compared with wild-type flies [14]. Although the circadian ventral lateral neurons (LN_{v,s}) of *dfmr1* mutant flies display axonal structural defects, the core clock pacemaker neurons are normal [15, 25]. Elevated mGluR signaling has been thought to be the leading pathogenic mechanism of FXS, but genetic reduction of mGluR signaling or administration of its antagonist does not ameliorate the circadian activity defects in FXS *Drosophila* [26], excluding the possibility that the mGluR signaling pathway underlies regulation of the circadian rhythm in FXS. Recently, a study demonstrated that FMRP functions in the insulin-producing cells (IPCs), confirming a role of FMRP in the circadian output pathway [27]. Yet how FMRP regulates circadian behaviors and circadian output in *Drosophila* is still not fully understood.

FMRP is encoded by *FMRI*, the pathogenic gene of FXS. FMRP, mainly enriched in the nervous system, is an RNA binding protein that regulates its target genes and predominantly functions as a translation inhibitor. Besides this function, FMRP also plays an essential role in regulating dendritic mRNA transport and the stability of its target mRNAs [18]. To better understand the molecular mechanisms of FXS, researchers employed many methods to identify FMRP target mRNAs, such as high-throughput sequencing of RNAs isolated by cross-linking immunoprecipitation (HITS-CLIP) and phospho-activatable ribonucleoside (PAR-CLIP) [28, 29]. In the mouse brain, 842 mRNAs associated with polyribosomes have been

identified as potential target genes of FMRP [28]. Recently, 4,174 mRNAs were predicted to be FMRP targets at an early developmental stage in the mouse, including 1,610 new targets [30]. Among the hundreds of proposed FMRP targets, only a few have been validated by direct biochemical interaction and genetic manipulation *in vivo* in FXS animal models to illustrate their roles in its pathogenesis. The deregulated proteins encoded by mRNA targets identified in the last twenty years such as ADCY1, DGK κ , APP, and MAP1B have been shown to participate in the synaptic plasticity and cognitive defects in FXS [31–33]. So far, none of the known targets clarified have been reported to regulate the circadian rhythm in FXS.

Among the genes identified as potential targets of FMRP, collapsing response mediator protein 2 (CRMP2) is of particular interest due to its involvement in the regulation of circadian rhythm and neuronal development [34–36]. As an axonal guidance molecule, vertebrate CRMP2 mediates a variety of neuronal growth cone dynamics through signal transduction pathways [37]. CRMP2 promotes microtubule assembly and also participates in Numb-mediated endocytosis, facilitating the rate of axonal growth [38–40]. *CRMP2*-KO mice show developmental defects of hippocampal neurons in addition to abnormal sociability and impaired long-term potentiation [36]. *Drosophila melanogaster* has a single conserved *CRMP* gene, encoding a protein termed CRMP, which shares 46% amino-acid identity with human CRMP2. Loss of *Drosophila CRMP* results in defective olfactory memory and circadian rhythm deficits [34]. Considering the important role of *CRMP* in neuronal morphology and its potential function in *Drosophila* rhythm, we investigated whether *CRMP* is an FMRP target mRNA that regulates the circadian activity rhythm in FXS flies.

Here we found that reduction of *CRMP* repressed the circadian arrhythmicity and neural structural defects in FXS *Drosophila* and identified *CRMP2* mRNA as a target of FMRP in cells. Our findings in *Drosophila* showed that genetic reduction of *CRMP* rescues the aberrant locomotor activity rhythm and LN_v structural defects in the FXS *Drosophila* model. And specific knockdown of *CRMP* expression in IPCs but not in clock neurons ameliorates circadian behaviors. Further, results with mammalian and *Drosophila* cells showed that FMRP selectively binds with *CRMP* mRNA, negatively regulating its translation. Our findings suggest that FMRP regulates circadian output by suppressing *CRMP* translation in IPCs of the *Drosophila* brain.

Materials and Methods

Cell Culture

Human embryonic kidney (HEK) 293 cells obtained from the Cell Bank of the Chinese Academy of Sciences (Shanghai, China) were cultured in Dulbecco's modified Eagle's medium (DMEM) (Sigma-Aldrich, St. Louis, USA, #D5546) containing 10% fetal bovine serum (FBS) (Thermo Fisher Scientific, Massachusetts, USA, #10099). To maintain N2a cells obtained from the Cell Bank of the Chinese Academy of Sciences (Shanghai, China), DMEM and Opti-MEM medium (Thermo Fisher Scientific, Massachusetts, USA, #A4124802) were mixed at 1:1 and then 10% FBS was added. And Epstein-Barr virus-transformed lymphoblastoid cell lines were derived from a normal male and an FXS male patient with deletion of the *FMR1* gene and cultured in RPMI-1640 medium (Thermo Fisher Scientific, Massachusetts, USA, #A4192301) supplemented with 20% FBS.

Ethics Approval and Consent to Participate

The experiments were undertaken with the understanding and written consent of each subject, and the study conformed with The Code of Ethics of the World Medical Association (Declaration of Helsinki), printed in the British Medical Journal (18 July 1964). This study was approved by the Ethics Committee of the Center for Medical Genetics, Central South University (approval number: 2013051201).

Drosophila Stocks and Maintenance

Fly strains containing *dfmr1*³ and *dfmr1*^{50M} alleles were kind gifts from Dr. Peng Jin, (Emory University, School of Medicine, USA) and the *Dilp2-Gal4* stock was from Dr. Luoying Zhang (Huanzhong University of Science and Technology, College of Life Science and Technology, China). The *dfmr1* mutant flies used in this study were *dfmr1*³/*dfmr1*^{450M} trans-heterozygotes. The *elav-Gal4*, and *CRMP*^{supK1} stocks were from Bloomington *Drosophila* Stock Center (Indiana University Bloomington, IN, USA, stock numbers 458 and 40954). Fly strains carrying *CRMP-RNAi-1* and *CRMP-RNAi-2* RNA interference transgenes were from the Tsinghua Fly Center (Tsinghua University, Beijing, China, stock number TH02545.N) and the Vienna *Drosophila* Resource Center (Vienna, Austria, stock number v101510), respectively. Fly stocks were reared on standard cornmeal-molasses medium at 25°C. Flies were anaesthetized with CO₂ to minimize suffering in the experiments.

RNA Co-immunoprecipitation

RNA co-immunoprecipitation was performed as described previously [41] with some modifications. Cells and *Drosophila* heads were lysed with lysis buffer (20 mmol/L Tris-HCl pH 7.4, 150 mmol/L NaCl, 5 mmol/L MgCl₂, 1 mmol/L DTT, 1% Triton X-100) supplemented with RNase inhibitor (Takara, Kusatsu, Japan, #2313A) and proteinase inhibitor cocktail (Sigma-Aldrich, St. Louis, USA, #P8340). Cleared lysates with 1 mg total protein were incubated with Dynabeads[®] Protein G (Invitrogen, Paisley, UK, #10003D) coated by either anti-FMRP antibody [Millipore, Darmstadt, Germany, #MAB2160] for HEK293 and N2a cells; anti-dFMRP (Abcam, Cambridge, UK, #ab10299) for *Drosophila* S2 cells and brains] or normal mouse IgGs (Sigma-Aldrich, Saint Louis, MO, USA, #I5381) overnight at 4°C, and 5% of the lysates were saved as input. About 30% of the beads were used for Western blot analysis and the rest for mRNA enrichment analysis. After addition of 10 pg of external control RNA from *Caenorhabditis elegans* into the input and RNA immunoprecipitation, RNA was extracted by TRIzol (Invitrogen, CA, USA, #15596-026) and reverse-transcribed using the RevertAid First Strand cDNA Synthesis Kit and random primers (Thermo Fisher Scientific, Waltham, USA, #K1622). Quantitative real-time PCR (qRT-PCR) was performed and the mRNA enrichment was calculated with *C. elegans* 18S rRNA as an external control and input for normalization. The primers used were as follows:

human-*CRMP2*-F: 5'-CTCGTTTCCAGATGCCTGAT-3',
 human-*CRMP2*-R: 5'-CTCAGGAACAACGTGGTCAA-3',
 mouse-*CRMP2*-F: 5'-ATTCCACGCATCACGAGCGA-3',
 mouse-*CRMP2*-R: 5'-GGTCTTACCCCTCCTGGTA-3',
 fly-*CRMP*-F: 5'-CCAGAATCGCGTCTACATCAA-3'
 fly-*CRMP*-R: 5'-TCCGCCAGGTATCGTTATTTC-3'
C. elegans 18S rRNA-F: 5'-TAGTGAGACGCCCAA-CAGC-3',
C. elegans 18S rRNA-R: 5'-TGGCATCGTTTACGGT-CAG-3'.

Polyribosome Profile Analysis

Polyribosome profiling was carried out according to the modified method described previously [41, 42]. FXS and normal lymphoblastoid cells were treated with 100 µg/mL cycloheximide (Sigma-Aldrich, St. Louis, USA, #D5546) and incubated for 15 min at 37°C. Then cell lysates were

prepared on ice in lysis buffer (10 mmol/L HEPES-KOH pH 7.4, 150 mmol/L KCl, 10 mmol/L MgCl₂, 1 mmol/L DTT, 100 µg/mL cycloheximide, 1% Triton X-100, and RNase and proteinase inhibitors). The resulting supernatant of cytoplasmic lysate was loaded on a 15%–60% sucrose gradient prepared in the lysis buffer and spun at 45,000 rpm for 1 h at 4°C in an SW-55 rotor (Beckman Coulter, Inc., CA, USA). The sucrose gradients were separated into 11 fractions. *C. elegans* RNA (10 pg) was added into each fraction and total RNA was isolated, and the mRNA levels were quantified and analyzed by qRT-PCR as described above.

Immunohistochemistry and Sholl Analysis

Immunohistochemistry of adult brains and the analyses of LN_v neurons were performed as previously described [25, 43]. The brains from adult flies (0–3 days old) were dissected in phosphate-buffered saline (PBS, pH 7.4) and then fixed with 4% paraformaldehyde in PBS for 60 min at 4°C. The brains were rinsed with PBS and then permeabilized with 0.1% triton X-100 in PBS (PBST) for 40 min. After blocking for 60 min with 5% goat serum (Thermo Fisher Scientific, Massachusetts, USA, #16210072) in 0.1% PBST at room temperature, the brains were incubated with anti-PDF (pigment-dispersing factor) antibody (C7 monoclonal, Developmental Studies Hybridoma Bank, University of Iowa, USA) at 1:100 dilution in 0.1% PBST overnight at 4°C. The brains were incubated with the secondary antibody mCy3 (Abcam, Cambridge, UK, #ab97035) at 1:200 for 2 h at room temperature in darkness. All images were captured on a Leica TCS SP5 confocal laser scanning microscope (Leica Microsystems, Wetzlar, Germany). The posterior optic tract (POT) from the circadian large ventral lateral neurons (ILN_{v,s}) neurons was measured using the previous method [25], and POT splitting was defined as defasciculation of the POT for >25% of its length. The synaptic architecture of the small Lateral Neurons ventral (sLN_{v,s}) were analyzed using modified Sholl analysis to assess the arborization of their arbor terminals [43, 44]. Concentric rings in 10-µm steps were centered on the sLN_v dorsal arbor bifurcation. PDF-positive puncta (diameter ≥ 1 µm) were counted in each ring to reflect the complexity of synaptic arborization. The terminal arborization of sLN_v arbors were evaluated in both hemispheres and each hemisphere was represented as $n = 1$.

Circadian Behavior Analysis

Adult male flies were loaded into tubes for locomotor activity recording using the *Drosophila* Activity Monitoring system from Trikinetics (Los Angeles, CA, USA) as

described previously [27, 45]. The experiment was conducted during the relative light time. Flies were entrained to a 12:12 h light/dark (LD) cycle for 4 days and then transferred to constant darkness for >7 days. More than 3 independent experiments were performed, and activity data from >20 flies per genotype were pooled and analyzed with Clocklab software (Actimetrics, Wilmette, USA). Circadian rhythm power is a measure of rhythmicity strength and flies with a power value ≥ 10 are defined as rhythmic. Relative rhythmicity power represents the average rhythmicity of each genotype compared to the average rhythmicity of the wild-type controls used in each experiment. Relative rhythmic power = $\text{power}_{\text{experimental}} / \text{power}_{\text{wild-type}} \times 100$.

Statistical Analysis

Statistical tests were performed and diagrams were constructed using GraphPad Prism 7 (RRID: RDG_1346427 GraphPad Software, Inc., San Diego, CA, USA). Unpaired two-tailed Student's *t*-tests were performed for two conditions or samples. One-way ANOVA with two-tailed Tukey's multiple comparison tests were performed for 3 or more conditions or samples. Two-way ANOVA was performed for Sholl analysis of PDF puncta distribution. All data obeyed normal distribution characteristics. All data are presented as the mean ± SEM; **P* < 0.05, ***P* < 0.01, ****P* < 0.001.

Results

Knockdown of *CRMP* Restores the Circadian Activity Rhythm in FXS *Drosophila*

In previous studies, *dfmr1* mutants displayed arrhythmic locomotor activity in constant darkness, revealing an essential role of FMRP in the regulation of the *Drosophila* circadian rhythm. To find potential FMRP target genes in the circadian regulation and to dissect the explicit underlying molecular pathway in *Drosophila*, we analyzed genes from the large-scale identification of mRNAs interacting with FMRP in FXS mouse brains that appeared in two independent studies using HITS-CLIP. We focused on those mediating functions in neural circuits and synaptic plasticity, and especially playing roles in the regulation of circadian rhythm. The microtubule-associated protein *CRMP2* was noted due to its function in neuronal development and circadian regulation in *Drosophila*.

As *CRMP*-deficient flies also exhibited circadian rhythm defects, we speculated that *CRMP* may have a functional interaction with FMRP in regulating circadian behaviors, so we investigated the role of *CRMP* in the circadian

activity rhythm of FXS *Drosophila*. Flies of all genotypes tested were entrained to a 12:12 LD cycle for 4 days prior to transfer to constant darkness for 7 days of activity recording and they had a normal circadian cycle of 23h–24 h (Table 1). The rhythm of free-running rest/activity were impaired in *dfmr1* mutant flies with 34% of flies being arrhythmic, and the relative rhythmic power of *dfmr1* mutants was significantly lower than in control flies (Fig. 1 and Table 1). Knockdown of *CRMP* expression with two *CRMP* RNAi transgene lines driven by the pan-neuronal *elav-Gal4* showed decreases of approximately 70% and 45% in *CRMP* mRNA levels in the brain (Fig. S1A). The two *CRMP* RNAi lines both partially rescued the activity rhythm of *dfmr1* mutants, with the percentages of arrhythmic flies reduced to 14% and 18%, respectively (Fig. 1 and Table 1). Actograms of representative flies showed that the *dfmr1* mutants with *CRMP* knockdown had a normal circadian activity pattern (Fig. 1A). We also examined the rhythms in *CRMP*-knockdown lines and *CRMP^{supK1}* mutants. The latter showed significant arrhythmic behaviors as reported previously [34] (Fig. S1 and Table S1). Flies with *CRMP-RNAi-1* knockdown exhibited arrhythmic activity, while no significant change occurred in flies with another *CRMP*-knockdown line *CRMP-RNAi-2* (Fig. 1 and Table 1), indicating that the knockdown efficiency of *CRMP-RNAi-2* driven by *elav-Gal4* was not sufficient to cause the arrhythmic phenotype. These results indicate that dysregulated *CRMP* expression due to the absence of FMRP in the central nervous system contributes to the abnormal locomotor activity rhythm in *dfmr1* mutant *Drosophila*.

Knockdown of *CRMP* Ameliorates Structural Defects of LN_v Neurons in FXS *Drosophila*

The circadian clock circuit in the *Drosophila* brain consists of 150 pacemaker neurons that are divided into 5 categories: dorsal lateral neurons, dorsal neurons (DN1, DN2 and DN3), lateral posterior neurons, and small and large ventral lateral neuron (sLN_vs and lLN_vs) that express the neuropeptide pigment-dispersing factor (PDF) [4]. LN_vs have been shown to play an indispensable role in the regulation of circadian activity, and are reported to have

structural deficits in both the axonal termini of sLN_vs and the POT in *dfmr1* mutant flies [15, 25].

As *CRMP2* is essential in neuronal development and axonal growth, we examined whether *Drosophila* *CRMP* plays a role in the development of LN_v axons in FXS *Drosophila*. Axon terminals of sLN_vs in the dorsal protocerebrum were over-elaborated and a split POT from the lLN_vs was also observed in the *dfmr1* mutants (Fig. 2A, B). Structural abnormalities in both lLN_vs and sLN_vs were ameliorated by genetic reduction of *CRMP* with two *CRMP* RNAi transgenes in the central nervous system. Over-elaborated terminals of sLN_v axons indicate the elevated complexity of the synaptic architecture, which were assessed by PDF-positive puncta distributed at the terminals of sLN_v arbors. Sholl analysis of PDF-positive boutons within each 10-μm ring showed that the numbers of PDF-positive puncta were increased in each ring of *dfmr1* mutants compared to wild-type flies, and knockdown of *CRMP* significantly decreased the numbers of puncta in *dfmr1* mutants (Fig. 2D and Fig. S2). The total number of PDF-positive puncta throughout the axonal arbor was also measured (Fig. 2). The total number was increased in *dfmr1* mutant flies, and *CRMP* knock-down significantly rescued this phenotype (Fig. 2E; total puncta, 37.6 ± 2.94 control, 63.4 ± 3.88 *dfmr1³/dfmr1^{Δ50M}*, 36.4 ± 3.31 *elav-Gal4>CRMP-RNAi-1*; *dfmr1³/dfmr1^{Δ50M}*, 46.9 ± 3.81 *elav-Gal4>CRMP-RNAi-2*; *dfmr1³/dfmr1^{Δ50M}*, 40.6 ± 2.88 *elav-Gal4>CRMP-RNAi-1*, 37.8 ± 2.23 *elav-Gal4>CRMP-RNAi-2*; *n* >20 for all genotypes). Flies with a split POT from lLN_vs were reduced to 27% and 29% in *dfmr1* mutants with *CRMP-RNAi-1* and *CRMP-RNAi-2*, respectively, compared to 69% in *dfmr1* mutant flies (Fig. 2B and Table S2). As ectopic collateral branches arising from the sLN_vs have been reported in *dfmr1* mutant flies, we quantified the collateral branches in flies of all genotypes. Collateral branching was observed in 12% of *dfmr1* mutants, while *dfmr1* mutants with reduced *CRMP* expression displayed no such ectopic branching (Fig. 2C and Table S2). The structural morphology of sLN_vs and lLN_vs in *CRMP*-deficient flies was also documented. POT-splitting and ectopic collateral branches were observed in *CRMP^{supK1}* mutants at higher percentages than in wild-type control flies, although the structure of LN_v terminals was

Table 1 Circadian phenotypes in constant darkness

Genotype	Number	Average period (h)	% Arrhythmic flies
<i>elav-Gla4</i>	107	23.70 ± 0.07	0.93
<i>elav-Gal4;dfmr1^{3/Δ50M}</i>	131	23.59 ± 0.09	34.35
<i>elav>CRMP-RNAi-1;dfmr1^{3/Δ50M}</i>	63	23.64 ± 0.06	14.29
<i>elav>CRMP-RNAi-2;dfmr1^{3/Δ50M}</i>	61	23.70 ± 0.14	18.03
<i>elav>CRMP-RNAi-1</i>	93	23.40 ± 0.05	16.13
<i>elav>CRMP-RNAi-2</i>	83	23.34 ± 0.05	1.20

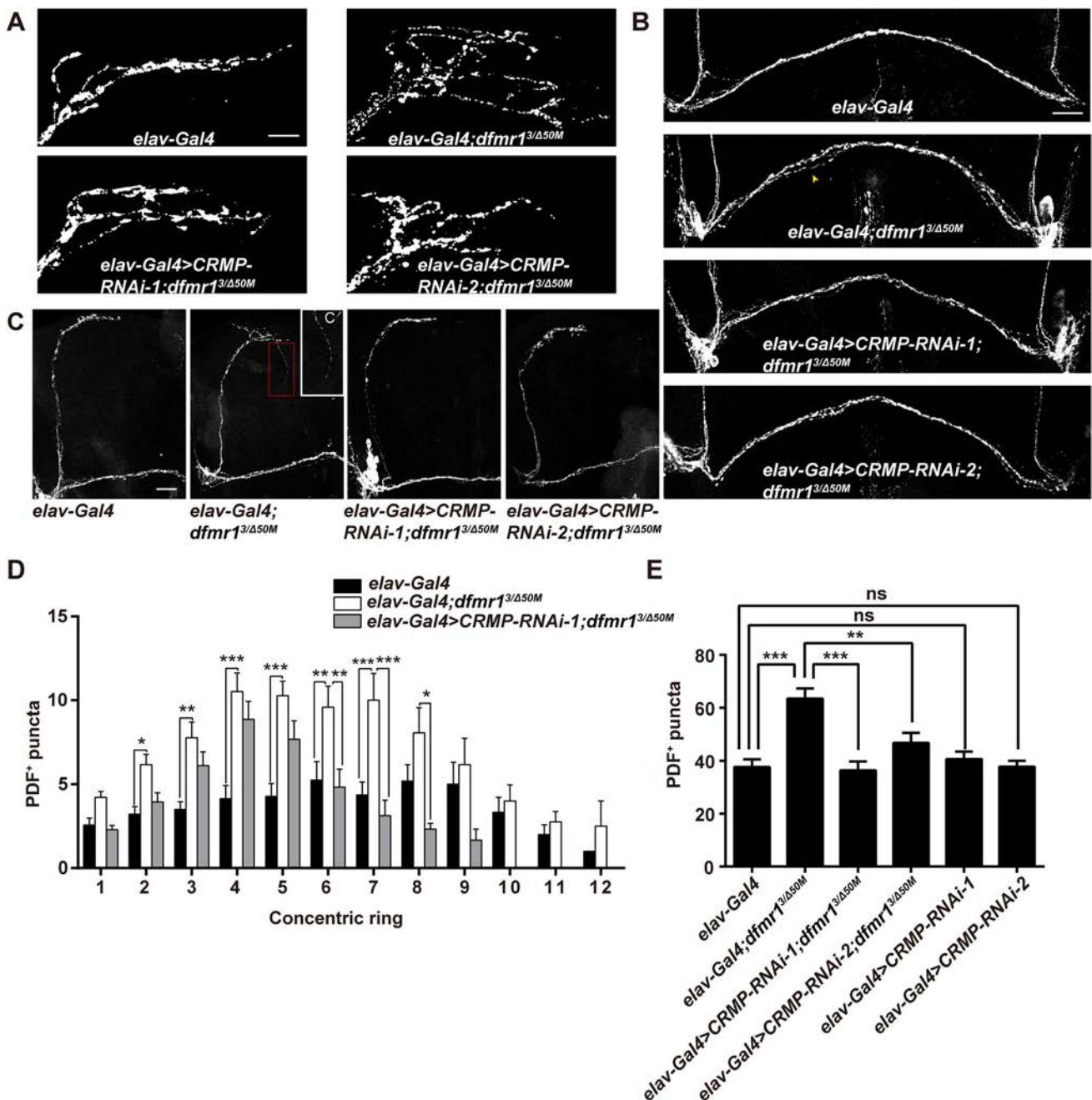


Fig. 2 Genetic reduction of *CRMP* rescues structural deficits of LN_v neurons in *dfmr1* mutants. **A** Terminals of sLN_vs at the dorsal protocerebrum of the depicted genotypes. *dfmr1* mutants show increased branching complexity, while knockdown of *CRMP* with both RNAi transgenes in the nervous system reduces the over-elaborated axonal branches (scale bar, 10 μm). **B** Representative split POT phenotype (indicated by arrowhead) in the indicated flies. *dfmr1* mutants show a POT defasciculation phenotype compared with the wild-type, and reduced *CRMP* expression rescues the POT splitting (scale bar, 75 μm). **C** Half brains of adult flies showing collateral branches. **C'** Magnification of the collateral branch in a *dfmr1* mutant *Drosophila*. Some of *dfmr1* mutants have ectopic collateral branches

(indicated by the red dash box), while mutant flies with two *CRMP* RNAi transgenes display no collateral branching, like wild-type flies (scale bar, 75 μm). **D** Sholl analysis of the distribution of PDF-reactive puncta throughout the sLN_v axonal arbors. *dfmr1* mutants harbor increased PDF puncta distributed in each ring, which is rescued by knockdown of *CRMP*. **E** Total numbers of PDF-positive (PDF⁺) puncta throughout the sLN_v axonal arbors. Knockdown of *CRMP* with both RNAi transgenes rescues the significantly elevated total number of PDF puncta in *dfmr1* mutants. **P* < 0.05, ***P* < 0.01, ****P* < 0.001, two-way ANOVA for **C** and one-way ANOVA for **D**. *n* > 20 hemispheres per genotype. Data are represented as the mean ± SEM. ns, not significant.

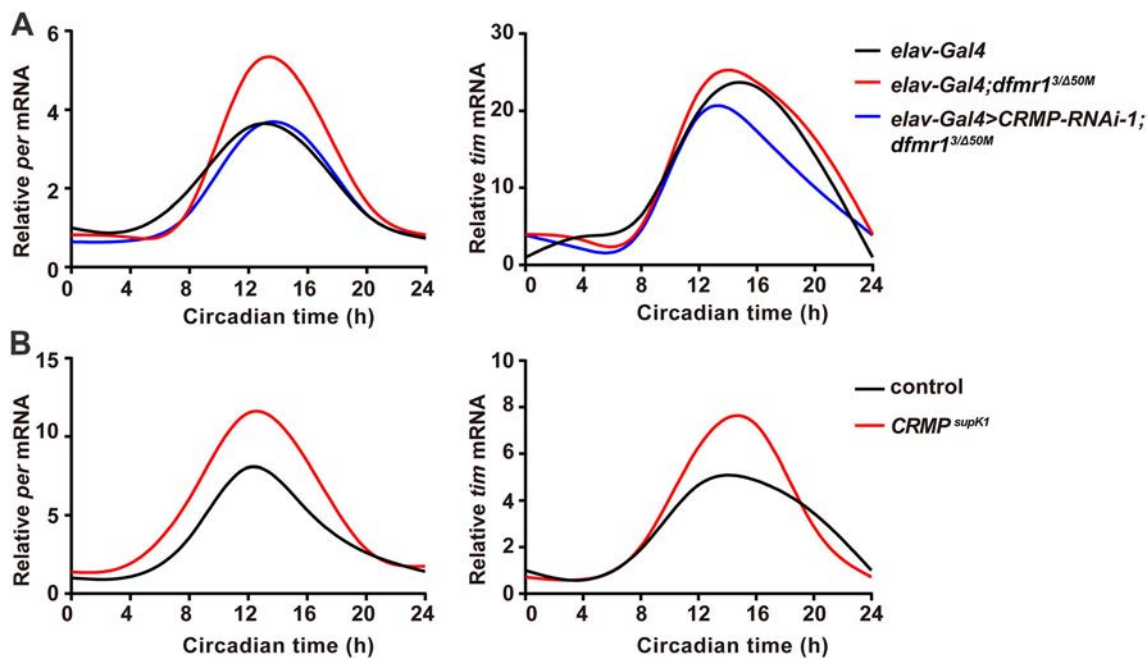


Fig. 3 *CRMP* does not alter the circadian oscillations of *per* and *tim* mRNA expression in FXS flies. **A** Both *dfmr1* mutant flies and *elav-Gal4>CRMP-RNAi-1;dfmr1^{3/Δ50M}* flies show normal circadian oscillations of *per* and *tim* mRNA like control flies. Circadian time (CT) starts at CT0. *dActin* was used as a reference gene. **B** mRNA

expression of *per* and *tim* display normal circadian oscillations in *CRMP* mutant flies like control flies. Circadian time (CT) starts at CT0, *dActin* was used as a reference gene. $n > 10$ heads per genotype at each time point.

circadian locomotor activity rhythm in *Drosophila* [14, 15, 27]. We examined the interaction of FMRP and *CRMP* in the circadian output pathways, using *Dilp2-Gal4* and *pdf-Gal4* to direct expression in IPC cells and in the circadian pacemaker neurons, respectively. Most of the *dfmr1* mutant flies with *Dilp2-Gal4* were arrhythmic compared with the *Dilp2-Gal4* controls. Knocking down *CRMP* in the circadian output IPC neurons with the specific *Dilp2-Gal4*, the free-running activity rhythm was significantly rescued in FXS flies, with elevated relative rhythmic power and an increased percentage of rhythmic flies (Fig. 4A). However, knockdown of *CRMP* by *pdf-Gal4* in the circadian pacemaker LN_v neurons, did not ameliorate the circadian defects (Fig. 4B). Taken together, our findings suggest that the translational regulation of *CRMP* by FMRP contributes to the circadian activity mediation in the output pathway in FXS *Drosophila*.

Interaction and Translational Regulation Between FMRP and *CRMP2* mRNA

Results in *Drosophila* provided evidence for the *in vivo* interaction between FMRP and *CRMP* mRNA, and implied that *CRMP* mRNA may be a target of FMRP. To better illuminate how FMRP controls *CRMP* mRNA in the regulation of circadian behavior and neuronal structures in *Drosophila*, we further analyzed their interaction in human

and mouse cells as well as *Drosophila* S2 cells. In three independent experiments performed in human HEK293 and mouse N2a cells, *CRMP2* mRNA showed a strong association with FMRP. *CRMP2* mRNAs were immunoprecipitated by FMRP but not the negative control IgG (Figs 5A, B and S4A). Experiments in *Drosophila* S2 cells showed similar results (Figs 5C and S4B), and the interaction of *CRMP* and FMRP was also verified in *Drosophila* brains (Fig. S4C).

As FMRP is an mRNA-binding protein mainly regulating the translation of target mRNAs, we tested whether it controls the translation of *CRMP2* mRNAs. We used polyribosome profile analysis to demonstrate the translation activity of *CRMP2*. Eleven fractions separated from the sucrose gradients were pooled into three groups: fractions 1–5 corresponding to messenger ribonucleoprotein (mRNP) and monosomes, fractions 6–7 corresponding to light polyribosomes, and fractions 8–11 corresponding to the most active translating pool of polysomes and associated mRNA (heavy polysomes). The polyribosome profile of *CRMP2* revealed that *CRMP2* mRNAs were associated with translationally-active polyribosomes in both normal and FXS patient-derived lymphoblastoid cells. And *CRMP2* enrichment significantly increased in the polysomal fractions of FXS cells, indicating that the translation activity of *CRMP2* mRNA was elevated in FXS due to the ablation of translational repression by FMRP

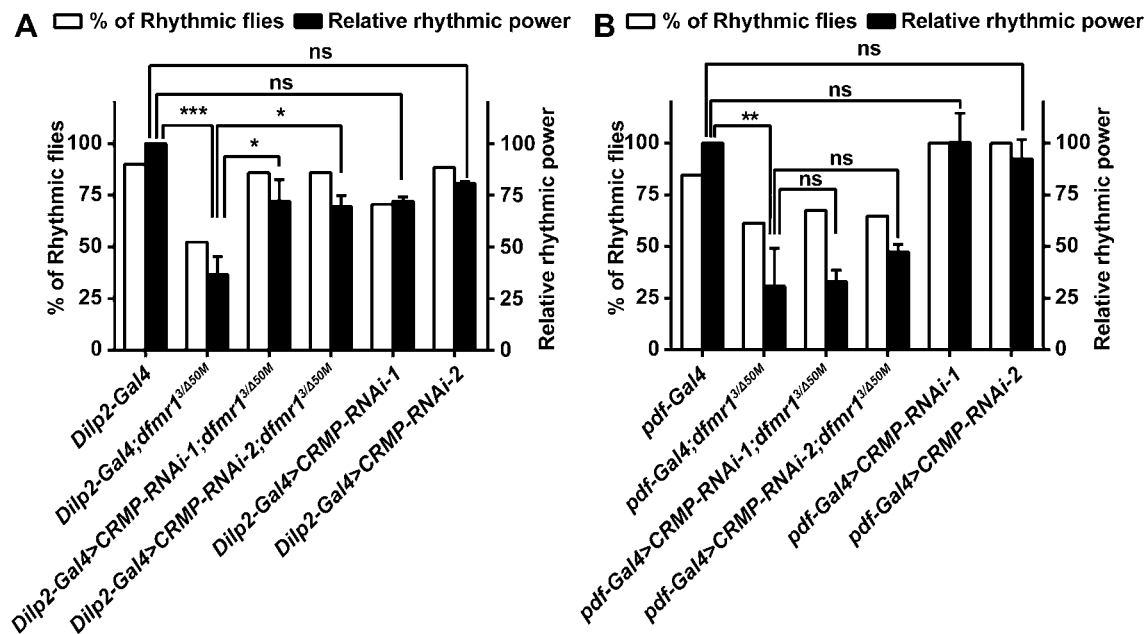


Fig. 4 Knocking down *CRMP* in IPCs rescues locomotor rhythms in FXS flies. The panels show the percentage of rhythmic flies (white) and relative rhythmic power values (black) of the indicated genotypes. **A** *dfmr1* mutants with both *CRMP* RNAi transgenes driven by *Dilp2-Gal4* show significant improvement in circadian locomotor

activity relative to *dfmr1* mutants. **B** *dfmr1* mutants with both *CRMP* RNAi transgenes driven by *pdf-Gal4* show no alterations in circadian behaviors compared with *dfmr1* mutants. * $P < 0.05$, ** $P < 0.01$, *** $P < 0.001$, one-way ANOVA. $n > 30$ flies per genotype. Data are represented as the mean \pm SEM. ns, not significant.

(Figs 5D and S4D). *CRMP2* protein levels and *CRMP2* mRNA levels were assessed, and *CRMP2* protein expression was elevated in FXS lymphoblastoid cells with no difference in mRNA expression between FXS and normal lymphoblastoid cells (Fig. S4E, F). Taken together, these results indicate that FMRP binds with its *CRMP2* mRNA target and represses *CRMP2* translational activity.

Discussion

FMRP binds with target mRNAs and participates in mRNA metabolism including translational regulation, mRNA stability, and dendritic transport. *CRMP2* mRNA has been implicated as a candidate FMRP target in mouse brain and HEK293 cells [28–30], indicating a possible interaction between FMRP and *CRMP2* mRNA. Our results first verified the genetic interaction between FMRP and *CRMP* in the *Drosophila* model of FXS, as demonstrated by the findings that knockdown of *CRMP* expression ameliorated the disrupted circadian activity rhythm and defective neuronal structures in FXS *Drosophila*. Furthermore, biochemical evidence from three different cell lines corroborated that *CRMP2* mRNA was bound to FMRP, which repressed the translation of *CRMP2* mRNA without altering its transcription. Our findings identified *CRMP* as a new target of FMRP, and showed that altered *CRMP*

expression may contribute to the abnormal regulation of behavioral rhythms in FXS *Drosophila*.

FMRP functions in neuronal development and neuronal defects are found in human cortical tissue and FXS animal models. The density of dendritic spines in hippocampal neurons is significantly elevated in FXS mice, and axonal structures in pacemaker neurons are disrupted in FXS *Drosophila* [31, 36, 46–50]. *CRMP2* also plays roles in the regulation of synaptic morphology and functions. Vertebrate *CRMP2* is an important axonal guidance cue that participates in several signal transduction pathways regulating synaptic growth cone dynamics. *CRMP2* promotes microtubule assembly by binding to tubulin heterodimers and promoting tubulin polymerization and facilitates the rate of axonal growth [38]. *CRMP2* is also involved in Numb-mediated endocytosis of the neuronal cell adhesion molecule L1 at the growth cone, promoting the axon elongation [51]. *CRMP2* has been shown to regulate neuronal development and neural function, in addition to its role in neuronal polarity and migration control. *CRMP2*-knockout mice have enlarged lateral ventricles, decreased dendritic spines, and defective synapse formation in the hippocampus [36]. In our study, *CRMP*-deficient flies exhibited axonal process growth defects in both pacemaker sLN_{v,s} and lLN_{v,s}. Consistent with this, axonal process defects in both sLN_{v,s} and lLN_{v,s} in FXS flies were rescued by reduction of *CRMP*, providing evidence that *CRMP* regulates synaptic morphology in FXS *Drosophila*.

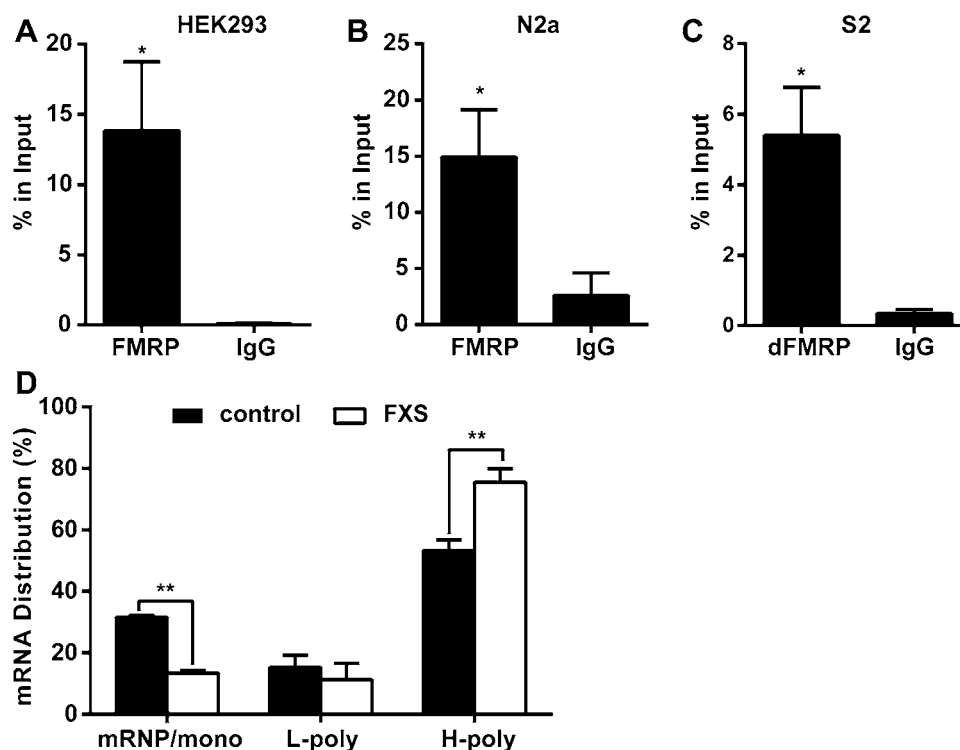


Fig. 5 FMRP interacts with *CRMP2* mRNA and negatively regulates *CRMP2* translation. **A–C** qPCR analysis of *CRMP2* mRNA levels coprecipitated with FMRP in human HEK293 cells (**A**), mouse N2a cells (**B**), and *Drosophila* S2 cells (**C**). *CRMP2* mRNA levels were normalized to the control *C. elegans* 18S rRNA and quantified by the relative value of percentage in input. *CRMP2* mRNAs display an enrichment in FMRP antibody precipitates compared to the negative control IgG (* $P < 0.05$, unpaired *t*-test; $n = 3$ independent experiments). Data are represented as the mean \pm SEM. **D** qRT-PCR quantification analysis of *CRMP2* mRNA levels in fractions of

sucrose gradients from normal and FXS patient-derived lymphoblastoid cells. The sucrose gradient fractions are divided to three groups: fractions 1–5 mRNP/monosomes, fractions 6–7 light polysomes (L-poly), and fractions 8–11 heavy polysomes (H-poly). *CRMP2* mRNAs are increased in the actively translating polyribosomes (H-poly) in FXS cells with a decreased distribution in the mRNP/mono fractions compared with the wild-type (* $P < 0.05$, ** $P < 0.001$, unpaired *t*-test; $n = 3$ independent experiments). Data are represented as the mean \pm SEM.

Sleep problems have been reported in individuals with FXS. Patients mainly have difficulty falling asleep and experience frequent night awakenings, and some have snoring and obstructive sleep apnea [19, 52]. FXS mouse and *Drosophila* models also display sleep disorders, and besides significantly abnormal sleep profiles, impaired rhythmic locomotor activity has been reported in FXS mice and flies [22–24]. Several studies have corroborated the function of FMRP in the circadian output pathway to mediate rest/activity rhythms in *Drosophila*. Clock genes and proteins form the core transcription-translation feedback loop, regulating the output pathways to generate daily rhythms in organisms [1, 4]. The *Drosophila* clock genes *per* and *tim* display circadian oscillations at both the mRNA and protein levels. Loss of FMRP in *Drosophila* does not alter the circadian oscillations of both *per* and *tim* mRNA and proteins. While the core clock is intact and functions normally in FXS *Drosophila*, loss of FMRP disturbs circadian output, including the locomotor activity rhythm and the eclosion rhythm [15, 53, 54]. Furthermore,

FMRP has been shown to function in the IPCs downstream of the clock neurons to regulate circadian behaviors in FXS flies [27]. This evidence, along with the current study, support the hypothesis that, instead of impacting the core circadian clock, FMRP mainly functions in the circadian output pathway to regulate the circadian activity rhythm in *Drosophila*. Previous studies have shown marked structural abnormalities in both ILN_vs and sLN_vs of FXS *Drosophila*. We found that FMRP regulates *CRMP* in the control of the synaptic morphology of LN_vs, while reduction of *CRMP* in LN_vs does not attenuate the rhythmic behavior deficits. Although FMRP controls the structural morphology of LN_v axons, loss of FMRP has no evident effect on their rhythmic release of PDF neuropeptide. Moreover, Monyak *et al.* reported that FMRP functions mainly in the IPCs by restoring *dfmr1* expression through *Gal4* expressed in both clock neurons and downstream IPCs [27]. It will take further efforts to illustrate how the structural defects in LN_vs contribute to the functional abnormality in downstream IPCs. While specifically knocking down *CRMP*

expression in IPCs rescues the circadian activity rhythms, our findings show that dysregulated *CRMP* in IPCs contributes to the circadian output in FXS *Drosophila*.

Circadian rhythms are an emergent property of the intrinsic clock network. Interdependent clock neuron populations and output circuits are both required to maintain normal behavioral and physiological rhythms. Proper neuronal activity and synaptic connections are essential for the functional circadian neural circuit, which is fundamental to circadian rhythms in behavior [55–57]. The pars intercerebralis (PI) region of the *Drosophila* brain has been implicated in the circadian output regulation of locomotor behaviors. DH44+ SIFamide+ subsets of PI neurons comprise part of a circuit extending from sLN_vs and passing through DN1 neurons, involved in the regulation of behavioral rhythms [55, 56, 58]. IPC cells are a cluster of insulin-producing neurons in the PI, and are also functionally connected to the clock circuit *via* synaptic contacts with DN1 [55, 59]. It has been reported that IPCs exhibit circadian patterns of neuronal activity, including firing frequency and proportion of bursting, and that the electrophysiological rhythm of IPCs is controlled by the circadian clock [59]. In line with previous evidence, our findings show that FMRP mediates behavioral rhythms through the translational regulation of *CRMP* mRNA in IPCs in FXS *Drosophila*.

Acknowledgements This work was supported by the Hunan Science and Technology major project of Birth Defect Cooperative Control (2019SK1010), the National Natural Science Foundation of China (81571253 and 81771385), the Hunan Provincial Natural Science Foundation (2016JJ3135), and the Changsha Municipal Natural Science Foundation (kq2007073).

Conflict of interest The authors declare no conflict of interest.

References

- Musiek ES, Holtzman DM. Mechanisms linking circadian clocks, sleep, and neurodegeneration. *Science* 2016, 354: 1004–1008.
- Dubowy C, Sehgal A. Circadian rhythms and sleep in *drosophila melanogaster*. *Genetics* 2017, 205: 1373–1397.
- Top D, Young MW. Coordination between differentially regulated circadian clocks generates rhythmic behavior. *Cold Spring Harb Perspect Biol* 2018, 10. <https://doi.org/10.1101/cshperspect.a033589>.
- Franco DL, Frenkel L, Ceriani MF. The underlying genetics of *drosophila* circadian behaviors. *Physiology (Bethesda)* 2018, 33: 50–62.
- Bu B, He W, Song L, Zhang L. Nuclear envelope protein MAN1 regulates the *drosophila* circadian clock via period. *Neurosci Bull* 2019, 35: 969–978.
- Lu Y, Zhu ZG, Ma QQ, Su YT, Han Y, Wang X. A critical time-window for the selective induction of hippocampal memory consolidation by a brief episode of slow-wave sleep. *Neurosci Bull* 2018, 34: 1091–1099.
- Heyde I, Kiehn JT, Oster H. Mutual influence of sleep and circadian clocks on physiology and cognition. *Free Radic Biol Med* 2018, 119: 8–16.
- Coulson RL, LaSalle JM. Epigenetics of circadian rhythms in imprinted neurodevelopmental disorders. *Prog Mol Biol Transl Sci* 2018, 157: 67–92.
- Allen CN, Nitabach MN, Colwell CS. Membrane currents, gene expression, and circadian clocks. *Cold Spring Harb Perspect Biol* 2017, 9. <https://doi.org/10.1101/cshperspect.a027714>.
- Lassi G, Priano L, Maggi S, Garcia-Garcia C, Balzani E, El-Assawy N, *et al.* Deletion of the Snord116/SNORD116 alters sleep in mice and patients with Prader-Willi syndrome. *Sleep* 2016, 39: 637–644.
- Buiting K, Williams C, Horsthemke B. Angelman syndrome - insights into a rare neurogenetic disorder. *Nat Rev Neurol* 2016, 12: 584–593.
- Powell WT, Coulson RL, Crary FK, Wong SS, Ach RA, Tsang P, *et al.* A Prader-Willi locus lncRNA cloud modulates diurnal genes and energy expenditure. *Hum Mol Genet* 2013, 22: 4318–4328.
- Shi SQ, Bichell TJ, Ihrle RA, Johnson CH. Ube3a imprinting impairs circadian robustness in Angelman syndrome models. *Curr Biol* 2015, 25: 537–545.
- Inoue S, Shimoda M, Nishinokubi I, Siomi MC, Okamura M, Nakamura A, *et al.* A role for the *drosophila* fragile X-related gene in circadian output. *Curr Biol* 2002, 12: 1331–1335.
- Dockendorff TC, Su HS, McBride SM, Yang Z, Choi CH, Siwicki KK, *et al.* *Drosophila* lacking *dfmr1* activity show defects in circadian output and fail to maintain courtship interest. *Neuron* 2002, 34: 973–984.
- Li JZ, Bunney BG, Meng F, Hagenauer MH, Walsh DM, Vawter MP, *et al.* Circadian patterns of gene expression in the human brain and disruption in major depressive disorder. *Proc Natl Acad Sci U S A* 2013, 110: 9950–9955.
- Wang XL, Yuan K, Zhang W, Li SX, Gao GF, Lu L. Regulation of circadian genes by the MAPK pathway: implications for rapid antidepressant action. *Neurosci Bull* 2020, 36: 66–76.
- Davis JK, Broadie K. Multifarious functions of the fragile X mental retardation protein. *Trends Genet* 2017, 33: 703–714.
- Hagerman RJ, Berry-Kravis E, Hazlett HC, Bailey DB Jr, Moine H, Kooy RF, *et al.* Fragile X syndrome. *Nat Rev Dis Primers* 2017, 3: 17065. <https://doi.org/10.1038/nrdp.2017.65>.
- Berry-Kravis EM, Lindemann L, Jonch AE, Apostol G, Bear MF, Carpenter RL, *et al.* Drug development for neurodevelopmental disorders: lessons learned from fragile X syndrome. *Nat Rev Drug Discov* 2018, 17: 280–299.
- Dahlhaus R. Of Men and Mice: Modeling the fragile X syndrome. *Front Mol Neurosci* 2018, 11: 41. <https://doi.org/10.3389/fnmol.2018.00041>.
- Zhang J, Fang Z, Jud C, Vansteensel MJ, Kaasik K, Lee CC, *et al.* Fragile X-related proteins regulate mammalian circadian behavioral rhythms. *Am J Hum Genet* 2008, 83: 43–52.
- Sare RM, Harkless L, Levine M, Torossian A, Sheeler CA, Smith CB. Deficient sleep in mouse models of fragile X syndrome. *Front Mol Neurosci* 2017, 10: 280. <https://doi.org/10.3389/fnmol.2017.00280>.
- Bushey D, Tononi G, Cirelli C. The *drosophila* fragile X mental retardation gene regulates sleep need. *J Neurosci* 2009, 29: 1948–1961.
- Reeve SP, Bassetto L, Genova GK, Kleyner Y, Leyssen M, Jackson FR, *et al.* The *drosophila* fragile X mental retardation protein controls actin dynamics by directly regulating profilin in the brain. *Curr Biol* 2005, 15: 1156–1163.
- McBride SM, Choi CH, Wang Y, Liebelt D, Braunstein E, Ferreira D, *et al.* Pharmacological rescue of synaptic plasticity,

- courtship behavior, and mushroom body defects in a *drosophila* model of fragile X syndrome. *Neuron* 2005, 45: 753–764.
27. Monyak RE, Emerson D, Schoenfeld BP, Zheng X, Chambers DB, Rosenfelt C, *et al.* Insulin signaling misregulation underlies circadian and cognitive deficits in a *drosophila* fragile X model. *Mol Psychiatry* 2017, 22: 1140–1148.
 28. Darnell JC, Van Driesche SJ, Zhang C, Hung KY, Mele A, Fraser CE, *et al.* FMRP stalls ribosomal translocation on mRNAs linked to synaptic function and autism. *Cell* 2011, 146: 247–261.
 29. Ascano M Jr, Mukherjee N, Bandaru P, Miller JB, Nusbaum JD, Corcoran DL, *et al.* FMRP targets distinct mRNA sequence elements to regulate protein expression. *Nature* 2012, 492: 382–386.
 30. Maurin T, Lebrigand K, Castagnola S, Paquet A, Jarjat M, Popa A, *et al.* HITS-CLIP in various brain areas reveals new targets and new modalities of RNA binding by fragile X mental retardation protein. *Nucleic Acids Res* 2018, 46: 6344–6355.
 31. Sethna F, Feng W, Ding Q, Robison AJ, Feng Y, Wang H. Enhanced expression of ADCY1 underlies aberrant neuronal signalling and behaviour in a syndromic autism model. *Nat Commun* 2017, 8: 14359. <https://doi.org/10.1038/ncomms14359>.
 32. Westmark CJ, Malter JS. FMRP mediates mGluR5-dependent translation of amyloid precursor protein. *PLoS Biol* 2007, 5: e52. <https://doi.org/10.1371/journal.pbio.0050052>.
 33. Zhang YQ, Bailey AM, Matthies HJ, Renden RB, Smith MA, Speese SD, *et al.* *Drosophila* fragile X-related gene regulates the MAPIB homolog Futsch to control synaptic structure and function. *Cell* 2001, 107: 591–603.
 34. Morris DH, Dubnau J, Park JH, Rawls JM Jr. Divergent functions through alternative splicing: the *drosophila* CRMP gene in pyrimidine metabolism, brain, and behavior. *Genetics* 2012, 191: 1227–1238.
 35. Ip JP, Fu AK, Ip NY. CRMP2: functional roles in neural development and therapeutic potential in neurological diseases. *Neuroscientist* 2014, 20: 589–598.
 36. Zhang H, Kang E, Wang Y, Yang C, Yu H, Wang Q, *et al.* Brain-specific Crmp2 deletion leads to neuronal development deficits and behavioural impairments in mice. *Nat Commun* 2016, 7. <https://doi.org/10.1038/ncomms11773>.
 37. Fang W, Gao G, Zhao H, Xia Y, Guo X, Li N, *et al.* Role of the Akt/GSK-3beta/CRMP-2 pathway in axon degeneration of dopaminergic neurons resulting from MPP+ toxicity. *Brain Res* 2015, 1602: 9–19.
 38. Fukata Y, Itoh TJ, Kimura T, Menager C, Nishimura T, Shiromizu T, *et al.* CRMP-2 binds to tubulin heterodimers to promote microtubule assembly. *Nat Cell Biol* 2002, 4: 583–591.
 39. Nishimura T, Fukata Y, Kato K, Yamaguchi T, Matsuura Y, Kamiguchi H, *et al.* CRMP-2 regulates polarized Numb-mediated endocytosis for axon growth. *Nat Cell Biol* 2003, 5: 819–826.
 40. Tan M, Cha C, Ye Y, Zhang J, Li S, Wu F, *et al.* CRMP4 and CRMP2 interact to coordinate cytoskeleton dynamics, regulating growth cone development and axon elongation. *Neural Plast* 2015, 2015: 947423. <https://doi.org/10.1155/2015/947423>.
 41. Janusz A, Milek J, Perycz M, Pacini L, Bagni C, Kaczmarek L, *et al.* The Fragile X mental retardation protein regulates matrix metalloproteinase 9 mRNA at synapses. *J Neurosci* 2013, 33: 18234–18241.
 42. Muddashetty RS, Kelic S, Gross C, Xu M, Bassell GJ. Dysregulated metabotropic glutamate receptor-dependent translation of AMPA receptor and postsynaptic density-95 mRNAs at synapses in a mouse model of fragile X syndrome. *J Neurosci* 2007, 27: 5338–5348.
 43. Gatto CL, Broadie K. Temporal requirements of the fragile X mental retardation protein in modulating circadian clock circuit synaptic architecture. *Front Neural Circuits* 2009, 3: 8. <https://doi.org/10.3389/neuro.04.008.2009>.
 44. Fernandez MP, Berni J, Ceriani MF. Circadian remodeling of neuronal circuits involved in rhythmic behavior. *PLoS Biol* 2008, 6: e69. <https://doi.org/10.1371/journal.pbio.0060069>.
 45. Li Q, Li Y, Wang X, Qi J, Jin X, Tong H, *et al.* Fbx14 Serves as a clock output molecule that regulates sleep through promotion of rhythmic degradation of the GABAA receptor. *Curr Biol* 2017, 27(3616–3625): e3615.
 46. Hinton VJ, Brown WT, Wisniewski K, Rudelli RD. Analysis of neocortex in three males with the fragile X syndrome. *Am J Med Genet* 1991, 41: 289–294.
 47. Galvez R, Greenough WT. Sequence of abnormal dendritic spine development in primary somatosensory cortex of a mouse model of the fragile X mental retardation syndrome. *Am J Med Genet A* 2005, 135: 155–160.
 48. Aloisi E, Le Corf K, Dupuis J, Zhang P, Ginger M, Labrousse V, *et al.* Altered surface mGluR5 dynamics provoke synaptic NMDAR dysfunction and cognitive defects in Fmr1 knockout mice. *Nat Commun* 2017, 8: 1103. <https://doi.org/10.1038/s41467-017-01191-2>.
 49. Dolen G, Osterweil E, Rao BS, Smith GB, Auerbach BD, Chattarji S, *et al.* Correction of fragile X syndrome in mice. *Neuron* 2007, 56: 955–962.
 50. Zhang K, Li YJ, Guo Y, Zheng KY, Yang Q, Yang L, *et al.* Elevated progranulin contributes to synaptic and learning deficit due to loss of fragile X mental retardation protein. *Brain* 2017, 140: 3215–3232.
 51. Arimura N, Menager C, Kawano Y, Yoshimura T, Kawabata S, Hattori A, *et al.* Phosphorylation by Rho kinase regulates CRMP-2 activity in growth cones. *Mol Cell Biol* 2005, 25: 9973–9984.
 52. Kronk R, Bishop EE, Raspa M, Bickel JO, Mandel DA, Bailey DB Jr. Prevalence, nature, and correlates of sleep problems among children with fragile X syndrome based on a large scale parent survey. *Sleep* 2010, 33: 679–687.
 53. Morales J, Hiesinger PR, Schroeder AJ, Kume K, Verstreken P, Jackson FR, *et al.* *Drosophila* fragile X protein, DFXR, regulates neuronal morphology and function in the brain. *Neuron* 2002, 34: 961–972.
 54. Xu S, Poidevin M, Han E, Bi J, Jin P. Circadian rhythm-dependent alterations of gene expression in *drosophila* brain lacking fragile X mental retardation protein. *PLoS One* 2012, 7: e37937. <https://doi.org/10.1371/journal.pone.0037937>.
 55. Cavanaugh DJ, Geratowski JD, Wooltorton JR, Spaethling JM, Hector CE, Zheng X, *et al.* Identification of a circadian output circuit for rest: activity rhythms in *drosophila*. *Cell* 2014, 157: 689–701.
 56. Cavey M, Collins B, Bertet C, Blau J. Circadian rhythms in neuronal activity propagate through output circuits. *Nat Neurosci* 2016, 19: 587–595.
 57. Guo C, Pan Y, Gong Z. Recent advances in the genetic dissection of neural circuits in *drosophila*. *Neurosci Bull* 2019, 35: 1058–1072.
 58. Dreyer AP, Martin MM, Fulgham CV, Jabr DA, Bai L, Beshel J, *et al.* A circadian output center controlling feeding: fasting rhythms in *drosophila*. *PLoS Genet* 2019, 15: e1008478. <https://doi.org/10.1371/journal.pgen.1008478>.
 59. Barber AF, Erion R, Holmes TC, Sehgal A. Circadian and feeding cues integrate to drive rhythms of physiology in *drosophila* insulin-producing cells. *Genes Dev* 2016, 30: 2596–2606.



Homeobox Gene *Six3* is Required for the Differentiation of D2-Type Medium Spiny Neurons

Xiaolei Song¹ · Haotian Chen¹ · Zicong Shang¹ · Heng Du¹ · Zhenmeiyu Li¹ · Yan Wen¹ · Guoping Liu¹ · Dashi Qi¹ · Yan You¹ · Zhengang Yang¹ · Zhuangzhi Zhang¹ · Zhejun Xu¹

Received: 5 May 2020 / Accepted: 9 January 2021 / Published online: 20 May 2021
© The Author(s) 2021

Abstract Medium spiny neurons (MSNs) in the striatum, which can be divided into D1 and D2 MSNs, originate from the lateral ganglionic eminence (LGE). Previously, we reported that *Six3* is a downstream target of *Sp8/Sp9* in the transcriptional regulatory cascade of D2 MSN development and that conditionally knocking out *Six3* leads to a severe loss of D2 MSNs. Here, we showed that *Six3* mainly functions in D2 MSN precursor cells and gradually loses its function as D2 MSNs mature. Conditional deletion of *Six3* had little effect on cell proliferation but blocked the differentiation of D2 MSN precursor cells. In addition, conditional overexpression of *Six3* promoted the differentiation of precursor cells in the LGE. We measured an increase of apoptosis in the postnatal striatum of conditional *Six3*-knockout mice. This suggests that, in the absence of *Six3*, abnormally differentiated D2 MSNs are eliminated by programmed cell death. These results further identify *Six3* as an important regulatory element during D2 MSN differentiation.

Keywords *Six3* · LGE · *Drd2* · striatum · Medium spiny neuron

Introduction

The basal ganglia consist of several interconnected nuclei, the largest of which is the striatum [1, 2]. Abnormal functions of the striatum are closely associated with Huntington's disease and Parkinson's disease [2–4]. The striatum can be divided into the dorsal and ventral parts [2, 5]. The dorsal striatum comprises the caudate nucleus and putamen, while the ventral striatum includes the nucleus accumbens and olfactory tubercles [6]. Medium spiny neurons (MSNs) constitute as many as 90%–95% of striatal neurons. Also, MSNs can be divided into direct-pathway MSNs, which specifically express dopamine receptor D1 (*Drd1*), and indirect-pathway MSNs, which specifically express dopamine receptor D2 (*Drd2*), according to their axonal projections [7, 8]. Both DRD1- and DRD2-expressing MSNs (D1 and D2 MSNs) have distinct molecular features. For example, D1 MSNs express *Ebf1*, *Isl1*, and *Tac1*, while D2 MSNs specifically express *Adora2a* and *Penk* [8–11].

The ventral lateral ganglionic eminence (vLGE) is the origin of striatal MSNs, while the dorsal LGE (dLGE) mainly generates olfactory bulb interneurons [12, 13]. Based on gene-expression patterns, it has been suggested that the vLGE can be divided into the pLGE3 and pLGE4 (progenitor LGE), and the dLGE can be divided into the pLGE1 and pLGE2 [14]. A variety of transcription factors regulate the development of the LGE. In the dLGE, *Pax6* regulates the development of neurons expressing tyrosine hydroxylase in the olfactory bulb [15, 16]. *Sp8* and *Sp9* are required for the production and survival, as well as the tangential and radial migration of interneurons in the olfactory bulb [12]. In the vLGE, early overexpression of the *Gsx2* gene induces the generation of striatal MSNs. *Gsx2*-null mutants have significantly reduced generation of

Xiaolei Song and Haotian Chen have contributed equally to this work

✉ Zhuangzhi Zhang
zz_zhang@fudan.edu.cn

✉ Zhejun Xu
14111520028@fudan.edu.cn

¹ Institute of Pediatrics, Children's Hospital of Fudan University, State Key Laboratory of Medical Neurobiology and Ministry of Education Frontiers Center for Brain Science, Institutes of Brain Science, Fudan University, Shanghai 200032, China

striatal MSNs [17, 18]. Progenitor cell differentiation is blocked in the LGE subventricular zone (SVZ) of *Dlx1/2* mutant mice [19, 20]. D1 and D2 MSNs are also regulated by specific transcription factors. *Isl1*, *Ebf1*, and *Zfhx3* regulate the development of D1 MSNs [9, 21–24]. Recently, we reported that *Sp8* and *Sp9* are coordinated to regulate D2 MSN generation, differentiation, and survival. *Six3* expression in the LGE is significantly decreased in *Sp8*- and *Sp9*-knockout mice. Accordingly, conditional knockout of *Six3* results in a significant reduction in the number of D2 MSNs, similar to the phenotype in the striatum of *Sp8*- and *Sp9*-knockout mice [25, 26].

The homeobox transcription factor *Six3*, which contains a conserved Six domain and a Six-type homeobox domain, belongs to the *Six* gene family [27]. *Six3* is expressed as early as E6.5–E7.0 at the most anterior region of the embryo and plays important roles in the development of the forebrain and visual system [28–31]. Mutation of *Six3* causes holoprosencephaly [32, 33]. *Six3* is also expressed in ependymal cells, and its dysfunction leads to the inability of ependymal cells to inhibit radial glial activity, which leads to developmental defects of the lateral ventricle wall and abnormal neuroblast migration and differentiation [34]. As a direct downstream target of SP9 and SP8, the transcription factor *Six3* is required for the production of D2 MSNs [26], but the cellular and molecular mechanisms were unknown.

In this study, we investigated the mechanism underlying the effect of a reduction in the number of D2 MSNs in *Dlx5/6-CIE*, *Six3*^{fllox/fllox} (referred to as *Six3*-cKO) mice. We found that knocked out *Six3* in progenitor cells using *Nestin-Cre* line resulted in severe D2 MSN developmental defect, consistent with the results of *Dlx5/6-CIE* line, but not in *Drd2-Cre* line, which eliminate *Six3* in immature D2 MSNs, indicating *Six3* primarily function in progenitor cells at embryonic stage. The reduction in the number of D2 MSNs in *Six3*-cKO mice mainly ascribe to the abnormal differentiation, but not proliferation defect, of progenitor cells, identifying *Six3* as an important regulatory element of MSN development. These findings broaden our comprehension of the transcriptional mechanisms underlying the development of striatal projection neurons.

Materials and Methods

Animals

All experiments were performed in accordance with the National Institutes of Health Guide for the Care and Use of Laboratory Animals and were approved by Animal Ethics Committee of Fudan University. We generated mice that

conditionally overexpressed *Six3* by knocking *CAG-promoter-Flox-STOP-Flox-Six3-IRES-LacZ* into the *Rosa26* locus. *Dlx5/6-CIE* [35], *Nestin-Cre* [36, 37], *Six3* floxed [26, 38], and *Drd2-Cre* mice (from the Mutant Mouse Resource and Research Center) [39] were previously described. Wild-type, *Dlx5/6-CIE*, *Drd2-Cre*; *Six3*^{F/+} and *Six3* floxed littermate mice without the *Cre* allele were used as controls. These mice were on mixed genetic backgrounds of C57BL/6J, 129S6, and CD1. The day on which a vaginal plug was detected was considered embryonic day 0.5 (E0.5), and the day of birth was calculated as postnatal day 0 (P0).

BrdU Labeling

Pregnant mice were pulsed with 5-bromo-2'-deoxyuridine (BrdU) (50 mg/kg body weight) on E14.5 or E16.5 and embryos were collected and analyzed 30 min after administration.

Immunohistochemistry

Immunohistochemistry was performed as previously described [26]. Briefly, postnatal and embryonic brains were collected and placed in 4% paraformaldehyde overnight at 4 °C, cryoprotected in 30% sucrose for at least 24 h, frozen in optimal cutting temperature and cryosectioned. All tissues were sectioned coronally at 12 or 20 μm and stained on glass slides.

For SP9, BCL11B, and SIX3 immunohistochemistry, sections were boiled briefly in 10 mmol/L sodium citrate for antigen retrieval. Immunohistochemistry for BrdU⁺ cells was performed after 45 min of incubation in 2 N HCl and rinsing twice in 0.1 mol/L borate buffer at room temperature. Immunofluorescence labeling was performed with the following primary antibodies: rat anti-BCL11B (Abcam, Ab18465), rat anti-BrdU (Accurate Chemical, OBT0030s), chicken anti-β-gal (Abcam, ab9361), rabbit anti-cleaved Caspase-3 (Cell Signaling, #9661), rabbit anti-CRE (Millipore, 69050-3), rabbit anti-EBF1 (Merck, AB10523), rabbit anti-FOXP1 (Abcam, Ab16645), rabbit anti-KI67 (Abcam, ab15580), mouse anti-SIX3 (Santa Cruz Biotechnology, sc-398797), goat anti-SP8 (Santa Cruz Biotechnology, sc-104661), rabbit anti-SP9 [25]. Appropriate Alexa Fluor 488-, Cy3- or Alexa Fluor 647-conjugated secondary antibodies from Jackson ImmunoResearch were used.

In situ RNA Hybridization

In situ hybridization was performed on 20-μm cryostat sections as previously described using digoxigenin-labeled

riboprobes [25, 26]. Riboprobes were amplified by PCR using the following primers:

Drd2 forward: CGGGAGCTGGAAGCCTCGA
Drd2 reverse: TGCAGGGTCAAGAGAAGGCCG
Adora2a forward: ATGGGCTCCTCGGTGTACATCA
 TG
Adora2a reverse: TCAGGAAGGGGCAAACCTCTGAA
 GAC
Drd1 forward: ATGGCTCCTAACACTTCTACCATGG
Drd1 reverse: TCAGGTTGAATGCTGTCCGCTGTG
Tac1 forward: CCCCTGAACGCACTATCTATTC
Tac1 reverse: TAGAGTCAAATACCGAAGTCTCAG
Ebf1 forward: TGACATGAGTCCCAGAGTGGAACTT
Ebf1 reverse: CACTTCATTCTCCCCTTCCATAGCT
Isl1 forward: TACGGGATCAAATGCGCCAA
Isl1 reverse: ACTCAGTACTTTCCAGGGCG
Six3OS forward: GGCCGCGCCTTGTAAGCGCTA
Six3OS reverse: GTTGAGAATCAGTCTGGGGTCCGC

Microscopy

Images were captured using an Olympus BX 51 microscope or an Olympus FV1000 confocal microscope system. FV10-ASW software was used to reconstruct the Z-stack confocal images. All images were merged, cropped, and optimized equally using Adobe Photoshop CC.

Quantification and Statistics

The numbers of *Drd2*⁻, *Adora2a*⁻, *Drd1*⁻, and *Tac1*⁻ positive cells in the striatum were counted in 3 randomly-chosen 20- μ m sections from each mouse. Three or four control and *Six3* conditional knockout mice from each group were analyzed at P11.

The number of FOXP1⁺ cells and the integrated density of *Ebf1* and *Isl1* measured by ImageJ in the LGE SVZ were quantified in 3 randomly-chosen 12- μ m or 20- μ m sections from each mouse. Three or four *Dlx5/6-CIE* control and *Six3*-cKO mice from each group were analyzed at E16.5.

The numbers of BCL11B⁺ and BCL11B⁺/EBF1⁺ cells in the striatum was counted in 3 randomly-chosen 12- μ m sections from each mouse. Three *Dlx5/6-CIE* control and *Six3*-cKO mice from each group were analyzed at P0.

The number of FOXP1⁺ cells and the integrated density of BCL11B measured by ImageJ in the LGE SVZ were quantified in 3 randomly-chosen 12- μ m sections from each mouse, and three *Dlx5/6-CIE* control and *Dlx5/6-CIE*, *Rosa-Six3OE/+* mice from each group were analyzed at E14.5 and E16.5.

The numbers of BrdU⁺ and KI67⁺ cells in the LGE were counted in 3 randomly-chosen 20- μ m sections from each mouse, and 3 control and *Six3*-cKO mice from each group were analyzed at E14.5 or E16.5.

The numbers of SP8⁺ and SP9⁺ cells in the LGE SVZ were counted in 3 randomly-chosen 12- μ m sections from each mouse. Three or four *Dlx5/6-CIE* control and *Six3*-cKO mice from each group were analyzed at E14.5 or E16.5. The integrated density of *Six3OS*, *Adora2a*, and *Drd2* measured by ImageJ in the LGE or striatum were quantified in 3 randomly chosen 20 μ m sections from each mouse. Three or four *Dlx5/6-CIE* control and *Six3*-cKO mice from each group were analyzed at E16.5 or P0.

The number of cleaved Caspase-3⁺ cells in the striatum was counted in 3 randomly-chosen 20- μ m sections from each mouse, and 3 *Dlx5/6-CIE* control and *Six3*-cKO mice from each group were analyzed at P0, P3, P7, and P11.

Statistical significance was determined using unpaired Student's *t*-test (**P* < 0.05, ***P* < 0.01, and ****P* < 0.001). The results are presented as the mean + SEM.

Results

Six3 Mainly Functions in D2 MSN Precursor Cells

We previously reported that the number of striatal D2 MSNs is significantly decreased in *Six3* conditional knockout mice [26]. We crossed *Six3* floxed mice with *Nestin-Cre* and *Drd2-Cre* lines to further examine the function of *Six3* (Fig. 1). According to our previously published paper, SIX3 is prominently expressed in the pLGE3 domain of the SVZ and scattered in the LGE mantle zone (MZ) at the embryonic stage. Its expression is later than that of *Sp9* but earlier than that of *Drd2-EGFP*. The expression of *Six3* is rapidly down-regulated in the striatum at the postnatal stage [26]. The *Nestin-Cre* line, in which *Six3* was knocked out earlier than in *Dlx5/6-CIE* mice, expressed CRE protein in neural stem cells in the LGE [40–42], whereas in the *Drd2-Cre* line, *Six3* was deleted in immature D2 MSNs after it was expressed for a short time, as *Drd2* was expressed later than *Six3* in the LGE [26]. At P11, the volume of the lateral ventricles was increased while that of the striatum was reduced in *Nestin-Cre*, *Six3*^{F/F} mice compared with wild-type control mice (Fig. 1A). This is consistent with our previous results [26]. The numbers of *Drd2*⁺ and *Adora2a*⁺ MSNs in the striatum of *Nestin-Cre*, *Six3*^{F/F} mice were greatly decreased compared with those in control mice. The reductions of *Drd2*⁺ and *Adora2a*⁺ MSNs mainly occurred in the medial striatum, indicating that the generation of late-born D2 MSNs was compromised in *Nestin-Cre*, *Six3*^{F/F} mice (Fig. 1A). The numbers of *Drd1*⁺ and *Tac1*⁺ cells, though significantly decreased, were relatively less affected (Fig. 1A). These decreased *Drd1*⁺ and *Tac1*⁺ cells might be ascribed to an ependymal cell defect since the development of ependymal cells was disturbed in *Nestin-Cre*,

Six3^{F/F} mice [34]. In contrast, *Drd2*⁺, *Adora2a*⁺ and *Drd1*⁺, and *Tac1*⁺ MSNs were densely distributed in the striatum of both *Drd2-Cre*, *Six3*^{F/F} mice and *Drd2-Cre*, *Six3*^{F/+} control mice at P11 (Fig. 1B). The numbers of both D1 and D2 MSNs were comparable in *Drd2-Cre*, *Six3*^{F/+} mice and *Drd2-Cre*, *Six3*^{F/+} control mice at P11 (Fig. 1B).

This indicates that the development of D2 MSNs is unaffected when *Six3* function is blocked in immature D2 MSNs. These results suggest that *Six3* mainly functions before D2 MSNs differentiate and gradually loses its function as they mature.

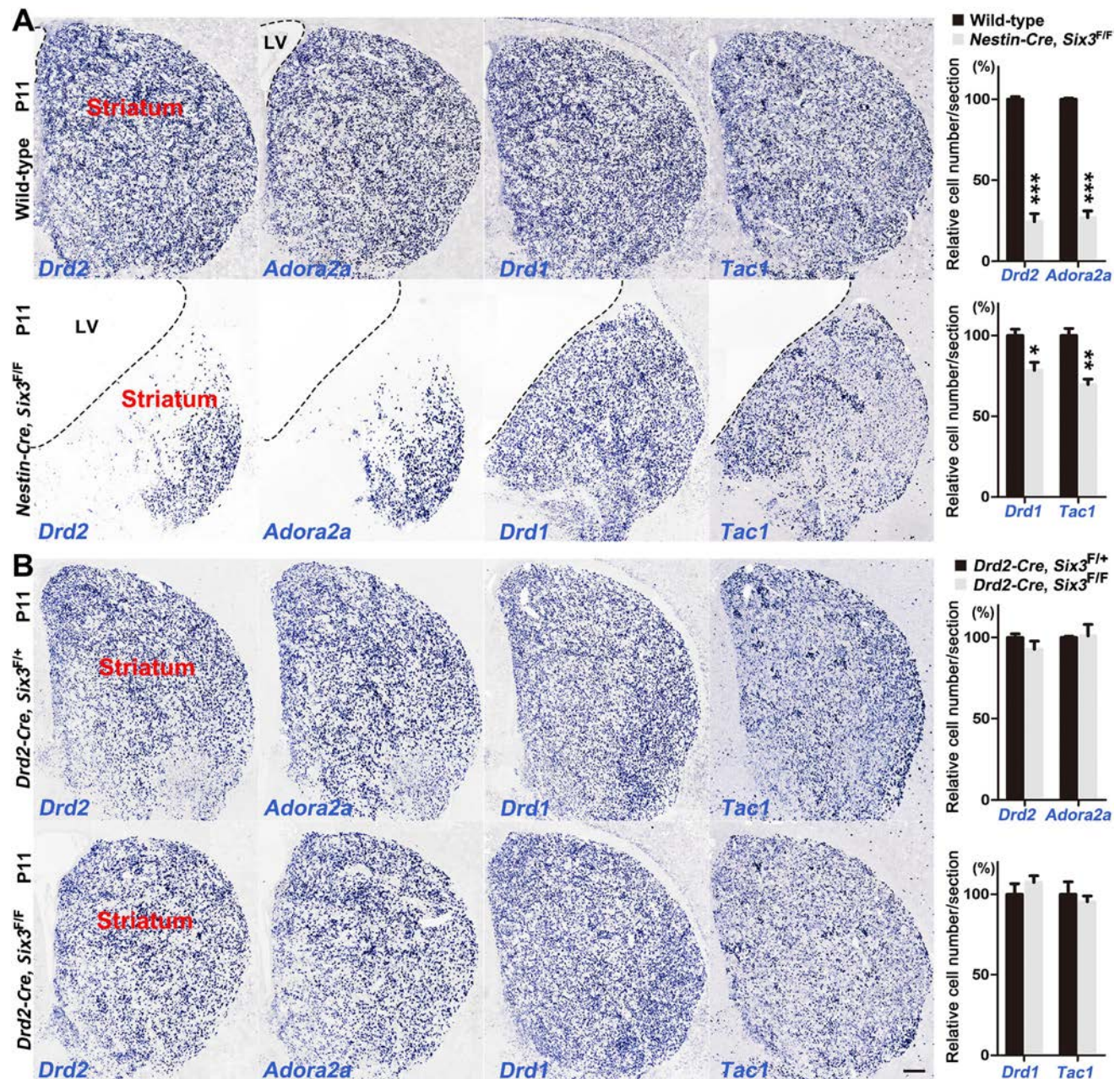


Fig. 1 *Six3* mainly functions in D2 MSN precursor cells. **A** Left panels, *in situ* RNA hybridization for *Drd2*, *Adora2a*, *Drd1* and *Tac1* in the striatum of wild-type control and *Nestin-Cre*, *Six3*^{F/F} mice at P11. Note that most of the *Drd2*⁺ and *Adora2a*⁺ cells in the medial LGE of *Nestin-Cre*, *Six3*^{F/F} mice were lost. Right panel, quantification of *Drd2*, *Adora2a*, *Drd1* and *Tac1* ($n = 3-4$). The dotted lines indicate the border of the lateral ventricle (LV) and striatum. **B** Left panels,

in situ hybridization for *Drd2*, *Adora2a*, *Drd1* and *Tac1* in the striatum of control and *Drd2-Cre*, *Six3*^{F/F} mice at P11. Note that the development of both D1 and D2 MSNs was unaffected in the striatum of *Drd2-Cre*, *Six3*^{F/F} mice compared to the controls (*Drd2-Cre*, *Six3*^{F/+}). Right panel, quantification of *Drd2*, *Adora2a*, *Drd1*, and *Tac1* ($n = 3-4$). Data shown are the mean + SEM (* $P < 0.05$, ** $P < 0.01$, *** $P < 0.001$, Student's *t*-test; scale bar, 200 μm).

D2 MSN Neurogenesis is Reduced in the LGE SVZ of *Six3*-cKO Mice

To investigate the cause of the significant reduction in the number of striatal D2 MSNs in the absence of *Six3*, we further examined neurogenesis in the striatum of *Six3*-cKO and *Dlx5/6-CIE* control mice. The LGE SVZ at later developmental stages contains proliferating cells and differentiated cells [43]. FOXP1⁺ cells in the LGE SVZ are differentiated newborn MSNs [44]. We found that the expression of FOXP1 in the LGE SVZ was severely reduced in *Six3*-cKO mice compared to control mice at E16.5 (Fig. 2A), indicating a reduction of neurogenesis in both D1 and D2 MSNs. Consistent with this result, we found that the D1 MSN-specific marker *Ebf1* [9] was significantly reduced in the LGE SVZ of *Six3*-cKO mice at E16.5 (Fig. 2A). The expression of *Isl1*, another D1 MSN-specific marker [9], was also greatly reduced in the LGE SVZ of *Six3*-cKO mice compared to that in control mice at E16.5 (Fig. 2A).

We next examined the number of striatal MSNs at P0 using BCL11B, a pan-striatal MSN marker, combined with EBF1 expression to distinguish D1 MSNs from D2 MSNs [9, 45]. BCL11B⁺/EBF1⁺ cells represented D1 MSNs, BCL11B⁺ and EBF1 immuno-negative (BCL11B⁺/EBF1⁻) cells represented D2 MSNs (Fig. 2B). We found no significant difference in the number of EBF1⁺ cells (D1 MSNs), but the number of BCL11B⁺/EBF1⁻ cells (D2 MSNs) was significantly lower in *Six3*-cKO mice than in controls at P0 (Fig. 2B). These results suggest that neurogenesis of D1 MSNs is reduced at the embryonic stage, but not at the postnatal stage. This indicates that the absence of *Six3* results in a subpopulation of D1 MSNs with delayed differentiation at the embryonic stage. In contrast, the neurogenesis of D2 MSNs was significantly decreased in the LGE of *Six3*-cKO mice from the embryonic to the postnatal stage (Figs 1A and 2).

Cell Proliferation is Unaffected in the LGE of *Six3*-cKO Mice

Next, we determined whether LGE cell proliferation was changed in *Six3*-cKO mice, as a small population of SIX3⁺ cells were in S-phase, and *Six3* has been reported to regulate cell proliferation [46, 47]. It is possible that *Six3* functions by regulating the cell cycle during LGE development. We performed 30-min BrdU pulse-labeling experiments at E14.5 and E16.5 (Fig. 3A, B). The number of BrdU⁺ cells was comparable in *Six3*-cKO and control mice at E14.5 (Fig. 3A). Consistent with this, the data showed that the total number of BrdU⁺ cells in the LGE was also unchanged in the LGE of *Six3*-cKO mice compared to that of control mice at E16.5 (Fig. 3B). Notably, BrdU⁺ cells

seemed to accumulate in the ventricular zone (VZ) at E14.5 and E16.5, since we saw more BrdU⁺ cells (but no significant difference) in the VZ of *Six3*-cKO mice (Fig. 3B). Because *Dlx5/6-CIE* mice expressed little CRE in the VZ, we proposed that the slight accumulation of BrdU⁺ cells in the VZ was a secondary effect of the blocked differentiation of progenitor cells in the LGE SVZ. We also found that the expression of KI67, a classical cell proliferation marker, in the LGE was slightly but not significantly higher in *Six3*-cKO mice than that in control mice (Fig. 3C). These results suggest that cell proliferation during LGE development is little affected in the absence of *Six3* function.

Differentiation of D2 MSN Precursor Cells is Blocked in *Six3*-cKO Mice

Since cell proliferation was not compromised in *Six3*-cKO mice, we hypothesized that the significant loss of D2 MSNs was due to abnormal differentiation of precursor cells. We assessed *Sp8* and *Sp9* expression in the LGE as they are expressed earlier than *Six3* and are upstream of it in the LGE SVZ [26]. Normally, cells with high SP8 expression were located in the dLGE SVZ, while cells with low expression level of SP8 were located in the vLGE SVZ at E14.5 and E16.5 (Fig. 4A). SP9⁺ cells located in the SVZ were mainly precursor cells, and those in the MZ were mainly D2 MSNs [25]. SP8⁺ cells were significantly higher in the vLGE SVZ in *Six3*-cKO embryos than in controls at E14.5 and E16.5 (Fig. 4A). The number of SP9⁺ cells was also significantly increased in the LGE SVZ of *Six3*-cKO embryos at E16.5 (Fig. 4A). The increased number of SP8⁺ and SP9⁺ cells in the LGE SVZ indicated that MSN precursor cells accumulated in *Six3*-cKO embryos. Although SP8⁺ and SP9⁺ precursor cells accumulated in the LGE SVZ, we still observed many SP9⁺ cells in the LGE MZ of *Six3*-cKO embryos (Fig. 4A). Because SP9 is mainly expressed in D2 MSNs in the striatum [25], these SP9⁺ cells in the LGE MZ of *Six3*-cKO embryos were putative D2 MSNs.

As described above, BCL11B⁺/EBF1⁻ cells in the striatum were visualized as white dots (Fig. 2B). The numbers of BCL11B⁺/EBF1⁻ cells was lower in *Six3*-cKO mice than in controls (Fig. 2B), but there were still many BCL11B⁺/EBF1⁻ cells in the striatum (Fig. 2B). This also indicated that putative D2 MSNs were generated in the LGE MZ of *Six3*-cKO mice, consistent with above result (Fig. 4A). Besides, the ratio of D1 MSNs was increased while that of D2 MSNs was decreased in *Six3*-cKO mice, indicating that losing *Six3* function in LGE leads to abnormal neural differentiation.

Six3OS has been reported to be co-expressed with *Six3* in the hypothalamus and retina to indirectly regulate the

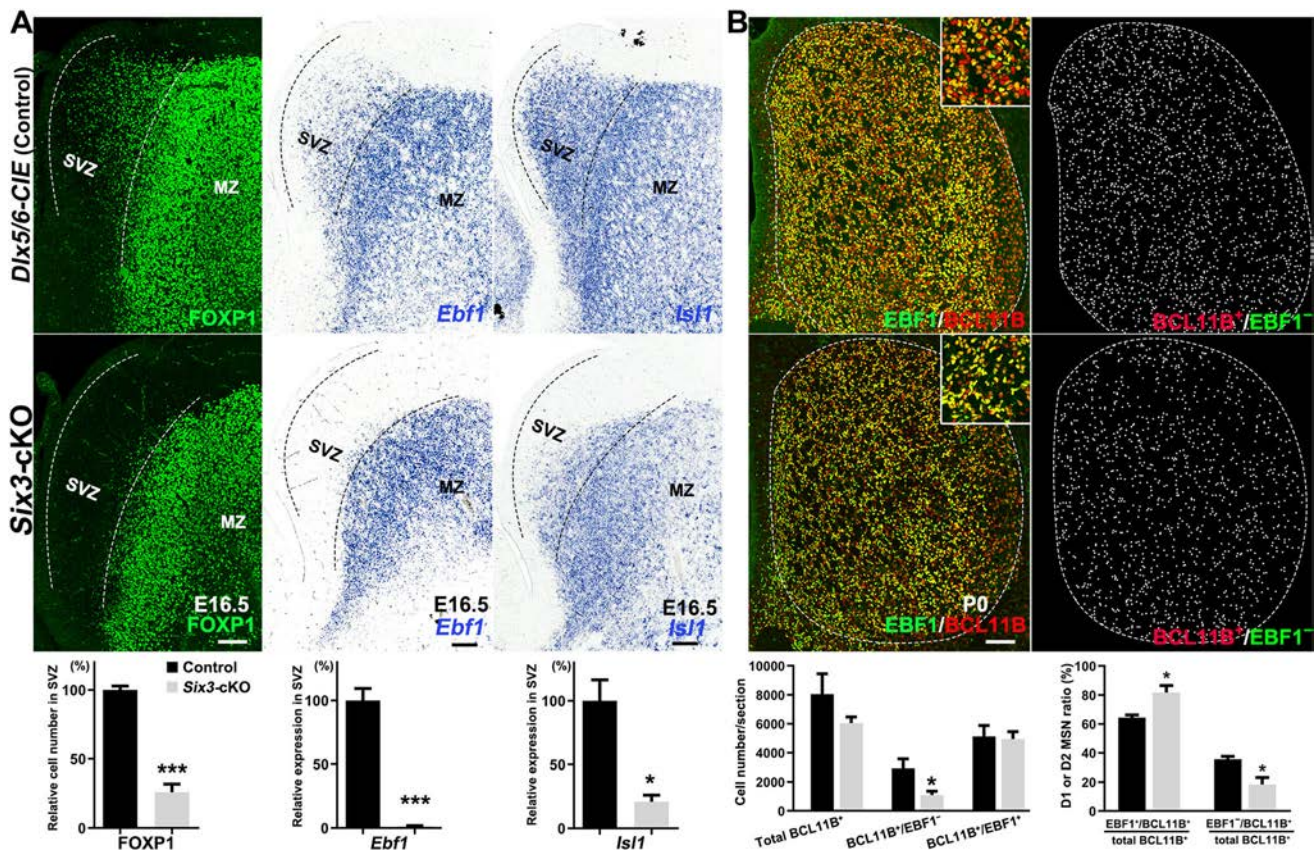


Fig. 2 Neurogenesis is reduced in the LGE of *Six3*-cKO mice. **A** Upper panels. FOXP1 immunofluorescence and *Ebf1* and *Isl1* *in situ* hybridization in the LGE of control and *Six3*-cKO mice at E16.5. The LGE SVZ of *Six3*-cKO mice contains fewer FOXP1⁺, *Ebf1*⁺ and *Isl1*⁺ cells than those of controls. The dotted lines indicate the border of the LGE SVZ and MZ. Lower panels, quantification of FOXP1, *Ebf1*, and *Isl1*. Data shown are the mean + SEM ($n = 3-4$; * $P < 0.05$, *** $P < 0.001$, Student's *t*-test). **B** Upper panels, BCL11B and EBF1 immunofluorescence in the striatum of control and *Six3*-cKO mice at P0. BCL11B⁺/EBF1⁺ cells represent D1 MSNs, and

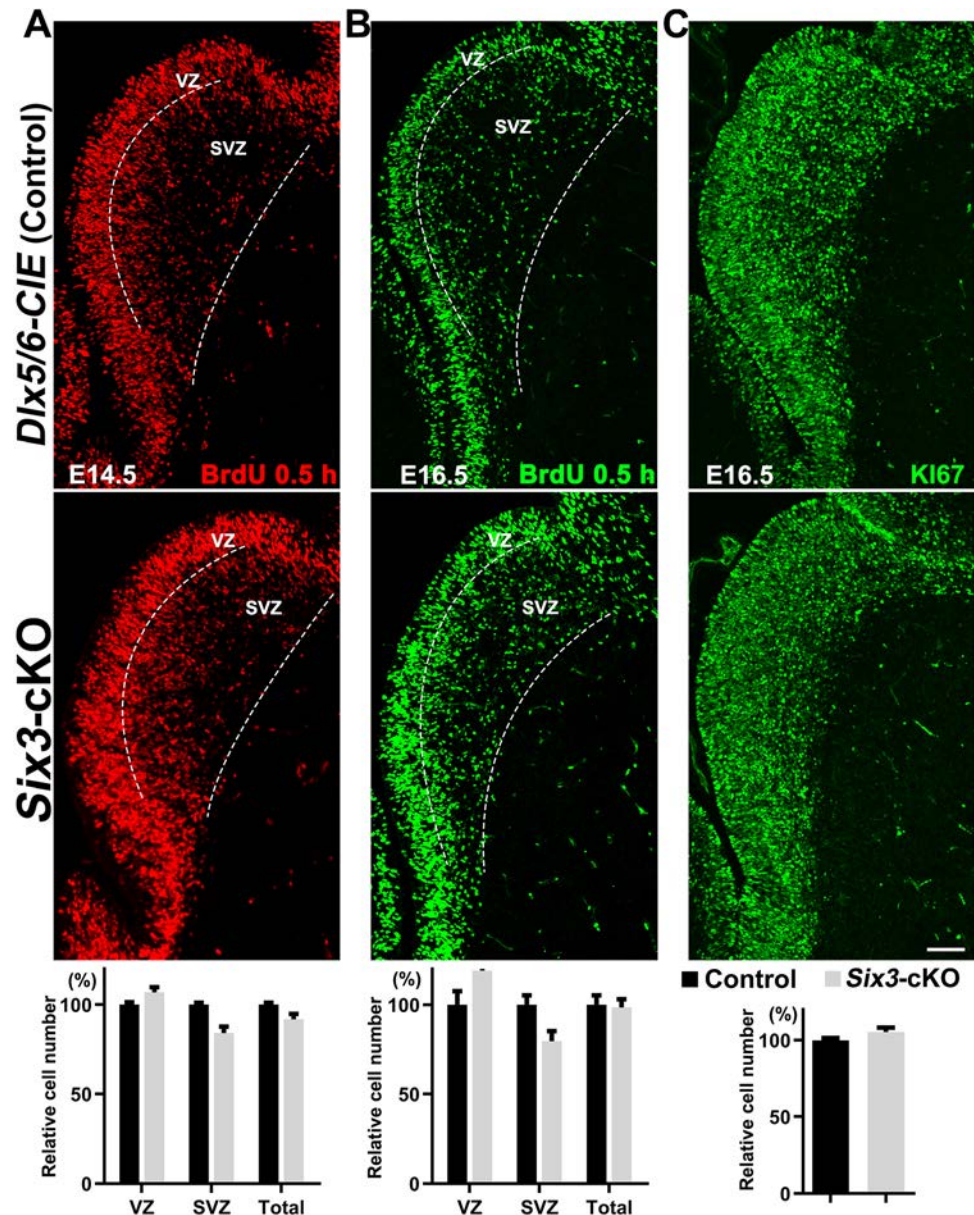
BCL11B⁺/EBF1⁻ cells represent D2 MSNs. Inserts show magnified images of BCL11B and EBF1 co-expression in control and *Six3*-cKO mice. BCL11B⁺/EBF1⁻ cells (D2 MSNs) are indicated by white dots in the right panel. Lower left panel, quantification showing that the number of BCL11B⁺/EBF1⁻ cells, but not BCL11B⁺/EBF1⁺ cells, was significantly lower in the striatum of *Six3*-cKO mice than in control. Lower right panel, percentages of (BCL11B⁺/EBF1⁺)/BCL11B⁺ and (BCL11B⁺/EBF1⁻)/BCL11B⁺ cells. Dotted line indicates the striatal border. Data shown are the mean + SEM ($n = 3$; * $P < 0.05$, Student's *t*-test; scale bar, 200 μ m).

function of *Six3* [48, 49]. We immunostained for SIX3 after *in situ* hybridization for *Six3OS* mRNA, and found that most, if not all, *Six3OS*⁺ cells expressed SIX3 (Fig. 4B). This indicated that *Six3OS* and SIX3 are expressed in the same cell type in the LGE SVZ. *Six3OS* was strongly expressed in the LGE SVZ but seldom in the MZ of control mice (Fig. 4C), suggesting that *Six3OS* is mainly expressed in precursor cells. *Six3OS* expression was significantly up-regulated in the LGE SVZ of *Six3*-cKO mice (Fig. 4C), indicating that *Six3OS*⁺ precursor cells accumulate in the LGE SVZ in the absence of *Six3*. Surprisingly, we also found that many *Six3OS*⁺ cells were located in the LGE MZ or striatum at E16.5 and P0, suggesting that *Six3OS* expression in those precursor cells is not down-regulated and they then migrated into the MZ or striatum with insufficient maturation after loss of *Six3* (Fig. 4C). Once again, *Six3OS*⁺ cells in the MZ indicated

that *Six3OS*⁺ putative D2 MSNs are generated in the LGE of *Six3*-cKO mice, consistent with the above results.

We then examined the expression of the differentiated D2 MSN markers *Drd2* and *Adora2a* at E16.5 and P0 (Fig. 4D). *Drd2* and *Adora2a* were strongly expressed in the LGE SVZ and MZ in control mice (Fig. 4D). However, only a few cells expressing high levels of *Drd2* and very few *Adora2a*⁺ cells were located in the LGE MZ of *Six3*-cKO mice at E16.5 (Fig. 4D). Similarly, *Drd2* and *Adora2a* were strongly expressed in the striatum of control mice but significantly reduced in that of *Six3*-cKO mice at P0 (Fig. 4D). We previously reported that the cells that express *Drd2* strongly are mainly striatal cholinergic interneurons [25, 26]. Thus, SP8⁺ and SP9⁺ precursor cells accumulated in the LGE SVZ, SP9⁺ cells and many BCL11B⁺/EBF1⁻ putative D2 MSNs located in the LGE MZ and striatum, but few *Drd2*⁺ and *Adora2a*⁺ cells were

Fig. 3 Cell proliferation is unaffected in *Six3*-cKO mice. **A, B** Upper panels, immunofluorescence images showing BrdU-pulse labeling for 0.5 h in the LGE of control and *Six3*-cKO mice at E14.5 (**A**) and E16.5 (**B**). Lower panels, numbers of BrdU⁺ cells in the LGE VZ and SVZ at E14.5 (**A**) and E16.5 (**B**). There is no significant difference in the number of BrdU⁺ cells between the LGEs of *Six3*-cKO and control mice. **C** Upper panels, KI67 immunofluorescence in the LGE of control and *Six3*-cKO mice at E16.5. Dotted lines indicate the border of the LGE VZ, SVZ, and MZ. Lower panel, quantification data (mean + SEM, $n = 3$, Student's *t*-test; scale bar, 100 μm).



found in the LGE and striatum, providing strong evidence that D2 MSN precursor cells differentiate abnormally in the striatum without *Six3*.

Overexpression of *Six3* Promotes the Differentiation of MSN Precursor Cells

To investigate the differentiation action of *Six3*, we generated a mouse line that conditionally overexpressing *Six3* by knocking *CAG promoter-Flox-STOP-Flox-Six3-IRES-LacZ* into the *Rosa26* locus (*Rosa-Six3OE* allele) and using *Dlx5/6-CIE* to drive continuous *Six3* expression (Fig. 5A). SIX3 was expressed in almost all of the MSNs in

Dlx5/6-CIE, Rosa-Six3OE/+ mice, and the expression of β -galactosidase, with a nuclear localization sequence, confirmed this phenotype (Fig. 5B–D). Accordingly, SIX3⁺ cells were distributed in the cortices of *Dlx5/6-CIE, Rosa-Six3OE/+* mice (Fig. 5B), although *Six3* is not normally expressed in the cortex [26]. These results demonstrated that *Six3* was ectopically overexpressed in the *Dlx5/6-CIE, Rosa-Six3OE/+* mice.

We used BCL11B and FOXP1 to assess whether *Six3* overexpression promotes precursor cell differentiation (Fig. 6). Both BCL11B and FOXP1 were weakly expressed in the LGE SVZ but strongly expressed in the MZ of *Dlx5/6-CIE* control mice (Fig. 6). We found that the expression

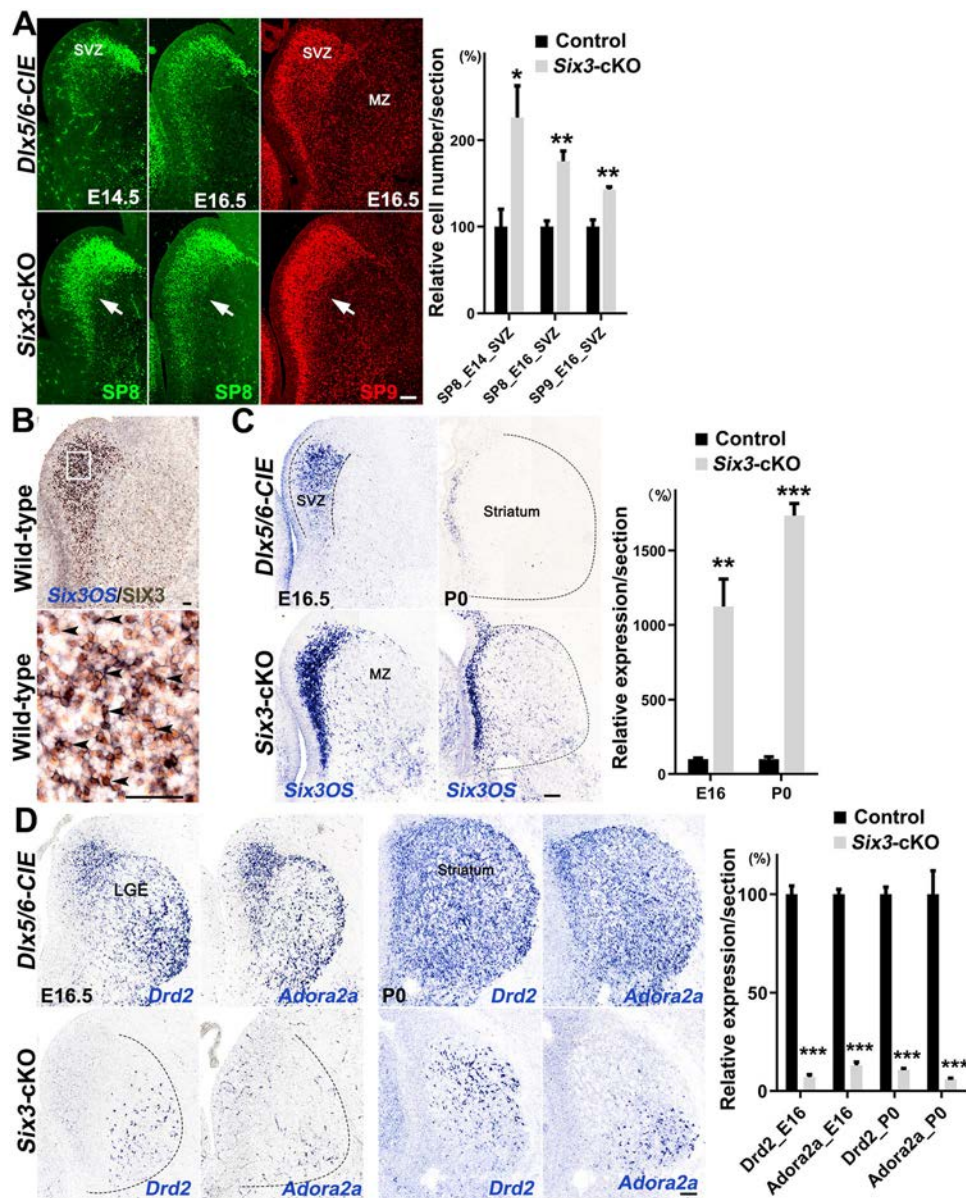


Fig. 4 Differentiation of striatal D2 MSNs is blocked in *Six3*-cKO mice. **A** Left panels, immunofluorescence images showing SP8 (E14.5 and E16.5) and SP9 (E16.5) expression in the LGE. Arrows indicate that SP8⁺ and SP9⁺ cells are accumulated in the vLGE SVZ of *Six3*-cKO mice compared to controls. Right panel, quantification data is shown ($n = 3-4$). **B** Left panels, immunohistochemistry images showing SIX3 protein and *Six3OS* mRNA expression in the LGE of wild-type mice at E16.5. The magnified image shows that most, if not all, of the *Six3OS*⁺ cells in the LGE SVZ express the SIX3 protein. Right panels, quantification. **C** Left panels, *in situ* hybridization for *Six3OS* in the LGE of control and *Six3*-cKO mice at E16.5 and P0. *Six3OS* is mainly expressed in the LGE SVZ, but the expression of *Six3OS* is greatly increased in the LGE of *Six3*-cKO

mice. Note that many *Six3OS*⁺ cells are distributed in the LGE MZ and striatum of *Six3*-cKO mice. Right panel, quantification data ($n = 3-4$). **D** Left panels, *in situ* hybridization for *Drd2* and *Adora2a* in control and *Six3*-cKO mice at E16.5 and P0. *Drd2* and *Adora2a* are strongly expressed in the controls at both E16.5 and P0. However, very little *Drd2* and *Adora2a* mRNA is expressed in the LGE and striatum of *Six3*-cKO mice at E16.5 and P0. Right panel, quantification data ($n = 3$; mean + SEM; * $P < 0.05$, ** $P < 0.01$, *** $P < 0.001$, Student's *t*-test). Note that many SP9⁺ cells, BCL11B⁺/EBF1⁻ cells, and *Six3OS*⁺ cells are located in the LGE MZ and striatum of *Six3*-cKO mice in **A** and **B**. Dotted lines indicate the borders of the LGE. Scale bars, 100 μm in **A**, **C**, and **D**; 50 μm in **B**.

of BCL11B was significantly increased in the LGE SVZ of *Six3* conditional overexpression mice at E14.5 (Fig. 6A). Similarly, very few FOXP1⁺ cells were located in the LGE SVZ of control mice, but many FOXP1⁺ cells were

distributed in the LGE SVZ of *Six3* conditional overexpression mice at E14.5 (Fig. 6A). The quantification confirmed that the number of FOXP1⁺ cells was significantly higher in the LGE SVZ of *Six3* conditional

overexpression mice than in controls (Fig. 6A). We also analyzed BCL11B and FOXP1 expression at E16.5 (Fig. 6B). The expression of BCL11B in the LGE SVZ of *Dlx5/6-CIE, Rosa-Six3OE/+* mice was slightly up-regulated compared to controls (Fig. 6B). We confirmed this phenotype by counting the FOXP1⁺ cells in the LGE SVZ and found that the number of these cells was significantly increased in *Dlx5/6-CIE, Rosa-Six3OE/+* mice (Fig. 6B). These results suggested that *Six3* promotes precursor cell differentiation in the LGE.

Loss of *Six3* Induces Apoptosis in the Postnatal Striatum

We analyzed cell death by evaluating cleaved Caspase-3 expression to investigate whether abnormally differentiated D2 MSNs survived in the striatum of postnatal *Six3*-cKO mice. The data showed that in control mice, the number of Caspase-3⁺ cells increased from P0, peaked at P3, and then decreased to a very low level as the striatum developed (Fig. 7). Without *Six3* function, we found that the number of Caspase-3⁺ cells was significantly higher than in

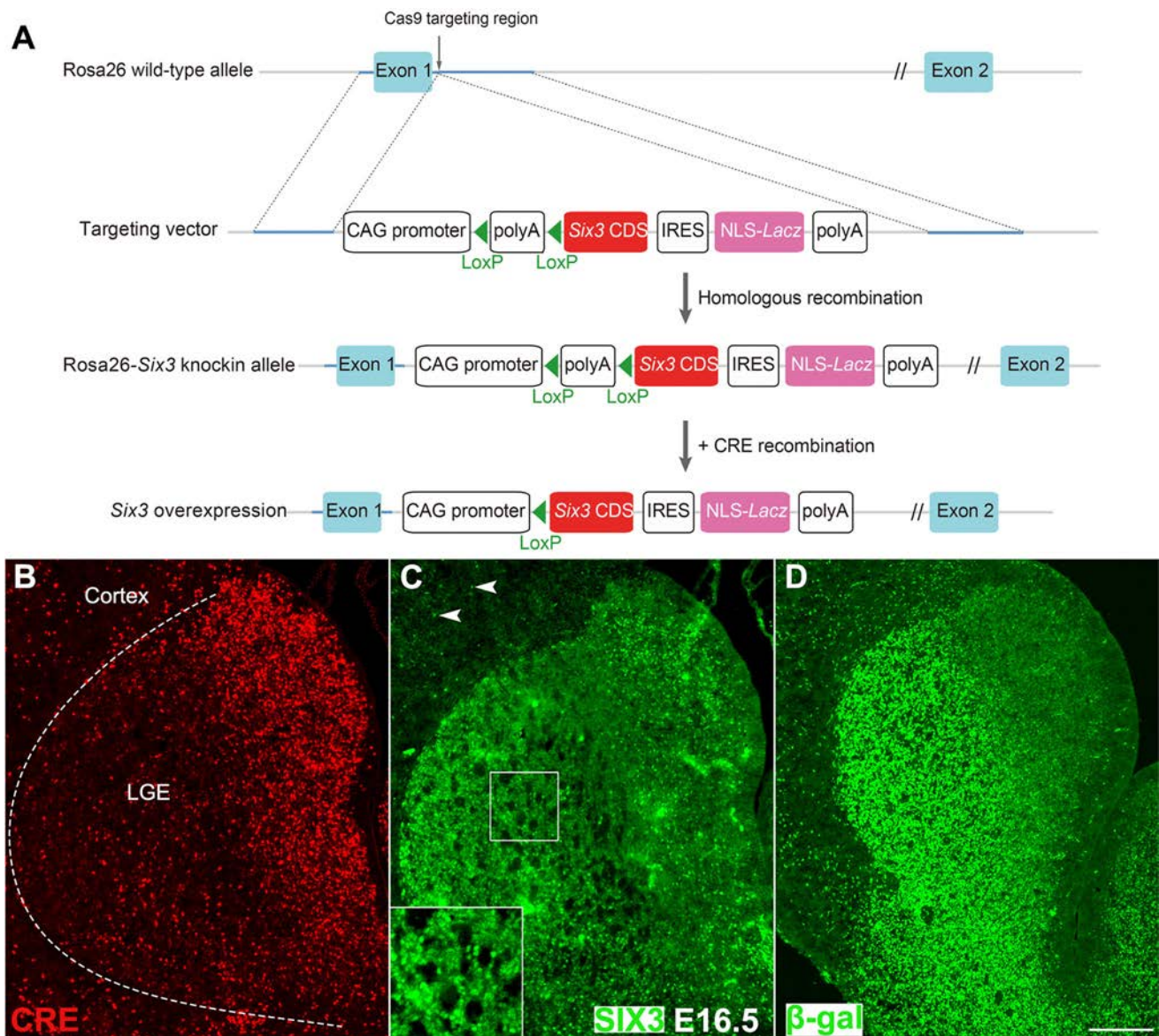


Fig. 5 Generation of mice with conditional overexpression of *Six3*. **A** A cassette containing the *CAG promoter-Flox-STOP-Flox-Six3-IRES-LacZ* sequence was knocked into the downstream of exon 1 of *Rosa26* (gene trap ROSA 26). The *LacZ* gene contains a nuclear localization sequence (NLS). **B–D** Immunofluorescence images

showing CRE, SIX3, and β -galactosidase (β -gal) expression in *Dlx5/6-CIE, Rosa26-Six3OE/+* mice at E16.5. Arrowheads in **C** show ectopic expression of SIX3 in *Dlx5/6*⁺ cells in the cortex. Boxes show magnified images of SIX3 expression in the LGE MZ (scale bar, 200 μ m).

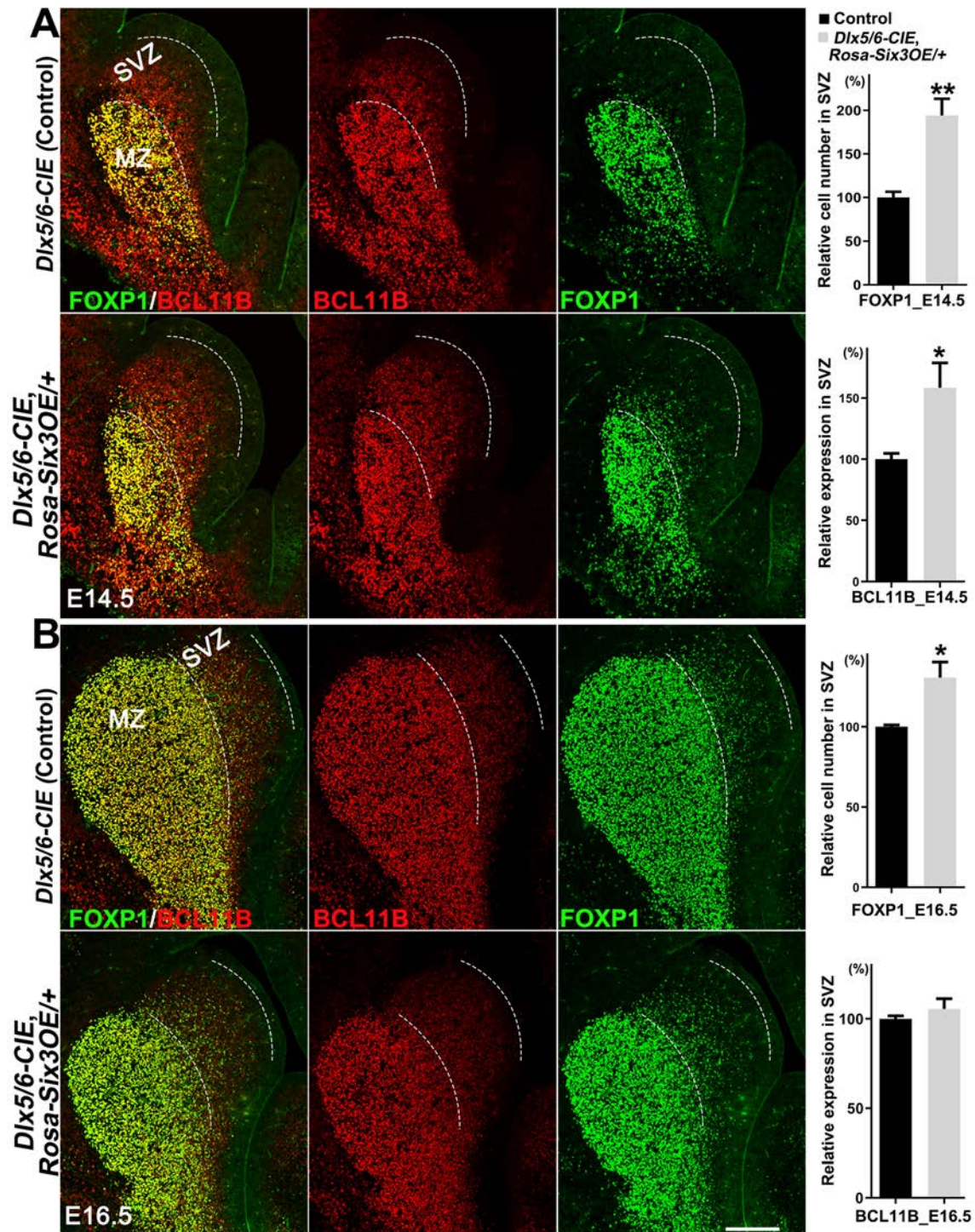


Fig. 6 Overexpression of *Six3* in the LGE promotes the differentiation of MSN precursor cells. **A** Left, immunofluorescence images showing FOXP1 and BCL11B expression in the LGE of control and *Dlx5/6-CIE, Rosa-Six3OE/+* mice at E14.5. Note that there are very few FOXP1⁺ cells in the LGE SVZ of controls. BCL11B expression is up-regulated in the LGE SVZ of *Dlx5/6-CIE, Rosa-Six3OE/+* mice compared to controls. Right, quantification showing that the number

of FOXP1⁺ cells in the LGE SVZ is significantly higher in *Dlx5/6-CIE, Rosa-Six3OE/+* mice than in controls. **B** Left, immunofluorescence images showing FOXP1 and BCL11B expression in the LGE of control and *Dlx5/6-CIE, Rosa-Six3OE/+* mice at E16.5. BCL11B expression is higher in the LGE SVZ of *Dlx5/6-CIE, Rosa-Six3OE/+* mice than in controls. Right, quantification data ($n = 3$; mean + SEM; * $P < 0.05$, ** $P < 0.01$, Student's *t*-test; scale bar, 200 μm).

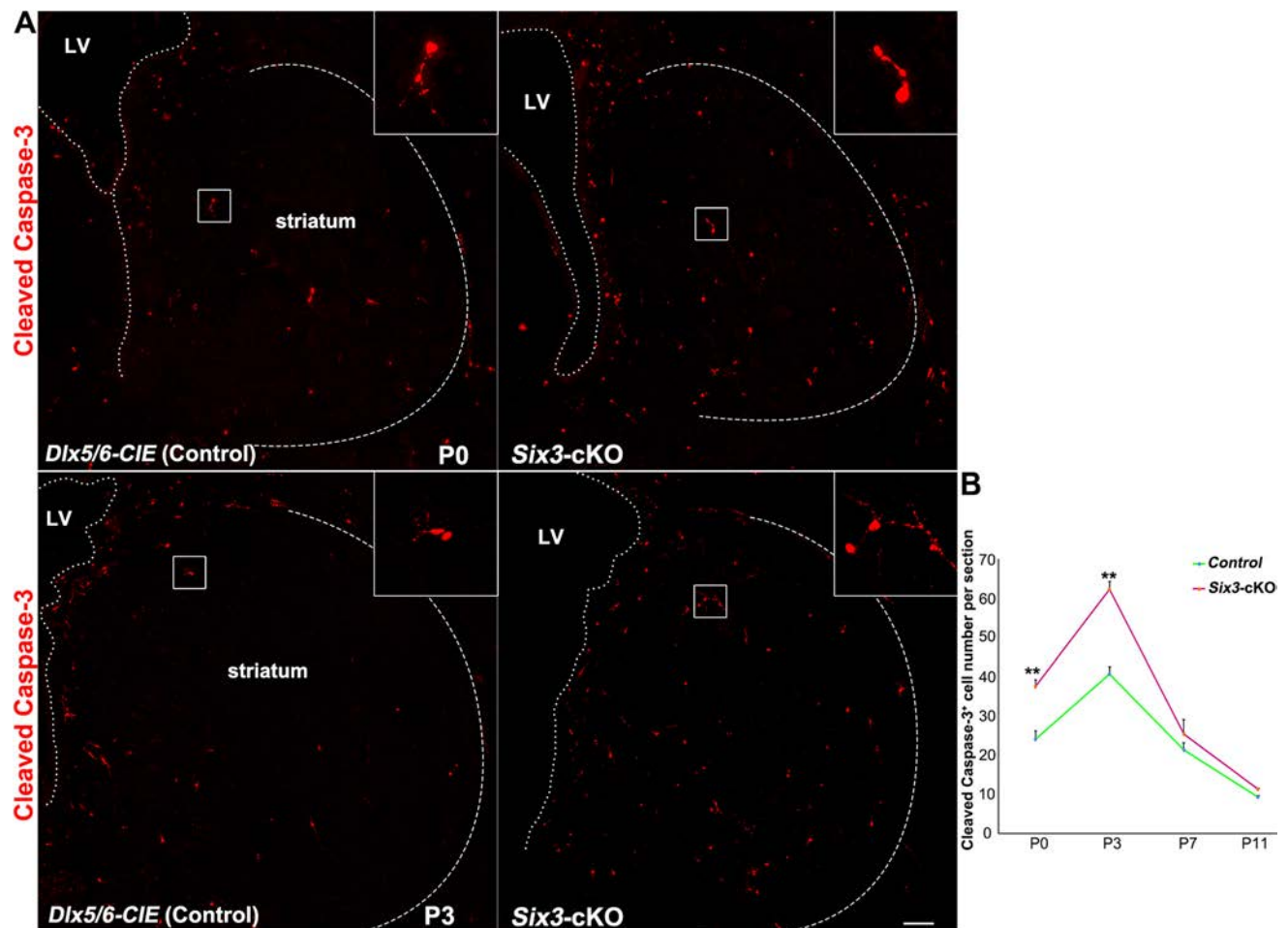


Fig. 7 Apoptosis is increased in the striatum of postnatal *Six3*-cKO mice. **A** Immunofluorescence images showing cleaved Caspase-3 expression in the striatum of *Dlx5/6-CIE* controls and *Six3*-cKO mice at P0 and P3 (dotted lines, border of the striatum; inserts, magnified images of cleaved Caspase-3). **B** Quantification showing the number

of cleaved Caspase-3⁺ cells was significantly higher in *Six3*-cKO mice than in control at P0 and P3, while there was no significant difference at P7 and P11 ($n = 3$; mean + SEM; ** $P < 0.01$, Student's t -test; scale bar, 100 μ m).

controls at P0 and P3, but that there was no significant difference at P7 or P11 (Fig. 7). We inferred that most of the dying cells were abnormally-differentiated D2 MSN precursor cells and that these cells were finally eliminated by programmed cell death, as we did not find a severe reduction in the number of D1 MSNs in *Six3*-cKO mice (Fig. 1).

Discussion

Striatal MSNs originate from the vLGE, while olfactory bulb interneurons are generated in the dLGE [13]. The LGE VZ was subdivided into 4 domains according to the combinatorial expression of several transcription factors. *Pax6*, *Gsx2*, and *Er81* (*Etv1*) were used to identify the dLGE. The vLGE contained the pLGE3, in which *Isl1* was strongly expressed while there was no expression of *Er81*,

and the pLGE4, in which *Nkx6.2* was strongly expressed while there was little expression of *Isl1*. The development of the two types of MSNs is regulated by many transcription factors [14]. For example, *Gsx2*, *Ascl1*, and *Dlx1/2* are required for pan-striatal MSN development [50]; *Ebf1* and *Isl1* specifically regulate D1 MSN differentiation and axonal guidance [9, 21–23]; *Sp8* and *Sp9* regulate D2 MSN generation and survival [25, 26]. Here, we found that *Six3* is required for D2 MSN differentiation and that its function is gradually reduced during D2 MSN maturation.

Six3 is expressed in ependymal cells of postnatal mice, and is essential for the maturation of ependymal cells. In mice in which *Six3* is conditionally knocked out by *Nestin-Cre*, cells located in the lateral ventricle wall contain mixed characteristics of ependymal cells and radial glia [34]. These defective cells result in the abnormal migration and differentiation of neuroblasts, markedly enlarged lateral ventricles, and hydrocephalus [34]. In this study, we

obtained the same results, i.e., a reduction in the number of D2 MSNs and enlarged lateral ventricles, in both *Dlx5/6-CIE*, *Six3^{F/F}* and *Nestin-Cre*, *Six3^{F/F}* mice. The *Six3* gene was deleted in ependymal cells in *Nestin-Cre*, *Six3^{F/F}* mice, but not in *Dlx5/6-CIE*, *Six3^{F/F}* mice, as *Dlx5/6* were rarely expressed in the progenitors (neural stem cells) of ependymal cells. However, the lateral ventricles of both *Dlx5/6-CIE*, *Six3^{F/F}* and *Nestin-Cre*, *Six3^{F/F}* mice were significantly enlarged, consistent with our previous report on *Sp9* mutant mice [25, 26]. This might indicate that enlargement of the lateral ventricle in *Nestin-Cre*, *Six3^{F/F}* mice is caused by the significant reduction in the number of D2 MSNs in the striatum.

It has been reported that *Isl1*, the conditional knockout of which results in a significant reduction in the number of D1 MSNs, regulates the development of D1 MSNs through semaphorin 3E (*Sema3e*) signaling, and that *Ebf1* also regulates the differentiation of D1 MSNs [9, 21, 22]. We previously showed that few *ISL1⁺* or *EBF1⁺* cells express the SIX3 protein [26]. In this study, we found that the numbers of *Isl1⁺* and *Ebf1⁺* cells were reduced in the LGE SVZ of *Six3*-cKO mice at E16.5 but that there was no significant difference at P0. The accumulation of progenitor cells such as *Ascl1⁺* cells in the LGE SVZ of *Six3*-cKO mice may retard differentiation by enhancing the Notching signal. We propose that *Six3* might cell-non-autonomously promote the differentiation of a subpopulation of D1 MSNs that experience delayed differentiation to a certain degree when *Six3* is knocked out in the LGE SVZ.

Six3 was mainly expressed in precursor cells and newborn immature D2 MSNs in the LGE SVZ. Loss of *Six3* function in progenitor cells resulted in a significant reduction in the number of mature D2 MSNs, whereas *Six3*-knockout in differentiated D2 MSNs (*Drd2⁺*) had little effect on striatal MSN development. This indicates that the functions of *Six3* decrease as D2 MSNs mature. The increased apoptosis in the absence of *Six3* may be because *Six3* is required for the survival of immature D2 MSNs, since SIX3 is expressed in immature D2 MSNs. However, in *Drd2-cre*, *Six3^{F/F}* mice, in which *Six3* was deleted in immature D2 MSNs, the number of D2 MSNs was comparable to that of control mice. This demonstrates that *Six3* plays a minor role in immature D2 MSN survival. Apart from that, large numbers of *SP9⁺*, *Six3OS⁺* putative D2 MSNs were found in the LGE SVZ and MZ of *Six3*-cKO mice. But few *Drd2⁺*, *Adora2a⁺* immature D2 MSNs were observed. This suggests that the differentiation of precursor cells is blocked in the absence of *Six3*. Thus, the increased apoptosis and reduction in the number of D2 MSNs in the absence of *Six3* occurs mainly in response to the abnormal differentiation of D2 MSNs.

Here, we found that *Six3OS* was also co-expressed with *Six3* in the LGE SVZ but down-regulated in the LGE MZ.

Six3 was strongly expressed in the LGE SVZ and its expression was scattered in the LGE MZ. The difference in expression patterns between *Six3* and *Six3OS* indicates that they have different functions in LGE development. The *Six3OS/Six3* co-expression pattern in the LGE SVZ indicates that *Six3OS⁺/Six3⁺* cells are precursor cells and that *Six3OS⁻/Six3⁺* cells are differentiated D2 MSNs. Thus, the accumulation of many *Six3OS⁺* progenitor cells in the LGE SVZ of *Six3*-cKO mice suggests that D2 MSN differentiation was blocked due to the loss of *Six3*; however, the migration of D2 MSNs was less affected in *Six3*-cKO mice, as we found that many *Six3OS⁺* and *BCL11B⁺/EBF⁻* cells were distributed in the LGE MZ.

It is noteworthy that the numbers of *Drd2⁺* and *Adora2a⁺* cells in the LGE MZ at E16.5 and P0 were significantly fewer than those in the *Six3*-cKO striatum at P11, indicating that a small population of precursor cells differentiates into mature D2 MSNs postnatally. We hypothesize that these mature D2 MSNs are largely generated in the pLGE4, as *Six3* is most prominently expressed in the pLGE3. Thus, we propose that most D2 MSNs are generated in the pLGE3 and that a small number of D2 MSNs are derived from the pLGE4. Whether D2 MSNs with different origins exhibit different axonal guidance and functions requires further study. Our RNA-seq data showed that expression of *Six2*, a homologous gene of *Six3*, in the LGE was significantly up-regulated in *Six3*-cKO mice compared to control mice (data not shown). This suggests that *Six2* may have functional redundancy with *Six3* and in turn partly promotes the generation of a subset of D2 MSNs.

In summary, in this study, we provide evidence that *Six3* is an important regulatory element in the LGE SVZ, where it specifically promotes the differentiation of D2 MSN precursor cells. Ongoing studies are aimed at elucidating the molecular mechanisms underlying the distinct functions of *Six3*. These findings broaden our comprehension of the transcriptional mechanisms underlying the development of striatal projection neurons.

Acknowledgements We are grateful to Dr. G. Oliver at Northwestern University for the generous gift of *Six3*-floxed mice, and Dr. K. Campbell at University of Cincinnati College of Medicine for the *Dlx5/6-CIE* mice. This work was supported by the National Key Research and Development Program of China (2018YFA0108000), the National Natural Science Foundation of China (31630032, 81974175, and 31820103006), the Shanghai Municipal Science and Technology Major Project (2018SHZDZX01).

Conflict of interest The authors declare that they have no conflict of interest.

Open Access This article is licensed under a Creative Commons Attribution 4.0 International License, which permits use, sharing, adaptation, distribution and reproduction in any medium or format, as long as you give appropriate credit to the original author(s) and the

source, provide a link to the Creative Commons licence, and indicate if changes were made. The images or other third party material in this article are included in the article's Creative Commons licence, unless indicated otherwise in a credit line to the material. If material is not included in the article's Creative Commons licence and your intended use is not permitted by statutory regulation or exceeds the permitted use, you will need to obtain permission directly from the copyright holder. To view a copy of this licence, visit <http://creativecommons.org/licenses/by/4.0/>.

References

- Gerfen CR, Paletzki R, Heintz N. GENSAT BAC cre-recombinase driver lines to study the functional organization of cerebral cortical and basal ganglia circuits. *Neuron* 2013, 80: 1368–1383.
- Gerfen CR, Surmeier DJ. Modulation of striatal projection systems by dopamine. *Annu Rev Neurosci* 2011, 34: 441–466.
- Reiner A, Albin RL, Anderson KD, D'Amato CJ, Penney JB, Young AB. Differential loss of striatal projection neurons in Huntington disease. *Proc Natl Acad Sci USA* 1988, 85: 5733–5737.
- Ni RJ, Huang ZH, Shu YM, Wang Y, Li T, Zhou JN. Atlas of the striatum and globus pallidus in the tree shrew: Comparison with rat and mouse. *Neurosci Bull* 2018, 34: 405–418.
- Zhang H, Yang J, Wang X, Yao X, Han H, Gao Y. Altered local field potential relationship between the parafascicular thalamic nucleus and dorsal striatum in hemiparkinsonian rats. *Neurosci Bull* 2019, 35: 315–324.
- Maia TV, Frank MJ. From reinforcement learning models to psychiatric and neurological disorders. *Nat Neurosci* 2011, 14: 154–162.
- Stanley G, Gokce O, Malenka RC, Sudhof TC, Quake SR. Continuous and discrete neuron types of the adult murine striatum. *Neuron* 2020, 105(688–699): e688.
- Heiman M, Schaefer A, Gong S, Peterson JD, Day M, Ramsey KE, *et al.* A translational profiling approach for the molecular characterization of CNS cell types. *Cell* 2008, 135: 738–748.
- Lobo MK, Karsten SL, Gray M, Geschwind DH, Yang XW. FACS-array profiling of striatal projection neuron subtypes in juvenile and adult mouse brains. *Nat Neurosci* 2006, 9: 443–452.
- Gokce O, Stanley GM, Treutlein B, Neff NF, Camp JG, Malenka RC, *et al.* Cellular taxonomy of the mouse striatum as revealed by single-cell RNA-seq. *Cell Rep* 2016, 16: 1126–1137.
- Gerfen CR, Engber TM, Mahan LC, Susel Z, Chase TN, Monsma FJ Jr, *et al.* D1 and D2 dopamine receptor-regulated gene expression of striatonigral and striatopallidal neurons. *Science* 1990, 250: 1429–1432.
- Li J, Wang C, Zhang Z, Wen Y, An L, Liang Q, *et al.* Transcription factors Sp8 and Sp9 coordinately regulate olfactory bulb interneuron development. *Cereb Cortex* 2018, 28: 3278–3294.
- Tepe B, Hill MC, Pekarek BT, Hunt PJ, Martin TJ, Martin JF, *et al.* Single-cell RNA-seq of mouse olfactory bulb reveals cellular heterogeneity and activity-dependent molecular census of adult-born neurons. *Cell Rep* 2018, 25(2689–2703): e2683.
- Flames N, Pla R, Gelman DM, Rubenstein JL, Puelles L, Marin O. Delineation of multiple subpallial progenitor domains by the combinatorial expression of transcriptional codes. *J Neurosci* 2007, 27: 9682–9695.
- Kohwi M, Osumi N, Rubenstein JL, Alvarez-Buylla A. Pax6 is required for making specific subpopulations of granule and periglomerular neurons in the olfactory bulb. *J Neurosci* 2005, 25: 6997–7003.
- Guo T, Liu G, Du H, Wen Y, Wei S, Li Z, *et al.* *Dlx1/2* are central and essential components in the transcriptional code for generating olfactory bulb interneurons. *Cereb Cortex* 2019, 29: 4831–4849.
- Waclaw RR, Wang B, Pei Z, Ehrman LA, Campbell K. Distinct temporal requirements for the homeobox gene *Gsx2* in specifying striatal and olfactory bulb neuronal fates. *Neuron* 2009, 63: 451–465.
- Toresson H, Potter SS, Campbell K. Genetic control of dorsal-ventral identity in the telencephalon: opposing roles for Pax6 and Gsh2. *Development* 2000, 127: 4361–4371.
- Anderson SA, Qiu M, Bulfone A, Eisenstat DD, Meneses J, Pedersen R, *et al.* Mutations of the homeobox genes *Dlx-1* and *Dlx-2* disrupt the striatal subventricular zone and differentiation of late born striatal neurons. *Neuron* 1997, 19: 27–37.
- Corbin JG, Gaiano N, Machold RP, Langston A, Fishell G. The Gsh2 homeodomain gene controls multiple aspects of telencephalic development. *Development* 2000, 127: 5007–5020.
- Garel S, Marin F, Grosschedl R, Charnay P. Ebf1 controls early cell differentiation in the embryonic striatum. *Development* 1999, 126: 5285–5294.
- Ehrman LA, Mu X, Waclaw RR, Yoshida Y, Vorhees CV, Klein WH, *et al.* The LIM homeobox gene *Isl1* is required for the correct development of the striatonigral pathway in the mouse. *Proc Natl Acad Sci USA* 2013, 110: E4026–4035.
- Lu KM, Evans SM, Hirano S, Liu FC. Dual role for *Islet-1* in promoting striatonigral and repressing striatopallidal genetic programs to specify striatonigral cell identity. *Proc Natl Acad Sci USA* 2014, 111: E168–177.
- Zhang Z, Wei S, Du H, Su Z, Wen Y, Shang Z, *et al.* *Zfhx3* is required for the differentiation of late born D1-type medium spiny neurons. *Exp Neurol* 2019, 322: 113055.
- Zhang Q, Zhang Y, Wang C, Xu Z, Liang Q, An L, *et al.* The zinc finger transcription factor Sp9 is required for the development of striatopallidal projection neurons. *Cell Rep* 2016, 16: 1431–1444.
- Xu Z, Liang Q, Song X, Zhang Z, Lindtner S, Li Z, *et al.* SP8 and SP9 coordinately promote D2-type medium spiny neuron production by activating *Six3* expression. *Development* 2018, 145.
- Kawakami K, Sato S, Ozaki H, Ikeda K. Six family genes—structure and function as transcription factors and their roles in development. *Bioessays* 2000, 22: 616–626.
- Liu W, Lagutin OV, Mende M, Streit A, Oliver G. *Six3* activation of Pax6 expression is essential for mammalian lens induction and specification. *EMBO J* 2006, 25: 5383–5395.
- Lagutin OV, Zhu CC, Kobayashi D, Topczewski J, Shimamura K, Puelles L, *et al.* *Six3* repression of Wnt signaling in the anterior neuroectoderm is essential for vertebrate forebrain development. *Genes Dev* 2003, 17: 368–379.
- Oliver G, Mailhos A, Wehr R, Copeland NG, Jenkins NA, Gruss P. *Six3*, a murine homologue of the sine oculis gene, demarcates the most anterior border of the developing neural plate and is expressed during eye development. *Development* 1995, 121: 4045–4055.
- Seimiya M, Gehring WJ. The Drosophila homeobox gene *optix* is capable of inducing ectopic eyes by an eyeless-independent mechanism. *Development* 2000, 127: 1879–1886.
- Geng X, Speirs C, Lagutin O, Inbal A, Liu W, Solnica-Krezel L, *et al.* Haploinsufficiency of *Six3* fails to activate Sonic hedgehog expression in the ventral forebrain and causes holoprosencephaly. *Dev Cell* 2008, 15: 236–247.
- Geng X, Acosta S, Lagutin O, Gil HJ, Oliver G. *Six3* dosage mediates the pathogenesis of holoprosencephaly. *Development* 2016, 143: 4462–4473.
- Lavado A, Oliver G. *Six3* is required for ependymal cell maturation. *Development* 2011, 138: 5291–5300.

35. Stenman J, Toresson H, Campbell K. Identification of two distinct progenitor populations in the lateral ganglionic eminence: implications for striatal and olfactory bulb neurogenesis. *J Neurosci* 2003, 23: 167–174.
36. Tronche F, Kellendonk C, Kretz O, Gass P, Anlag K, Orban PC, *et al.* Disruption of the glucocorticoid receptor gene in the nervous system results in reduced anxiety. *Nat Genet* 1999, 23: 99–103.
37. Graus-Porta D, Blaess S, Senften M, Littlewood-Evans A, Damsky C, Huang Z, *et al.* Beta1-class integrins regulate the development of laminae and folia in the cerebral and cerebellar cortex. *Neuron* 2001, 31: 367–379.
38. Liu W, Lagutin OV, Mende M, Streit A, Oliver G. Six3 activation of Pax6 expression is essential for mammalian lens induction and specification. *EMBO J* 2006, 25: 5383–5395.
39. Gong S, Doughty M, Harbaugh CR, Cummins A, Hatten ME, Heintz N, *et al.* Targeting Cre recombinase to specific neuron populations with bacterial artificial chromosome constructs. *J Neurosci* 2007, 27: 9817–9823.
40. Lendahl U, Zimmerman LB, McKay RD. CNS stem cells express a new class of intermediate filament protein. *Cell* 1990, 60: 585–595.
41. Panganiban G, Rubenstein JL. Developmental functions of the Distal-less/Dlx homeobox genes. *Development* 2002, 129: 4371–4386.
42. Walker AS, Goings GE, Kim Y, Miller RJ, Chenn A, Szele FG. Nestin reporter transgene labels multiple central nervous system precursor cells. *Neural Plast* 2010, 2010: 894374.
43. Petryniak MA, Potter GB, Rowitch DH, Rubenstein JL. Dlx1 and Dlx2 control neuronal versus oligodendroglial cell fate acquisition in the developing forebrain. *Neuron* 2007, 55: 417–433.
44. Tamura S, Morikawa Y, Iwanishi H, Hisaoka T, Senba E. Foxp1 gene expression in projection neurons of the mouse striatum. *Neuroscience* 2004, 124: 261–267.
45. Arlotta P, Molyneaux BJ, Jabaudon D, Yoshida Y, Macklis JD. Ctip2 controls the differentiation of medium spiny neurons and the establishment of the cellular architecture of the striatum. *J Neurosci* 2008, 28: 622–632.
46. Appolloni I, Calzolari F, Corte G, Perris R, Malatesta P. Six3 controls the neural progenitor status in the murine CNS. *Cereb Cortex* 2008, 18: 553–562.
47. Gestri G, Carl M, Appolloni I, Wilson SW, Barsacchi G, Andreazzoli M. Six3 functions in anterior neural plate specification by promoting cell proliferation and inhibiting Bmp4 expression. *Development* 2005, 132: 2401–2413.
48. Rapicavoli NA, Poth EM, Zhu H, Blackshaw S. The long noncoding RNA Six3OS acts in trans to regulate retinal development by modulating Six3 activity. *Neural Dev* 2011, 6: 32.
49. Geng X, Lavado A, Lagutin OV, Liu W, Oliver G. Expression of Six3 Opposite Strand (Six3OS) during mouse embryonic development. *Gene Expr Patterns* 2007, 7: 252–257.
50. Evans AE, Kelly CM, Precious SV, Rosser AE. Molecular regulation of striatal development: a review. *Anat Res Int* 2012, 2012: 106529.



Restricted Feeding Resets Endogenous Circadian Rhythm in Female Mice Under Constant Darkness

Yue Mei^{1,2,3} · Huajing Teng^{1,4} · Zhigang Li¹ · Cheng Zeng^{1,2} · Yuanyuan Li^{1,2} · Wei Song^{1,2} · Kaifan Zhang⁵ · Zhong Sheng Sun^{1,2,5,6} · Yan Wang^{1,2}

Received: 24 July 2020 / Accepted: 10 October 2020 / Published online: 29 March 2021
© Center for Excellence in Brain Science and Intelligence Technology, CAS 2021

Dear Editor,

Circadian rhythms are driven by a complex, profoundly integrated network of clocks that maintain physiology and behaviors occurring at precise times and in the right order [1–3]. Light, the most powerful zeitgeber, entrains the central clock in the suprachiasmatic nucleus (SCN) *via* the retinohypothalamic tract with a precise 24-h rhythm in mammals [4, 5]. Due to irregular exposure to light conditions, such as an arrhythmic lifestyle, jet lag, and shift-work, circadian disturbance occurs quite often in modern societies and promotes a series of health problems

such as obesity, depression, and neurodegenerative diseases [6, 7]. Thus, adjusting or resetting an arrhythmic circadian rhythm by using external cues has attracted wide attention [8]. Notably, food-induced cues have been documented to have effects on certain circadian rhythms in rodents and humans [9, 10]. In nocturnal rodents, time-restricted feeding during the light phase can produce a rhythmic behavior prior to mealtime, named food-anticipatory activity (FAA) [11–14] and can reset the phase of peripheral clocks [15]. Sex differences in response to FAA and an activity-based anorexia model have been reported in mice [12, 16]. However, timed feeding-induced effects on circadian rhythm are quite different from those induced by photic cues at both the molecular and behavioral levels [17]. In particular, feeding restricted to daytime has limited effects on the SCN rhythms of rodents exposed to normal light-dark conditions [18, 19]. Considering that circadian clocks also adapted to energetic demands during evolution, whether food-induced cues solely function as a potent zeitgeber for clock resetting remains debatable. Specifically, whether timed feeding during the subjective day under constant darkness can reset the endogenous circadian rhythm of the SCN in rodents is dependent on sex needs to be addressed.

To investigate the influence of feeding timing on circadian rhythm, we first examined the effect of restricted feeding (RF) on the wheel-running activity of mice under regular light/dark (LD) cycles. Both male and female mice aged 2 months were entrained to a 12:12 h LD cycle with food available *ad libitum* (AL) for 10 days, after which they were subjected to an RF schedule with food available in the light phase (0 h–12 h) (Fig. S1A). Under normal light and food conditions, all male and female mice exhibited 24-h rhythmic wheel-running activity. However, when food was available at 0 h–12 h, the phase of wheel-running

Supplementary Information The online version contains supplementary material available at <https://doi.org/10.1007/s12264-021-00669-w>.

✉ Zhong Sheng Sun
sunzs@biols.ac.cn

✉ Yan Wang
wangy@biols.ac.cn

¹ Beijing Institutes of Life Science, Chinese Academy of Sciences, Beijing 100101, China

² CAS Center for Excellence in Biotic Interactions, University of the Chinese Academy of Sciences, Beijing 100049, China

³ Center for Translational Medicine, Second Military Medical University, Shanghai 200080, China

⁴ Key Laboratory of Carcinogenesis and Translational Research (Ministry of Education/Beijing), Department of Radiation Oncology, Peking University Cancer Hospital & Institute, Beijing 100142, China

⁵ Institute of Genomic Medicine, Wenzhou Medical University, Wenzhou 325000, China

⁶ State Key Laboratory of Integrated Management of Pest Insects and Rodents, Chinese Academy of Sciences, Beijing 100101, China

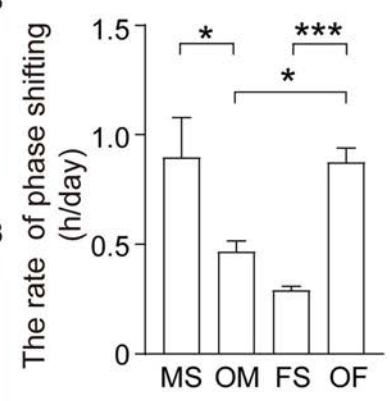
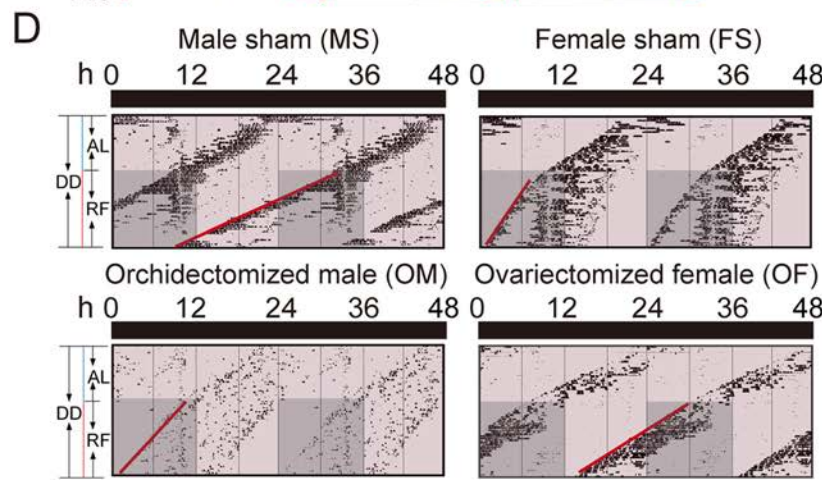
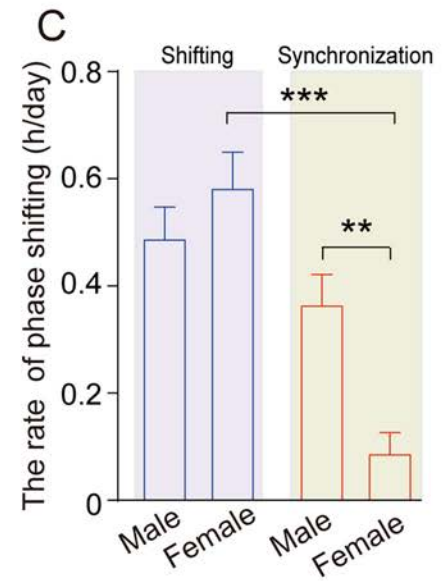
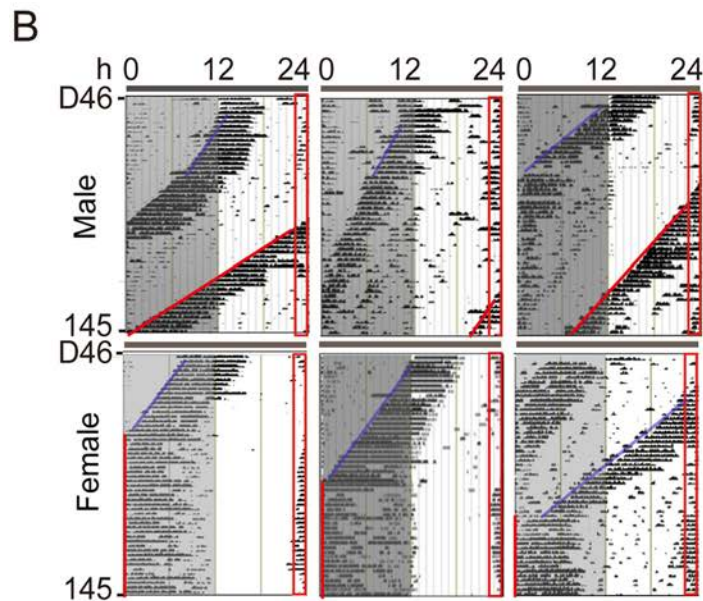
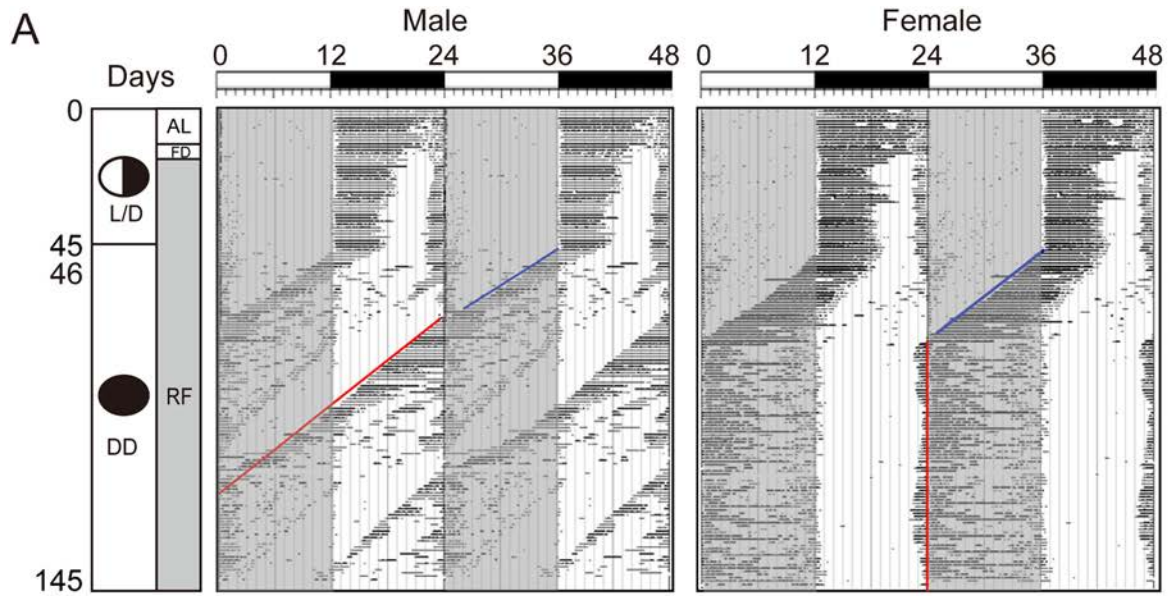


Fig. 1 The wheel-running activity of male and female mice with restricted feeding (RF) under constant darkness (DD). **A** Representative activity of male and female mice (horizontal axis, 48 h; vertical axis, 145 consecutive days; blue lines, shifting stage; red lines, synchronization stage). **B** Activity of mice with RF under DD [grey region, feeding time; region enclosed by red lines, food anticipatory activity (FAA); $n = 7$ for male and $n = 8$ for female mice]. **C** Phase-shifting rate in male and female mice with DD/RF at 0 h–12 h (left, shifting stage; right, synchronization stage; $**P < 0.01$, $***P < 0.001$). **D** Activity and rate of phase-shifting of male and female mice with intact gonads (upper) or gonadectomy (lower) under DD/RF 0–12 h ($n = 8$ per group; horizontal axis, 48 h; vertical axis, consecutive days; light grey, feeding time; light red, dark phase; red line, general phase shifting; $*P < 0.05$, $***P < 0.001$).

activity in both male and female mice was divided into endogenous circadian activity (occupying most of the wheel-running activity and showing phase-shifting under constant darkness), FAA (occurring at 2 h–3 h before feeding time), and food-related activity (Fig. S1B), suggesting that two oscillators, one light-entrainable and one food-entrainable, coordinately regulate the wheel-running activity of mice under LD cycles. Compared with the AL condition, the wheel-running activity during 12 h–24 h under RF remained at $90.885\% \pm 1.338\%$ in males and $92.969\% \pm 1.653\%$ in females [$P = 0.001$ for the stage factor (RF and AL), two-way ANOVA; $P = 0.141$ for the gender factor (female and male); Fig. S1C]. In contrast, RF at 0 h–12 h induced wheel-running activity of both male and female mice during the light period (0 h–12 h) (for males, $4.417\% \pm 0.328\%$ under AL and $9.115\% \pm 1.338\%$ under RF, $P = 0.035$; for females $3.077\% \pm 0.607\%$ under AL and $7.031\% \pm 1.653\%$ under RF, $P = 0.091$; for the stage factor, $P = 0.001$; two-way ANOVA with Tukey's multiple comparison test, Fig. S1D). In addition, there was no significant difference in the wheel-running activity between male and female mice under the LD/RF condition (Fig. S1E). These results indicated that although RF at 0 h–12 h had no significant effect on the phase of the circadian rhythm, it decreased the free wheel-running activity during the dark period and induced light-phase activity in nocturnal mice under normal light conditions.

To explore the effect of a food signal on circadian rhythm without light cues, male and female mice that were first habituated under normal LD/AL conditions were then transferred to restricted feeding (LD/RF 0 h–12 h), followed by constant darkness (DD) on the subjective day (DD/RF 0 h–12 h) (Fig. 1A). We found that the activity of male and female mice displayed two stages under DD/RF 0 h–12 h: an endogenous rhythm-induced shifting stage under DD and a synchronization stage with feeding time [$P < 0.0001$ for the stage factor (shifting and synchronization), two-way ANOVA; $P = 0.014$ for the gender factor; Fig. 1A–C). Male and female mice showed no difference in the shifting rate in

the shifting stages ($P = 0.995$, Fig. 1A–C). In the synchronization stage, however, the free-running phase of all (7/7) male mice remained shifting, and there was no significant difference in the shifting rate of male mice between the two stages ($P = 0.451$, Fig. 1A–C). In contrast, female mice displayed different shifting rates between the two stages with decreased shifting at the synchronization stage ($P = 0.0002$, two-way ANOVA with Tukey's multiple comparisons; Fig. 1A–C). Surprisingly, the majority of female mice (5/8) were finally entrained to a rhythm completely coinciding with the feeding time ($P = 0.003$ for the synchronization stage, male vs female, two-way ANOVA with Tukey's multiple comparisons, Fig. 1C). These results indicated that DD/RF 0 h–12 h induces sex-specific effects on the phases of free-running activity. Considering that several of the circadian-related characteristics induced by RF, such as FAA [12] and insomnia [16], differ between males and females, our results suggested that under constant darkness, food signals adjust the circadian system in a sex-specific manner, with stronger adjustment or even resetting in females than in males. Notably, we found that gonadectomy significantly changed the shifting rate induced by DD/RF 0 h–12 h in male and female mice (Fig. 1D). After gonadectomy, the shifting rate of orchidectomized males (OM) was significantly lower than that of ovariectomized females (OF) ($P = 0.010$, OM vs OF; $P = 0.013$, male sham (MS) vs OM; $P = 0.001$, female sham (FS) vs OF, two-way ANOVA with Tukey's multiple comparisons; Fig. 1D). This result suggested that gonadal hormones contribute to sex-specific entrainment of circadian rhythm by the DD/RF schedule.

To determine whether other restricted feeding schedules also contribute to the sex-specific effect on the phase shifting of free-running activity in mice, male and female mice were subjected to a feeding window with food available in a 5-h period (4 h–9 h) under constant darkness (Fig. 2A, DD/RF 4 h–9 h). Consistent with the results of DD/RF 0 h–12 h, DD/RF 4 h–9 h also induced sex-specific effects on free-running activity, with faster shifting rates in male sham (MS) mice and a more synchronized effect in female sham (FS) mice ($P = 0.022$, MS vs FS, DD/RF 4 h–9 h, Fig. 2A, B). After gonadectomy, however, OM displayed a significantly lower shifting rate than OF ($P = 0.007$). Moreover, compared to MS mice, OM displayed a significantly decreased shifting rate ($P = 0.045$; Fig. 2A, B), similar to that of FS. In contrast, OF mice displayed a significantly higher shifting rate than FS mice ($P = 0.003$, two-way ANOVA with Tukey's multiple comparisons; Fig. 2A, B), similar to MS mice. We found that daily food consumption varied among the 4 groups with RF at DD/RF 4 h–9 h ($P < 0.0001$ for the time factor, three-way ANOVA; $P = 0.027$ for the gender factor; $P < 0.0001$ for the gonad function factor; $P = 0.0002$ for the combined gender and gonadal function factors; Fig. 2C). After normalization to body weight, we obtained similar results ($P < 0.0001$ for

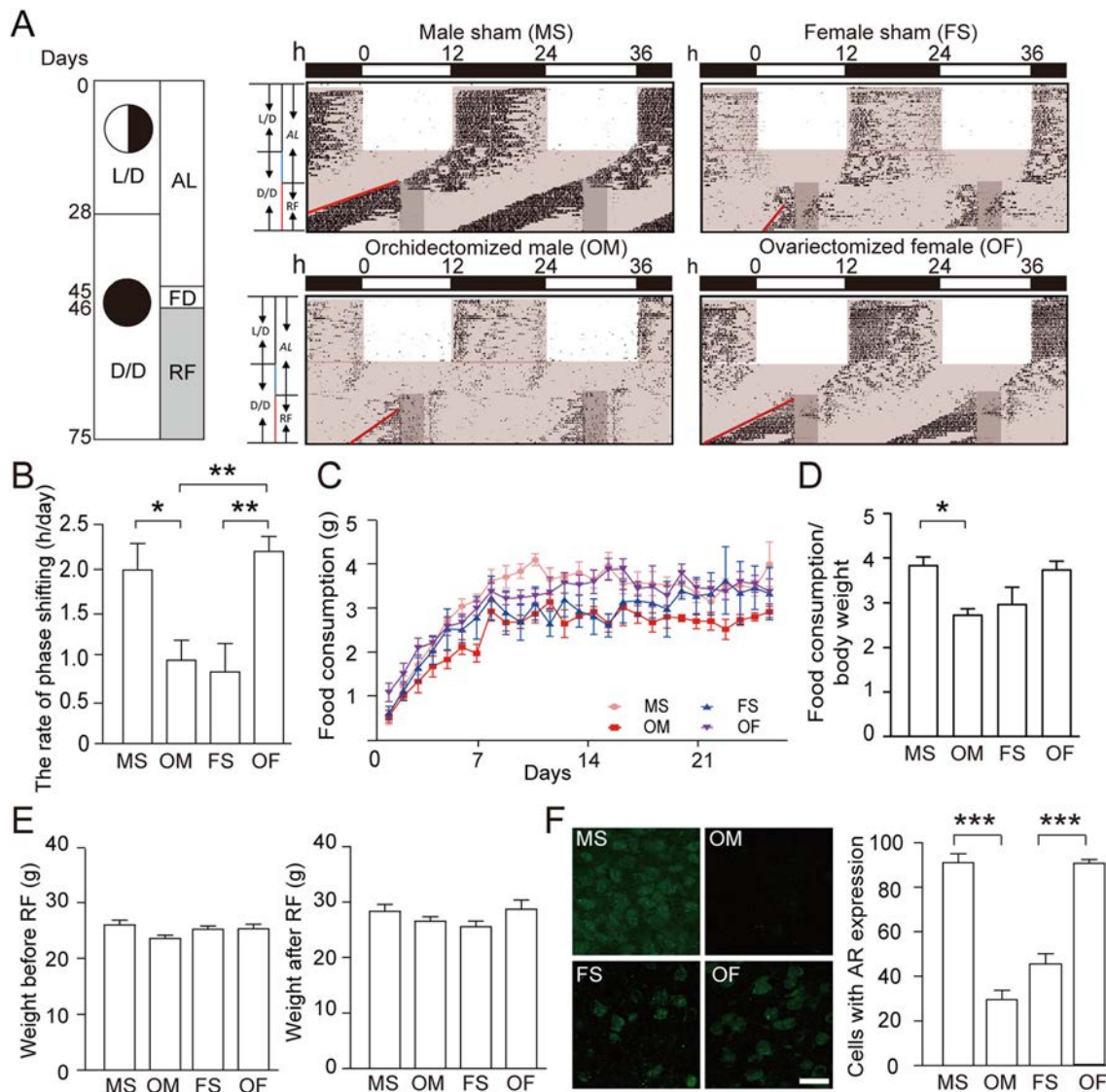


Fig. 2 Gonadectomy changes the wheel-running activity of mice under DD/RF at 4 h–9 h. **A** Representative phases of male and female mice with intact gonads (upper) or gonadectomy (lower) under DD/RF at 4 h–9 h over a period of 75 days (light grey, feeding time; light red, dark phase; $n = 8$ mice per group). **B** Phase-shifting rates of male and female mice with intact gonads or gonadectomy under DD/RF at 4 h–9 h ($n = 8$ mice per group; * $P < 0.05$, ** $P < 0.01$). **C** Daily food consumption of male and female mice with intact gonads or gonadectomy under DD/RF at 4 h–9 h ($n = 8$ mice per group).

D Average food consumption normalized to body weight of male and female mice with intact gonads or gonadectomy under DD/RF at 4 h–9 h ($n = 8$ mice per group, * $P < 0.05$). **E** Body weight of male and female mice with intact gonads or gonadectomy before and after DD/RF at 4 h–9 h ($n = 8$ mice per group). **F** Androgen receptor (AR) levels in the ventromedial core region of the SCN in male and female mice with intact gonads or gonadectomy under DD/RF at 4 h–9 h ($n = 8$ sections in 4 mice per group; *** $P < 0.001$; scale bar, 25 μm).

the time factor, three-way ANOVA; $P = 0.155$ for the gender factor; $P < 0.0001$ for the gonad function factor; $P = 0.003$ for the combined gender and gonadal function factors; Fig. S2A). Specifically, orchidectomy significantly decreased the average food consumption in male mice with DD/RF 4 h–9 h (MS vs OM, $P = 0.011$, two-way ANOVA with Tukey's multiple comparisons; Fig. 2D). However, ovariectomy had no effect on food consumption (FS vs OF, $P > 0.05$, Fig. 2D), suggesting that orchidectomy and ovariectomy affect food intake in opposite directions in the DD/RF 4

h–9 h protocol. These results suggested that gonadal hormones contribute to metabolic adaptation to restricted feeding [20] and phase shifting of wheel-running activity. Although the window of DD/RF 4 h–9 h was shorter than DD/RF 0 h–12 h, food intake under these conditions were generally comparable (Fig. S2B), and a significant difference only occurred in the OF groups (Fig. S2C). These results suggested that the time and window of restricted feeding plays an important role in the pattern of phase shifting under the DD/RF condition. In addition, we noted that neither

ovariectomy nor orchidectomy affected the body weight of mice in response to DD/RF 4 h–9 h ($P = 0.45$ before RF, for the gender factor, $P = 0.081$ for the gonadal function; $P = 0.785$ after RF, for the gender factor, $P = 0.551$ for the gonad function, two-way ANOVA; Fig. 2E).

Given that androgens are important in driving the rhythmic expression of clock genes and modulating circadian rhythms, we next examined the expression levels of the androgen receptor (AR) in the ventromedial core region of the SCN in male and female mice with DD/RF 4 h–9 h by immunofluorescence. We found that female sham mice had fewer AR-containing cells than male sham mice in the core region of the SCN (Fig. 2F), suggesting sex-specific expression of AR levels in the SCN. Moreover, we found that gonadectomy significantly changed the AR levels in the SCN of male and female mice. Specifically, OM mice showed lower AR expression than MS mice, while OF mice showed a higher level of AR than FS in the SCN (Fig. 2F; $P = 0.047$ for the gender factor; $P = 0.031$ for the gonad function; $P < 0.0001$, OF vs FS; $P < 0.0001$, OM vs MS, two-way ANOVA with Tukey's multiple comparisons), suggesting that AR expression levels in SCN can be affected by circulating hormone levels induced by gonadectomy. Considering that the gonadal hormone levels can interact with the SCN master clock, leading to sex difference in behavioral and physiological processes related to circadian rhythm, the results suggested the potential contribution of AR on the circadian rhythm induced by DD/RF.

In summary, for the first time, we found that restricted feeding under constant darkness can adjust and even synchronize the endogenous clock in female mice, while the phase shifting of the circadian rhythm is slightly affected in male mice. Gonadectomy significantly altered the shifting rate of male and female mice induced by RF. The differential expression of AR in the ventromedial core region of the SCN in male and female mice may contribute to the shifting of the circadian rhythm induced by restricted feeding under constant darkness though its role needs to be further explored. Nevertheless, our findings indicate that male and female mice respond to and adapt to environmental timing cues differently due to their gonadal hormones, suggesting that their circadian systems are adjusted in a sex-specific context. Our findings may have wide implications in differentially correcting circadian disturbances in men and women by external timing cues.

Acknowledgements This work was supported by the National Natural Science Foundation of China (32070590, 31871191, and 32071156), and the Key Scientific Project of Guangdong Province (2018B030335001).

Conflict of interest The authors declare that they have no conflict of interest.

References

- Bu B, He W, Song L, Zhang L. Nuclear envelope protein MAN1 regulates the drosophila circadian clock *via* period. *Neurosci Bull* 2019, 35: 969–978.
- Panda S. Circadian physiology of metabolism. *Science* 2016, 354: 1008–1015.
- Takahashi JS. Transcriptional architecture of the mammalian circadian clock. *Nat Rev Genet* 2017, 18: 164–179.
- Albrecht U, Sun ZS, Eichele G, Lee CC. A differential response of two putative mammalian circadian regulators, *mper1* and *mper2*, to light. *Cell* 1997, 91: 1055–1064.
- Sun ZS, Albrecht U, Zhuchenko O, Bailey J, Eichele G, Lee CC. RIGUI, a putative mammalian ortholog of the *Drosophila* period gene. *Cell* 1997, 90: 1003–1011.
- Logan RW, McClung CA. Rhythms of life: circadian disruption and brain disorders across the lifespan. *Nat Rev Neurosci* 2019, 20: 49–65.
- Musiek ES, Holtzman DM. Mechanisms linking circadian clocks, sleep, and neurodegeneration. *Science* 2016, 354: 1004–1008.
- Greenhill C. Benefits of time-restricted feeding. *Nat Rev Endocrinol* 2018, 14: 626.
- Wehrens SMT, Christou S, Isherwood C, Middleton B, Gibbs MA, Archer SN. Meal timing regulates the human circadian system. *Curr Biol* 2017, 27(1768–1775): e1763.
- Asher G, Sassone-Corsi P. Time for food: the intimate interplay between nutrition, metabolism, and the circadian clock. *Cell* 2015, 161: 84–92.
- Akiyama M, Yuasa T, Hayasaka N, Horikawa K, Sakurai T, Shibata S. Reduced food anticipatory activity in genetically orexin (hypocretin) neuron-ablated mice. *Eur J Neurosci* 2004, 20: 3054–3062.
- Li Z, Wang Y, Sun KK, Wang K, Sun ZS, Zhao M, *et al.* Sex-related difference in food-anticipatory activity of mice. *Horm Behav* 2015, 70: 38–46.
- Mei Y, Zhang J, Li Z, Teng H, Wang Y, Sun Z. Altered expressions of memory genes in food-entrained circadian rhythm. *Acta Biochim Biophys Sin (Shanghai)* 2018, 50: 1068–1071.
- White W, Timberlake W. Two meals promote entrainment of rat food-anticipatory and rest-activity rhythms. *Physiol Behav* 1995, 57: 1067–1074.
- Stokkan KA, Yamazaki S, Tei H, Sakaki Y, Menaker M. Entrainment of the circadian clock in the liver by feeding. *Science* 2001, 291: 490–493.
- Achamrah N, Nobis S, Goichon A, Breton J, Legrand R, do Rego JL, *et al.* Sex differences in response to activity-based anorexia model in C57Bl/6 mice. *Physiol Behav* 2017, 170: 1–5.
- Storch KF, Weitz CJ. Daily rhythms of food-anticipatory behavioral activity do not require the known circadian clock. *Proc Natl Acad Sci U S A* 2009, 106: 6808–6813.
- Damiola F, Le Minh N, Preitner N, Kornmann B, Fleury-Olela F, Schibler U. Restricted feeding uncouples circadian oscillators in peripheral tissues from the central pacemaker in the suprachiasmatic nucleus. *Genes Dev* 2000, 14: 2950–2961.
- Mendoza J, Graff C, Dardente H, Pevet P, Challet E. Feeding cues alter clock gene oscillations and photic responses in the suprachiasmatic nuclei of mice exposed to a light/dark cycle. *J Neurosci* 2005, 25: 1514–1522.
- Naukam RJ, Curtis KS. Estradiol and body weight during temporally targeted food restriction: Central pathways and peripheral metabolic factors. *Horm Behav* 2019, 115: 104566.



Recent Progress in Non-motor Features of Parkinson's Disease with a Focus on Circadian Rhythm Dysregulation

Yufei Liu^{1,2} · Long Niu^{1,2} · Xinyao Liu^{1,2} · Cheng Cheng^{1,2} · Weidong Le^{1,2,3} 

Received: 25 August 2020 / Accepted: 31 March 2021 / Published online: 15 June 2021

© Center for Excellence in Brain Science and Intelligence Technology, Chinese Academy of Sciences 2021

Abstract Parkinson's disease (PD) is the second most common neurodegenerative disease, which manifests with both motor and non-motor symptoms. Circadian rhythm dysregulation, as one of the most challenging non-motor features of PD, usually appears long before obvious motor symptoms. Moreover, the dysregulated circadian rhythm has recently been reported to play pivotal roles in PD pathogenesis, and it has emerged as a hot topic in PD research. In this review, we briefly introduce the circadian rhythm and circadian rhythm-related genes, and then summarize recent research progress on the altered circadian rhythm in PD, ranging from clinical features to the possible causes of PD-related circadian disorders. We believe that future comprehensive studies on the topic may not only help us to explore the mechanisms of PD, but also shed light on the better management of PD.

Keywords Circadian rhythm dysregulation · Circadian rhythm gene · Parkinson's disease · REM sleep behavior disorder · Dopamine

Abbreviations

PD	Parkinson's disease
DA	Dopamine
SCN	Suprachiasmatic nucleus
Clock	Circadian locomotor output cycles kaput
Bmal1	Brain and muscle Arnt-like protein 1
Per	Period
Cry	Cryptochrome
NPAS2	Neuronal PAS domain protein 2
ROR	Retinal related orphan receptor
RREs	ROR response elements
NR1D1	Nuclear receptor subfamily 1 group D member 1
Bhlhe	Basic helix-loop-helix family member
Tim	Timeless
DBP	D-box-binding protein
REM	Rapid eye movement
RBD	Rapid eye movement sleep behavior disorder
BP	Blood pressure
CBT	Core-body temperature
HRV	Heart rate variability
GI	Gastrointestinal
MRI	Magnetic resonance imaging
PET	Positron emission tomography
SPECT	Single photon emission computed tomography
NURR1	Nuclear receptor-related 1 protein
TH	Tyrosine hydroxylase
EDS	Excessive daytime sleepiness
RLS	Restless leg syndrome
MIBG	Meta-iodobenzylguanidine
PSG	Polysomnograph
MSE	Multiscale entropy
NREM	Non-REM
CAP	Cycling alternating pattern

✉ Weidong Le
wdle_sibs@163.com

¹ Liaoning Provincial Key Laboratory for Research on the Pathogenic Mechanisms of Neurological Diseases, the First Affiliated Hospital, Dalian Medical University, Dalian 116021, China

² Liaoning Provincial Center for Clinical Research on Neurological Diseases, the First Affiliated Hospital, Dalian Medical University, Dalian 116021, China

³ Institute of Neurology, Sichuan Academy of Medical Science-Sichuan Provincial Hospital, University of Electronic Science and Technology of China, Chengdu 610072, China

6-OHDA	6-Hydroxydopamine
MPTP	1-Methyl-4-phenyl-1,2,3,6-tetrahydropyridine
Mn	Manganese
SIRT1	Silent information regulator 1
HSF1	Heat shock factor 1
RT-qPCR	Real-time quantitative polymerase chain reaction
HPLC	High-performance liquid chromatography
WB	Western blotting
RIPD	Rotenone-induced PD
LPS	Lipopolysaccharides
ROT	Rotenone
ATG5	Autophagy-related gene 5
AMPK	Adenosine 5'-monophosphate (AMP)-activated protein kinase
ATP	Adenosine 5'-triphosphate
ASO	Alpha-synuclein overexpressing
IHC	Immunohistochemical staining
ELISA	Enzyme linked immunosorbent assay
MSP	Methylation-specific PCR
PCR-RFLP	Polymerase chain reaction-restriction fragment length polymorphism
PPAR γ	Peroxisome proliferator-activated γ

Introduction

Parkinson's disease (PD) is the second most common neurodegenerative disease, affecting 1% of people aged over 60, and 3% of those older than 80 years [1, 2]. Many genetic and environmental factors have been identified to be involved in the extremely complicated pathogenesis of PD [3]. The degeneration of dopamine (DA) neurons in the substantia nigra and the deposition of Lewy bodies containing α -synuclein are its main pathological features [4, 5]. Clinically, PD is characterized by a wide range of motor symptoms (such as resting tremor, rigidity, bradykinesia, and postural and gait disturbance) and non-motor symptoms (such as mental and cognitive disorders, autonomic dysfunction, sensory impairment, and especially sleep disorders) [4, 6]. So far the diagnosis of PD mainly relies on the presence of motor symptoms as the disease progresses, but it is difficult to make an early diagnosis of this disease, since there are still no specific blood or other laboratory tests [7, 8]. Non-motor symptoms of PD usually occur earlier than motor symptoms and have been accepted as a promising research topic due to their close correlations with the progress of PD pathology [8], which may help the early diagnosis and treatment of PD [8, 9].

Non-motor symptoms of PD include sleep disorders, emotional disorders, autonomic dysfunction, neuroendocrine dysregulation and gastrointestinal (GI) dysfunctions [8]. Sleep disorders in PD patients usually manifest with disturbances of sleep structure and disorders of the sleep-wake cycle, mainly presenting with rapid eye movement (REM) sleep behavior disorder (RBD), restless legs syndrome (RLS), and excessive daytime sleepiness (EDS) [10–12]. Emotional disorders in PD include depression, anxiety, increased agitation, aggression, restlessness, and delirium [13]. Autonomic dysfunctions in PD include disturbances of the rhythm of blood pressure (BP), heart rate variability (HRV), and core-body temperature (CBT) [14–17]. Neuroendocrine function in PD is also disturbed and manifested by dysregulated hormones secretion [18]. The entire GI tract function is disturbed in PD patients featuring drooling, swallowing problems, delays in gastric emptying, and constipation [19, 20].

Interestingly, almost all non-motor symptoms in PD are associated to a certain extent with an impaired circadian rhythm [20]. Circadian rhythm is controlled by the neuronal circadian oscillators located in the central suprachiasmatic nucleus (SCN) of the hypothalamus and is executed by the interaction network of various circadian rhythm genes in almost all organs and tissues [21–23]. In this review, we update recent progress on the non-motor symptoms, pathologies, diagnosis, auxiliary examinations and treatments of PD, with a focus on circadian rhythm dysregulation. The implications of imaging and the electroencephalogram (EEG) for PD diagnosis are highlighted, and the impacts of pharmacological and non-pharmacological therapy for PD on the circadian rhythm system are also discussed. In addition, we present the recent findings on the alteration of circadian rhythm genes in PD, which may help us understand the mechanism of circadian rhythm dysregulation in this devastating disease. Our review provides an insight into the important roles of circadian rhythm dysregulation in PD pathogenesis and may help to establish a new diagnostic strategy for this disease.

Circadian Rhythm and Circadian Rhythm Genes

Circadian rhythms are 24-h cycles that are part of the body's internal clock, running in the background to carry out essential functions and processes [24]. The circadian rhythm modulates many physiological processes including CBT, BP, pulse rate, oxygen consumption, hormone levels, metabolism, sleep-wake cycles, and GI function [20, 23]. The circadian rhythm is mostly governed by the pacemaker neurons in the SCN, and is regulated by various circadian rhythm genes distributed in almost all organs and tissues [21, 25, 26]. So far, many circadian rhythm genes have been identified, including circadian locomotor output cycle

kaput (CLOCK), brain and muscle Arnt-like protein 1 (BMAL1, also called aryl hydrocarbon receptor nuclear translocator-like), period (PER, including 3 homologs PER1, PER2, and PER3), cryptochrome (CRY, including CRY1 and CRY2), neuronal PAS domain protein 2 (NPAS2), retinoic acid related orphan receptor (ROR, including ROR α , ROR β , and ROR γ), nuclear receptor subfamily 1 group D member 1 (NR1D1, also called Rev-erb α), basic helix-loop-helix family members e40 and e41, timeless (TIM), D-box-binding protein (DBP), and casein kinases 1 and 2 [21].

These circadian rhythm genes interact with each other to form complex networks, mainly *via* negative feedback loops, to maintain the homeostasis of the circadian rhythm at the levels of transcription, translation, and post-translation [21, 22]. It has been reported that at the beginning of the night, the expression of Per and Tim is activated by Clock/Bmal1 heterodimer, and at the end of the night, Per and Tim proteins are synthesized to form heterodimers [27, 28]. Per, Tim, or the Per/Tim heterodimer somehow restrain the activity of Clock and Bmal1 and their own transcription by entering the nucleus [27, 28]. CLOCK and BMAL1, two well-known control genes of the family of basic helix PAS transcription factors, guide the transcriptions of related genes and activate the expressions of PER and CRY genes to form heterodimers [29–31]. Once Per and Cry proteins accumulate to a certain level, they form a complex with Clock/Bmal1 heterodimer, thus inhibiting the transcription of their own genes [29–31]. At night, the Per/Cry complex is degraded to start another cycle [29–31]. DA can induce the expression of Per2 by promoting transcription of the Clock/Bmal1 complex [32]. NPAS2 promotes the expression of ROR α and nuclear receptor Rev-erb α , main regulators of Bmal1 expression [33], to regulate the activity of the Clock/Bmal1 heterodimer [34]. The underlying mechanism is that these receptors bind to the ROR response elements (RREs) located in the Bmal1 promoter, activate Bmal1 transcription through RORs, and inhibit Bmal1 transcription through Rev-erbs, leading to a Bmal1 rhythm [13, 34, 35] (Fig. 1). Changes in the expression spectrum or functions of circadian rhythm genes may result in a circadian rhythm dysregulation [36].

Circadian Rhythm Dysregulation in Parkinson's Disease

Almost all non-motor symptoms in PD are associated with impaired circadian rhythm [20]. Recently, increasing lines of evidence suggested that circadian rhythm dysregulation acts as the chief culprit leading to the non-motor symptoms of PD [20] (Fig. 1), especially sleep-wake disorders. The sleep-wake cycle is one of the most important and well-known circadian rhythms, regulated by the hypothalamus

and reticular formation [8, 37]. About 60%–70% of PD patients suffer from sleep disorders [10–12]. Among the various sleep disorders, RBD is a potential early sign of PD and a parasomnia characterized by abnormal behaviors and loss of muscle atonia, manifesting in the main forms related to the REM-related dream-world of vocalizations, jerks, and motor behaviors during REM sleep [12, 38, 39]. RBD has a low incidence in the normal population but a high incidence in PD patients [40], causing a greater burden for care-givers and a higher mortality rate [40, 41]. The physiological nocturnal increase in REM sleep duration is lost in patients with PD and the increase of REM frequency across the night in PD patients with RBD is lost, supporting an alteration in the circadian system in RBD of PD patients [42]. Polysomnography reveals abnormal skeletal muscle atonia during RBD and consequently dream-enactment behavior marked by various redundant motor activity ranging from simple limb twitches to violent, complicated movements that may cause injury to the patient and/or the sleeping partner [10]. These behaviors can arise as early as 90 min after the first REM sleep episode, and occur more likely during a sleep session when REM sleep is more frequent, especially in the morning [12, 43]. RBD, as a potent predictor of PD and contributor to a poor prognosis, is more specific than any of the other prodromal markers of PD [38, 40].

RLS is also a frequent sleep disorder in PD [44]. Patients with RLS are characterized by the symptoms of moving the legs with or without sensory alterations which worsen at rest or with diminished activity and improve with movement, usually worse at night and in the evening [45, 46]. The diagnosis of RLS requires the patient's symptoms to show circadian variation [47]. It has been reported that the rhythm of melatonin may be involved in RLS circadian variability [47, 48]. RLS patients who take melatonin in the evening often experience worse RLS symptoms, and bright light exposure may decrease melatonin secretion and reduce RLS motor symptoms [48]. EDS is also a common manifestation of sleep disorders in PD. Patients with EDS exhibit the most prominent impairment in circadian melatonin secretion, indicating an important role of circadian regulation in the manifestation of the EDS associated with PD [49].

PD patients who are often disturbed by disrupted sleep-wake circadian cycles and poor sleep quality may manifest emotional disorders including depression and anxiety [50]. Sleep, especially REM, is a process of emotional and brain homeostasis, optimally preparing the whole-body organs for the restoration of social and emotional function for the next day [51, 52]. Emotional disorders also affects subsequent sleep quality, especially the REM latency and REM duration, probably as a consequence of emotionally stressful events [53]. Approximately 45% of patients with

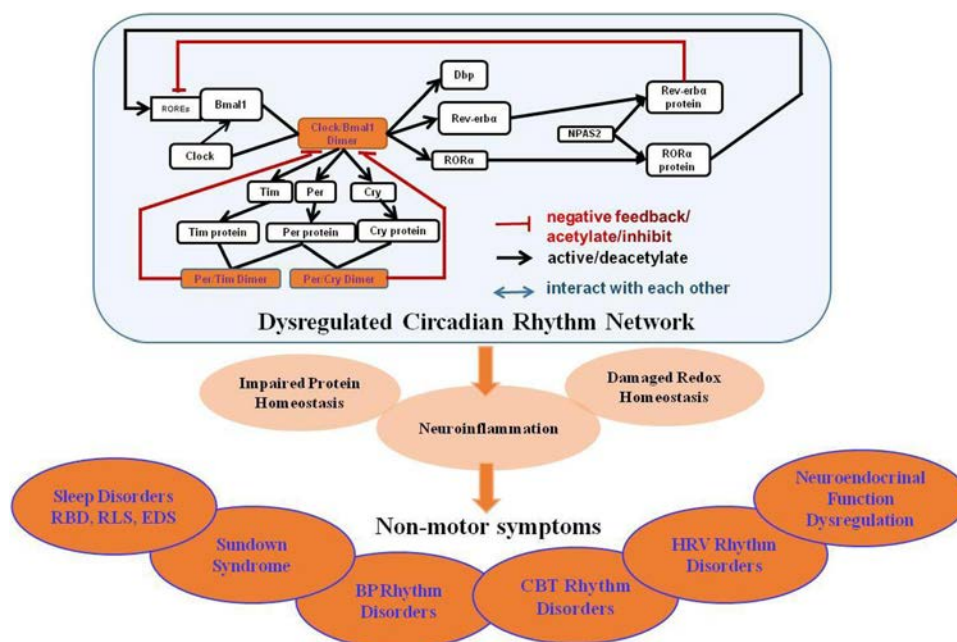


Fig. 1 Dysregulated circadian rhythm network in Parkinson's disease. Circadian rhythm genes interact with each other to form a complex network. The Clock/Bmal1 heterodimer activates Per and Tim gene expression, and the Per and Tim proteins form heterodimers. Per, Tim, or Per/Tim heterodimer restrains Clock and Bmal1 activity and their transcription. The Clock/Bmal1 heterodimer activates Per and Cry gene expression to form heterodimers. Once Per and Cry proteins accumulate to a certain extent, they form complexes with Bmal1/Clock heterodimers, and inhibit their own transcription. Then, the Per/Cry inhibitory complex degrades into the next cycle. NPAS2 mediates Bmal1 expression *via* the acid-related orphan receptor ROR α and Rev-erb α , and further regulates the activity of Clock/Bmal1 heterodimers. These receptors bind with

retinoic acid-related orphan nuclear receptor response elements, which are located in the Bmal1 promoter, activate Bmal1 transcription through RORs and inhibit Bmal1 transcription through Rev-erb α . Circadian rhythm dysregulation may impact PD through the induction of neuroinflammation, impaired protein homeostasis, and redox homeostasis, manifested by various non-motor symptoms including sleep disorders such as RBD, RLS, EDS, sundown syndrome, BP rhythm disorders, CBT rhythm disorders, HRV rhythm disorders, neuroendocrine function dysregulation, and GI dysfunction. *RBD* rapid eye movement sleep behavior disorder, *BP* blood pressure, *CBT* core-body temperature, *HRV* Heart rate variability, *RLS* restless leg syndrome, *EDS* excessive daytime sleepiness, *GI* gastrointestinal.

PD suffer from depression, and 50% experience comorbidity of anxiety [54, 55]. Increasing lines of evidence have shown that depression and anxiety are associated with circadian rhythm dysregulation in PD patients [56, 57]. 'Sundown syndrome', also referred to as 'nocturnal delirium', which is used to describe mood disorders peaking in the late afternoon or evening in a daily pattern, can be found in PD [13], implying a strong relationship between circadian rhythm dysfunction and mood regulation impairment in patients with PD [58, 59]. Anxiety has been considered to be related to the pathology of the basal ganglia with DA and noradrenaline as the responsible neurotransmitters [8]. DAergic neurons in the midbrain ventral area innervate the prefrontal cortex, which is implicated in PD patients with mood disorders [59]. It has been reported that circadian rhythm dysregulation exacerbates DAergic neuronal loss in animal models of PD [60]. RRE overlaps with nerve growth factor inducible-B response element (NBRE), which is recognized by the nuclear receptor-related 1 protein (NURR1) in the tyrosine hydroxylase (TH) promoter [59, 61]. REV-ERB α

antagonizes NURR1-induced activation of the TH promoter *via* binding to RRE/NBRE, driving circadian TH expression to regulate the circadian rhythmicity of the DAergic system [59, 61]. Rev-erb α is a key upstream regulator circadian rhythm gene to regulate mood *via* controlling the circadian rhythm of the DAergic system, suggesting that it is a potential therapeutic target for those PD patients with comorbid mood disorders [59, 61]. Polymorphisms of circadian rhythm genes have been shown to be associated with depression in PD patients [57]. Animal models of PD with emotional disorders need to be developed to explore the interaction between circadian rhythm dysregulation and emotion [56].

PD patients often manifest characteristic changes in the circadian rhythm of BP [14, 62, 63]. Nocturnal hypertension and postprandial hypotension are distinctive features in PD patients [14]. The difference between daytime and night-time BP is significantly smaller in PD than healthy control subjects [63]. In addition, the difference of CBT between the daytime and night is also significantly reduced in PD patients [17]. Moreover, the CBT change is

significantly and negatively related to the severity of RBD [17]. Recently, it has been reported that changes in the thermo-regulatory circadian rhythm are associated with RBD rather than α -synucleinopathy [64], which may provide a prognostic means of evaluating the risk of developing PD in patients with idiopathic RBD (iRBD) [17, 65].

HRV is an index for measuring the autonomic, especially parasympathetic, functions [66]. A significantly decreased HRV has been found in PD patients all day but more severe at night [15, 16]. Moreover, this phenomenon becomes more profound with the motor symptoms, implying impaired autonomic, especially parasympathetic, cardiovascular regulation in PD [15, 16, 67, 68]. Moreover, HRV is significantly attenuated in patients with iRBD in the waking state, also indicating abnormalities of autonomic function in RBD [68]. Considering the important roles of iRBD in PD [65], the clinical value of impaired HRV as an early sign of cardiovascular autonomic circadian rhythm in PD should be emphasized [15, 68].

Neuroendocrine function has also been correlated with circadian rhythm. Circadian rhythmic regulation of melatonin secretion is blunted in PD, as shown by the decreased amplitude of the melatonin rhythm and the reduced 24-h secreted melatonin level [49]. Breen *et al.* proposed that the degenerative changes of the neural structures controlling pineal function, especially the hypothalamic gray matter volume loss, are responsible for the reduced melatonin, which might be associated with the severity of PD [69]. These findings provide anatomical and physiological evidence of an intrinsic sleep and circadian phenotype [69]. In PD, after DAergic treatment, the secretion of melatonin is profoundly increased [70]. Despite melatonin, the circadian rhythm of cortisol secretion as a sensitive marker of circadian function is also influenced in PD [20]. At approximately 01:00, cortisol begins to rise with a peak at approximately 06:00, then declines with some small fluctuations; this trend also occurs in normal healthy volunteers, but the secretory pattern in PD patients from 18:00 to 01:00 tends to be flatter [18]. This curve indicates that cortisol release retains its daily rhythmic pattern but the total diurnal amount of cortisol secretion is elevated in PD [18]. This disturbed circadian rhythm of hormone secretion results in endocrine imbalance and has been demonstrated to be associated with the impaired alertness and sleep disorders of PD [18, 49].

GI dysfunction in PD has also been associated with circadian rhythm dysregulation [71]. PD patients without GI dysfunction show a higher plasma melatonin concentration than those with GI dysfunction [72]. Researchers have found that the GI tract is the largest organ to produce exogenous melatonin other than the pineal gland, and

melatonin may serve important GI barrier functions [72, 73]. This implies a certain relationship between GI dysfunction and circadian rhythm dysregulation in PD [72].

Although increasing evidence has predicted potential correlations between circadian rhythm dysregulation and motor and/or non-motor symptoms fluctuations, the underlying pathological mechanisms are still far from being clearly investigated [74]. It has been hypothesized that circadian rhythm dysregulation impacts PD via the induction of neuroinflammation, impaired protein homeostasis, and redox homeostasis [75, 76]. Circadian rhythm dysregulation can trigger strong neuroinflammation and degeneration of the nigral DAergic neuronal system, exacerbating the motor deficit, as an environmental risk factor for PD development [60, 76]. Interestingly, α -synuclein is rhythmic in various tissues and the synuclein-interacting protein synphilin shows a strong circadian rhythm in the brain [77]. Circadian rhythm dysregulation may contribute to PD with aberrant α -synuclein aggregation [77]. Another study has proposed that circadian rhythm disturbs the redox homeostasis resulting in PD [78].

Changes of Imaging and Electroencephalogram in Parkinson's Disease Patients with Circadian Rhythm Dysregulation

While the current diagnosis of PD mainly depends on clinicians' subjective judgment of clinical symptoms, imaging and the EEG may provide assistance in the early diagnosis and detection of PD pathology [79]. Structural and functional magnetic resonance imaging (MRI), positron emission tomography (PET)/single photon emission computed tomography (SPECT), and cardiac uptake of ^{123}I -labeled meta-iodobenzylguanidine (MIBG) scintigrams are commonly used for PD diagnosis [80, 81]. The circadian rhythm modulates the neuronal activity in specific areas and widespread networks across the brain. Imaging and the EEG can present some of these abnormalities that are directly related to the ongoing neurodegeneration in the brain of patients with PD [82].

In structural imaging, alterations of gray matter and white matter in PD are usually identified [83]. White matter changes are usually associated with circadian autonomic dysfunctions, including HR and BP variability [84]. Circadian rhythm dysregulation of melatonin levels is associated with significant hypothalamic gray matter volume loss and the severity of PD, which may provide anatomical and physiological evidence for circadian rhythm dysfunction in PD [69]. The reduced thalamic volume in PD patients with RBD suggests a pathophysiological role of the thalamus the underlying mechanism [85]. Sleep impairment in PD patients has also been determined in association with widespread white matter disintegration

[86]. Specifically, PD patients with nocturnal hallucinations often exhibit a prominently reduced basal ganglia volume [87]. PD patients with sleep impairment display smaller cortical thickness in more extensive areas, including the bilateral frontoparietal and lateral temporal regions [86]. Reduced gray matter volume has been detected in PD patients with EDS and RLS [83]. Despite structural imaging, functional MRI is widely used to measure the functional changes in patients suffering from sleep impairment by estimating the abnormal patterns of brain connectivity [88]. As a whole, during the basic process of circadian rhythm patterns, basal ganglia dysfunction can lead to a more complex signal in task-relevant areas, such as the planum temporale and the inferior parietal lobule, and in the sequential activation of brain areas, circadian rhythm onset may result in high activity in the saliency network and widespread motor areas, and the caudate nucleus in patients with PD [82].

Combined with molecular imaging including PET and SPECT, these methods are often used to investigate the striatal DAergic function by measuring the extent of neuronal loss in PD [83]. A more severe deafferentation in the caudate of PD patients with RBD compared to those without RBD has been reported [80, 89], and the putamen DAergic function is more severely damaged in PD patients with RBD than those without RBD [80, 89]. PD patients with RBD exhibit more severe striatal DAergic deficiency, indicating a strong association between the presynaptic DAergic defect and RBD [83]. Molecular imaging reveals negative correlations between metabolic activity and DAergic function of the caudate and the severity of EDS [83]. Other than the DAergic system, cholinergic deficiency has been detected in PD patients with RBD, and the iron level is altered in PD patients with RLS [83]. Interestingly, cardiac uptake in 123I-labeled MIBG scintigrams, which measures the function of cardiac sympathetic neurons, has revealed a significant correlation between the systemic BP circadian patterns and cardiac 123I-MIBG uptake in patients with PD [90]. Furthermore, cardiac uptake of 123I-labeled MIBG is decreased in PD patients with clinical RBD compared to those with subclinical RBD and without sleep disorders [91, 92].

Neuroelectrophysiological examination is becoming another important technique for detecting the sleep disorders in PD [93, 94]. Polysomnography can be used to monitor the whole-night EEG followed by multiscale entropy (MSE) analysis [93]. PD patients usually show longer sleep latency and a higher spontaneous EEG arousal index [93]. During non-REM (NREM) sleep, the stage-specific MSE is increased in PD [93]. Cycling alternating pattern is a sensitive marker of the early NREM sleep instability of sleep microstructure altered in PD [94]. EEG α and σ activity are often increased during NREM sleep at

an early stage of PD [95]. Disruption of REM sleep homeostasis has also been reported in PD with high θ/α (7.8 Hz–10.5 Hz) frequency during 23.00 to 01.40 at night [96]. Moreover, local field potentials of subthalamic nucleus activity are significantly increased for β power values during REM sleep.

While neuroimaging provides spatial evidence about the structural and functional basis of circadian rhythm dysregulation, neuroelectrophysiological examination is usually a supplement for neuroimaging measurement, considering its high temporal resolution [97, 98]. Both are useful tools to determine the changes of PD-related circadian rhythm dysregulation, and may serve as potential biomarkers to help the early diagnosis of PD.

Altered Circadian Rhythm Genes in Animal Models of Parkinson's Disease

Increasing lines of evidence have revealed the altered expression of circadian rhythm genes in various animal models of PD (as summarized in Table 1), including 6-hydroxydopamine (6-OHDA) and 1-methyl-4-phenyl-1,2,3,6-tetrahydropyridine (MPTP)-lesioned rodents, and transgenic animal models [99, 100]. For example, decreased *Bmal1* and increased *ROR α* have been reported in the brain of 6-OHDA model mice [101]. Repeated Mn^{2+} administration produces abnormal circadian rhythm gene expression in the brain, together with non-motor symptoms and PD-like motor impairments in mice [102].

The MPTP marmoset model of PD shows a significant sleep disturbance remarkably similar to PD patients manifesting with sleep-onset insomnia and disturbances in the circadian rhythm [103]. Circadian rhythm alterations in MPTP-induced DAergic nigro-striatal system lesions in non-human primates have been evaluated by *in vivo* PET and *post-mortem* TH and DA transporter quantification [104]. Interestingly, in the light-dark cycle, MPTP-treated non-human primates show rest-wake locomotor rhythms, although DA-depleted non-human primates exhibit low amplitude, decreased stability, and increased fragmentation [104]. When the circadian system is exposed to constant light, controls are less influenced whereas in DA-depleted non-human primates, locomotor rhythms are severely disturbed or completely abolished together with unaltered hormonal rhythms [104]. Expression of the circadian rhythm in MPTP monkeys requires environmental timing cues [104]. In other words, the central circadian rhythm in the SCN remains complete in PD primates with DA lesions, but in the absence of regulation by light, circadian rhythmic processes of striatal and DAergic functions that control locomotor output are unable to drive [104]. The circadian rhythm system of the sleep-wake disturbances in PD is more profoundly affected than previously thought.

Table 1 Altered circadian rhythm genes in animal models and patients with Parkinson's disease.

PD models	Samples	Methods	Results and conclusions	References
Rats induced by 6-OHDA	Striatum	RT-qPCR; WB	Bmal1, Per2↓, Rorα↑. A link between attenuated antioxidative response and circadian dysregulations in PD.	Wang <i>et al.</i> [101]
Rats induced by 6-OHDA treated with levodopa	Striatum, SCN, Plasma	RT- qPCR; ELISA; HPLC	After levodopa treatment, Bmal1↓, peak of Per2 delayed, cortisol secretion↑, melatonin↓	Li <i>et al.</i> [163]
RIPD rats	Substantia nigra	RT-qPCR; WB	Bmal1, Clock, NPAS2, Per1 and Per2, Rev-erbα and DBP↓. Chronic low-grade neuroinflammation aggravates circadian dysregulation in RIPD rats.	Li <i>et al.</i> [110]
Mul1A6 and park1 mutants <i>Drosophila</i>	Brain	RT-qPCR; IHC; WB	Mul1 and park mutations disrupt Per, Tim, and Clock normal circadian rhythmic expression during the day. ATG5↓, autophagy involved in circadian dysregulation	Doktór <i>et al.</i> [27]
MPTP mouse	SCN	Bioluminescence, RT-PCR	Bmal1, Cry1, Rev-erbα↓, activation of AMPK causes circadian dysfunction	Hayashi <i>et al.</i> [152]
Rats injected with Mn ²⁺	Hypothalamus	RT-qPCR; IHC	Bmal1, Clock, NPAS2, Cry1, Per1 and Per2↓, Nr1d1 and DBP↑. Mn ²⁺ administration produces abnormal circadian rhythm gene expression	Li <i>et al.</i> [102]
ASO transgenic mice	SCN	IHC	Per2 expression is not altered in the SCN of ASO mice, weakening of circadian output is a core feature of PD	Kudo <i>et al.</i> [99]
17 PD patients	PBL	RT-qPCR	Bmal1, Bmal2↓.The relative Bmal1 level correlates positively with PD severity	Cai <i>et al.</i> [132] Ding <i>et al.</i> [133]
239 PD patients	PBL	ELISA, RT-qPCR	Serum cortisol level↑, circulating melatonin level↓	Breen <i>et al.</i> [6]
206 PD patients	PBL	MSP and sequencing	Methylation only detected in the CRY1 and NPAS2 promoters. NPAS2 hypomethylation detected in PD vs control	Lin <i>et al.</i> [134]
480 PD patients	PBL	PCR-RFLP	Polymorphism of Tef rs738499 is associated with depression symptoms in PD	Hua <i>et al.</i> [57]
1394 PD patients	PBL	Illumina GoldenGate chips	Genetic polymorphisms in Bmal1 and Per1 genes contribute to PD	Gu <i>et al.</i> [136]
646 PD patients	PBL	Competitive allele-specific PCR	CLOCK 311T/C variant can be an independent risk factor for motor fluctuation and sleep disorders in PD	Lou <i>et al.</i> [138]

The animal models of PD as well as the number of patients with PD, the tissues, methods of examination, and the conclusions in each study are displayed

In addition, the relationship between circadian rhythm genes and PD pathology has become a hot research topic (Fig. 2). Based on recent discoveries of circadian rhythm gene networks associated with PD, a clear linkage has been found between the antioxidative response and circadian rhythm gene networks [101, 105]. For example, the melatonin rhythm modulates the daily rhythmic expression and activity of several antioxidant enzymes; at night, melatonin promotes the activity of glutathione peroxidase, a free radical scavenger, and increases the levels of oxidized glutathione [105]. Per2 is decreased in mice injected with 6-OHDA [101], whereas Cry1 binds to the Clock/Bmal1 complex and inhibits Clock/Bmal1-dependent transcription of Per2, therefore attenuating the

antioxidative response in PD [106]. Silent information regulator 1 (SIRT1), a highly conserved nicotinamide adenine dinucleotide (+)-dependent class III deacetylase, deacetylates Bmal1 and Per2 and exerts protective effects against PD [101, 107]. The SIRT1 activator resveratrol reverses the 6-OHDA-induced damage of antioxidative activity in PD models by decreasing the acetylation of Bmal1 [101]. Interestingly, light entrainment including impaired masking, entrainment, and re-entrainment are affected in the SCN of human mutant A53T-SNCA transgenic mice [108]. This is associated with reduced vesicular glutamate transporter 2 immunoreactivity in the SCN, indicating affected glutamatergic signaling of retinal ganglion cells, which contributes to the input into the

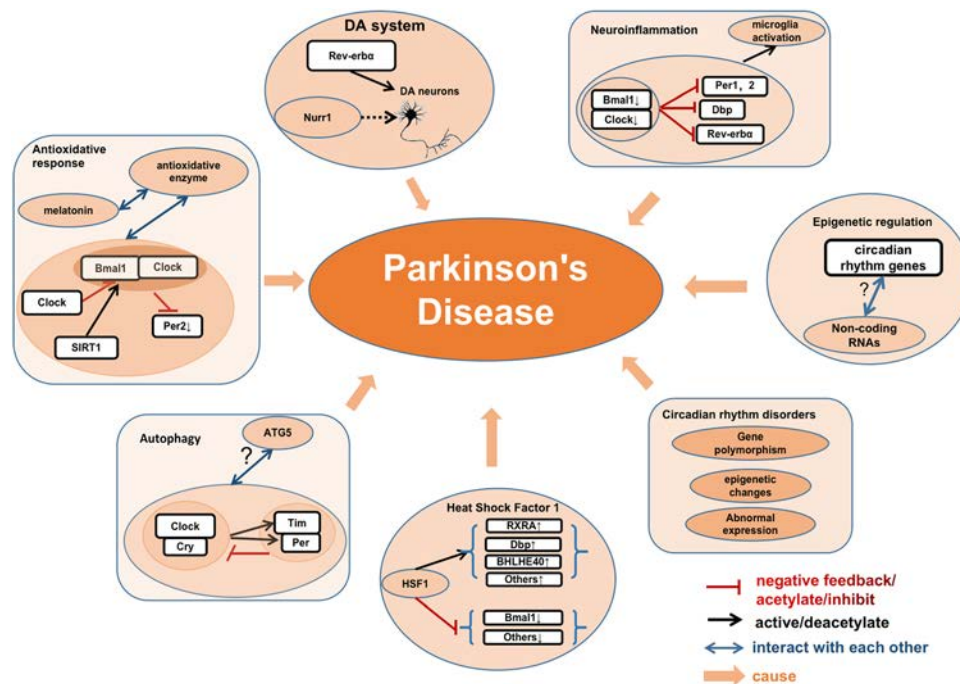


Fig. 2 Circadian rhythm genes and Parkinson's disease. Circadian rhythm genes participate in PD pathology *via* various pathways. The Clock/Cry complex activates Tim and Per expression to form complexes and inhibits Clock/Cry complex activity. This network interacts with ATG5 to regulate autophagy in PD. Clock acetylates Bmal1, and inhibits the Bmal1/Clock-dependent transcription of Per2. SIRT1 deacetylates Per2 and Bmal1. This network along with melatonin interacts with antioxidant enzymes yielding an antioxidative response in PD. Bmal1 and Clock are lower in PD and the Bmal1/Clock complex-dependent transcription of Per1, Per2, Dbp, and Rev-

erb α is inhibited. This network activates microglia-dependent neuroinflammation in PD. Rev-erb α competitively cooperates with Nurr1 to control DA gene transcription and the development and function of DA neurons. Some HSF1 targets that are associated with circadian rhythm genes (RXRA, Bhlhe40, and DBP) are upregulated, while some others (Bmal1) are inhibited. Non-coding RNAs undertake epigenetic regulation of the circadian rhythm system, but the mechanism is not clear. Circadian rhythm alterations, including abnormal expression of circadian rhythm genes, epigenetic changes, and gene polymorphisms, participate in the pathogenesis of PD.

circadian system [108]. In mice overexpressing α -synuclein, Per2 expression is not altered, but the firing rate of SCN neurons is reduced, implying that weakened circadian output is a critical characteristic of PD [99]. The increased frequency of Tregs expressing Helios and NRP-1 is associated with the severity of PD [109]. Previous studies have reported that chronic low-grade neuroinflammation induced by lipopolysaccharides potentiates the neurotoxicity of rotenone and disrupts circadian rhythm gene or protein expression [110]. BMAL1 plays an important role in the survival of DAergic neurons and maintain normal function of the DAergic signaling pathway through regulating microglia-mediated neuroinflammation [111]. Rev-erb α has also been reported to regulate neuroinflammation [112].

Adult mammals undergo diurnal cycles of autophagy, which plays a key role in the cellular metabolic cycle [113]. In the absence of rhythmic autophagy, the accumulation and aggregation of misfolded proteins may lead to neurodegeneration [113–116]. Circadian rhythm dysregulation during cognitive loss and aging has been tied to the

induction of autophagy [114]. Rev-erb α links the circadian and DA systems and competitively cooperates with Nurr1, which control the DAergic neuron-associated gene transcription, and further the optimal development and function of DAergic neurons [117–121]. Nur77, a member of the nuclear steroid receptor subgroup together with Nurr1 and NOR-1 participating in DAergic neuron loss and dyskinesia induced by levodopa in PD [122], displays an obvious circadian rhythm with an elevated mRNA level at night [123].

It has been reported that heat shock factor 1 (HSF1) participates in neurodegeneration [124, 125]. Some of the HSF1 targets are associated with alterations of the circadian rhythm, evidenced by upregulated Bhlhe40 and DBP and downregulated Bmal1 [124]. Non-coding RNAs, which control the development of neuronal stem cells and neuronal differentiation [126, 127], undertake epigenetic regulation of the brain clock system at the transcriptional and post-transcriptional levels [128, 129]. Although the mechanisms underlying the interplay between circadian rhythm genes and PD pathology are still largely unknown,

increasing evidence from clinical or experimental studies has revealed the interactions between circadian rhythm and PD related genes [130]. Mutations in the PARK2 gene coding for parkin is a crucial pathogenic gene for the disruption of mitophagy-mediated mitochondrial quality control [131]. Using fibroblasts from PD patients carrying PARK2 mutations, Pacelli *et al.* revealed that the dramatic impact of metabolic fluxes on cell circadian rhythm and circadian rhythm genes relies on mutations in parkin [130]. *Drosophila* with mutations in genes encoding mitochondrial ligases MUL1 and PARKIN, a commonly used model for research on PD, show an increasing level of total Per protein, accompanied by elevated total activity, shorter sleep, higher levels of free radicals, and inhibited autophagy [27].

Increasing evidence has indicated that the expressions of circadian rhythm genes are abnormal in various PD models, and may predict the mechanisms underlying PD [27, 74, 99]. It is likely that the network of circadian rhythm genes may play a role in the pathogenic mechanism of PD. All these findings indicate a potential role of the circadian rhythm gene network in PD pathogenesis. The exact modulating mechanisms between the key molecules such as Nurr1, α -synuclein, and circadian rhythm genes needs further investigation.

Altered Circadian Rhythm Genes in Patients with Parkinson's Disease

More and more clinical studies have investigated the alteration of circadian rhythm gene expression in peripheral blood lymphocytes (PBLs) from patients with PD [57, 132–138] (Table 1). Several studies have found abnormal expression of circadian rhythm genes in PBLs from PD patients. Bmal1 and Bmal2 are significantly decreased in PD, while the relative Bmal1 level is positively correlated with PD severity [132, 133]. Most circadian rhythm gene promoters are devoid of methylation, except for CRY1 and NPAS2 [134]. However, compared with healthy controls, epigenetic changes of hypomethylation in the NPAS2 promoter have been found in the early stage of disease in PBLs from PD patients [134, 135]. This finding provides a potential biomarker for discerning PD patients from healthy subjects [134, 135]. The negative feedback loop of circadian rhythm genes prompting epigenetic changes of NPAS2 expression may be the main cause of abnormal Bmal1 and Bmal2 levels in PD patients' leukocytes [134]. Gene polymorphisms in the promoter region of the circadian rhythm genes Bmal1 and Per1 may play a role in the development of PD [136]. The variation of Bmal1 rs900147 is more robust in tremor-dominant patients than postural-instability and gait-difficulty cases, while the association of the PER1 rs2253820

variant is stronger in postural-instability and gait-disturbance cases than tremor-dominant cases [136]. The polymorphism of Tef rs738499 is often associated with the depression symptoms and sleep disturbances in PD [57, 137]. The Clock 3111T/C variant can be regarded as an independent risk factor for non-motor sleep impairment and motor fluctuation in PD [138]. The abnormal expression of circadian rhythm genes, epigenetic changes, and gene polymorphisms may provide a new perspective for future study of PD pathogenesis and serve as potential biomarkers for PD diagnosis.

The possible mechanisms of RBD neuropathology associated with PD have not been clearly investigated. It is likely that RBD arises from the same pathogenic mechanisms that underlie synucleinopathies, with disease processes beginning in the caudal brain stem where REM sleep atonia is controlled [139]. Interestingly, Liu *et al.* recently found that sleep-wake brain states and motor behaviors are co-regulated by glutamic acid decarboxylase 2 neurons in the substantia nigra pars reticulata [111]. It is well accepted that early basal ganglia network dysfunction during RBD contributes to the development of PD [140]. In addition, sleep is proposed to help remove the aggregates of neurotoxic α -synuclein from the brain *via* the lymphatic system [141, 142]. REM sleep disorders, especially RBD, circadian rhythms, and circadian rhythm gene dysfunctions are proposed to disturb the glymphatic flow and are linked with Lewy body aggregates and substantia nigra DAergic cell loss [142]. Furthermore, RBD is associated with altered expression of clock genes and delayed melatonin secretion, and circadian rhythm dysregulation is a part of RBD [143]. Weissova *et al.* assessed the expression levels of circadian rhythm genes in PBLs by real-time quantitative PCR and analyzed 24-h melatonin profiles in peripheral blood serum by radioimmunoassay in 10 RBD patients and 9 controls [143]. In the RBD patients, Per2, Bmal1, and Rev-erb α circadian rhythms disappear, the amplitude of Per3 diminished, and melatonin secretion was delayed [143]. It is proposed that alterations in the expression of circadian rhythm genes and melatonin levels in patients with RBD might be a potential biomarker in the early stage of synucleinopathies including PD [143]. The intimate relationship between circadian rhythm disorders and PD with RBD pathology should be further explored.

Potential Impact of Pharmacological and Non-pharmacological Therapies on the Circadian Rhythm

The recent therapies for PD, including levodopa, dopamine agonists, and monoamine oxidase-B inhibitors, are useful initial therapies. However the efficacy decreases over time due to medication tolerance [144]. Then the subsequent

therapy is started through increasing the dose of the initial therapy or adding new kinds of treatment including catechol-O-methyltransferase inhibitors, istradefylline, and amantadine. Levodopa carbidopa enteral suspension infusion and unilateral or bilateral deep brain stimulation as advanced therapy are further added for long-duration PD patients [144]. Much more interestingly, therapeutic approaches targeting circadian rhythm system may hold efficacy and promise. Circadian rhythm dysregulation, as a potential contributor to the development and progression of PD, has been proposed as a target for either pharmacological or non-pharmacological therapy against PD [13, 18, 49, 127, 145, 146]. Among PD patients, especially those with daytime sleepiness and impaired circadian melatonin secretion [49], exogenous supplementation of melatonin is considered to be therapeutic for impaired alertness and poor sleep [49]. However, so far, the outcome from randomized controlled clinical trials of melatonin supplements on sleep quality and activity rhythms in patients with PD has yielded inconsistent results [13]. Melatonin administration successfully improves self-report measures of sleep as evaluated by Pittsburgh Sleep Quality Index, but fails to ameliorate sleep quality monitored by polysomnography and motor dysfunction assessed by the United Parkinson's Disease Rating Scale [147]. In addition, melatonin may be neuroprotective *via* the MT1 and MT2 high-affinity G protein-coupled melatonin receptors [148]. The discovery of MT1 or MT2 melatonin receptor-selective drugs may improve the efficacy and lead to new therapeutic candidates [148]. The WNT/ β -catenin pathway plays an important role in maintaining mitochondrial functions [149]. The activation of peroxisome proliferator-activated γ (PPAR γ) can be induced by inhibition of the WNT/ β -catenin pathway [150]. The circadian rhythm can directly regulate the WNT/ β -catenin pathway and PPAR γ involved in the reprogramming of cellular energy metabolism, resulting in down-regulation of the classical WNT/ β -catenin pathway and upregulation of PPAR γ [150, 151]. The WNT/ β -catenin pathway and PPAR γ could serve as potential therapeutic targets against PD [151]. Activation of adenosine 5'-monophosphate-activated protein kinase (AMPK) results in circadian dysfunction, suggesting that adenosine 5'-triphosphate (ATP) might be a novel therapeutic strategy in PD [152]. It is well-accepted that DA regulates the circadian rhythm system both directly and indirectly [153]. Interestingly, researchers have found that sodium can activate neurons in the SCN by regulating the circadian rhythm system and output via an excitatory GABAergic pathway [154]. It seems that pharmacological therapies alleviating various symptoms of circadian rhythm dysregulation need to be appraised [153].

Non-pharmacological therapies also play a vital role in PD treatment. Results from recent clinical trials suggest

that timed light therapy may be a feasible intervention for improving the sleep-wake cycle, reducing daytime sleepiness, and increasing daily physical activity for PD [127]. It seems that the combination of timed light therapy with timed melatonin supplements may be more effective [13]. Daily time-dependent physical exercise at moderate intensity has differential effects on the circadian melatonin rhythm [146]. Morning exercise may increase parasympathetic activity, while evening exercise may enhance sympathetic activity during sleep [146]. The specific characteristics of the autonomic nervous system could be responsible; furthermore, evening exercise may shift the offset phase of the nocturnal melatonin rise [146]. Thus, the sleep-wake cycle is regulated primarily by physical exercise [146], which gives timed physical exercise the potential to treat circadian rhythm dysregulation in PD [49]. Reduction in caloric intake and fasting extends the life span in animal models [71]. The underlying mechanism has been attributed the strong antioxidant capacity of melatonin which is produced by the GI tract [71, 155]. Fasting in animals increases the level of melatonin produced by the GI tract [155]. Recently, researchers have founded that intake of melatonin before going to bed might achieve the same effect as fasting [156]. More and more patients taking advantage of the antioxidant capacity of melatonin are taking melatonin daily to treat age-related PD [71].

It is worth noting that almost all DAergic anti-PD medications impact sleep [157]. A 'sleep attack' which describes suddenly and unintendedly falling asleep, may place patients at risk during daily activities such as eating and driving [157, 158]. PD patients treated with DA receptor agonists alone or in combination with levodopa, have a higher incidence of sleep attacks than patients treated with other agents [157]. To date, sleep attacks have been occasionally reported in PD patients treated with the DA receptor agonists pramipexole, ropinirole, piriabedil, and pergolide [158–162]. The potential impact of medications on the circadian rhythm system in PD have not been fully investigated. Anti-PD medications may also disturb the circadian rhythm. PD patients receiving the classical anti-PD drug levodopa usually suffer from severe circadian dysfunction [163]. In contrast, melatonin administration can restore the daily rhythms of serotonin metabolism and the expression of clock genes in PD animal models [164].

Conclusions

This review summarizes recent research progress on the non-motor features of PD with special focus on circadian rhythm dysregulation and altered circadian rhythm genes. The circadian rhythm gene network maintains the

generation and regulation of the circadian rhythm. Circadian rhythm dysregulation, especially sleep impairment, is an early symptom of PD. Findings from imaging and EEG are useful supplements for the diagnosis of PD associated with circadian rhythm dysregulation. Many studies have confirmed the abnormal expression of circadian rhythm genes in cell and animal models of PD, and occasionally in patients with PD, indicating a possible involvement of circadian rhythm genes in disease development. Among so many etiologies and mechanisms of PD, these findings of circadian rhythm dysregulation may provide a new perspective for further study of its pathogenesis. The alterations of circadian rhythm genes reported in PD patients may become a new biomarker for its diagnosis and evaluation of its severity. Moreover, the impacts of pharmacological and non-pharmacological therapies for PD on the circadian rhythm system may provide a novel and prognostic target for its management.

Acknowledgements This review was supported by the National Nature Science Foundation of China (81771521), Key Research and Development Plan of Liaoning Science and Technology Department (2018225051), Guangdong Provincial Key R&D Program (2018B030337001), and the National Key Research and Development Program of China (2016YFC1306600).

Conflict of interest The authors declare that they have no conflict of interest.

References

- Erkkinen MG, Kim MO, Geschwind MD. Clinical neurology and epidemiology of the major neurodegenerative diseases. *Cold Spring Harb Perspect Biol* 2018, 10: a033118.
- Li TB, Yang ZF, Li S, Cheng C, Shen BR, Le WD. Alterations of *NURRI* and cytokines in the peripheral blood mononuclear cells: Combined biomarkers for Parkinson's disease. *Front Aging Neurosci* 2018, 10: 392.
- Chung SJ, Armasu SM, Anderson KJ, Biernacka JM, Lesnick TG, Rider DN. Genetic susceptibility loci, environmental exposures, and Parkinson's disease: A case-control study of gene-environment interactions. *Parkinsonism Relat Disord* 2013, 19: 595–599.
- Li TB, Le WD. Biomarkers for Parkinson's disease: How good are they? *Neurosci Bull* 2020, 36: 183–194.
- Dickson DW. Parkinson's disease and Parkinsonism: Neuropathology. *Cold Spring Harb Perspect Med* 2012, 2: a009258.
- Breen DP, Vuono R, Nawarathna U, Fisher K, Shneerson JM, Reddy AB, *et al.* Sleep and circadian rhythm regulation in early Parkinson disease. *JAMA Neurol* 2014, 71: 589–595.
- Radhakrishnan DM, Goyal V. Parkinson's disease: A review. *Neurol India* 2018, 66: S26–S35.
- Schapiro AHV, Chaudhuri KR, Jenner P. Non-motor features of Parkinson disease. *Nat Rev Neurosci* 2017, 18: 435–450.
- Schrag A, Horsfall L, Walters K, Noyce A, Petersen I. Prediagnostic presentations of Parkinson's disease in primary care: A case-control study. *Lancet Neurol* 2015, 14: 57–64.
- Ma JF, Hou MM, Tang HD, Gao X, Liang L, Zhu LF, *et al.* REM sleep behavior disorder was associated with Parkinson's disease: A community-based study. *BMC Neurol* 2016, 16: 123.
- Trenkwalder C. Sleep dysfunction in Parkinson's disease. *Clin Neurosci N Y N Y* 1998, 5: 107–114.
- Zhang F, Niu L, Liu X, Liu Y, Li S, Yu H, *et al.* Rapid eye movement sleep behavior disorder and neurodegenerative diseases: An update. *Aging Dis* 2020, 11: 315–326.
- Hood S, Amir S. Neurodegeneration and the circadian clock. *Front Aging Neurosci* 2017, 9: 170.
- Ahsan Ejaz A, Sekhon IS, Munjal S. Characteristic findings on 24-h ambulatory blood pressure monitoring in a series of patients with Parkinson's disease. *Eur J Intern Med* 2006, 17: 417–420.
- Kallio M, Haapaniemi T, Turkka J, Suominen K, Tolonen U, Sotaniemi K, *et al.* Heart rate variability in patients with untreated Parkinson's disease. *Eur J Neurol* 2000, 7: 667–672.
- Pursiainen V, Haapaniemi TH, Korpelainen JT, Huikuri HV, Sotaniemi KA, Myllylä VV. Circadian heart rate variability in Parkinson's disease. *J Neurol* 2002, 249: 1535–1540.
- Zhong G, Bolitho S, Grunstein R, Naismith SL, Lewis SJ. The relationship between thermoregulation and REM sleep behaviour disorder in Parkinson's disease. *PLoS ONE* 2013, 8: e72661.
- Hartmann A, Veldhuis JD, Deuschle M, Standhardt H, Heuser I. Twenty-four hour cortisol release profiles in patients with Alzheimer's and Parkinson's disease compared to normal controls: Ultradian secretory pulsatility and diurnal variation. *Neurobiol Aging* 1997, 18: 285–289.
- Fasano A, Visanji NP, Liu LWC, Lang AE, Pfeiffer RF. Gastrointestinal dysfunction in Parkinson's disease. *Lancet Neurol* 2015, 14: 625–639.
- Li SY, Wang YL, Wang F, Hu LF, Liu CF. A new perspective for Parkinson's disease: Circadian rhythm. *Neurosci Bull* 2017, 33: 62–72.
- Patke A, Young MW, Axelrod S. Molecular mechanisms and physiological importance of circadian rhythms. *Nat Rev Mol Cell Biol* 2020, 21: 67–84.
- Dardente H, Cermakian N. Molecular circadian rhythms in central and peripheral clocks in mammals. *Chronobiol Int* 2007, 24: 195–213.
- Mohawk JA, Green CB, Takahashi JS. Central and peripheral circadian clocks in mammals. *Annu Rev Neurosci* 2012, 35: 445–462.
- Logan RW, McClung CA. Rhythms of life: Circadian disruption and brain disorders across the lifespan. *Nat Rev Neurosci* 2019, 20: 49–65.
- Yamamoto T, Nakahata Y, Soma H, Akashi M, Mamine T, Takumi T. Transcriptional oscillation of canonical clock genes in mouse peripheral tissues. *BMC Mol Biol* 2004, 5: 18.
- Guo H, Brewer JM, Champhekar A, Harris RB, Bittman EL. Differential control of peripheral circadian rhythms by suprachiasmatic-dependent neural signals. *PNAS* 2005, 102: 3111–3116.
- Doktor B, Damulewicz M, Pyza E. Effects of *MUL1* and *PARKIN* on the circadian clock, brain and behaviour in *Drosophila* Parkinson's disease models. *BMC Neurosci* 2019, 20: 24.
- Lee C, Bae K, Edery I. *PER* and *TIM* inhibit the DNA binding activity of a *Drosophila* *CLOCK-CYC/DBMAL1* heterodimer without disrupting formation of the heterodimer: A basis for circadian transcription. *Mol Cell Biol* 1999, 19: 5316–5325.
- Videnovic A, Willis GL. Circadian system - A novel diagnostic and therapeutic target in Parkinson's disease? *Mov Disord* 2016, 31: 260–269.

30. Takahashi JS, Hong HK, Ko CH, McDearmon EL. The genetics of mammalian circadian order and disorder: Implications for physiology and disease. *Nat Rev Genet* 2008, 9: 764–775.
31. Lee C, Etchegaray JP, Cagampang FR, Loudon AS, Reppert SM. Posttranslational mechanisms regulate the mammalian circadian clock. *Cell* 2001, 107: 855–867.
32. Ujnovsky I, Hirayama J, Doi M, Borrelli E, Sassone-Corsi P. Signaling mediated by the dopamine D2 receptor potentiates circadian regulation by CLOCK: BMAL1. *PNAS* 2006, 103: 6386–6391.
33. Reinke H, Asher G. Crosstalk between metabolism and circadian clocks. *Nat Rev Mol Cell Biol* 2019, 20: 227–241.
34. Akashi M, Takumi T. The orphan nuclear receptor ROR α regulates circadian transcription of the mammalian core-clock Bmal1. *Nat Struct Mol Biol* 2005, 12: 441–448.
35. Bunney BG, Li JZ, Walsh DM, Stein R, Vawter MP, Cartagena P, *et al.* Circadian dysregulation of clock genes: Clues to rapid treatments in major depressive disorder. *Mol Psychiatry* 2015, 20: 48–55.
36. Videnovic A, Lazar AS, Barker RA, Overeem S. 'The clocks that time us'—circadian rhythms in neurodegenerative disorders. *Nat Rev Neurol* 2014, 10: 683–693.
37. Gros P, Videnovic A. Overview of sleep and circadian rhythm disorders in Parkinson disease. *Clin Geriatr Med* 2020, 36: 119–130.
38. Jin H, Zhang JR, Shen Y, Liu CF. Clinical significance of REM sleep behavior disorders and other non-motor symptoms of Parkinsonism. *Neurosci Bull* 2017, 33: 576–584.
39. Lin CY, Yu RL, Wu RM, Tan CH. Effect of ALDH2 on sleep disturbances in patients with Parkinson's disease. *Sci Rep* 2019, 9: 18950.
40. Arnaldi D, Latimier A, Leu-Semenescu S, Vidailhet M, Arnulf I. Loss of REM sleep features across nighttime in REM sleep behavior disorder. *Sleep Med* 2016, 17: 134–137.
41. Rodriguez CL, Jaimchariyatam N, Budur K. Rapid eye movement sleep behavior disorder: A review of the literature and update on current concepts. *Chest* 2017, 152: 650–662.
42. Kim Y, Kim YE, Park EO, Shin CW, Kim HJ, Jeon B. REM sleep behavior disorder portends poor prognosis in Parkinson's disease: A systematic review. *J Clin Neurosci* 2018, 47: 6–13.
43. Yan YY, Lei K, Li YY, Liu XF, Chang Y. The correlation between possible RBD and cognitive function in Parkinson's disease patients in China. *Ann Clin Transl Neurol* 2019, 6: 848–853.
44. Schrempf W, Brandt MD, Storch A, Reichmann H. Sleep disorders in Parkinson's disease. *J Parkinsons Dis* 2014, 4: 211–221.
45. Fereshtehnejad SM, Shafieesabet M, Shahidi GA, Delbari A, Lökk J. Restless legs syndrome in patients with Parkinson's disease: A comparative study on prevalence, clinical characteristics, quality of life and nutritional status. *Acta Neurol Scand* 2015, 131: 211–218.
46. Allen RP, Picchiotti D, Hening WA, Trenkwalder C, Walters AS, Montplaisi J, *et al.* Restless legs syndrome: Diagnostic criteria, special considerations, and epidemiology. A report from the restless legs syndrome diagnosis and epidemiology workshop at the National Institutes of Health. *Sleep Med* 2003, 4: 101–119.
47. Jung JS, Lee HJ, Cho CH, Kang SG, Yoon HK, Park YM, *et al.* Association between restless legs syndrome and CLOCK and NPAS2 gene polymorphisms in schizophrenia. *Chronobiol Int* 2014, 31: 838–844.
48. Whittom S, Dumont M, Petit D, Desautels A, Adam B, Lavigne G, *et al.* Effects of melatonin and bright light administration on motor and sensory symptoms of RLS. *Sleep Med* 2010, 11: 351–355.
49. Videnovic A, Noble C, Reid KJ, Peng J, Turek FW, Marconi A, *et al.* Circadian melatonin rhythm and excessive daytime sleepiness in Parkinson disease. *JAMA Neurol* 2014, 71: 463–469.
50. Walker WH 2nd, Walton JC, DeVries AC, Nelson RJ. Circadian rhythm disruption and mental health. *Transl Psychiatry* 2020, 10: 28.
51. Goldstein AN, Walker MP. The role of sleep in emotional brain function. *Annu Rev Clin Psychol* 2014, 10: 679–708.
52. Armitage R. Sleep and circadian rhythms in mood disorders. *Acta Psychiatr Scand Suppl* 2007: 104–115.
53. Vandekerckhove M, Cluydts R. The emotional brain and sleep: An intimate relationship. *Sleep Med Rev* 2010, 14: 219–226.
54. Chaudhuri KR, Schapira AH. Non-motor symptoms of Parkinson's disease: Dopaminergic pathophysiology and treatment. *Lancet Neurol* 2009, 8: 464–474.
55. Brown RG, Landau S, Hindle JV, Playfer J, Samuel M, Wilson KC, *et al.* Depression and anxiety related subtypes in Parkinson's disease. *J Neurol Neurosurg Psychiatry* 2011, 82: 803–809.
56. Kronfeld-Schor N, Einat H. Circadian rhythms and depression: Human psychopathology and animal models. *Neuropharmacology* 2012, 62: 101–114.
57. Hua P, Liu WG, Kuo SH, Zhao YY, Chen L, Zhang N, *et al.* Association of Tef polymorphism with depression in Parkinson disease. *Mov Disord* 2012, 27: 1694–1697.
58. Bedrosian TA, Nelson RJ. Sundowning syndrome in aging and dementia: Research in mouse models. *Exp Neurol* 2013, 243: 67–73.
59. Kim J, Jang S, Choe HK, Chung S, Son GH, Kim K. Implications of circadian rhythm in dopamine and mood regulation. *Mol Cells* 2017, 40: 450–456.
60. Lauretti E, Di Meco A, Merali S, Praticò D. Circadian rhythm dysfunction: A novel environmental risk factor for Parkinson's disease. *Mol Psychiatry* 2017, 22: 280–286.
61. Chung S, Lee EJ, Yun S, Choe HK, Park SB, Son HJ, *et al.* Impact of circadian nuclear receptor REV-ERB α on midbrain dopamine production and mood regulation. *Cell* 2014, 157: 858–868.
62. Vallelonga F, di Stefano C, Merola A, Romagnolo A, Sobrero G, Milazzo V, *et al.* Blood pressure circadian rhythm alterations in alpha-synucleinopathies. *J Neurol* 2019, 266: 1141–1152.
63. Kanegusuku H, Silva-Batista C, Peçanha T, Silva-Junior N, Queiroz A, Costa L, *et al.* Patients with Parkinson disease present high ambulatory blood pressure variability. *Clin Physiol Funct Imaging* 2017, 37: 530–535.
64. Raupach AK, Ehgoetz Martens KA, Memarian N, Zhong G, Matar E, Halliday GM, *et al.* Assessing the role of nocturnal core body temperature dysregulation as a biomarker of neurodegeneration. *J Sleep Res* 2020, 29: e12939. <https://doi.org/10.1111/jsr.12939>.
65. Iranzo A, Molinuevo JL, Santamaría J, Serradell M, Martí MJ, Valldeoriola F, *et al.* Rapid-eye-movement sleep behaviour disorder as an early marker for a neurodegenerative disorder: A descriptive study. *Lancet Neurol* 2006, 5: 572–577.
66. Heart rate variability. standards of measurement, physiological interpretation, and clinical use. task force of the European society of cardiology and the North American society of pacing and electrophysiology. *Eur Heart J* 1996, 17: 354–381.
67. Harnod D, Wen SH, Chen SY, Harnod T. The association of heart rate variability with parkinsonian motor symptom duration. *Yonsei Med J* 2014, 55: 1297–1302.
68. Haapaniemi TH, Pursiainen V, Korpelainen JT, Huikuri HV, Sotaniemi KA, Myllylä VV. Ambulatory ECG and analysis of heart rate variability in Parkinson's disease. *J Neurol Neurosurg Psychiatry* 2001, 70: 305–310.

69. Breen DP, Nombela C, Vuono R, Jones PS, Fisher K, Burn DJ, *et al.* Hypothalamic volume loss is associated with reduced melatonin output in Parkinson's disease. *Mov Disord* 2016, 31: 1062–1066.
70. Bolitho SJ, Naismith SL, Rajaratnam SM, Grunstein RR, Hodges JR, Terpening Z, *et al.* Disturbances in melatonin secretion and circadian sleep-wake regulation in Parkinson disease. *Sleep Med* 2014, 15: 342–347.
71. Bubenik GA, Konturek SJ. Melatonin and aging: Prospects for human treatment. *J Physiol Pharmacol* 2011, 62: 13–19.
72. Li LY, Zhao ZX, Ma JJ, Zheng JH, Huang S, Hu SY, *et al.* Elevated plasma melatonin levels are correlated with the non-motor symptoms in Parkinson's disease: A cross-sectional study. *Front Neurosci* 2020, 14: 505.
73. Sommanson A, Saudi WS, Nylander O, Sjöblom M. Melatonin inhibits alcohol-induced increases in duodenal mucosal permeability in rats *in vivo*. *Am J Physiol Gastrointest Liver Physiol* 2013, 305: G95–G105.
74. De Lazzari F, Bisaglia M, Zordan MA, Sandrelli F. Circadian rhythm abnormalities in Parkinson's disease from humans to flies and back. *Int J Mol Sci* 2018, 19: E3911.
75. Leng Y, Goldman SM, Cawthon PM, Stone KL, Ancoli-Israel S, Yaffe K. Excessive daytime sleepiness, objective napping and 11-year risk of Parkinson's disease in older men. *Int J Epidemiol* 2018, 47: 1679–1686.
76. Leng Y, Musiek ES, Hu K, Cappuccio FP, Yaffe K. Association between circadian rhythms and neurodegenerative diseases. *Lancet Neurol* 2019, 18: 307–318.
77. Hastings MH, Goedert M. Circadian clocks and neurodegenerative diseases: Time to aggregate?. *Curr Opin Neurobiol* 2013, 23: 880–887.
78. Musiek ES, Lim MM, Yang GR, Bauer AQ, Qi L, Lee Y, *et al.* Circadian clock proteins regulate neuronal redox homeostasis and neurodegeneration. *J Clin Invest* 2013, 123: 5389–5400.
79. Lotankar S, Prabhavalkar KS, Bhatt LK. Biomarkers for Parkinson's disease: Recent advancement. *Neurosci Bull* 2017, 33: 585–597.
80. Orimo S. New development of diagnosis and treatment for Parkinson's disease. *Rinsho Shinkeigaku* 2017, 57: 259–273.
81. Bourgouin PA, Rahayel S, Gaubert M, Arnaldi D, Hu M, Heidbreder A, *et al.* Neuroimaging of rapid eye movement sleep behavior disorder. *Int Rev Neurobiol* 2019, 144: 185–210.
82. Vikene K, Skeie GO, Specht K. Abnormal phasic activity in saliency network, motor areas, and basal Ganglia in Parkinson's disease during rhythm perception. *Hum Brain Mapp* 2019, 40: 916–927.
83. Yousaf T, Pagano G, Wilson H, Politis M. Neuroimaging of sleep disturbances in movement disorders. *Front Neurol* 2018, 9: 767.
84. Oh YS, Kim JS, Yang DW, Koo JS, Kim YI, Jung HO, *et al.* Nighttime blood pressure and white matter hyperintensities in patients with Parkinson disease. *Chronobiol Int* 2013, 30: 811–817.
85. Salsone M, Cerasa A, Arabia G, Morelli M, Gambardella A, Mumoli L, *et al.* Reduced thalamic volume in Parkinson disease with REM sleep behavior disorder: Volumetric study. *Parkinsonism Relat Disord* 2014, 20: 1004–1008.
86. Chung SJ, Choi YH, Kwon H, Park YH, Yun HJ, Yoo HS, *et al.* Sleep disturbance may alter white matter and resting state functional connectivities in Parkinson's disease. *Sleep* 2017, 40. <https://doi.org/10.1093/sleep/zsx009>.
87. Radziunas A, Deltuva VP, Tamasauskas A, Gleizniene R, Pranckeviciene A, Petrikonis K, *et al.* Brain MRI morphometric analysis in Parkinson's disease patients with sleep disturbances. *BMC Neurol* 2018, 18: 88.
88. Filippi M, Elisabetta S, Piramide N, Agosta F. Functional MRI in idiopathic Parkinson's disease. *Int Rev Neurobiol* 2018, 141: 439–467.
89. Arnaldi D, Famà F, de Carli F, Morbelli S, Ferrara M, Picco A, *et al.* The role of the serotonergic system in REM sleep behavior disorder. *Sleep* 2015, 38: 1505–1509.
90. Manabe Y, Fujii D, Kono S, Sakai Y, Tanaka T, Narai H, *et al.* Systemic blood pressure profile correlates with cardiac 123I-MIBG uptake in patients with Parkinson's disease. *J Neurol Sci* 2011, 307: 153–156.
91. Kashiwara K, Imamura T, Shinya T. Cardiac 123I-MIBG uptake is reduced more markedly in patients with REM sleep behavior disorder than in those with early stage Parkinson's disease. *Parkinsonism Relat Disord* 2010, 16: 252–255.
92. Nomura T, Inoue Y, Högl B, Uemura Y, Kitayama M, Abe T, *et al.* Relationship between (123I)-MIBG scintigrams and REM sleep behavior disorder in Parkinson's disease. *Parkinsonism Relat Disord* 2010, 16: 683–685.
93. Chung CC, Kang JH, Yuan RY, Wu DA, Chen CC, Chi NF, *et al.* Multiscale entropy analysis of electroencephalography during sleep in patients with Parkinson disease. *Clin EEG Neurosci* 2013, 44: 221–226.
94. Priano L, Bigoni M, Albani G, Sellitti L, Giacomotti E, Picconi R, *et al.* Sleep microstructure in Parkinson's disease: Cycling alternating pattern (CAP) as a sensitive marker of early NREM sleep instability. *Sleep Med* 2019, 61: 57–62.
95. Margis R, Schönwald SV, Carvalho DZ, Gerhardt GJ, Riederer CR. NREM sleep alpha and *Sigma* activity in Parkinson's disease: Evidence for conflicting electrophysiological activity?. *Clin Neurophysiol* 2015, 126: 951–958.
96. Wetter TC, Brunner H, Högl B, Yassouridis A, Trenkwalder C, Friess E. Increased alpha activity in REM sleep in de novo patients with Parkinson's disease. *Mov Disord* 2001, 16: 928–933.
97. Jankovic J. Parkinson's disease: Clinical features and diagnosis. *J Neurol Neurosurg Psychiatry* 2008, 79: 368–376.
98. Shokrollahi M, Krishnan S. A review of sleep disorder diagnosis by electromyogram signal analysis. *Crit Rev Biomed Eng* 2015, 43: 1–20.
99. Kudo T, Loh DH, Truong D, Wu YF, Colwell CS. Circadian dysfunction in a mouse model of Parkinson's disease. *Exp Neurol* 2011, 232: 66–75.
100. Le WD, Sayana P, Jankovic J. Animal models of Parkinson's disease: A gateway to therapeutics?. *Neurotherapeutics* 2014, 11: 92–110.
101. Wang YL, Lv D, Liu WW, Li SY, Chen J, Shen Y, *et al.* Disruption of the circadian clock alters antioxidative defense via the SIRT1-BMAL1 pathway in 6-OHDA-induced models of Parkinson's disease. *Oxid Med Cell Longev* 2018, 2018: 4854732.
102. Li H, Fan XM, Luo Y, Song S, Liu J, Fan QY. Repeated manganese administration produced abnormal expression of circadian clock genes in the hypothalamus and liver of rats. *Neurotoxicology* 2017, 62: 39–45.
103. Choudhury GR, Daadi MM. Charting the onset of Parkinson-like motor and non-motor symptoms in nonhuman primate model of Parkinson's disease. *PLoS One* 2018, 13: e0202770. <https://doi.org/10.1371/journal.pone.0202770>.
104. Fifel K, Vezoli J, Dzahini K, Claustrat B, Leviel V, Kennedy H, *et al.* Alteration of daily and circadian rhythms following dopamine depletion in MPTP treated non-human Primates. *PLoS One* 2014, 9: e86240. <https://doi.org/10.1371/journal.pone.0086240>.
105. Baydas G, Gursu MF, Yilmaz S, Canpolat S, Yasar A, Cikim G, *et al.* Daily rhythm of glutathione peroxidase activity, lipid

- peroxidation and glutathione levels in tissues of pinealectomized rats. *Neurosci Lett* 2002, 323: 195–198.
106. Nakahata Y, Kaluzova M, Grimaldi B, Sahar S, Hirayama J, Chen D, *et al.* The NAD⁺-dependent deacetylase SIRT1 modulates CLOCK-mediated chromatin remodeling and circadian control. *Cell* 2008, 134: 329–340.
 107. Asher G, Gatfield D, Stratmann M, Reinke H, Dibner C, Kreppel F, *et al.* SIRT1 regulates circadian clock gene expression through PER2 deacetylation. *Cell* 2008, 134: 317–328.
 108. Pfeiffer M, Zimmermann Z, Gispert S, Auburger G, Korf HW, von Gall C. Impaired photic entrainment of spontaneous locomotor activity in mice overexpressing human mutant α -synuclein. *Int J Mol Sci* 2018, 19: E1651.
 109. Daneshvar Kakhaki R, Kouchaki E, Dadgostar E, Behnam M, Tamtaji OR, Nikouejad H, *et al.* The correlation of helios and neuropilin-1 frequencies with parkinson disease severity. *Clin Neurol Neurosurg* 2020, 192: 105833.
 110. Li H, Song S, Wang Y, Huang C, Zhang F, Liu J, *et al.* Correction to: Low-grade inflammation aggravates rotenone neurotoxicity and disrupts circadian clock gene expression in rats. *Neurotox Res* 2019, 35: 999–1000.
 111. Liu WW, Wei SZ, Huang GD, Liu LB, Gu C, Shen Y, *et al.* BMAL1 regulation of microglia-mediated neuroinflammation in MPTP-induced Parkinson's disease mouse model. *FASEB J* 2020, 34: 6570–6581.
 112. Griffin P, Dimitry JM, Sheehan PW, Lananna BV, Guo C, Robinette ML, *et al.* Circadian clock protein Rev-erb α regulates neuroinflammation. *Proc Natl Acad Sci USA* 2019, 116: 5102–5107.
 113. Sachdeva UM, Thompson CB. Diurnal rhythms of autophagy: Implications for cell biology and human disease. *Autophagy* 2008, 4: 581–589.
 114. Maiese K. Moving to the rhythm with clock (circadian) genes, autophagy, mTOR, and SIRT1 in degenerative disease and cancer. *Curr Neurovasc Res* 2017, 14: 299–304.
 115. Moors TE, Hoozemans JJ, Ingrassia A, Beccari T, Parnetti L, Chartier-Harlin MC, *et al.* Therapeutic potential of autophagy-enhancing agents in Parkinson's disease. *Mol Neurodegener* 2017, 12: 11.
 116. Guo F, Liu X, Cai H, Le W. Autophagy in neurodegenerative diseases: Pathogenesis and therapy. *Brain Pathol* 2018, 28: 3–13.
 117. Kim J, Jang S, Choi M, Chung S, Choe Y, Choe HK, *et al.* Abrogation of the circadian nuclear receptor REV-ERB α exacerbates 6-hydroxydopamine-induced dopaminergic neurodegeneration. *Mol Cells* 2018, 41: 742–752.
 118. Heng X, Jin G, Zhang X, Yang DH, Zhu MZ, Fu SJ, *et al.* Nurr1 regulates Top II β and functions in axon genesis of mesencephalic dopaminergic neurons. *Mol Neurodegener* 2012, 7: 4.
 119. Chu YP, Le WD, Kompoliti K, Jankovic J, Mufson EJ, Kordower JH. Nurr1 in Parkinson's disease and related disorders. *J Comp Neurol* 2006, 494: 495–514.
 120. Le W, Pan T, Huang M, Xu P, Xie W, Zhu W, *et al.* Decreased NURR1 gene expression in patients with Parkinson's disease. *J Neurol Sci* 2008, 273: 29–33.
 121. Jankovic J, Chen S, Le WD. The role of Nurr1 in the development of dopaminergic neurons and Parkinson's disease. *Prog Neurobiol* 2005, 77: 128–138.
 122. Rouillard C, Baillargeon J, Paquet B, St-Hilaire M, Maheux J, Lévesque C, *et al.* Genetic disruption of the nuclear receptor Nur77 (Nr4a1) in rat reduces dopamine cell loss and l-Dopa-induced dyskinesia in experimental Parkinson's disease. *Exp Neurol* 2018, 304: 143–153.
 123. Humphries A, Weller J, Klein D, Baler R, Carter DA. NGFI-B (Nurr77/Nr4a1) orphan nuclear receptor in rat pinealocytes: Circadian expression involves an adrenergic-cyclic AMP mechanism. *J Neurochem* 2004, 91: 946–955.
 124. Kovács D, Sigmond T, Hotzi B, Bohár B, Fazekas D, Deák V, *et al.* HSF1Base: A comprehensive database of HSF₁ (heat shock factor 1) target genes. *Int J Mol Sci* 2019, 20: E5815.
 125. Du YL, Wang F, Zou J, Le WD, Dong Q, Wang ZY, *et al.* Histone deacetylase 6 regulates cytotoxic α -synuclein accumulation through induction of the heat shock response. *Neurobiol Aging* 2014, 35: 2316–2328.
 126. Maiese K. Novel treatment strategies for the nervous system: Circadian clock genes, non-coding RNAs, and forkhead transcription factors. *Curr Neurovasc Res* 2018, 15: 81–91.
 127. Videnovic A, Klerman EB, Wang W, Marconi A, Kuhta T, Zee PC. Timed light therapy for sleep and daytime sleepiness associated with parkinson disease: A randomized clinical trial. *JAMA Neurol* 2017, 74: 411–418.
 128. Bhadra U, Patra P, Pal-Bhadra M. Cardinal epigenetic role of non-coding regulatory RNAs in circadian rhythm. *Mol Neurobiol* 2018, 55: 3564–3576.
 129. Mehta N, Cheng HY. Micro-managing the circadian clock: The role of microRNAs in biological timekeeping. *J Mol Biol* 2013, 425: 3609–3624.
 130. Pacelli C, Rotundo G, Lecce L, Menga M, Bidollari E, Scrima R, *et al.* Parkin mutation affects clock gene-dependent energy metabolism. *Int J Mol Sci* 2019, 20: E2772.
 131. Okuzumi A, Hatano T, Ueno SI, Ogawa T, Saiki S, Mori A, *et al.* Metabolomics-based identification of metabolic alterations in PARK2. *Ann Clin Transl Neurol* 2019, 6: 525–536.
 132. Cai Y, Liu S, Sothorn RB, Xu S, Chan P. Expression of clock genes Per1 and Bmal1 in total leukocytes in health and Parkinson's disease. *Eur J Neurol* 2010, 17: 550–554.
 133. Ding H, Liu S, Yuan YP, Lin QL, Chan P, Cai YN. Decreased expression of Bmal2 in patients with Parkinson's disease. *Neurosci Lett* 2011, 499: 186–188.
 134. Lin Q, Ding H, Zheng Z, Gu Z, Ma J, Chen L, *et al.* Promoter methylation analysis of seven clock genes in Parkinson's disease. *Neurosci Lett* 2012, 507: 147–150.
 135. Mao W, Zhao CS, Ding H, Liang K, Xue JH, Chan P, *et al.* Pyrosequencing analysis of methylation levels of clock genes in leukocytes from Parkinson's disease patients. *Neurosci Lett* 2018, 668: 115–119.
 136. Gu ZQ, Wang BB, Zhang YB, Ding H, Zhang YL, Yu J, *et al.* Association of ARNTL and PER1 genes with Parkinson's disease: A case-control study of Han Chinese. *Sci Rep* 2015, 5: 15891.
 137. Hua P, Liu WG, Chen DH, Zhao YY, Chen L, Zhang N, *et al.* Cry1 and Tef gene polymorphisms are associated with major depressive disorder in the Chinese population. *J Affect Disord* 2014, 157: 100–103.
 138. Lou F, Li M, Luo XG, Ren Y. CLOCK 3111T/C variant correlates with motor fluctuation and sleep disorders in Chinese patients with Parkinson's disease. *Parkinsons Dis* 2018, 2018: 4670380.
 139. McKenna D, Peever J. Degeneration of rapid eye movement sleep circuitry underlies rapid eye movement sleep behavior disorder. *Mov Disord* 2017, 32: 636–644.
 140. Rolinski M, Griffanti L, Piccini P, Roussakis AA, Szezyk-Krolikowski K, Menke RA, *et al.* Basal Ganglia dysfunction in idiopathic REM sleep behaviour disorder parallels that in early Parkinson's disease. *Brain* 2016, 139: 2224–2234.
 141. Videnovic A, Golombek D. Circadian dysregulation in Parkinson's disease. *Neurobiol Sleep Circadian Rhythms* 2017, 2: 53–58.
 142. Sundaram S, Hughes RL, Peterson E, Müller-Oehring EM, Bronté-Stewart HM, Poston KL, *et al.* Establishing a framework for neuropathological correlates and glymphatic system

- functioning in Parkinson's disease. *Neurosci Biobehav Rev* 2019, 103: 305–315.
143. Weissová K, Škrabalová J, Skálová K, Červená K, Bendová Z, Miletínová E, *et al.* Circadian rhythms of melatonin and peripheral clock gene expression in idiopathic REM sleep behavior disorder. *Sleep Med* 2018, 52: 1–6.
 144. Armstrong MJ, Okun MS. Diagnosis and treatment of parkinson disease: A review. *JAMA* 2020, 323: 548–560.
 145. Yamanaka Y, Hashimoto S, Masubuchi S, Natsubori A, Nishide SY, Honma S, *et al.* Differential regulation of circadian melatonin rhythm and sleep-wake cycle by bright lights and nonphotic time cues in humans. *Am J Physiol Regul Integr Comp Physiol* 2014, 307: R546–R557.
 146. Yamanaka Y, Hashimoto S, Takasu NN, Tanahashi Y, Nishide SY, Honma S, *et al.* Morning and evening physical exercise differentially regulate the autonomic nervous system during nocturnal sleep in humans. *Am J Physiol Regul Integr Comp Physiol* 2015, 309: R1112–R1121.
 147. Medeiros CAM, Carvalhede Bruin PF, Lopes LA, Magalhães MC, de Lourdes Seabra M, Sales de Bruin VM. Effect of exogenous melatonin on sleep and motor dysfunction in Parkinson's disease. *J Neurol* 2007, 254: 459–464.
 148. Liu JB, Clough SJ, Hutchinson AJ, Adamah-Biassi EB, Popovska-Gorevski M, Dubocovich ML. MT1 and MT2 melatonin receptors: A therapeutic perspective. *Annu Rev Pharmacol Toxicol* 2016, 56: 361–383.
 149. Mishra A, Singh S, Tiwari V, Chaturvedi S, Wahajuddin M, Shukla S. Dopamine receptor activation mitigates mitochondrial dysfunction and oxidative stress to enhance dopaminergic neurogenesis in 6-OHDA lesioned rats: A role of Wnt signalling. *Neurochem Int* 2019, 129: 104463.
 150. Vallée A, Lecarpentier Y, Guillevin R, Vallée JN. Opposite interplay between the canonical WNT/β-catenin pathway and PPAR gamma: A potential therapeutic target in gliomas. *Neurosci Bull* 2018, 34: 573–588.
 151. Vallée A, Lecarpentier Y, Vallée JN. Circadian rhythms and energy metabolism reprogramming in Parkinson's disease. *Curr Issues Mol Biol* 2019, 31: 21–44.
 152. Hayashi A, Matsunaga N, Okazaki H, Kakimoto K, Kimura Y, Azuma H, *et al.* A disruption mechanism of the molecular clock in a MPTP mouse model of Parkinson's disease. *Neuromolecular Med* 2013, 15: 238–251.
 153. Korshunov KS, Blakemore LJ, Trombley PQ. Dopamine: A modulator of circadian rhythms in the central nervous system. *Front Cell Neurosci* 2017, 11: 91.
 154. Gizowski C, Bourque CW. Sodium regulates clock time and output via an excitatory GABAergic pathway. *Nature* 2020, 583: 421–424.
 155. Bubenik GA, Ball RO, Pang SF. The effect of food deprivation on brain and gastrointestinal tissue levels of tryptophan, serotonin, 5-hydroxyindoleacetic acid, and melatonin. *J Pineal Res* 1992, 12: 7–16.
 156. Rasmussen DD, Mitton DR, Larsen SA, Yellon SM. Aging-dependent changes in the effect of daily melatonin supplementation on rat metabolic and behavioral responses. *J Pineal Res* 2001, 31: 89–94.
 157. Zesiewicz TA, Hauser RA. Sleep attacks and dopamine agonists for Parkinson's disease: What is currently known?. *CNS Drugs* 2003, 17: 593–600.
 158. Plowman BK, Boggie DT, Morreale AP, Schaefer MG, Delattre ML, Chan H. Sleep attacks in patients receiving dopamine-receptor agonists. *Am J Health Syst Pharm* 2005, 62: 537–540.
 159. Ryan M, Slevin JT, Wells A. Non-ergot dopamine agonist-induced sleep attacks. *Pharmacotherapy* 2000, 20: 724–726.
 160. Tan EK. Piribedil-induced sleep attacks in Parkinson's disease. *Fundam Clin Pharmacol* 2003, 17: 117–119.
 161. Frucht S, Rogers JD, Greene PE, Gordon MF, Fahn S. Falling asleep at the wheel: Motor vehicle mishaps in persons taking pramipexole and ropinirole. *Neurology* 1999, 52: 1908–1910.
 162. Chaudhuri KR, Pal S, Brefel-Courbon C. 'Sleep attacks' or 'unintended sleep episodes' occur with dopamine agonists: Is this a class effect?. *Drug Saf* 2002, 25: 473–483.
 163. Li SY, Wang YL, Liu WW, Lyu DJ, Wang F, Mao CJ, *et al.* Long-term levodopa treatment accelerates the circadian rhythm dysfunction in a 6-hydroxydopamine rat model of Parkinson's disease. *Chin Med J* 2017, 130: 1085–1092.
 164. Mattam U, Jagota A. Daily rhythms of serotonin metabolism and the expression of clock genes in suprachiasmatic nucleus of rotenone-induced Parkinson's disease male Wistar rat model and effect of melatonin administration. *Biogerontology* 2015, 16: 109–123.



Oligodendroglial GABAergic Signaling: More Than Inhibition!

Xianshu Bai¹ · Frank Kirchhoff¹ · Anja Scheller¹

Received: 10 October 2020 / Accepted: 22 November 2020 / Published online: 29 April 2021
© The Author(s) 2021

Abstract GABA is the main inhibitory neurotransmitter in the CNS acting at two distinct types of receptor: ligand-gated ionotropic GABA_A receptors and G protein-coupled metabotropic GABA_B receptors, thus mediating fast and slow inhibition of excitability at central synapses. GABAergic signal transmission has been intensively studied in neurons in contrast to oligodendrocytes and their precursors (OPCs), although the latter express both types of GABA receptor. Recent studies focusing on interneuron myelination and interneuron-OPC synapses have shed light on the importance of GABA signaling in the oligodendrocyte lineage. In this review, we start with a short summary on GABA itself and neuronal GABAergic signaling. Then, we elaborate on the physiological role of GABA receptors within the oligodendrocyte lineage and conclude with a description of these receptors as putative targets in treatments of CNS diseases.

Keywords GABA · GABA_A receptor · GABA_B receptor · OPC · Oligodendrocyte lineage

Introduction

GABA (γ -aminobutyric acid), besides glycine, is the main inhibitory neurotransmitter in the central nervous system (CNS) [1]. The existence of GABA in the brain was first detected in 1950 [2], without knowing its biological

function. Seven years later, studies found that GABA was the “I factor”, the inhibitory neurotransmitter of the mammalian CNS [3]. Thereafter, GABA and GABAergic signaling on neurons were extensively studied [1]. GABA binds to two classes of receptor in the CNS, GABA_A and GABA_B receptors, and exerts fast or slow inhibition at synaptic terminals. Decades later, since 1978 [4], glial GABA signaling started to attract interest and is now a major research focus while new roles of glial cells are emerging. Oligodendrocytes (OLs) are the myelinating cells of CNS making them indispensable for fast and efficient action potential conduction. They differentiate from precursor cells (OPCs) [5–8]. Despite lifelong ongoing differentiation into OLs, OPCs maintain a certain cell density due to continuous self-renewal [9–12]. Proliferation and differentiation of OPCs are modulated by growth factors [13–15], as well as by communication between OPCs and axons [16–18]. OPCs are the only glial cells receiving direct synaptic input mediated by glutamate and GABA from excitatory and inhibitory synapses, respectively [17, 19–23]. Furthermore, the myelination of interneurons by mature OLs appears to be a direct consequence of GABA-based interneuron-OPC communication [24–26].

GABA Synthesis, Release, and Uptake in the Brain

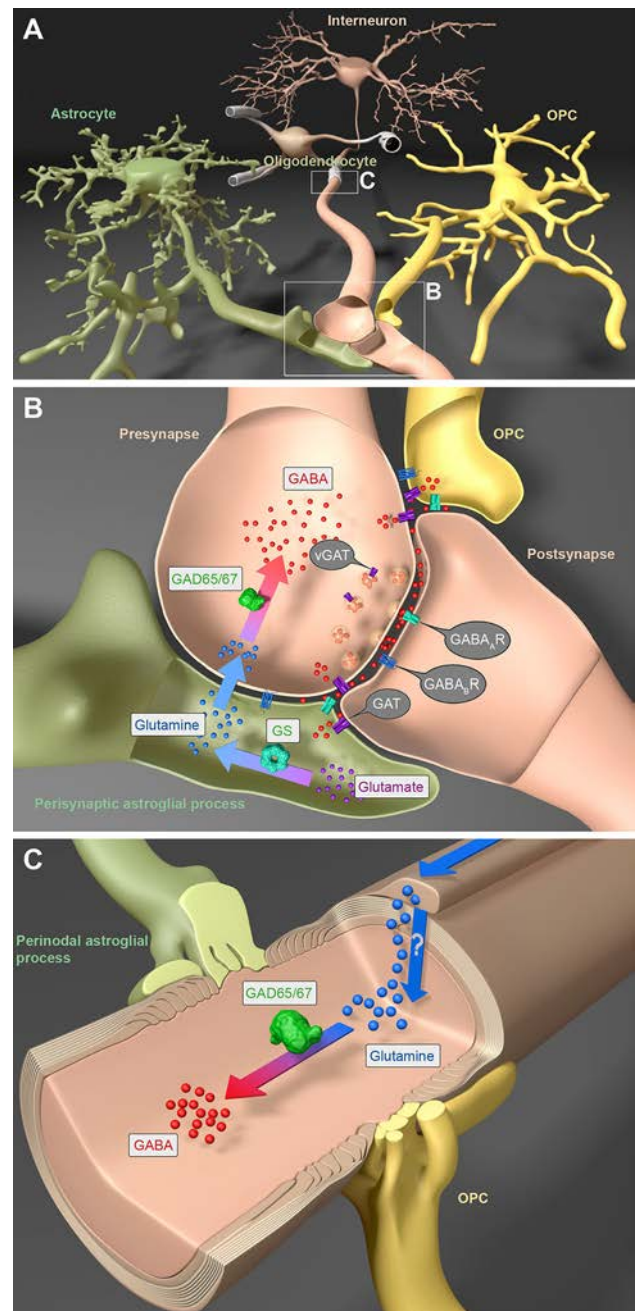
GABA availability in the CNS is either ensured by synthesis from glutamate by the glutamic acid decarboxylase enzymes (GAD) 67 and GAD65 [27, 28] or by monoacetylation of putrescine [29, 30]. Synthesis by GADs in the glutamine-glutamate cycle (GGC) is the most common pathway and GABA level are mostly determined by the activity of GADs. Briefly, in the GGC, glutamate is

✉ Frank Kirchhoff
frank.kirchhoff@uks.eu

¹ Molecular Physiology, Center for Integrative Physiology and Molecular Medicine (CIPMM), University of Saarland, 66421 Homburg, Germany

Fig. 1 GABA cycling between interneurons, cells of the oligodendrocyte (OL) lineage, and astrocytes. **A** In the central nervous system, interneurons form an intricate signaling network with cells of the OL lineage, i.e., myelinating OLs and their precursors (OPCs), and with perisynaptic as well as perinodal processes of astrocytes. **B** In the synaptic microenvironment, extracellular glutamate is converted into glutamine in astrocytes by glutamine synthetase (GS). After release, glutamine is taken up by interneurons and transformed into GABA by the glutamate decarboxylases GAD65 and/or GAD67. Upon action potential arrival, GABA is released into the synaptic cleft by vesicles expressing GABA transporters (vGAT). After binding to postsynaptic neuronal GABA_A and/or GABA_B receptors, GABA induces postsynaptic neuronal hyperpolarization. But neuron-released GABA can also act on the GABA receptors of OPCs modulating axonal myelination. In addition, extrasynaptic GABA is taken up by neuronal GAT1 and astroglial GAT3 transporters. Both transporters, however, are also expressed by OPCs, but functional studies are still required to determine their roles. **C** Also, OLs can express GS to produce glutamine. The latter might be transported to myelinated axons, where it can be converted into GABA. Additional experiments are still required to test this hypothesis.

transformed into glutamine by glutamine synthetase of astrocytes (Fig. 1A, B). Glutamine is released by several types of glutamine transporter and taken up by neurons, where it is converted into glutamate. The latter is finally processed by GADs to produce GABA in GABAergic neurons [31] (Fig. 1B). Although GAD67 and GAD65 share a large similarity of their genes (*GAD1* and *GAD2*, respectively), their expression pattern and functions are quite disparate. GAD67 is uniformly distributed in the whole cell while GAD65 is mainly found in the axonal terminals [32]. In addition, GAD67 is already expressed during early development while GAD65 is more prominent in later stages (reviewed by [27]). These spatial and temporal differences are highly related to their functions. GABA produced by GAD67 mainly functions as a neurotrophic factor and is independent of neurotransmission, e.g., involved in synaptogenesis during development (reviewed by [27]). GAD65, however, is responsible for synaptic neurotransmission. Therefore, it is not surprising that GAD67-null mice cannot survive longer than a day after birth, while GAD65-null mice are born with slowly developing spontaneous seizures [33, 34]. Although these deficits are highly likely attributable to disordered neuronal GABA synthesis, the GABA contribution from glial cells must not be neglected. GAD65 and GAD67 are both expressed in glial cells [35]. Astrocytes of the olfactory bulb, hippocampus, thalamus, and cerebellum (i.e., Bergmann glia) release GABA to inhibit neighboring neuronal activity [36–39]. Recently, GAD65/67 and monoamine oxidase B, as well as GABA were found in OPCs and oligodendrocytes *in vitro* [40]. These findings suggest the potential of autocrine or paracrine GABAergic signaling pathways for oligodendrocyte (OL) development and/or neural circuit formation. Besides astrocytes, OLs also



express glutamine synthetase in caudal regions and the spinal cord [41], providing a potential source of glutamine for axons *via* myelin-axon communication (Fig. 1A, C). In the case of inhibitory axons, glutamine is further transformed into GABA (Fig. 1C). More studies are required to confirm the functional GABA synthesis, release, and uptake in cells of the OL lineage.

GABA-containing transmitter vesicles (vGAT) are filled in synaptic terminals (Fig. 1B) and released in a Ca²⁺-dependent manner. The general mechanism of vesicular exocytosis, membrane fusion, and release of anchored GABA vesicles is triggered by Ca²⁺ influx through

voltage-gated Ca^{2+} channels (VGCCs). In addition, GABA can reach the extracellular space *via* reversal of GABA transporters (GATs), called non-vesicular release [42–44]. Previously, GATs were mainly considered to be responsible for GABA uptake from the synaptic cleft. For this GABA uptake, GATs utilize the chemical Na^+ gradient, aided by a Cl^- gradient; e.g., neuronal GAT1 co-transport two Na^+ and one Cl^- together with one GABA molecule. This transport not only increases the intracellular levels of GABA, Na^+ , and Cl^- , it also depolarizes the neuron. Under baseline conditions, GATs operate near equilibrium [43]. Therefore, upon moderate depolarization evoked by a short series of action potentials, transporter reversal occurs [45, 46]. However, during excessive network activity and enhanced synaptic GABA release, elevated levels of extracellular GABA favor GABA uptake by GATs [47]. Therefore, how the operation of GATs, including their reversal, is exactly controlled and how this process is related to physiological functions is yet unclear.

As a very complex but highly precise organ, our brain keeps a balance of excitatory and inhibitory signals to control proper behavioral performance. As reported, both vGAT-null (little, if any, GABA release) [48] and GAT1-null (no GABA clearance) mice cannot survive beyond birth [49]. Therefore, it is critical to maintain GABA homeostasis in the extracellular space by synchronized regulation of GABA release and uptake. In the brain, two different GATs fine-tune the neuronal excitability: GAT1 (*SLC6A1*) on presynaptic terminals and GAT3 (*SLC6A11*) on perisynaptic astroglial processes (Fig. 1B). Transcriptome studies have revealed that astroglial GAT3 dominates over GAT1. In addition to neurons, OPCs and OLs express functional GAT1, though at rather low levels [35, 40, 50] (Fig. 1B). However, functional studies demonstrating the biological impact of GAT1 for cells of the OL lineage are still missing. In addition to GAT1 and 3, some GAT2 (*SLC6A13*) immunoreactivity has been observed on CNS blood vessels [51]. GAT2 mainly permits efflux of GABA and taurine from the brain to the circulating blood stream [51]. Therefore, GAT2-deficient mice have slightly increased taurine in the brain [52]; however, they perform normally under physiological conditions. Transcriptome data suggest GAT2 expression by OPCs, though at a low level. This is interesting in respect to the current notion that OPCs can also contribute to the blood-brain barrier (BBB) while migrating along blood vessels during development [53]. Taken together, these findings suggest a potential novel function of OPCs in neural circuits, by either taking up GABA from extracellular space or by being associated with the overall GABA efflux through the BBB to the periphery. Nevertheless, more functional studies are required to identify the role of GAT2 in OPCs. In juvenile rats, GAT1 and GAT3 have also been detected in OLs [40],

however, it is yet elusive whether and how both GATs function in OL GABA circulation.

GABA Receptors and Their Biological Actions on Neurons

To exert inhibition, GABA binds to two distinct receptors: GABA_A and GABA_B . GABA_A receptors are ligand-gated ionotropic transmembrane receptors, permeating Cl^- ions in both directions [54]. To date, a plethora of 19 GABA_A receptor subunits have been identified in the mammalian CNS: $\alpha 1$ –6, $\beta 1$ –3, $\gamma 1$ –3, δ , ϵ , θ , π , and $\rho 1$ –3 [55]. In general, the pentameric receptor assembly is composed of two α , two β and one γ subunit (Fig. 2A, B). Due to various subunit compositions and distinct regional distributions, GABA_A receptors exhibit tremendous diversity in terms of biophysical properties and dynamic regulation [55, 56]. Since the subunits $\rho 1$ –3 form complexes with themselves only, and not with other subunits, they are designated as GABA_C or $\text{GABA}_{A-\rho}$ receptors. However, they are similar to GABA_A receptors in structure, function, and mechanism of action [57].

The GABA_A receptor is permeable to Cl^- anions in both directions depending on the difference between extra- and intracellular Cl^- concentrations. In general, extracellular Cl^- is above its equilibrium potential. Therefore, upon postsynaptic GABA_A receptor activation, a fast Cl^- influx generates neuronal hyperpolarization. This raises the threshold for postsynaptic action potentials and thereby decreases excitatory neurotransmitter release, i.e., inhibitory neurotransmission [58, 59] (Fig. 2A). Notably, GABA_A receptors are also expressed at extra-synaptic regions. These receptors can be activated by GABA spillover, leading to tonic inhibition [55].

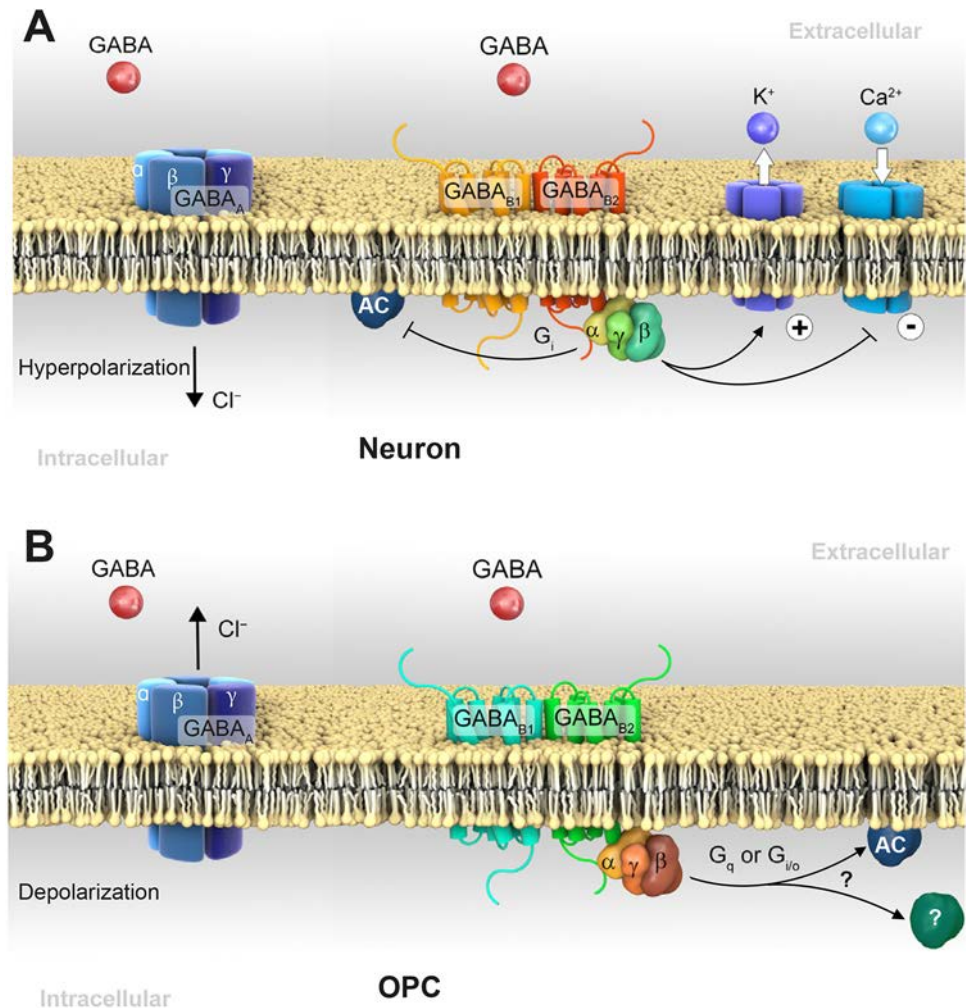
GABA_B receptors are metabotropic G-protein-coupled receptors. Two major GABA_B receptor isoforms (GABA_{B1} and GABA_{B2}) and various splice variants (GABA_{B1a-g}) have been described [60, 61]. GABA_{B1} and GABA_{B2} are co-expressed, generating functional receptors in a heterodimeric assembly [62–64], although some functional homodimers have been described as well [65]. The ligand-binding B1 subunit remains in the endoplasmic reticulum through a retention signal until assembly with the B2 subunit [66]. Only the assembled receptor dimers reach the cell surface and function. GABA activation occurs *via* a Venus flytrap domain of the B1 subunit [60, 67].

Neuronal GABA_B receptors are located in both pre- and postsynaptic membranes. Its G protein activation triggers dissociation of G_α and $G_{\beta\gamma}$ subunits. Binding of $G_{\beta\gamma}$ to VGCCs leads to reduced presynaptic Ca^{2+} influx preventing vesicular release (Fig. 2A) [68, 69], while decreased postsynaptic Ca^{2+} current suppresses neuronal excitability

Fig. 2 GABA receptor expression in neurons and OPCs.

A Activation of ionotropic GABA_A receptors induces Cl^- influx to hyperpolarize neurons. The GABA_{B1} subunit confers ligand-binding, while the B2 subunit transduces the GABA signal into the cell. Activation of the neuronal GABA_B receptor induces dissociation of G_α and $G_{\beta\gamma}$ subunits. The G_α subunit inhibits adenylyl cyclase (AC), while $G_{\beta\gamma}$ activates G protein-gated inwardly rectifying K^+ channels and inhibits voltage-gated Ca^{2+} channels (VGCCs), thereby reducing neurotransmitter release. The regulation of VGCCs can occur pre- and postsynaptically.

B Different from neurons, in OPCs, activation of GABA_A receptors causes a Cl^- efflux and depolarization based on the higher levels of cytosolic Cl^- . GABA_B receptors expressed in OPCs are thought to transduce signals *via* G_α with or without association of $G_{\beta\gamma}$; or *via* the G_q pathway linked to phospholipase C, further increasing intracellular Ca^{2+} release from the endoplasmic reticulum.



[70, 71]. In addition, postsynaptically, $G_{\alpha i/o}$ inhibits adenylyl cyclase, thereby reducing cAMP levels, while $G_{\beta\gamma}$ activates G protein-gated inwardly-rectifying K^+ channels, hyperpolarizing the postsynaptic membrane (Fig. 2A). GABA_B receptors regulate gene expression by interacting with activating transcription factor 4 (ATF-4), a member of the cAMP response element-binding protein (CREB)/ATF family [60, 72, 73]. Disruption of GABA_B receptor-mediated responses has been associated with several neuropathologies including epilepsy and hyperalgesia [74].

Apart from acting as an inhibitory neurotransmitter, GABA is also considered to be a neurotrophic factor. In cultured cerebellar granule cells, retinal neurons, and neuroblastoma neurons, GABA promotes neurite growth [75]. Another peculiar finding is that GABA can act as an excitatory neurotransmitter in cortical and hippocampal neurons during early postnatal days [76–78]. At this age, the Nernst potential of Cl^- is positive in respect to the resting membrane potential due to higher activity of the cation-chloride importer Na-K-Cl cotransporter in

comparison to the extruder K^+-Cl^- cotransporter 2, and the opening of GABA_A receptors results in Cl^- efflux with subsequent depolarization [79].

Expression of GABA Receptors in Cells of the Oligodendrocyte Lineage

Already in 1984, GABA-evoked responses were reported in a subpopulation of OLs from explant cultures of the mouse spinal cord [54]. These cells were depolarized by GABA (1 mmol/L, 4 mV depolarization). This depolarization was sensitive to competitive as well as non-competitive GABA_A receptor antagonists [54]. These experiments provided the first evidence of the functional expression of GABA_A receptors in OLs. A follow-up study on cultured OPCs and OLs further demonstrated that the GABA-induced depolarization (10^{-2} mmol/L, 30–680 pA in 60% of the OL lineage cells) was due to Cl^- efflux [80] (Fig. 2B). Also, in acutely isolated slices of corpus callosum and hippocampus, GABA_A receptors evoked

depolarization in OPCs (1 mmol/L GABA, 75 pA and 324 pA, respectively) [81, 82]. Notably, GABA_A receptor expression was found to be down-regulated during the lineage progression from proliferating OPCs to myelinating OLs. The current response to GABA as well as intracellular Ca²⁺ increases were drastically reduced *in situ* [80, 81, 83] and *in vitro* [84]. In line with this, recent transcriptome studies as well as single-cell qRT-PCR have shown a decrease of all GABA_A receptor subunits (α 1–5, β 1–3, and γ 1–3) through OL development [35, 85, 86]. In particular, the γ 2 subunit is only expressed in OPCs and not in OLs [35, 85, 86]. Interestingly, the γ 2 subunit is specifically detected at the postsynaptic OPC membranes of parvalbumin fast-spiking interneuron-OPC synapses [87], at levels comparable to neuronal postsynaptic expression [88, 89]. Of note, the γ 2 subunit is required for the postsynaptic clustering of GABA_A receptor subunits [88]. From post-natal week 2 to 4, the number of OPCs expressing α 2, α 5, β 1, and γ 2 is decreased while that of α 3 and 4 is increased [86]. Of interest, this is the exact age when the synaptic transmission of OPCs switches to extra-synaptic communication [20]. However, the γ 2 subunit does not appear to affect OPC proliferation and differentiation, which appears unperturbed in mice with conditional deletion of the γ 2 subunit in OPCs [90].

While GABA_A receptor levels are strongly reduced in mature OLs [35, 80, 83, 84], axonal contacts trigger the expression of α 1 and α 3 *in vitro* as well as *in situ* [83]. However, neuronal activity does not appear to be required, since blocking it with tetrodotoxin did not alter the OL response to GABA in neuron-OL co-cultures. It is not clear yet whether these two subunits co-assemble in the same GABA_A receptor complex or whether they are components of separate and distinct receptors. Additional studies are required to address the functional role of α 1 and α 3, but also of other GABA_A receptor subunits in OPCs and OLs.

It will be exciting to learn how the spatial-temporal pattern of each subunit, including its subcellular localization, can be correlated with distinct functions in the various subpopulations of the OL lineage. The heterogeneity of OLs, in terms of anatomical location in the brain, was already described at 1921 by del Río Hortega [91]. A century later, using the single-cell RNAseq approach, studies have provided direct evidence for and confirmed an even more complex heterogeneity of OL lineage cells [92–94]. Reconsidering the early finding that only a subpopulation of OLs respond to GABA [54], we are now confronted with numerous subgroups of OLs that may or may not express GABA receptors. And, even if they are expressed, the pentameric composition of each receptor might differ in each subgroup and result in a huge diversity of GABA responses. So far, it is too early to speculate about the exact role of each subunit.

The metabotropic GABA receptor subunits GABA_{B1} and GABA_{B2} are both expressed throughout the OL lineage [35], from the subventricular zone [95] to the corpus callosum [40] and spinal cord [65]. However, so far, GABA_B receptors have not been detected in compact myelin structures [96]. Both B1 and B2 subunits were found to be down-regulated during OPC differentiation to OLs *in vitro* [95]. Intriguingly, the ratio of GABA_{B1} to GABA_{B2} also changes with the differentiation of OPCs into OLs, suggesting that B1 or B2 subunits can cooperate with other elements, even forming homodimers with novel functions as is known for some neurons [97, 98]. In the hippocampus of GABA_{B2}-null mice, an atypical electrophysiological GABA_B response has been recorded, suggesting that GABA_{B2} is not indispensable for GABA_B receptor signaling [97]. In addition, several studies also reported coupling of the GABA_{B2} subunit with other G-protein-coupled, heptahelical receptors. The GABA_{B2} subunit is functionally paired with the M2 muscarinic receptor in cortical neurons [98]. As well, functional cooperation of GABA_{B2} subunits and somatostatin receptor 4 has been found in the non-perisynaptic processes of astrocytes [99]. All these reports point to close interactions of GABA_B receptor subunits with other G-protein-coupled receptors. However, additional studies are necessary to determine whether this applies to OPCs and/or OLs and if this might change with aging.

Physiological Functions of GABA Receptors in the Lineage of Oligodendrocyte

Proliferation, Differentiation, and Myelination

While the sensitivity to GABA is largely reduced in mature OLs [65, 81, 95], a pivotal role of GABA signaling has been suggested during the origin of OPCs and the initial stages of axon recognition and myelination [22, 100]. Systemic application of the GABA_A receptor antagonist bicuculline drastically increased OPC proliferation while an increase of GABA evoked the opposite in cerebellar white matter [22]. In addition, endogenous GABA bisected the number of OPCs and mature OLs in organotypic slice cultures of mouse cortex, and this was reversed by the GABA_A receptor blocker GABAzine [18], suggesting an inhibitory role of GABA_A receptor signaling on OPC self-renewal and myelination [18]. However, it is still elusive whether this occurs by direct activation of OPC GABA_A receptors or by a more complex process integrating the activation of OPC GABA_A receptors and signals from a GABA-evoked neuronal response.

GABAergic signaling of the OL lineage seems to be essential for interneuron myelination. First of all, in layers

2/3 and 4 of cortex, the majority of myelinated axons are interneurons [26]. Among these, parvalbumin (PV)-positive interneurons account for a large proportion. Secondly, interneuron myelination is positively related to axonal activity and caliber [24, 25]. Considering that PV neurons are fast-spiking interneurons in the neocortex [101, 102], these studies strongly suggest a putative GABAergic communication between PV interneurons and OPCs. Indeed, a recent study revealed that disruption of PV interneuron-OPC interaction due to a loss of the $\gamma 2$ subunit of GABA_A receptors in OPCs results in hypomyelination of PV neurons in the barrel cortex [103]. PV-OPC synaptic structures were visualized by Tanaka *et al.* in 2009 [104]. A few years earlier, interneuron-OPC synapses were first detected in acute hippocampal slice preparations by Lin and Bergles [105]. CA1 interneurons directly release GABA, acting on the postsynaptic GABA_A receptors of OPCs. These inhibitory neuron-OPC synaptic structures have been subsequently confirmed in numerous studies [20–22, 104] in both grey and white matter [20–22, 86, 87, 90, 105, 106] (Fig. 3A). In cortex, for instance, OPC synapses are ~90% inhibitory [87]. This synaptic transmission (*via* GABA_A receptors) peaks at the second postnatal week (p10), and is immediately followed by a drastic increase in the OL population [20]. However, the communication pattern switches to extra-synaptic until the fourth postnatal week, when the GABAergic currents of

OPCs are mainly elicited by GABA spillover. Of note, at this time point, the differentiation of cortical OLs is largely completed, further suggesting that, in the early postnatal cortex, synaptic interneuron-OPC contacts are essential for OPC differentiation and interneuron myelination. Extra-synaptic GABA level, however, could be involved in the adaptive regulation of myelination. Indeed, forced increases of GABAergic connectivity between interneurons and first-wave OPCs favor deep layer myelination in the somatosensory cortex [106]. It will be interesting to investigate whether different waves of OPCs [107] form synapses with impact on distinct neuronal network activity or other biological processes. In addition, it is important to state that GABA-mediated myelination might be very different from glutamate-based processes, as indicated by shortened nodes and internodes as well as higher myelin basic protein expression of myelinated GABAergic axons than in non-GABAergic axons [26].

To date, no direct evidence is available demonstrating a decisive role of GABAergic signaling for the development of OL lineage cells *in vivo*. *In vitro*, GABA application fails to affect primary OPC proliferation [108, 109], while selective activation of GABA_B receptors with baclofen promotes the proliferation of the OPC cell line CG-4 [95]. These results further suggest the manifold roles of GABA when activating both GABA_A and GABA_B receptors leading to a complex series of events. However, the

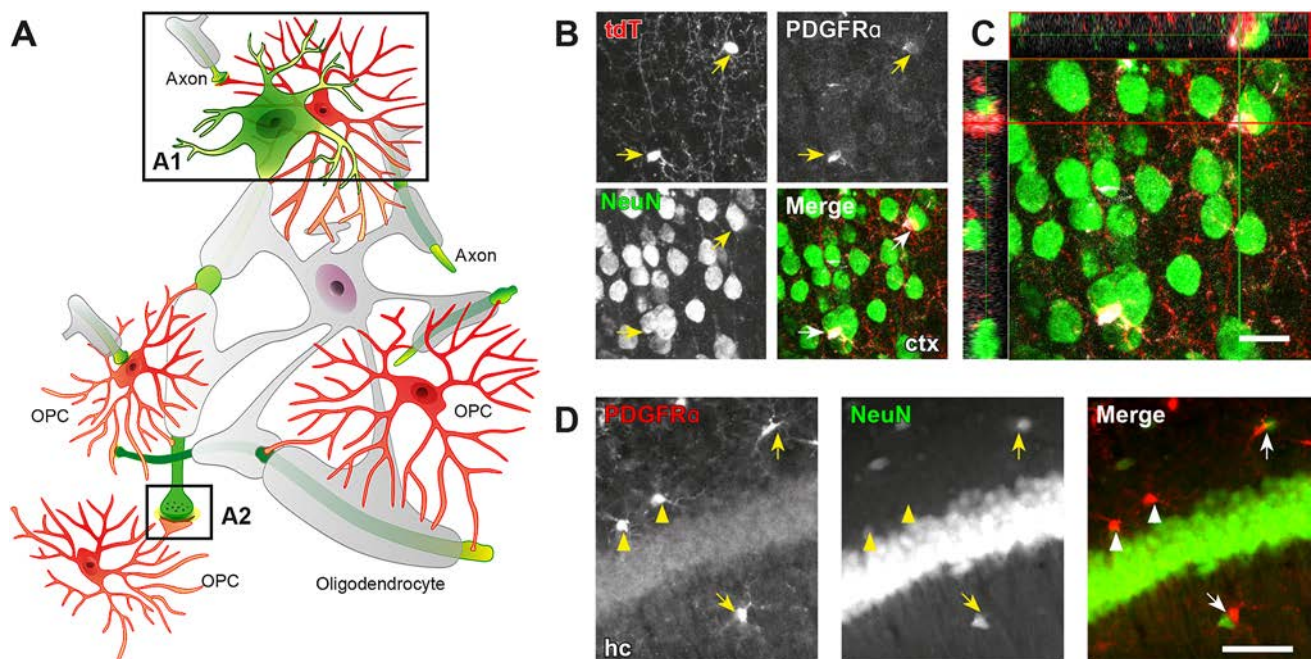


Fig. 3 Synaptic and non-synaptic neuron-OPC communication. **A** Schematic of neuron-OPC communication in the brain, including direct soma-soma (**A1**) and synaptic contact (**A2**). **B–D** OPC somata (PDGFR α^+ , red) are in close contact with neuronal somata (NeuN $^+$, green) (arrows) in cortex (ctx, **B** and **C**) and hippocampus (hc, **D**).

Micrographs in **B** and **C** are from the cortex of NG2-CreER^{T2} \times Rosa26-CAG-Is1-tdTomato mice [6, 133]. Images were acquired by confocal laser-scanning (LSM710, **B** and **C**) or automated epifluorescence microscopy (AxioScan.Z1) (**D**) with appropriate filters and objectives. Scale bars, 20 μ m for **B** and 50 μ m for **D**.

expression and even the functions of GABA receptors could differ between primary OPCs and stable cell lines. Indeed, a recent *in vitro* study showed that GABA_B receptor activation favors primary OPC differentiation rather than self-renewal and survival [40]. Nevertheless, an *in vivo* investigation is necessary to clarify the exact biological function of GABA receptors. In fact, the conditional knockout of the GABA_A receptor $\gamma 2$ subunit during early development (p3–p5) does not influence OPC proliferation and differentiation [90]. Absence of the $\gamma 2$ subunit reduces the number of OPCs without affecting differentiation into OLs, suggesting that $\gamma 2$ -mediated interneuron-to-OPC synapses might be required for the fine tuning of OPC self-maintenance [90].

Migration

OPCs maintain their density while migrating to either their target areas followed by differentiation or into sites of injury where they contribute to scar formation [9]. The migration is partially modulated by GABAergic signaling [95, 110], as has been shown for isolated primary OPCs and OPCs in explant preparations. Furthermore, this impact on migration appears to be more dominated by GABA_A than GABA_B receptor signaling, since it is blocked by the GABA_A antagonist bicuculline, but not affected by GABA_B antagonists [110]. However, GABA_B receptors have been found to promote the migration of CG-4 cells [95]. Again, such differences might be due to the distinct properties of OPCs *in vivo* versus *in vitro* and changes in stable cell lines. Receptor expression as well as the ratio of GABA_A/GABA_B receptors might change during the isolation and culturing processes. And most importantly, the microenvironment, i.e., the three-dimensional tissue organization including the stiffness and composition of the extracellular space, strongly influences migration. Therefore, *in vivo* studies are inevitably needed to address the impact of GABAergic signaling on OPC migration.

Monitoring Network Activity

OPCs receive GABAergic input in two non-exclusive modes, either directly *via* neuron-OPC synapses, i.e., contact sites between OPC processes and neuronal compartments including nodes of Ranvier, or, more diffusely, from GABA spillover from adjacent neuron-neuron synapses [20]. Close contacts between neuronal somata and OPCs have also been observed, although neurotransmitter-based connectivity is absent at such locations [111, 112] (Fig. 3A–D). About 40% of all cortical OPCs are in close contact with $\sim 4\%$ of all cortical neurons, and

these are mostly GABAergic. These anatomically close pairs of neurons and OPCs do not communicate *via* synaptic structures. However, these cell-cell contacts could very well monitor neural network activity [113], similar to the way astrocytes sense their adjacent environment [114]. In the hippocampus, the pairs of OPCs and neurons can receive the same synaptic input from another neuron. OPCs closely apposed to neurons exhibit strongly synchronized excitatory postsynaptic currents [111]. Interestingly, in the cortex, such anatomical proximity is increased when mice are treated with the GABA_B receptor agonist baclofen or the GABA_A receptor antagonist picrotoxin. OPCs can sense presynaptic excitatory signals after positioning their soma and synapse close to interneurons and thereby regulate the local network. Considering the heterogeneity of OPCs [115], it is also possible that a certain subpopulation of OPCs favors this soma-soma communication. However, more *in vivo* experiments are necessary to address the cause and importance of such contacts.

Signaling Pathways of GABA Receptors in the OL Lineage

In OPCs, the activation of GABA_A receptors induces membrane depolarization *via* Cl[−] efflux. Concomitantly, AMPA (α -amino-3-hydroxy-5-methyl-4-isoxazolepropionic acid)-type glutamate receptor currents are inhibited [105]. The activation of GABA_A receptors also raises the intracellular Ca²⁺ concentration [20, 84, 104, 116, 117] *via* at least two distinct pathways. (1) GABA-induced depolarization activates voltage-gated Na⁺ channels expressed by OPCs. Subsequently, increases of intracellular Na⁺ reverses the activity of the Na⁺-Ca²⁺ exchanger and causes Ca²⁺ elevation in OPCs. This Ca²⁺ signaling pathway, without using VGCCs, is involved in the migration of OPCs [110]. (2) In the adult mouse cortex, GABA-evoked depolarization activates VGCCs, thereby directly elevating [Ca²⁺]_i and promoting the release of BDNF (brain derived neurotrophic factor) in the sensory-motor area and entorhinal cortex [104].

In contrast, the activation of GABA_B receptors negatively regulates adenylyl cyclase *via* G_{z_{i/o}} proteins and dampens the intracellular cAMP levels of OPCs [95]. Subsequently reduced protein kinase A activity suppresses gene transcription for BDNF and AMPA receptors *via* altered phosphorylation and the nuclear translocation of transcription factors such as CREB protein, thereby modulating synaptic and neural plasticity [118–120]. In cultured OPCs, GABA_B receptor-mediated differentiation has also been shown to involve Src-family kinases, which are known to be associated with myelination [40]. Again, additional *in vivo* studies need to be carried out to elucidate

the exact downstream pathways of OL GABA_B receptors (G_{αi/o} and/or G_q) and the potential involvement of cAMP and/or Ca²⁺ (Fig. 2B).

GABA Signaling Under Pathological Conditions

As the major inhibitory neurotransmitter in the brain, GABA plays crucial roles not only in physiological processes but also in many neurological disorders [121, 122]. To date, disturbances of GABAergic signaling have been robustly studied, but significantly less is known for the cells of the OL lineage.

In hypoxic regions associated with a stroke insult, GABA release is drastically increased at the penumbra [123, 124]. Counterintuitively, the GABA_A receptor-mediated synaptic input to OPCs is reduced [22], but accompanied by extensive proliferation of OPCs, delayed OL maturation, and abnormal myelination [22]. This coincides with the finding that under physiological conditions GABA acts as neurotrophic factor. GABA *via* GABA_A (at least γ2 subunit) receptors does not influence OPC proliferation and myelination [108], while GABA_B receptor activation promotes myelination, at least *in vitro* [40], suggesting an inhibitory function of GABA_A receptors in myelination. However, whether this communication is synaptic or extrasynaptic is unclear. Upon GABAergic stimulation, adult cortical OPCs produce neurotrophic factors like BDNF, which are increased after stroke [104]. BDNF, in turn, promotes OPC proliferation under physiological and pathological conditions [13, 14]. Whether the newly generated OPCs participate in the regeneration is unknown.

In a rat model of temporal lobe epilepsy, GABA-mediated inhibition is reduced due to two processes: (1) GABA synthesis is decreased mainly due to decreased GAD65 levels and (2) inhibitory postsynaptic currents (IPSCs) decline because of down-regulation of GABA_A (especially subunits α1, γ, and δ) and GABA_B receptors. However, GABA_{A-α5} and CREB are up-regulated [125]. As an effector of CREB, BDNF expression is increased by seizure activity, which in turn induces hyperexcitability in hippocampal neurons [126]. In mice with mutant CREB, epilepsy is suppressed, suggesting a potential therapeutic option to target epilepsy [127]. However, whether and how GABA_A and GABA_B receptor-CREB signaling pathways in OPCs and OLs also contribute to epileptogenesis needs further analysis.

Dysfunction of GABA-mediated OPC neurotransmission has not yet been demonstrated in multiple sclerosis (MS), a disease with progressive demyelination. But several reports suggest the importance of GABAergic signaling during the course of MS. In the brain of MS

patients, both pre- and postsynaptic GABAergic neurotransmission are decreased [128, 129]. However, GABA level are increased in the sensorimotor cortex of MS patients but decreased in the hippocampus [130, 131]. With the knowledge that both GABA_A and GABA_B receptors are involved in OPC proliferation and differentiation under physiological conditions [18, 95], GABAergic neurotransmission of OPCs and OLs could also affect the disease progression of MS. Indeed, a recent single-cell RNAseq transcriptome study of mature OLs prepared from experimental autoimmune encephalomyelitis (EAE) mice revealed reduced levels of the GABA_{B1} subunit, but unchanged levels of the GABA_{B2} and GABA_A receptor subunits [132]. As under physiological conditions, GABA_B receptors of OLs also influence myelination in EAE. Interestingly, in these EAE mice, the expression of GABA transporter GAT3 is down-regulated in OPCs, while GAT1 is increased in OLs. However, the mRNA level of the transporter might not coincide with the respective transport activity. Therefore, elevations or reductions of extracellular GABA level cannot be inferred readily. In addition, under pathological conditions, GATs can reverse-transport GABA to the extracellular space. The scenario gets even more complex in light of the according timeline: Are expression changes of GATs a result of demyelination and thereby ahead of the remyelination failure or rather a consequence? Answering how GABAergic signaling in cells of the OL lineage is involved in de- and remyelination remains for the future.

Conclusion

GABA, a neurotransmitter as well as a neurotrophic factor, is synthesized and taken up by OPCs and OLs. For a long time, GABA has been recognized as the main mediator of neuronal inhibition. Now, we have learnt that this transmitter is broadly sensed by the OL lineage, i.e., OL precursor cells as well as mature OLs. In contrast to neurons, however, in OPCs and OLs, GABA positively stimulates signaling cascades, mainly leading to enhanced Ca²⁺ levels. Thereby, GABA promotes myelination as well as neural recovery. GABAergic signaling in cells of the OL lineage cells represents an exciting novel field of research, especially the GABA-dependent interneuron-OPC communication. The concomitant analysis of OL differentiation and the modulation of neuronal network activity by distinct patterns of myelination will not only help to understand the normal brain but will be pivotal in complex neuropathologies that depend on temporally precise neuronal firing and transmission.

Acknowledgements The authors thank Dr. Jens Grosche (Effligos AG, Leipzig, Germany) for help with Figs. 1 and 2.

Funding The authors' research received support from Deutsche Forschungsgemeinschaft (SFB 894; SPP 1757, FOR2289), EraNet-Neuron BrIE, and the HOMFORexcellenz2017 program of the University of Saarland Medical School. Open Access funding was enabled and organized by Projekt DEAL.

Conflict of interest The authors declare no competing interests.

Open Access This article is licensed under a Creative Commons Attribution 4.0 International License, which permits use, sharing, adaptation, distribution and reproduction in any medium or format, as long as you give appropriate credit to the original author(s) and the source, provide a link to the Creative Commons licence, and indicate if changes were made. The images or other third party material in this article are included in the article's Creative Commons licence, unless indicated otherwise in a credit line to the material. If material is not included in the article's Creative Commons licence and your intended use is not permitted by statutory regulation or exceeds the permitted use, you will need to obtain permission directly from the copyright holder. To view a copy of this licence, visit <http://creativecommons.org/licenses/by/4.0/>.

References

- Lee SE, Lee Y, Lee GH. The regulation of glutamic acid decarboxylases in GABA neurotransmission in the brain. *Arch Pharm Res* 2019, 42: 1031–1039.
- Roberts E, Frankel S. gamma-Aminobutyric acid in brain: its formation from glutamic acid. *J Biol Chem* 1950, 187: 55–63.
- Krnjević K, Schwartz S. The action of gamma-aminobutyric acid on cortical neurones. *Exp Brain Res* 1967, 3: 320–336.
- Hösl L, Andrès PF, Hösl E. Neuron-glia interactions: indirect effect of GABA on cultured glial cells. *Exp Brain Res* 1978, 33: 425–434.
- Nishiyama A, Komitova M, Suzuki R, Zhu X. Polydendrocytes (NG2 cells): multifunctional cells with lineage plasticity. *Nat Rev Neurosci* 2009, 10: 9–22.
- Huang W, Zhao N, Bai X, Karram K, Trotter J, Goebbels S. Novel NG2-CreERT2 knock-in mice demonstrate heterogeneous differentiation potential of NG2 glia during development. *Glia* 2014, 62: 896–913.
- Huang W, Bai X, Stopper L, Catalin B, Cartarozzi LP, Scheller A, *et al.* During development NG2 glial cells of the spinal cord are restricted to the oligodendrocyte lineage, but generate astrocytes upon acute injury. *Neuroscience* 2018, 385: 154–165.
- Huang W, Guo Q, Bai X, Scheller A, Kirchhoff F. Early embryonic NG2 glia are exclusively gliogenic and do not generate neurons in the brain. *Glia* 2019, 67: 1094–1103.
- Hughes EG, Kang SH, Fukaya M, Bergles DE. Oligodendrocyte progenitors balance growth with self-repulsion to achieve homeostasis in the adult brain. *Nat Neurosci* 2013, 16: 668–676.
- Dimou L, Götz M. Glial cells as progenitors and stem cells: new roles in the healthy and diseased brain. *Physiol Rev* 2014, 94: 709–737.
- Scheller A, Bai X, Kirchhoff F. The role of the oligodendrocyte lineage in acute brain trauma. *Neurochem Res* 2017, 42: 2479–2489.
- Guo Q, Scheller A, Huang W. Progenies of NG2 glia: what do we learn from transgenic mouse models?. *Neural Regen Res* 2021, 16: 43–48.
- Van't Veer A, Du Y, Fischer TZ, Boetig DR, Wood MR, Dreyfus CF. Brain-derived neurotrophic factor effects on oligodendrocyte progenitors of the basal forebrain are mediated through trkB and the MAP kinase pathway. *J Neurosci Res* 2009, 87: 69–78.
- Tsiperson V, Huang Y, Bagayogo I, Song Y, VonDran MW, DiCiccio-Bloom E, *et al.* Brain-derived neurotrophic factor deficiency restricts proliferation of oligodendrocyte progenitors following cuprizone-induced demyelination. *ASN Neuro* 2015, 7. <https://doi.org/10.1177/1759091414566878>.
- Jiang C, Yang W, Fan Z, Teng P, Mei R, Yang J, *et al.* AATYK is a novel regulator of oligodendrocyte differentiation and myelination. *Neurosci Bull* 2018, 34: 527–533.
- Kukley M, Capetillo-Zarate E, Dietrich D. Vesicular glutamate release from axons in white matter. *Nat Neurosci* 2007, 10: 311–320.
- Kukley M, Kiladze M, Tognatta R, Hans M, Swandulla D, Schramm J, *et al.* Glial cells are born with synapses. *FASEB J* 2008, 22: 2957–2969.
- Hamilton NB, Clarke LE, Arancibia-Carcamo IL, Kougioumtzidou E, Matthey M, Káradóttir R, *et al.* Endogenous GABA controls oligodendrocyte lineage cell number, myelination, and CNS internode length. *Glia* 2017, 65: 309–321.
- Bergles DE, Roberts JD, Somogyi P, Jahr CE. Glutamatergic synapses on oligodendrocyte precursor cells in the hippocampus. *Nature* 2000, 405: 187–191.
- Vélez-Fort M, Maldonado PP, Butt AM, Audinat E, Angulo MC. Postnatal switch from synaptic to extrasynaptic transmission between interneurons and NG2 cells. *J Neurosci* 2010, 30: 6921–6929.
- Káradóttir R, Hamilton NB, Bakiri Y, Attwell D. Spiking and nonspiking classes of oligodendrocyte precursor glia in CNS white matter. *Nat Neurosci* 2008, 11: 450–456.
- Zonouzi M, Scafidi J, Li P, McEllin B, Edwards J, Dupree JL, *et al.* GABAergic regulation of cerebellar NG2 cell development is altered in perinatal white matter injury. *Nat Neurosci* 2015, 18: 674–682.
- Ge WP, Yang XJ, Zhang Z, Wang HK, Shen W, Deng QD, *et al.* Long-term potentiation of neuron-glia synapses mediated by Ca²⁺-permeable AMPA receptors. *Science* 2006, 312: 1533–1537.
- Stedehouder J, Couey JJ, Brizee D, Hosseini B, Slotman JA, Dirven CMF, *et al.* Fast-spiking parvalbumin interneurons are frequently myelinated in the cerebral cortex of mice and humans. *Cereb Cortex* 2017, 27: 5001–5013.
- Stedehouder J, Brizee D, Slotman JA, Pascual-Garcia M, Leyrer ML, Bouwen BL, *et al.* Local axonal morphology guides the topography of interneuron myelination in mouse and human neocortex. *Elife* 2019, 8. <https://doi.org/10.7554/eLife.48615>.
- Micheva KD, Wolman D, Mensh BD, Pax E, Buchanan J, Smith SJ, *et al.* A large fraction of neocortical myelin ensheathes axons of local inhibitory neurons. *Elife* 2016, 5. <https://doi.org/10.7554/eLife.15784>.
- Pinal CS, Tobin AJ. Uniqueness and redundancy in GABA production. *Perspect Dev Neurobiol* 1998, 5: 109–118.
- Deidda G, Bozarth IF, Cancedda L. Modulation of GABAergic transmission in development and neurodevelopmental disorders: investigating physiology and pathology to gain therapeutic perspectives. *Front Cell Neurosci* 2014, 8: 119.
- Petroff OA. GABA and glutamate in the human brain. *Neuroscientist* 2002, 8: 562–573.
- Yoon BE, Woo J, Lee CJ. Astrocytes as GABA-ergic and GABA-ceptive cells. *Neurochem Res* 2012, 37: 2474–2479.
- Hertz L. The glutamate-glutamine (GABA) cycle: importance of late postnatal development and potential reciprocal interactions

- between biosynthesis and degradation. *Front Endocrinol (Lausanne)* 2013, 4: 59.
32. Kaufman DL, Houser CR, Tobin AJ. Two forms of the gamma-aminobutyric acid synthetic enzyme glutamate decarboxylase have distinct intraneuronal distributions and cofactor interactions. *J Neurochem* 1991, 56: 720–723.
 33. Asada H, Kawamura Y, Maruyama K, Kume H, Ding RG, Kanbara N, *et al.* Cleft palate and decreased brain gamma-aminobutyric acid in mice lacking the 67-kDa isoform of glutamic acid decarboxylase. *Proc Natl Acad Sci U S A* 1997, 94: 6496–6499.
 34. Kash SF, Johnson RS, Tecott LH, Noebels JL, Mayfield RD, Hanahan D, *et al.* Epilepsy in mice deficient in the 65-kDa isoform of glutamic acid decarboxylase. *Proc Natl Acad Sci U S A* 1997, 94: 14060–14065.
 35. Zhang Y, Chen K, Sloan SA, Bennett ML, Scholze AR, O’Keefe S, *et al.* An RNA-sequencing transcriptome and splicing database of glia, neurons, and vascular cells of the cerebral cortex. *J Neurosci* 2014, 34: 11929–11947.
 36. Kozlov AS, Angulo MC, Audinat E, Charpak S. Target cell-specific modulation of neuronal activity by astrocytes. *Proc Natl Acad Sci U S A* 2006, 103: 10058–10063.
 37. Le Meur K, Mendizabal-Zubiaga J, Grandes P, Audinat E. GABA release by hippocampal astrocytes. *Front Comput Neurosci* 2012, 6: 59.
 38. Jiménez-González C, Pirrtimaki T, Cope DW, Parri HR. Non-neuronal, slow GABA signalling in the ventrobasal thalamus targets δ -subunit-containing GABA_A receptors. *Eur J Neurosci* 2011, 33: 1471–1482.
 39. Barakat L, Bordey A. GAT-1 and reversible GABA transport in Bergmann glia in slices. *J Neurophysiol* 2002, 88: 1407–1419.
 40. Serrano-Regal MP, Luengas-Escuza I, Bayón-Cordero L, Ibarra-Aizpurua N, Alberdi E, Pérez-Samartín A, *et al.* Oligodendrocyte differentiation and myelination is potentiated *via* GABA. *Neuroscience* 2020, 439: 163–180.
 41. Xin W, Mironova YA, Shen H, Marino RAM, Waisman A, Lamers WH, *et al.* Oligodendrocytes support neuronal glutamatergic transmission via expression of glutamine synthetase. *Cell Rep* 2019, 27(2262–2271): e2265.
 42. Attwell D, Barbour B, Szatkowski M. Nonvesicular release of neurotransmitter. *Neuron* 1993, 11: 401–407.
 43. Richerson GB, Wu Y. Dynamic equilibrium of neurotransmitter transporters: not just for reuptake anymore. *J Neurophysiol* 2003, 90: 1363–1374.
 44. Schwartz EA. Depolarization without calcium can release gamma-aminobutyric acid from a retinal neuron. *Science* 1987, 238: 350–355.
 45. Wu Y, Wang W, Richerson GB. GABA transaminase inhibition induces spontaneous and enhances depolarization-evoked GABA efflux via reversal of the GABA transporter. *J Neurosci* 2001, 21: 2630–2639.
 46. Wu Y, Wang W, Díez-Sampedro A, Richerson GB. Nonvesicular inhibitory neurotransmission via reversal of the GABA transporter GAT-1. *Neuron* 2007, 56: 851–865.
 47. Savtchenko L, Megalogeni M, Rusakov DA, Walker MC, Pavlov I. Synaptic GABA release prevents GABA transporter type-1 reversal during excessive network activity. *Nat Commun* 2015, 6: 6597.
 48. Saito K, Kakizaki T, Hayashi R, Nishimaru H, Furukawa T, Nakazato Y, *et al.* The physiological roles of vesicular GABA transporter during embryonic development: a study using knockout mice. *Mol Brain* 2010, 3: 40.
 49. Jensen K, Chiu CS, Sokolova I, Lester HA, Mody I. GABA transporter-1 (GAT1)-deficient mice: differential tonic activation of GABA_A versus GABA_B receptors in the hippocampus. *J Neurophysiol* 2003, 90: 2690–2701.
 50. Fattorini G, Melone M, Sánchez-Gómez MV, Arellano RO, Bassi S, Matute C, *et al.* GAT-1 mediated GABA uptake in rat oligodendrocytes. *Glia* 2017, 65: 514–522.
 51. Takanaga H, Ohtsuki S, Hosoya Ki, Terasaki T. GAT2/BGT-1 as a system responsible for the transport of gamma-aminobutyric acid at the mouse blood-brain barrier. *J Cereb Blood Flow Metab* 2001, 21: 1232–1239.
 52. Zhou Y, Holmseth S, Guo C, Hassel B, Höfner G, Huitfeldt HS, *et al.* Deletion of the γ -aminobutyric acid transporter 2 (GAT2 and SLC6A13) gene in mice leads to changes in liver and brain taurine contents. *J Biol Chem* 2012, 287: 35733–35746.
 53. Tsai HH, Niu J, Munji R, Davalos D, Chang J, Zhang H, *et al.* Oligodendrocyte precursors migrate along vasculature in the developing nervous system. *Science* 2016, 351: 379–384.
 54. Gilbert P, Kettenmann H, Schachner M. gamma-Aminobutyric acid directly depolarizes cultured oligodendrocytes. *J Neurosci* 1984, 4: 561–569.
 55. Farrant M, Nusser Z. Variations on an inhibitory theme: phasic and tonic activation of GABA_A receptors. *Nat Rev Neurosci* 2005, 6: 215–229.
 56. Ben-Ari Y, Gaiarsa JL, Tyzio R, Khazipov R. GABA: a pioneer transmitter that excites immature neurons and generates primitive oscillations. *Physiol Rev* 2007, 87: 1215–1284.
 57. Naffaa MM, Hung S, Chebib M, Johnston GAR, Hanrahan JR. GABA- ρ receptors: distinctive functions and molecular pharmacology. *Br J Pharmacol* 2017, 174: 1881–1894.
 58. Kaila K. Ionic basis of GABA_A receptor channel function in the nervous system. *Prog Neurobiol* 1994, 42: 489–537.
 59. Hübner CA, Holthoff K. Anion transport and GABA signaling. *Front Cell Neurosci* 2013, 7: 177.
 60. Bettler B, Kaupmann K, Mosbacher J, Gassmann M. Molecular structure and physiological functions of GABA_B receptors. *Physiol Rev* 2004, 84: 835–867.
 61. Bettler B, Tiao JY. Molecular diversity, trafficking and subcellular localization of GABA_B receptors. *Pharmacol Ther* 2006, 110: 533–543.
 62. Kaupmann K, Malitschek B, Schuler V, Heid J, Froestl W, Beck P, *et al.* GABA_B-receptor subtypes assemble into functional heteromeric complexes. *Nature* 1998, 396: 683–687.
 63. Bowery NG, Bettler B, Froestl W, Gallagher JP, Marshall F, Raiteri M, *et al.* International Union of Pharmacology. XXXIII. Mammalian gamma-aminobutyric acid(B) receptors: structure and function. *Pharmacol Rev* 2002, 54: 247–264.
 64. Kuner R, Köhr G, Grünewald S, Eisenhardt G, Bach A, Kornau HC. Role of heteromer formation in GABA_B receptor function. *Science* 1999, 283: 74–77.
 65. Calver AR, Medhurst AD, Robbins MJ, Charles KJ, Evans ML, Harrison DC, *et al.* The expression of GABA_{B1} and GABA_{B2} receptor subunits in the CNS differs from that in peripheral tissues. *Neuroscience* 2000, 100: 155–170.
 66. Thuaux SJ, Brown JT, Sheardown SA, Jourdain S, Fairfax B, Spencer JP, *et al.* The GABA_{B2} subunit is critical for the trafficking and function of native GABA_B receptors. *Biochem Pharmacol* 2004, 68: 1655–1666.
 67. Galvez T, Parmentier ML, Joly C, Malitschek B, Kaupmann K, Kuhn R, *et al.* Mutagenesis and modeling of the GABA_B receptor extracellular domain support a venus flytrap mechanism for ligand binding. *J Biol Chem* 1999, 274: 13362–13369.
 68. Obrietan K, van den Pol AN. GABA_B receptor-mediated regulation of glutamate-activated calcium transients in hypothalamic and cortical neuron development. *J Neurophysiol* 1999, 82: 94–102.
 69. Menon-Johansson AS, Berrow N, Dolphin AC. G_o transduces GABA_B-receptor modulation of N-type calcium channels in cultured dorsal root ganglion neurons. *Pflugers Arch* 1993, 425: 335–343.

70. Li Y, Stern JE. Activation of postsynaptic GABA_B receptors modulate the firing activity of supraoptic oxytocin and vasopressin neurones: role of calcium channels. *J Neuroendocrinol* 2004, 16: 119–130.
71. Harayama N, Shibuya I, Tanaka K, Kabashima N, Ueta Y, Yamashita H. Inhibition of N- and P/Q-type calcium channels by postsynaptic GABA_B receptor activation in rat supraoptic neurones. *J Physiol* 1998, 509(Pt 2): 371–383.
72. Nehring RB, Horikawa HP, El Far O, Kneussel M, Brandstätter JH, Stamm S, *et al.* The metabotropic GABA_B receptor directly interacts with the activating transcription factor 4. *J Biol Chem* 2000, 275: 35185–35191.
73. White JH, McIllhinney RA, Wise A, Ciruela F, Chan WY, Emson PC, *et al.* The GABA_B receptor interacts directly with the related transcription factors CREB2 and ATFx. *Proc Natl Acad Sci U S A* 2000, 97: 13967–13972.
74. Schuler V, Lüscher C, Blanchet C, Klix N, Sansig G, Klebs K, *et al.* Epilepsy, hyperalgesia, impaired memory, and loss of pre- and postsynaptic GABA_B responses in mice lacking GABA_{B(1)}. *Neuron* 2001, 31: 47–58.
75. Redburn DA, Paul MJ. GABA-its role and development in retina. *Progress in retinal research* 1987, 6: 16.
76. Ben-Ari Y, Cherubini E. Zinc and GABA in developing brain. *Nature* 1991, 353: 220.
77. Ben-Ari Y, Tseeb V, Raggozzino D, Khazipov R, Gaiarsa JL. gamma-Aminobutyric acid (GABA): a fast excitatory transmitter which may regulate the development of hippocampal neurones in early postnatal life. *Prog Brain Res* 1994, 102: 261–273.
78. Ganguly K, Schinder AF, Wong ST, Poo M. GABA itself promotes the developmental switch of neuronal GABAergic responses from excitation to inhibition. *Cell* 2001, 105: 521–532.
79. Rivera C, Voipio J, Payne JA, Ruusuvuori E, Lahtinen H, Lamsa K, *et al.* The K⁺/Cl⁻ co-transporter KCC2 renders GABA hyperpolarizing during neuronal maturation. *Nature* 1999, 397: 251–255.
80. Von Blankenfeld G, Trotter J, Kettenmann H. Expression and developmental regulation of a GABA_A receptor in cultured murine cells of the oligodendrocyte lineage. *Eur J Neurosci* 1991, 3: 310–316.
81. Berger T, Walz W, Schnitzer J, Kettenmann H. GABA- and glutamate-activated currents in glial cells of the mouse corpus callosum slice. *J Neurosci Res* 1992, 31: 21–27.
82. Steinhäuser C, Jabs R, Kettenmann H. Properties of GABA and glutamate responses in identified glial cells of the mouse hippocampal slice. *Hippocampus* 1994, 4: 19–35.
83. Arellano RO, Sánchez-Gómez MV, Alberdi E, Canedo-Antelo M, Chara JC, Palomino A, *et al.* Axon-to-glia interaction regulates GABA_A receptor expression in oligodendrocytes. *Mol Pharmacol* 2016, 89: 63–74.
84. Kirchhoff F, Kettenmann H. GABA triggers a [Ca²⁺]_i increase in murine precursor cells of the oligodendrocyte lineage. *Eur J Neurosci* 1992, 4: 1049–1058.
85. Passlick S, Grauer M, Schäfer C, Jabs R, Seifert G, Steinhäuser C. Expression of the γ 2-subunit distinguishes synaptic and extrasynaptic GABA_A receptors in NG2 cells of the hippocampus. *J Neurosci* 2013, 33: 12030–12040.
86. Balia M, Vélez-Fort M, Passlick S, Schäfer C, Audinat E, Steinhäuser C, *et al.* Postnatal down-regulation of the GABA_A receptor γ 2 subunit in neocortical NG2 cells accompanies synaptic-to-extrasynaptic switch in the GABAergic transmission mode. *Cereb Cortex* 2015, 25: 1114–1123.
87. Orduz D, Maldonado PP, Balia M, Vélez-Fort M, de Sars V, Yanagawa Y, *et al.* Interneurons and oligodendrocyte progenitors form a structured synaptic network in the developing neocortex. *Elife* 2015, 4. <https://doi.org/10.7554/eLife.06953>.
88. Essrich C, Lorez M, Benson JA, Fritschy JM, Lüscher B. Postsynaptic clustering of major GABA_A receptor subtypes requires the gamma 2 subunit and gephyrin. *Nat Neurosci* 1998, 1: 563–571.
89. Kneussel M, Betz H. Clustering of inhibitory neurotransmitter receptors at developing postsynaptic sites: the membrane activation model. *Trends Neurosci* 2000, 23: 429–435.
90. Balia M, Benamer N, Angulo MC. A specific GABAergic synapse onto oligodendrocyte precursors does not regulate cortical oligodendrogenesis. *Glia* 2017, 65: 1821–1832.
91. Del Río Hortega P. La glía de escasas radiaciones (oligodendroglia). *Bol Real Soc Esp Hist Nat* 1921, 21: 63–92.
92. Marques S, Zeisel A, Codeluppi S, van Bruggen D, Mendanha Falcão A, Xiao L, *et al.* Oligodendrocyte heterogeneity in the mouse juvenile and adult central nervous system. *Science* 2016, 352: 1326–1329.
93. Marisca R, Hoche T, Agirre E, Hoodless LJ, Barkey W, Auer F, *et al.* Functionally distinct subgroups of oligodendrocyte precursor cells integrate neural activity and execute myelin formation. *Nat Neurosci* 2020, 23: 363–374.
94. Spitzer SO, Sitnikov S, Kamen Y, Evans KA, Kronenberg-Versteeg D, Dietmann S, *et al.* Oligodendrocyte progenitor cells become regionally diverse and heterogeneous with age. *Neuron* 2019, 101(459–471): e455.
95. Luyt K, Slade TP, Dorward JJ, Durant CF, Wu Y, Shigemoto R, *et al.* Developing oligodendrocytes express functional GABA_B receptors that stimulate cell proliferation and migration. *J Neurochem* 2007, 100: 822–840.
96. Charles KJ, Deuchars J, Davies CH, Pangalos MN. GABA_B receptor subunit expression in glia. *Mol Cell Neurosci* 2003, 24: 214–223.
97. Gassmann M, Shaban H, Vigot R, Sansig G, Haller C, Barbieri S, *et al.* Redistribution of GABA_{B(1)} protein and atypical GABA_B responses in GABA_{B(2)}-deficient mice. *J Neurosci* 2004, 24: 6086–6097.
98. Boyer SB, Clancy SM, Terunuma M, Revilla-Sanchez R, Thomas SM, Moss SJ, *et al.* Direct interaction of GABA_B receptors with M2 muscarinic receptors enhances muscarinic signaling. *J Neurosci* 2009, 29: 15796–15809.
99. Mariotti L, Losi G, Lia A, Melone M, Chiavegato A, Gómez-Gonzalo M, *et al.* Interneuron-specific signaling evokes distinctive somatostatin-mediated responses in adult cortical astrocytes. *Nat Commun* 2018, 9: 82.
100. Vélez-Fort M, Audinat E, Angulo MC. Central role of GABA in neuron-glia interactions. *Neuroscientist* 2012, 18: 237–250.
101. Hu H, Gan J, Jonas P. Interneurons. Fast-spiking, parvalbumin+ GABAergic interneurons: from cellular design to microcircuit function. *Science* 2014, 345: 1255263.
102. Kawaguchi Y, Katsumaru H, Kosaka T, Heizmann CW, Hama K. Fast spiking cells in rat hippocampus (CA1 region) contain the calcium-binding protein parvalbumin. *Brain Res* 1987, 416: 369–374.
103. Benamer N, Vidal M, Balia M, Angulo MC. Myelination of parvalbumin interneurons shapes the function of cortical sensory inhibitory circuits. *Nat Commun* 2020, 11: 5151.
104. Tanaka Y, Tozuka Y, Takata T, Shimazu N, Matsumura N, Ohta A, *et al.* Excitatory GABAergic activation of cortical dividing glial cells. *Cereb Cortex* 2009, 19: 2181–2195.
105. Lin SC, Bergles DE. Synaptic signaling between GABAergic interneurons and oligodendrocyte precursor cells in the hippocampus. *Nat Neurosci* 2004, 7: 24–32.
106. Orduz D, Benamer N, Ortolani D, Coppola E, Vigier L, Pierani A, *et al.* Developmental cell death regulates lineage-related

- interneuron-oligodendroglia functional clusters and oligodendrocyte homeostasis. *Nat Commun* 2019, 10: 4249.
107. Kessaris N, Fogarty M, Iannarelli P, Grist M, Wegner M, Richardson WD. Competing waves of oligodendrocytes in the forebrain and postnatal elimination of an embryonic lineage. *Nat Neurosci* 2006, 9: 173–179.
 108. Gallo V, Zhou JM, McBain CJ, Wright P, Knutson PL, Armstrong RC. Oligodendrocyte progenitor cell proliferation and lineage progression are regulated by glutamate receptor-mediated K^+ channel block. *J Neurosci* 1996, 16: 2659–2670.
 109. Yuan X, Eisen AM, McBain CJ, Gallo V. A role for glutamate and its receptors in the regulation of oligodendrocyte development in cerebellar tissue slices. *Development* 1998, 125: 2901–2914.
 110. Tong XP, Li XY, Zhou B, Shen W, Zhang ZJ, Xu TL, *et al.* Ca^{2+} signaling evoked by activation of Na^+ channels and Na^+/Ca^{2+} exchangers is required for GABA-induced NG2 cell migration. *J Cell Biol* 2009, 186: 113–128.
 111. Mangin JM, Kunze A, Chittajallu R, Gallo V. Satellite NG2 progenitor cells share common glutamatergic inputs with associated interneurons in the mouse dentate gyrus. *J Neurosci* 2008, 28: 7610–7623.
 112. Boulanger JJ, Messier C. Oligodendrocyte progenitor cells are paired with GABA neurons in the mouse dorsal cortex: Unbiased stereological analysis. *Neuroscience* 2017, 362: 127–140.
 113. Boulanger JJ, Messier C. Doublecortin in oligodendrocyte precursor cells in the adult mouse brain. *Front Neurosci* 2017, 11: 143.
 114. Araque A, Carmignoto G, Haydon PG, Oliet SH, Robitaille R, Volterra A. Gliotransmitters travel in time and space. *Neuron* 2014, 81: 728–739.
 115. Marques S, van Bruggen D, Vanichkina DP, Floriddia EM, Munguba H, Våremo L, *et al.* Transcriptional convergence of oligodendrocyte lineage progenitors during development. *Dev Cell* 2018, 46(504–517): e507.
 116. Belachew S, Malgrange B, Rigo JM, Rogister B, Coucke P, Mazy-Servais C, *et al.* Developmental regulation of neurotrophin-induced responses in cultured oligodendroglia. *Neuroreport* 1998, 9: 973–980.
 117. Bernstein M, Lyons SA, Möller T, Kettenmann H. Receptor-mediated calcium signalling in glial cells from mouse corpus callosum slices. *J Neurosci Res* 1996, 46: 152–163.
 118. Middei S, Houeland G, Cavallucci V, Ammassari-Teule M, D'Amelio M, Marie H. CREB is necessary for synaptic maintenance and learning-induced changes of the AMPA receptor GluA1 subunit. *Hippocampus* 2013, 23: 488–499.
 119. Finkbeiner S, Tavazoie SF, Maloratsky A, Jacobs KM, Harris KM, Greenberg ME. CREB: a major mediator of neuronal neurotrophin responses. *Neuron* 1997, 19: 1031–1047.
 120. Tao X, Finkbeiner S, Arnold DB, Shaywitz AJ, Greenberg ME. Ca^{2+} influx regulates BDNF transcription by a CREB family transcription factor-dependent mechanism. *Neuron* 1998, 20: 709–726.
 121. Wong CG, Bottiglieri T, Snead OC. GABA, gamma-hydroxybutyric acid, and neurological disease. *Ann Neurol* 2003, 54(Suppl 6): S3–12.
 122. Chang YY, Gong XW, Gong HQ, Liang PJ, Zhang PM, Lu QC. GABA_A receptor activity suppresses the transition from interictal to ictal epileptiform discharges in juvenile mouse hippocampus. *Neurosci Bull* 2018, 34: 1007–1016.
 123. Phillis JW, Smith-Barbour M, Perkins LM, O'Regan MH. Characterization of glutamate, aspartate, and GABA release from ischemic rat cerebral cortex. *Brain Res Bull* 1994, 34: 457–466.
 124. Matsumoto K, Lo EH, Pierce AR, Halpern EF, Newcomb R. Secondary elevation of extracellular neurotransmitter amino acids in the reperfusion phase following focal cerebral ischemia. *J Cereb Blood Flow Metab* 1996, 16: 114–124.
 125. Mathew J, Balakrishnan S, Antony S, Abraham PM, Paulose CS. Decreased GABA receptor in the cerebral cortex of epileptic rats: effect of *Bacopa monnieri* and *Bacoside-A*. *J Biomed Sci* 2012, 19: 25.
 126. Binder DK, Croll SD, Gall CM, Scharfman HE. BDNF and epilepsy: too much of a good thing?. *Trends Neurosci* 2001, 24: 47–53.
 127. Zhu X, Han X, Blendy JA, Porter BE. Decreased CREB levels suppress epilepsy. *Neurobiol Dis* 2012, 45: 253–263.
 128. Dutta R, McDonough J, Yin X, Peterson J, Chang A, Torres T, *et al.* Mitochondrial dysfunction as a cause of axonal degeneration in multiple sclerosis patients. *Ann Neurol* 2006, 59: 478–489.
 129. Rossi S, Studer V, Motta C, De Chiara V, Barbieri F, Bernardi G, *et al.* Inflammation inhibits GABA transmission in multiple sclerosis. *Mult Scler* 2012, 18: 1633–1635.
 130. Cawley N, Solanky BS, Muhlert N, Tur C, Edden RA, Wheeler-Kingshott CA, *et al.* Reduced gamma-aminobutyric acid concentration is associated with physical disability in progressive multiple sclerosis. *Brain* 2015, 138: 2584–2595.
 131. Bhattacharyya PK, Phillips MD, Stone LA, Bermel RA, Lowe MJ. Sensorimotor cortex gamma-aminobutyric acid concentration correlates with impaired performance in patients with MS. *AJNR Am J Neuroradiol* 2013, 34: 1733–1739.
 132. Falcão AM, van Bruggen D, Marques S, Meijer M, Jäkel S, Agirre E, *et al.* Disease-specific oligodendrocyte lineage cells arise in multiple sclerosis. *Nat Med* 2018, 24: 1837–1844.
 133. Madisen L, Zwingman TA, Sunkin SM, Oh SW, Zariwala HA, Gu H, *et al.* A robust and high-throughput Cre reporting and characterization system for the whole mouse brain. *Nat Neurosci* 2010, 13: 133–140.



Structural, Functional, and Molecular Imaging of Autism Spectrum Disorder

Xiaoyi Li^{1,2,6} · Kai Zhang⁴ · Xiao He^{1,2,6} · Jinyun Zhou^{1,2,6} · Chentao Jin^{1,2,6} · Lesang Shen⁵ · Yuanxue Gao^{1,2,6} · Mei Tian^{1,2,6} · Hong Zhang^{1,2,3,6,7} 

Received: 1 September 2020 / Accepted: 20 December 2020 / Published online: 29 March 2021
© Center for Excellence in Brain Science and Intelligence Technology, CAS 2021

Abstract Autism spectrum disorder (ASD) is a heterogeneous neurodevelopmental disorder associated with both genetic and environmental risks. Neuroimaging approaches have been widely employed to parse the neurophysiological mechanisms underlying ASD, and provide critical insights into the anatomical, functional, and neurochemical changes. We reviewed recent advances in neuroimaging studies that focused on ASD by using magnetic resonance imaging (MRI), positron emission tomography (PET), or single-positron emission tomography (SPECT). Longitudinal structural MRI has delineated an abnormal

developmental trajectory of ASD that is associated with cascading neurobiological processes, and functional MRI has pointed to disrupted functional neural networks. Meanwhile, PET and SPECT imaging have revealed that metabolic and neurotransmitter abnormalities may contribute to shaping the aberrant neural circuits of ASD. Future large-scale, multi-center, multimodal investigations are essential to elucidate the neurophysiological underpinnings of ASD, and facilitate the development of novel diagnostic biomarkers and better-targeted therapy.

Keywords Autism spectrum disorder · Positron emission tomography · Magnetic resonance imaging · Molecular imaging · Functional connectivity · Serotonin · Oxytocin

Xiaoyi Li and Kai Zhang have contributed equally to this work.

✉ Mei Tian
meitian@zju.edu.cn

✉ Hong Zhang
hzhang21@zju.edu.cn

¹ Department of Nuclear Medicine and Medical PET Center, The Second Hospital of Zhejiang University School of Medicine, Hangzhou 310009, China

² Key Laboratory of Medical Molecular Imaging of Zhejiang Province, Hangzhou 310009, China

³ Key Laboratory for Biomedical Engineering of Ministry of Education, Zhejiang University, Hangzhou 310027, China

⁴ Laboratory for Pathophysiological and Health Science, RIKEN Center for Biosystems Dynamics Research, Hyogo 650-0047, Japan

⁵ Department of Surgical Oncology, The Second Hospital of Zhejiang University School of Medicine, Hangzhou 310009, China

⁶ Institute of Nuclear Medicine and Molecular Imaging, Zhejiang University, Hangzhou 310009, China

⁷ The College of Biomedical Engineering and Instrument Science of Zhejiang University, Hangzhou 310027, China

Introduction

Autism spectrum disorder (ASD) is a heterogeneous neurodevelopmental disorder characterized by impaired social communication and restricted, repetitive behaviors [1], typically emerging at about 24 months of age. The global prevalence rate of ASD is about 1% [2], and its prevalence rate in Chinese children is estimated at 0.7% [3]. According to the latest report, ASD is associated with an annual economic burden of >250 billion dollars in the USA, mainly due to special education costs, higher medical costs, and loss of parental labor [4].

The etiologies of ASD are complex and are thought to be attributable to both genetic and environmental risk factors [5]. Evidence from genetic research has associated >100 genetic variants with ASD risk [6]. Currently, the clinical diagnosis of ASD is mainly based on observation of behaviors [7], and there is no valid biomarker that can aid in its diagnosis, or predict the onset, progression, or

severity. Furthermore, it is primarily treated through behavioral and educational interventions with no available medication for treating its core neurobiological determinants [8]. Hence, it is a priority to better understand the neurobiological mechanisms in order to provide early biologically-based diagnosis and more effective therapeutic interventions for ASD.

Neuroimaging provides a non-invasive window into the human brain. Over the past few decades, neuroimaging modalities including positron emission tomography (PET) and single-positron emission computed tomography (SPECT) combined with structural and functional magnetic resonance imaging (MRI) have been increasingly used to explore the neural anatomical, functional and molecular bases underlying ASD. Molecular imaging techniques such as PET and SPECT allow the mapping of biological processes *in vivo* at the cellular and molecular levels, and facilitate the non-invasive visualization of ASD-specific metabolic and neurochemical changes *in vivo* [9, 10]. MRI provides anatomical and functional information underlying ASD.

In the current review, we present the recent advances in structural, functional, and molecular neuroimaging for ASD. We included original neuroimaging articles on ASD published between 2010 and June 30, 2020, particularly structural MRI, resting-state functional MRI, PET, and SPECT, and briefly summarize the main findings followed by discussion of future directions. We did not cover task-related functional MRI due to space limitations. We searched PubMed using the following search terms: “autism”, “magnetic resonance imaging”, “connectivity”, “resting state”, “perfusion”, “positron emission tomography”, and “single photon emission computed tomography” alone and in combination. Neuroimaging studies examining ASD and typically developing (TD) subjects were included. We screened each retrieved article by the relevance of its abstract, and checked the reference list of each article for further relevant publications.

MRI

MRI is a versatile imaging modality that is capable of probing extensive physiological processes based on the special spin properties of protons and neutrons [11]. One key strength of MRI is its superb spatial resolution (micrometers), enabling the *in vivo* detection of subtle changes in brain morphology. Using specialized techniques, diffusion tensor MRI interrogates the microstructure of white matter based on free water diffusion, and arterial spin labeling (ASL) allows the quantitative measurement of tissue perfusion. In addition, functional MRI enables the investigation of functional connectivity

patterns based on the blood-oxygen-level-dependent signal [12]. In particular, resting-state functional MRI and structural MRI have been widely employed to investigate the neural correlates of ASD (Fig. 1).

MR Imaging of Brain Morphology

Numerous structural MRI studies on ASD have indicated alterations in brain morphology, mainly in cortical surface area and thickness, gray matter volume, and white matter connectivity, particularly in the frontal cortex, temporal cortex, and amygdala [13–17]. Table 1 summarizes the main findings of structural MRI studies in ASD.

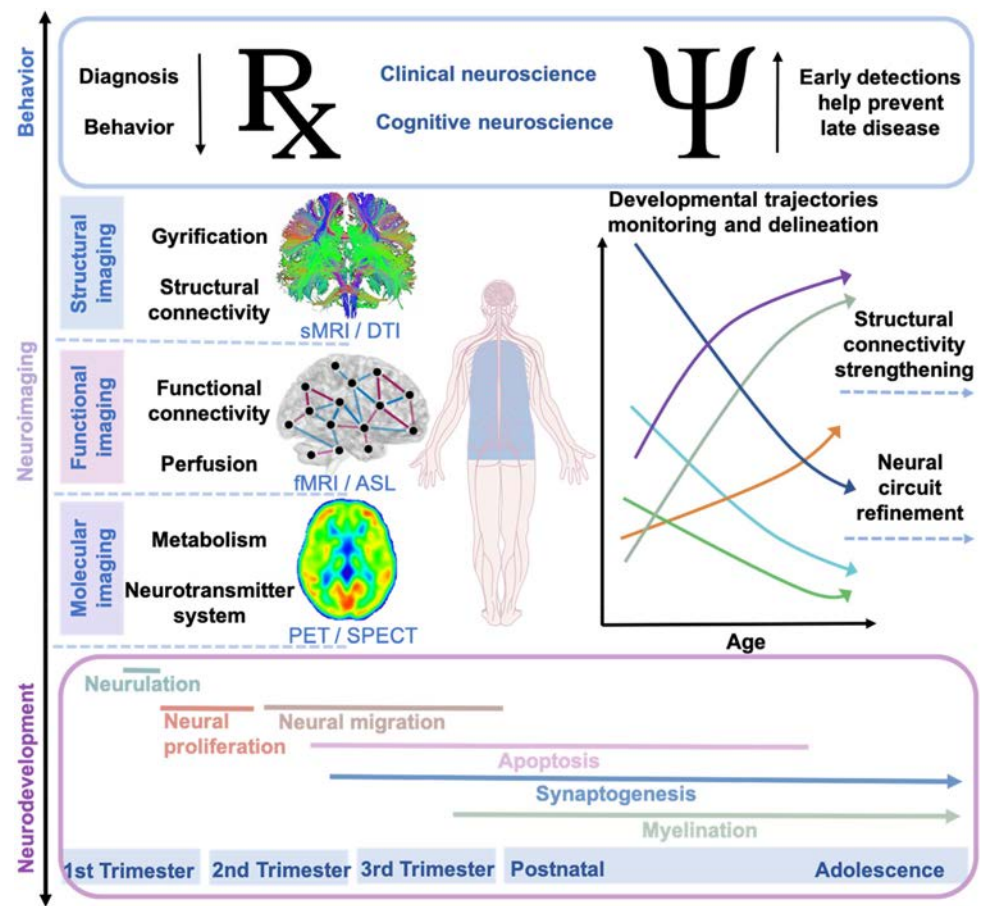
Cortex

Voxel-based morphometry is an objective and pragmatic approach to assessing anatomical abnormalities (for methodology, see [18]). By using voxel-based approaches, gray matter volume abnormalities have been identified throughout the brain in ASD [15, 16]. Recent meta-analysis of voxel-based studies in ASD has provided evidence of age-related cerebral enlargement, particularly gray matter overgrowth in the prefrontal cortex (PFC) [13, 14]. The PFC is involved in multiple cognitive and social functions, such as social cognition, inhibition [19, 20], working memory [21], language [22], motivation, and reward-based learning [20]. Thus, structural abnormalities in the PFC may be associated with the social impairment and language deficits in ASD.

Emerging evidence from longitudinal neuroimaging studies has indicated age-specific anatomical changes and atypical neurodevelopmental trajectories in ASD [16, 23–25]. For instance, autism is marked by brain overgrowth during infancy and the toddler years, followed by an accelerated rate of decline in size and perhaps degeneration from adolescence to adulthood when decreases in structural volume are observed. This has led to the theory of age-specific anatomic abnormalities in autism [23], which may be related to age-specific changes in gene expression, and molecular, synaptic, and cellular as well as circuit abnormalities. To address the original cause driving these age-specific changes in anatomical abnormalities is a challenge in autism research, and it has been suggested that the optimum age for studying the pathophysiology of autism is the first three postnatal years and prenatal life [23].

A number of longitudinal studies focused on infants and toddlers offer critical insights into the atypical neurodevelopmental trajectories of ASD in early postnatal life [17, 24–33]. A recent prospective study on infants at risk for ASD (106 high-risk and 42 low-risk) has revealed that children who go on to develop ASD show cortical surface

Fig. 1 Schematic of multilevel imaging-based studies on ASD brain development in the context of the temporal dimension (horizontal axis) at different scales (vertical axis). Different indices are derived from structural, functional, and molecular imaging, such as gyrification, structural connectivity, functional connectivity, perfusion, metabolism, and neurotransmitter systems. Longitudinal neuroimaging studies monitor and delineate brain developmental trajectories in ASD, which are postulated to be related to cascading neurodevelopmental processes. Bottom panel, prominent processes relevant to ASD during fetal and post-natal brain development. Adapted from [163].



area hyper-expansion from 6 months to 12 months of age. This hyper-expansion starts in domains mediating auditory and visual processing and is highly predictive (a positive predictive value of 81%) of the diagnosis of ASD in high-risk infants [29]. The presence of cortical surface area hyper-expansion precedes the onset of brain volume overgrowth in the second year after birth [26, 29, 33]. Besides, several studies found no differences in cortical thickness in ASD toddlers [29, 30, 33]. Thus, it has been suggested that the early cortical overgrowth in ASD may be driven by accelerated cortical surface area expansion rather than increased cortical thickness [29, 30, 33], since distinct developmental mechanisms may account for the radial expansion that produces the multilayered cortex of mammals and for the tangential expansion of cortical surface area [34]. Specifically, tangential expansion of the neocortical surface area is closely associated with the number of radial units formed by symmetrical divisions along the ventricular zone, whereas cortical thickness is controlled by the number of asymmetric radial glial cell divisions [35, 36]. Since each round of mitosis results in an exponential increase in the number of progenitor cells, small changes affecting the duration of symmetric growth will have a dramatic impact on surface area. Thus, cortical

surface area hyper-expansion in ASD individuals is possibly attributed to dysregulated neural progenitor cell proliferation and differentiation, and this has been supported by the findings from ASD patient-derived neural progenitor cells showing excessive proliferation compared with normal controls [37–39]. On the other hand, incomplete synaptic pruning could also contribute to the brain overgrowth in ASD [40], but the underlying mechanisms are not conclusive and need to be further elucidated in future studies.

Besides, atypical cortical folding has been indicated in ASD [41, 42], as measured by the local gyrification index (LGI). Gyrification, the process by which the brain forms sulcal and gyral regions, allows for optimized compact wiring of neuronal fibers that promotes efficient neural processing in the brain [43]. In individuals with ASD aged 7 years–19 years, LGI is increased in the left parietal and temporal and right frontal and temporal regions compared with TD [42]. LGI declines with age, but more steeply in ASD aged 41 years–61 years; compared with TD, LGI is decreased bilaterally in insular and anterior cingulate cortex (ACC), left postcentral, and orbitofrontal and supramarginal regions. Gyrification is postulated to be influenced by axonal tension [44] or differential expansion

Table 1 MR imaging of brain morphology.

Reference	Age range	Brain regions	Main findings in ASD group
Schumann <i>et al.</i> [15]	Longitudinal, 1.5-5 years	Cerebrum	↑ GMV and WMV in cerebrum; notably in frontal, temporal, and cingulate cortices
Hazlett <i>et al.</i> [17]	18-35 months	Cerebrum; cerebellum	↑ GMV and WMV in in frontal, temporal, and parietal-occipital lobes
Sparks <i>et al.</i> [70]	3-4 years	Cerebrum; cerebellum; hippocampus; amygdala	↑ Volumes in cerebrum, cerebellum, amygdala, and hippocampus
Courchesne <i>et al.</i> [24]	2-16 years	Cerebrum; cerebellum; cerebellar vermis	↑ Cerebral GMV and WMV; cerebellar WMV; ↓ cerebellar GMV, cerebellar vermis lobules VI–VII in 2- to 3- year-olds
Carper <i>et al.</i> [25]	2-9 years	Cerebrum; frontal lobe	↑ Volumes in dorsolateral and medial frontal regions in those under age 5
Shen <i>et al.</i> [26]	(Longitudinal, prospective) 6-9, 12–15, and 18–24 months	Cerebrum; extra-axial CSF	↑ Extra-axial CSF, particularly over the frontal lobes (6-9 mo); ↑ total cerebral volume (12-15 and 18–24 mo)
Hazlett <i>et al.</i> [29]	(Longitudinal, prospective) 6-7, 12-13, 24-25 months	Global brain tissue; surface area; cortical thickness	↑ Cortical surface area (6-12 mo); ↑ TBV (12-24 mo); no difference in cortical thickness
Ohta <i>et al.</i> [30]	3-3.5 years	Cortical grey matter; cortical thickness; surface area	↑ Cortical surface area (3 y); no difference in cortical thickness
Shen <i>et al.</i> [31]	(Longitudinal, prospective) 6-7, 12-13, 24-25 months	Extra-axial CSF; lateral ventricle	↑ Extra-axial CSF (6-24 mo); no difference in lateral ventricle volume
Shen <i>et al.</i> [32]	2-4 years	Extra-axial CSF; cerebrum	↑ Extra-axial CSF (2-4 y)
Hazlett <i>et al.</i> [33]	(Longitudinal, prospective) 2-3, 4-5 years	Cerebrum; cortical thickness	↑ Volume in cerebrum, particularly in temporal lobe white matter; no difference in cortical thickness
D'Mello <i>et al.</i> [49]	8-13 years	Cerebrum; cerebellum	↓ GM in cerebellar lobule VII (Crus I/II)
Pierce <i>et al.</i> [50]	3-8 years	Cerebellar vermis; cerebrum	↓ Area of cerebellar vermal lobules VI–VII
Foster <i>et al.</i> [51]	6-17 years	Global brain tissue; cortical thickness; surface area	↑ GM concentration in frontal, temporal lobes, putamen, and caudate nucleus; ↓ GM concentration in cerebellum
Wolff <i>et al.</i> [52]	(Longitudinal, prospective) 6-7, 12-13, 24-25 months	Corpus callosum (CC); global brain tissue	↑ Area and thickness in CC, particularly in the anterior CC (6-12 mo); correlation between CC area and thickness (1 y) and repetitive behaviors (2 y)
Haar <i>et al.</i> [53]	6-35 years	Global brain tissue; cortical thickness; surface area	↑ Ventricular volume; cortical thickness in several area; ↓ CC volume; no difference in intracranial volume, cerebellar and amygdala volume
Schumann <i>et al.</i> [55]	1-5 years	Amygdala	↑ Amygdala volume
Barnea-Goraly <i>et al.</i> [58]	8-12, 11-15	Amygdala; hippocampus	↑ Right hippocampus volume (8 y); ↓ right hippocampus volume (15 y)
Pote <i>et al.</i> [59]	4-6 months	Global brain tissue; CSF; lateral ventricle	↑ Cerebellar and subcortical volumes (4–6-mo)
Kohli <i>et al.</i> [41]	41-61 years	Cortical thickness; surface area; cortical folding	↓ IGI bilaterally in insular and ACC, left postcentral, and middle frontal and right orbitofrontal and supramarginal regions; positive correlations between IGI in the bilateral insula and right orbitofrontal cortex and executive function scores
Kohli <i>et al.</i> [42]	7-19 years	Cortical thickness; surface area; cortical folding	↑ IGI in left parietal and temporal and right frontal and temporal regions

ACC, anterior cingulate cortex; CT, cortical thickness; CSF, cerebrospinal fluid; GM, grey matter; GMV, grey matter volume; IGI, local gyrification index; ROI, region of interest; SA, surface area; SBM, surface-based morphometry; TBV, total brain volume; VBM, voxel-based morphometry; WMV, white matter volume.

rates of cortical layers [45]. In ASD, altered gyrification patterns can be impacted by abnormal neuronal proliferation and migration. Further investigations of cortical folding would deepen our understanding of cortical development, and allow us to better define the neurobiological mechanisms associated with ASD.

Recently, the largest study to date of brain asymmetry in ASD has mapped the differences in brain asymmetry between participants with ASD and TD [46], suggesting altered lateralization in ASD. Cerebral lateralization is a prominent feature of the brain in organizing certain motor and cognitive functions, such as handedness and language [47]. Individuals with ASD exhibit generally reduced asymmetry compared to TD, which suggests abnormal hemispheric specialization in autistic individuals. Interestingly, many of the regions that show significant alterations in asymmetry, including medial frontal, anterior cingulate, and inferior temporal regions, overlap with the default mode network (DMN), which further supports a role of abnormal functional lateralization of the DMN in ASD [48].

Cerebellum and Subcortical Areas

Other morphometric studies of ASD have also characterized abnormalities in the cerebellum [49–51], corpus callosum [52–54], amygdala [16, 55], caudate nucleus [51, 56], and cerebrospinal fluid (CSF) [26, 31, 32]. The posterior lobe of the cerebellum (lobules VI and VII) is functionally coupled to the PFC and the ACC [57]. It is thought to be engaged in cognitive-affective functions, and thus may play a critical role in the pathophysiology of ASD [49, 50]. Similarly, given the important role of the amygdala in emotion processing, the aberrant amygdala structure may underlie the social-emotional deficits in individuals with ASD [24, 58]. There is evidence that children with ASD have an enlarged amygdala that shows a significant correlation with the severity of their social and communication impairments [55]. Moreover, accumulating evidence has implicated enlargement of the caudate nucleus within the cortico-striatal circuits, and enlargement of the caudate is correlated with the repetitive behaviors in children with ASD [56, 59]. Notably, a disproportionately large midsagittal corpus callosum relative to total brain volume has been identified in a longitudinal study on ASD infants, particularly in the anterior region, which mediates sensory-motor functions and behavioral inhibition [52]. Besides, the authors reported that the increased area and thickness of the corpus callosum are significantly correlated with the severity of restricted, repetitive behaviors in ASD toddlers at age 2. In contrast, decreased corpus callosum volume has been reported in older children and adults with ASD compared to TD subjects [53, 54]. This

atypical trajectory of the corpus callosum fits the theory of age-specific anatomical abnormalities in ASD, and could be related to the early excessive thin axons and subsequent insufficient axon growth and refinement in ASD patients [52, 60]. In addition, patients with ASD have elevated extra-axial CSF (defined as CSF in the subarachnoid space surrounding the cortex) relative to TD children from infancy to age 3 [26, 31, 32]. Given the important role of normal CSF circulation for the delivery of neural tropic factors as well as the clearance of neurotoxins and metabolites [61, 62], it has been suggested that the abnormal cortical development in ASD may be attributable to a dysfunction of CSF circulation [32].

Notably, abnormal white matter connectivity has also been indicated in ASD (Table 2). Diffusion tensor imaging (DTI) is a specialized MRI technique for non-invasive detection of fiber orientation and white matter connectivity by assessing the diffusion of water molecules in nervous system tissue [63]. DTI-derived metrics like fractional anisotropy (FA) and mean diffusivity are used to measure the orientation and the magnitude of diffusion, respectively, indicative of the white-matter microstructural properties including axon composition and myelination. A longitudinal DTI study has characterized increased FA and volume of fiber tracts (12 out of 15) in infants who later developed ASD at 6 months of age [27], whereas decreased FA and volume were identified in older children with ASD compared with TD controls [27, 64, 65], suggesting that axonal plasticity is implicated in the development of ASD. The changes of white matter connectivity properties over time could be associated with the dynamic processes of axonal pruning and myelination [66], e.g. early excessive thin axons and subsequent insufficient axon refinement in ASD patients. Another longitudinal study in ASD toddlers has reported axonal over-connectivity, as indexed by FA, in the frontal white matter tracts including the uncinate fasciculus connecting the frontal cortex and the amygdala as well as the arcuate fasciculus that is involved in language transmission [28], in agreement with the findings of Wolff *et al.* [27]. Elevated FA has also been reported in the corpus callosum and superior and inferior longitudinal fasciculi, as well as the inferior frontal-occipital fasciculus in tract-based spatial statistical studies of preschool-aged children and adults with ASD [67, 68]. Intriguingly, one recent study using the high angular resolution diffusion-weighted imaging method, which is more sensitive to deep brain structures, has provided evidence of abnormal structure in the mesolimbic reward pathway which connects the nucleus accumbens and the ventral tegmental area in ASD children; this supports the hypothesis that impaired reward processing circuitry might be a mechanism underlying ASD [69].

Table 2 Diffusion tensor imaging studies.

Reference	Age range	Brain regions	Main findings in ASD group
Wolff <i>et al.</i> [27]	(Longitudinal, prospective) 6-7, 12-13, 24-25 months	Global main fiber tracts	↑ FA in the body of corpus callosum, left fornix, inferior longitudinal fasciculus, uncinate fasciculus at 6 months; ↑ FA in anterior thalamic radiations, anterior internal capsule at 24 months
Solso <i>et al.</i> [28]	(Longitudinal, prospective) 1-4 years	Frontal tracts	↑ FA and volume in forceps minor, inferior frontal superior frontal tract, uncinate, frontal projection of the superior corticostriatal tract; ↑ FA in arcuate fasciculus portion of the superior longitudinal fasciculus; ↑ volume in inferior frontal occipital fasciculus, inferior longitudinal fasciculus (12 months)
Nordahl <i>et al.</i> [54]	(Longitudinal) 2-4,3-5, 5-7 years	Corpus callosum (CC)	↓ CC regions with fibers directed to superior frontal cortex and midsagittal CC area in both males and females with ASD; ↓ CC region with fibers directed to the orbitofrontal cortex in males with ASD; ↓ CC region associated with the anterior frontal cortex in females with ASD; ↑ MD, AD and RD in females with ASD
Sundaram <i>et al.</i> [64]	2-7 years	Association fibers in frontal lobes	↑ MD in short- and long-range fibers; ↓ FA in short-range fibers
Langen <i>et al.</i> [65]	19-39 years	Fronto-striatal tracts; global brain volume	↓ FA of white matter tracts connecting putamen to frontal cortical areas; ↑ MD of white matter tracts connecting accumbens to frontal cortex; ↓ total brain WM volume
Andrews <i>et al.</i> [67]	3-5 years	Global main fiber tracts	↑ FA in CC, inferior frontal-occipital fasciculi, inferior and superior longitudinal fasciculi, middle and superior cerebellar peduncles, and corticospinal tract
Catani <i>et al.</i> [68]	18-41 years	Global main fiber tracts	↓ FA in regions that include frontal lobe pathways; ↑ MD in the left arcuate fasciculus, cingulum, uncinate and anterior portions of the CC connecting left and right frontal lobes

AD, axial diffusivity; FA, fractional anisotropy; MD, mean diffusivity; ROI, region of interest; PT, probabilistic tractography; RD, radial diffusivity; WM, white matter.

Taken together, MRI studies employing voxel-based morphometry and DTI have reported age-related alterations in surface area, cortical thickness, cortical folding, brain lateralization, white matter connectivity, and gray matter volume in the prefrontal and temporal cortex, cerebellum [49–51], corpus callosum [52–54], amygdala [55, 70], caudate nucleus [51, 56], and CSF [26, 31, 32] in ASD patients, which may partly account for the emotional, behavioral executive, and language impairments. Although demographic features, such as sex and intelligence quotient can to some extent explain these age-specific findings [71], individual differences in ASD, such as the level of impairment, and the presence of medical and behavioral comorbidities in the selected groups may be another important factor in these inconsistent patterns of abnormality related to age. Longitudinal studies have delineated several atypical developmental trajectories as early as 6 months, and provide critical insights into the atypical neurodevelopment of ASD in early postnatal life [17, 24–33]. The presence of several prodromal abnormalities, such as greater cerebellar and subcortical volumes at 4–6 months, elevated extra-axial CSF level at 6 months, increased thickness of the corpus callosum and cortical surface area hyper-expansion at 6 months–12 months, total

brain volume overgrowth between 12 months and 24 months, and hyper-connectivity in the frontal white matter tracts in high-risk infants at 6 months–24 months of age, may aid in pre-symptomatic diagnosis and progression prediction of ASD.

MR Imaging of Resting-State Functional Connectivity

An increasing number of resting-state functional MRI investigations have concentrated on the alterations in the cerebral functional connectivity of patients with ASD by measuring spatiotemporal patterns of blood-oxygen-level-dependent signals (Table 3). The upsurge of interest in this field stems from the theory that the intrinsic activity of the brain may play a pivotal role in higher-order cognition [72]. Diverse methodologies such as independent component analysis, seed-based correlation analysis, graph-theoretical analysis, and regional homogeneity have been widely used to analyze the functional connectivity (reviewed in [73]). Taking advantage of these methodologies, atypical functional connectivity has been characterized in ASD, including in the salience network (SN) [74–77], DMN [75–78], executive control network (ECN)

[75–77, 79], and dorsal attention network [77, 79, 80]. The SN, primarily composed of the anterior insula and dorsal ACC, is thought to be involved in detection and the allocation of attention to internal and external stimuli, and coordination between large-scale networks such as the DMN and the ECN to guide appropriate behaviors [81]. Disruption of the SN may account for reduced attention to social stimuli in ASD individuals. The DMN, comprising the medial PFC, posterior cingulate cortex, precuneus, and temporo-parietal junction, is implicated in autobiographical memory, introspective thought, and theory of mind [82–84]. A majority of studies have reported a trend of both global hypo-connectivity and local hyper-connectivity of the DMN in children with ASD [85–87]. It has been speculated that excess neurons may cause early brain overgrowth and produce a mis-wired brain with exuberant local and short-distance cortical interactions impeding the function of large-scale, long distance interactions between brain regions [88]. Dysfunction of the DMN may explain the disturbance of self-referential thought in ASD [87]. The ECN, predominantly anchored in the dorsal lateral PFC and parietal cortex, plays a crucial role in decision-making, working memory, and cognitive control [89]. Disruption of this network may account for the impairment in cognitive flexibility in ASD [79, 89]. The dorsal attention network, mainly consisting of the middle temporal area complex, intraparietal sulcus, and the frontal eye fields, underlies top-down control of attention [90], thus dysfunction of this network may contribute to the attention shift deficits in ASD.

One study investigated the DMN, SN, and ECN simultaneously using resting-state functional MRI [75] and revealed that all three large-scale networks showed atypical intrinsic connectivity in children and adolescents with ASD relative to TD controls. Specifically, the DMN and ECN had age-related over-connectivity in young children with ASD but not in adolescents with ASD, so this may reflect delayed network segregation in ASD. In addition, the SN was under-connected internally and with the ECN, and the connectivity within the SN was associated with socio-communicative impairment, indicating that reduced SN functional integrity may compromise its role in switching between DMN and ECN. Watanabe *et al.* [91] found that high-functioning adults with ASD showed fewer neural transitions than neurotypical controls, and such atypically stable brain dynamics underlay general cognitive ability and core symptoms in ASD. This study of brain network dynamics revealed that functional stability in neural circuits and atypical functional coordination among networks may underpin the aberrant decreases in the flexibility of dynamics in the brains of adults with ASD.

Besides the above networks, several other functional connections have also been reported to be compromised in

the development of ASD. Hahamy *et al.* [92] examined both intra- and inter-hemispheric functional connectivity in children with ASD using resting-state functional MRI. They found topographically distorted inter-hemispheric functional connectivity in ASD when compared to TD children, and indicated that the level of distortion in homotopic inter-hemispheric functional connectivity was correlated with autism severity. This study demonstrated that individualized differentiation of functional connectivity patterns might be a core neural characteristic of ASD, in accordance with the findings of Dickie *et al.* [93]. In addition, Shou *et al.* have reported alterations of functional connectivity in children with ASD in the vasopressin-related neural circuits that are critically implicated in social behaviors [94].

Notably, a growing number of neuroimaging studies have explored the diagnostic (that is, predictive) value of various measures of brain anatomy, functioning, and connectivity for ASD [29, 95]. To explore whether the pre-symptomatic pattern of functional connectivity can be used to predict the diagnosis in ASD, Emerson *et al.* [95] carried out a prospective investigation in 59 infants at high risk for ASD using resting-state functional MRI. The authors reported that a machine learning algorithm based on the functional connections (selected as those that correlated with 24-month ASD-related behaviors) of 6-month-old infants at high familial risk for ASD is highly predictive of an ASD diagnosis at 24 months (positive predictive value of 100%). This study indicates that atypical brain connectivity patterns precede the emergence of behavioral anomalies and functional MRI could facilitate the detection of ASD at the prodromal stage.

Taken together, patients with ASD exhibit patterns of under- and over-connectivity compared to TD in multiple brain regions and networks: the SN [74–77], DMN [75–78], ECN [75–77, 79], dorsal attention network [77, 79, 80], and corticostriatal [79] and vasopressin-related neural circuits [94]. Aberrant homotopic connectivity [92] and atypical brain dynamics [91] in ASD compared to controls have also been reported. Long-range under-connectivity and short-range over-connectivity have been hypothesized as brain abnormalities in autism [96]. Other hypotheses suggest abnormal segregation and integration of resting-state networks [97] and idiosyncratic connectivity [75, 85, 92]. Moreover, the functional connectivity pattern evaluated with a machine learning algorithm may be valuable in predicting a diagnosis before the onset of ASD.

MR Imaging of Perfusion

ASL is a noninvasive MR-based imaging technique using endogenous water in arterial blood as a freely-diffusible

Table 3 Resting-state functional MRI studies in ASD.

Reference	Age range (mean)	Brain regions examined	Main findings in ASD group/connectivity
Uddin <i>et al.</i> [74]	7-12 (9.9) years	Networks: SN (frontal-insular, ACC); ECN (dlPFC, PPC); DMN (medial PFC, PCC); dorsal attention network (intraparietal sulcus and frontal eye fields)	↑ Connectivity in SN and posterior DMN (precuneus, PCC, and left angular gyrus)
Abbott <i>et al.</i> [75]	9-17 (13.9) years	Networks: SN; DMN; ECN	↑ Connectivity between DMN (PCC seed) and rECN (right IPL seed); ↓ connectivity in SN internally (right anterior insular seed) and with IECN (left IPL seed)
Plitt <i>et al.</i> [76]	(17.9) years	Networks: SN; DMN; frontoparietal task control network	Connectivity involving SN, DMN, and frontoparietal task control network are highly predictive of future autistic traits and the change in autistic traits and adaptive behavior over the same time period; functional connectivity involving the SN predicted reliable improvement in adaptive behaviors with 100% sensitivity and 70.59% precision
Elton <i>et al.</i> [77]	6-18 (13.2) years	Networks: SN; DMN; ECN; dorsal attention network	↑ Connectivity between DMN and middle frontal gyrus, bilateral IPL, and right insula; ↑ connectivity between dorsal attention network and the precuneus, cerebellum, and right precentral gyrus; ↓ connectivity between dorsal attention network and medial frontal gyrus and lateral temporal cortices; ↑ connectivity between SN and dorsal ACC; ↓ connectivity between SN and the medial frontal gyrus, left middle frontal gyrus, and left postcentral gyrus; ↑ connectivity between ECN and the left cerebellum; ↓ connectivity between ECN and the medial PFC, right superior frontal gyrus, right precentral gyrus, left middle frontal gyrus, left postcentral gyrus, and medial frontal gyrus
Doyle-Thomas <i>et al.</i> [78]	6-17 (12.3) years	DMN; whole brain	↓ Connectivity between PCC-L and the left medial frontal gyrus, left and right angular gyri, and right inferior temporal gyrus; ↓ connectivity between PCC-R and the left medial frontal gyrus, left PCC, left and right angular gyrus, and right inferior temporal gyrus; ↑ connectivity between PCC-L and the left IPL, left superior frontal gyrus, left precentral gyrus, right middle frontal gyrus, right superior parietal lobule, and right IPL; ↑ connectivity between PCC-R, and the left and right IPL, right middle frontal gyrus, left precentral gyrus, left superior frontal gyrus
Holiga <i>et al.</i> [79]	7-12, 12-18, 18-30 (17.5) years	Whole brain	↓ Connectivity in sensory-motor regions and right temporal regions, insula, amygdala, and hippocampus; ↑ connectivity in PFC, ACC, PCC, and parietal cortices
Oldehinkel <i>et al.</i> [80]	7-30 years	Networks: SN; sensory and motor networks	↑ Connectivity of the cerebellum with sensory and motor networks; ↓ connectivity of the visual association network with somatosensory, medial and lateral motor networks
Yerys <i>et al.</i> [85]	8-13 years	Networks: DMN; SN	↓ Connectivity within DMN (PCC-MPFC); ↑ connectivity between DMN and SN
Hahamy <i>et al.</i> [92]	(26.6) years	Whole brain	↓ Homotopic interhemispheric connectivity, particularly in the primary somatosensory and motor cortices; ↑ connectivity in frontal and temporal cortex

Table 3 continued

Reference	Age range (mean)	Brain regions examined	Main findings in ASD group/connectivity
Dickie <i>et al.</i> [93]	6-65 years	DMN; dorsal attention; ventral attention; frontoparietal; sensory motor; and visual network	↓ Connectivity in DMN, dorsal attention, ventral attention, frontoparietal, sensory motor, and visual network; ↑ connectivity in DMN and ventral attention network
Jann <i>et al.</i> [99]	(13.8) years	DMN	Frontotemporal hyperperfusion and hypoperfusion in the dorsal ACC; increased local FC in the anterior module of the DMN accompanied by decreased CBF in the same area
Peterson <i>et al.</i> [100]	5-60 (24.9) years	Global brain tissue	↑ rCBF values throughout frontal white matter and subcortical gray; negative correlation with NAA metabolite levels throughout frontal white matter

ACC, anterior cingulate cortex; CBF, cerebral blood flow; dlPFC, dorsolateral prefrontal cortex; DMN, default mode network; ECN, executive control network; FC, functional connectivity; IPL, inferior parietal lobules; NAA, N-acetylaspartate; PCC, posterior cingulate cortex; PCC-L, left posterior cingulate cortex; PCC-MPFC, posterior cingulate cortex medial prefrontal cortex; PCC-R, right posterior cingulate cortex; PFC, prefrontal cortex; PPC, posterior parietal cortex; rCBF, resting cerebral blood flow; rECN, right executive control; Seed, seed-based correlation analysis; SN, salience network.

tracer for the measurement of tissue perfusion with high reproducibility [98] (Fig. 1). Altered cerebral perfusion has been indicated in both gray and white matter in ASD using ASL. One study explored the resting cerebral blood flow and functional connectivity simultaneously in high-functioning children with ASD using ASL MRI. The authors found frontotemporal hyper-perfusion as well as hypoperfusion in the dorsal ACC in children with ASD compared to TD children [99]. While the functional connectivity was positively associated with the perfusion in TD children, this association was abnormal in children with ASD [99]. The increased functional connectivity in the ACC was accompanied by hypo-perfusion in this same area in children with ASD [99], possibly reflecting neurovascular decoupling, which impairs the function of the ACC and contributes to the social impairments in ASD. It has been speculated that possible factors driving neurovascular decoupling in ASD could be changes of inhibitory gamma-aminobutyric acid (GABA) neurotransmitters, which has been well replicated in ASD. However, the specific neural mechanism still needs to be further clarified. Furthermore, the functional connectivity strength between the anterior and posterior modules of the DMN is reduced in ASD compared to TD children, indicating long-range hypo-connectivity. These results suggest that ASD children experience cerebral energetic inefficiency. More recently, Peterson *et al.* [100] measured both cortical and subcortical perfusion in ASD patients using ASL, and identified hyper-perfusion in cortical white and subcortical gray matter. Interestingly, the regional cerebral blood flow throughout the frontal white matter in the ASD group was inversely correlated with the N-acetylaspartate metabolite

levels, a marker for neuronal density and mitochondrial metabolism [101]. These results suggest increased myelin synthesis in ASD patients and that elevated cerebral blood flow might represent a compensation for maintaining the energy status of axons.

Taken together, these ASL-based studies indicate aberrant resting functional connectivity and altered resting perfusion in both gray and white matter, and significantly enhance our knowledge of brain network organization and energetic efficiency in patients with ASD. The ability of ASL to quantify the cerebral metabolic changes non-invasively with excellent reproducibility renders it a valuable imaging technique to inform the pathophysiology of ASD.

PET and SPECT

PET and SPECT are molecular imaging techniques that use radiolabeled tracers to probe molecular interactions of biological processes *in vivo*, with high sensitivity and specificity [102]. They offer critical insights into biological events *in vivo*, such as glucose metabolism [103], gene expression, blood flow, oxygen consumption, neurotransmitter release and receptor occupancy [104] (Fig. 1). PET, a representative mode of molecular imaging and transpathology [105], exhibits higher sensitivity and temporal resolution compared with SPECT, as well as the potential for quantitative and dynamic imaging [106]. Table 4 summarizes the main findings of PET/SPECT studies in ASD.

PET Imaging of Brain Metabolism

Using ^{18}F -fluorodeoxyglucose (^{18}F -FDG) PET, previous studies have characterized changes in cerebral glucose metabolism in patients with ASD while performing tasks. A recent study assessed cerebral glucose metabolic rates in ASD patients using ^{18}F -FDG PET [107]. The results showed decreased task-dependent glucose metabolism in the amygdala, frontal premotor and eye-field areas, and the parietal lobe in ASD patients relative to TD controls, which could be related to hypoactivation of these regions during a cognitive task [108]. Increased glucose metabolism has been detected in the hippocampus, occipital cortex, posterior cingulate cortex, and basal ganglia. The increased metabolic rate in the posterior cingulate cortex could reflect decreased cognitive task engagement of subjects with ASD, which in healthy participants typically leads to decreased metabolic activity in this central-to-DMN area [109]. Another possibility is that it could represent inefficient functioning of the DMN in ASD, e.g., a greater metabolic cost is devoted to the maintenance of a cohesive sense of self, a putative role of the posterior cingulate cortex [110]; this is thought to be the central impairment in autism.

In addition, other investigations have also characterized increased metabolism in white matter structures including the corpus callosum, internal capsule, and the white matter in the frontal and temporal lobes of patients with ASD compared to those of TD controls [111]. Theoretically, the metabolic and wiring costs in connections among anatomically adjacent brain areas are lower than those among distant brain regions [112]. The increased glucose metabolism in white matter structures of ASD patients might be associated with metabolically inefficient transfer of information in the autistic brain, possibly due to inefficient axonal wiring.

However, it is worth noting that metabolic abnormalities in these regions have also been indicated in schizophrenia [107], major depression [111], and bipolar disorder [113], thus further investigations are needed to identify specific metabolic alterations underlying the unique clinical features of ASD.

PET and SPECT Imaging of Neurotransmitter Systems

Serotonergic System

Multiple lines of evidence have indicated that serotonergic system dysfunction is implicated in ASD (reviewed in [114, 115]). For instance, the serotonin 5-HT_{1A} receptor agonist buspirone has been shown to ameliorate the obsessive–compulsive behaviors in children with ASD

[116]. However, there is also evidence indicating that selective serotonin (5-HT) reuptake inhibitors failed to show additional benefit for repetitive behaviors in ASD as compared to placebo [117]. The disparity in results may suggest only a subset of autistic patients benefit from modulation of the serotonergic system.

Several studies have focused on the changes of 5-HT synthesis in ASD. α - ^{11}C -methyl-L-tryptophan (AMT) is a radiolabeled tryptophan analogue that allows for the non-invasive visualization of 5-HT synthesis (Fig. 2). Using AMT PET, Chugani *et al.* [118–120] found global abnormalities [118], as well as asymmetric regional abnormalities of brain 5-HT synthesis in the dentato-thalamo-cortical pathway [119]; these were later suggested to be related to handedness and language function in ASD children [120].

Serotonin transmission abnormalities have also been indicated in ASD. ^{18}F -setoperone is a radioligand for visualization of 5-HT₂ receptors through PET (Fig. 2). Beversdorf *et al.* [121] explored 5-HT₂ receptor density in high-functioning autistic adults using ^{18}F -setoperone PET. They characterized lower 5-HT₂ receptor binding in the thalamus in high-functioning autistic adults compared to controls, and this was associated with language impairment. The lower 5-HT₂ receptor binding may occur as a consequence of increased synthesis of 5-HT [118], or inadequate activity of 5-HT₂ receptors in autism may result in increased synthesis in autism. This needs to be further clarified.

The serotonin transporter (SERT) regulates serotonergic signaling through the reuptake of released 5-HT into presynaptic neurons [122] (Fig. 2). Genetic studies have proposed links between SERT polymorphisms and autism in some families [123]. The SERT is also the target of the widely-used selective serotonin receptor inhibitors in ASD for symptom management. Iodine-123-labelled N-(2-fluoroethyl)-2 β -carbomethoxy-3 β -(4-iodophenyl)-nortropine (^{123}I nor- β -CIT) is a radioligand that binds specifically to the SERT (Fig. 2). Using ^{123}I nor- β -CIT SPECT, Makkonen *et al.* [124] evaluated the SERT availability in ASD children. They found significantly lower SERT binding in ASD patients compared to controls in various areas, including the medial frontal cortex, the midbrain, and the temporal lobe, indicating diminished SERT binding capacity in autistic individuals. These results have been supported by the findings of Nakamura *et al.* [125], who found markedly reduced SERT binding in the whole brain in adults with high-functioning autism compared to controls using carbon 11 (^{11}C)-labeled trans-1,2,3,5,6,10- β -hexahydro-6-[4-(methylthio)phenyl]pyrrolo-[2,1-a]isoquinoline (^{11}C)(+)McN-5652) PET to measure SERT availability (Fig. 2). Specifically, the reduction of SERT binding in the thalamus was correlated with the repetitive,

Table 4 PET/SPECT studies in ASD.

Reference	Modality	Target	ASD age: mean \pm SD, range	Number of participants (N)	ASD diagnosis	ASD IQ: mean \pm SD, range	ASD sedation	Control group	Main findings in ASD
Mitelman <i>et al.</i> [107]	PET	Glucose	31.5 years \pm 11.6	ASD: N = 25; CON: N = 55	ASD [DSM-IV and ADI-R]	IQ: 108.80 \pm 20.25	No	Matched by similar age (31.48 years \pm 11.57, 33.36 years \pm 12.85)	<p>↓ Metabolic rates in the parietal lobe, frontal premotor and eye-fields areas, and amygdala;</p> <p>↑ Rates in the posterior cingulate, occipital cortex, hippocampus and basal ganglia</p>
Mitelman <i>et al.</i> [111]	PET	Glucose	31.5 years \pm 11.6	ASD: N = 25; CON: N = 55	ASD [DSM-IV and ADI-R]	IQ: 108.80 \pm 20.25	No	Matched by similar age (31.48 years \pm 11.57, 33.36 years \pm 12.85)	<p>↑ Metabolic rates across the white matter regions assessed, including internal capsule, corpus callosum, and white matter in the frontal and temporal lobes</p>
Park <i>et al.</i> [158]	PET	Glucose	14 years	ASD: N = 1; CON: N = 0	ASD	IQ: 60 at 8 years of age	No	N/A, case study	<p>↓ Metabolism in the prefrontal and frontal cortex as well as the occipital cortex was marked</p>
Chugani <i>et al.</i> [118]	PET	Serotonin synthesis	6.41 years \pm 3.3	ASD: N = 30; CON: N = 8	Autism [ADI-R and DSM-IV]	OAB: 49 \pm 9.3	No	Matched by age	<p>↑/↓ Serotonin synthesis in autistic boys but not in autistic girls</p>
Chugani <i>et al.</i> [119]	PET	Serotonin synthesis	4.1–11.1 years	ASD: N = 8; CON: N = 5	ASD [DSM-IV]	OAB: 22 (mean)	Nembutal or midazolam for 8 autistic children and 3 siblings	Matched by age	<p>↓ Serotonin synthesis in the left frontal cortex and thalamus in 5 boys; ↑ AMT accumulation in the right dentate nucleus of the cerebellum;</p> <p>↓ AMT accumulation in the right frontal cortex and thalamus and elevated in the left dentate nucleus in the remaining 2 boys</p>
Beversdorf <i>et al.</i> [121]	PET	5-HT _{2A}	31.0 years \pm 8.0	ASD: N = 8; CON: N = 12	Autism [DSM-IV and ADI-R]	IQ: 114.7 \pm 14.7	No	Matched by age and FISQ	<p>↓ 5-HT_{2A} binding in thalamus</p>
Nakamura <i>et al.</i> [125]	PET	SERT and DAT	21.2 years \pm 2.0 18–26 years	ASD: N = 20; CON: N = 20	Autism [DSM-IV-TR, ADI and ADOS]	IQ: 99.3 \pm 18.1	No	Matched by sex and similar age: 21.9 years \pm 2.18–26 years, IQ not significantly different	<p>↓ SERT binding in AC and posterior cingulate correlated w/ASD symptomatology</p>
Ernst <i>et al.</i> [128]	PET	Presynaptic DA activity	13 years \pm 2	ASD: N = 14; CON: N = 10	Autism [DSM-III-R]	IQ: 74 \pm 23.1, range 46–123	Propofol	Similar age: 14 years \pm 2	<p>↓ FDOPA uptake in mPFC</p>
Mori <i>et al.</i> [133]	SPECT	GABA _A	7.0 years \pm 3.7	Autism: N = 9; AS: N = 15; CON: N = 10	ASD classified as autism or AS [DSM-IV]	IQ < 70 (N = 7); IQ > 70 (N = 17)	Triclofos sodium	Non-symptomatic partial epilepsy patients w/o intellectual delay, similar age: 7.8 years \pm 3.6	<p>↓ Binding in superior and medial frontal cortex in ASD</p>
Fung <i>et al.</i> [134]	PET	GABA _A	26.6 years \pm 8.3	ASD: N = 28; CON: N = 29	ASD [DSM-5, ADI-R and ADOS-2]	IQ: 102.1 \pm 16.5	No	Matched by IQ, sex and age	<p>No differences in GABA_A receptor density in bilateral thalami and left dorsolateral prefrontal cortex between ASD and TD group</p>

Table 4 continued

Reference	Modality	Target	ASD age: mean \pm SD, range	Number of participants (N)	ASD diagnosis	ASD IQ: mean \pm SD, range	ASD sedation	Control group	Main findings in ASD
Fatemi <i>et al.</i> [137]	PET	mGluR5	20 years \pm 2.1	ASD: N = 6; CON: N = 3	Autism [ADOS, ADI-R, ASSQ, CGI, ABC, SCQ and GAF]	Not specified	No	Matched by sex and race	\uparrow mGluR5 binding in cerebellum, postcentral gyrus, entorhinal area, and the precuneus
Zürcher <i>et al.</i> [141]	MR-PET	TSPO	24.1 years \pm 5.5	ASD: N = 15; CON: N = 18	ASD [DSM-IV-TR, ADI-R, ADOS-2 and DSM-5]	IQ: 86.1 \pm 19.2	No	Matched by sex and age	\downarrow TSPO expression in the bilateral insular cortex, putamen, precuneus/ posterior cingulate cortex, orbitofrontal cortex, lateral occipital cortex, superior temporal gyrus, angular gyrus, supramarginal gyrus, and left postcentral gyrus

5-HT_{2A}, serotonin 2A receptor; ABC, Autism Behavior Checklist; AC, Anterior Cingulate; ADI, Autism Diagnostic Interview; ADI-R, ADI- Revised; ADOS, Autism Diagnostic Observation Schedule; ADOS-2, Autism Diagnostic Observation Schedule, Second Edition-2; AMT, methyl-L-tryptophan; AS, Asperger Syndrome; ASSQ, Autism Spectrum Screening Questionnaire; CARS, Childhood Autism Rating Scale; CGI, Clinical Global Impression; DA, dopamine; DAT, Dopamine Transporter; DSM-III-R, DSM Third Edition Revised; DSM-IV, DSM Fourth Edition; DSM-IV-TR, DSM Fourth Edition Text Revised; DSM-5, DSM Fifth Edition; FDOPA, fluorine-18-labelled fluorodopa; FISQ, Full Scale Intelligence Quotient; GABA_A, GABA_A aminobutyric Acid Type A Receptor; GAF, Global Assessment of Functioning; ICD-10, International Classification of Diseases Tenth Revision; IQ, Intelligence Quotient; mGluR5, metabotropic glutamate receptor 5; mPFC, medial prefrontal cortex; OAB, overall adaptive behavior composite from Vineland Adaptive Behavior Scale in age equivalents (months of age); SCQ, Social Communication Questionnaire; SERT, Serotonin Transporter; TD, Typically Developing; TSPO, translocator protein.

obsessive behaviors, and the reduction in the anterior and posterior cingulate cortex was associated with the social cognition in ASD, compatible with previous studies [121, 126]. Taken together, these studies indicate a disturbed serotonergic system in ASD patients and highlight its involvement in social cognition, and the restricted, repetitive behaviors in ASD.

Dopaminergic System

Dopamine (DA) is a catecholamine neurotransmitter involved in reward and social motivation that may be central to the social deficits in autism [127]. Previous studies have characterized abnormalities in DA synthesis and DA transporters in ASD patients [124, 125, 128]. ^{18}F -labelled fluorodopa (^{18}F -FDOPA) is an L-DOPA analogue that allows the evaluation of DA synthesis. Using ^{18}F -FDOPA PET, Ernst *et al.* [128] have found decreased ^{18}F -FDOPA accumulation in the anterior medial PFC in 14 drug-naïve ASD children compared to age-matched healthy controls, indicating that prefrontal dopaminergic deficits may account for the cognitive impairment in ASD. Nakamura *et al.* [125] measured DA transporter binding in 20 adults with high-functioning autism and 20 age- and intelligence quotient-matched TD adults using 2- β -carbomethoxy-3- β -(4-fluorophenyl) tropane (^{11}C -WIN-35,428) PET. In the autistic group, they found significantly higher DA transporter binding in the orbitofrontal cortex, a key region in the network underlying emotional regulation [129]. Over-functioning of the dopaminergic system in the orbitofrontal-limbic circuit could be associated with the impulsive and aggressive behaviors in ASD.

GABAergic System

Gamma-aminobutyric acid (GABA) is the most prevalent inhibitory neurotransmitter in the mature central nervous system, mainly acting on GABA_A and GABA_B receptors. But GABA-mediated signaling also plays a central role in regulating key developmental processes, such as cell proliferation, neuron differentiation, and circuit refinement (reviewed in [130]). Emerging evidence has suggested that impaired GABA-mediated signaling lead to an imbalance of excitation and inhibition that may contribute to the pathogenesis of autism (reviewed in [131, 132]). To investigate the GABA_A receptor in ASD patients, Mori *et al.* [133] performed ^{123}I -iomazenil (^{123}I -IMZ) SPECT in children with ASD and found decreased ^{123}I -IMZ accumulation in the superior and medial frontal cortex, a region that is thought to be associated with theory of mind, in the ASD group compared to the control group. A more recent study examined the GABAergic system in 28 high-functioning adults with ASD [134]. While they did not

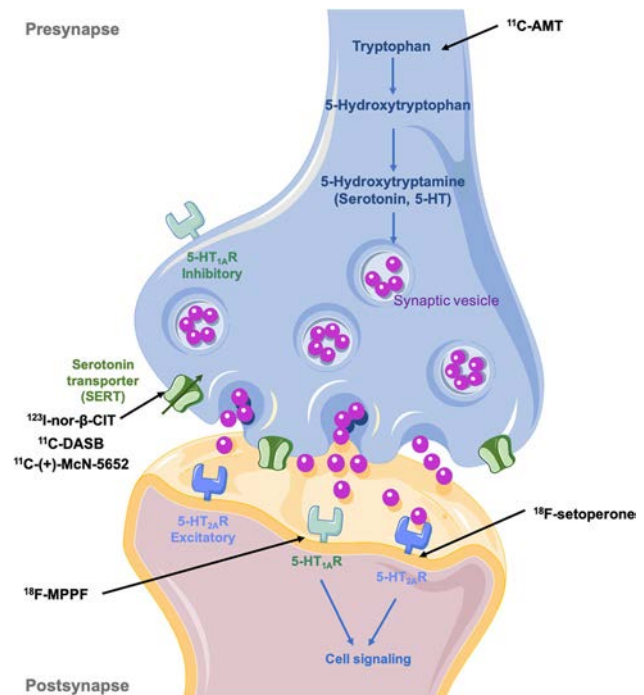


Fig. 2 Schematic of PET and SPECT modalities for assessing presynaptic and postsynaptic serotonergic targets. 5-Hydroxytryptamine (5-HT, serotonin) is synthesized from the amino-acid tryptophan *via* hydroxylation (forming the intermediate precursor 5-hydroxytryptophan), and then stored in synaptic vesicles. α - ^{11}C -methyl-L-tryptophan (^{11}C -AMT) is a radiolabeled tryptophan analogue that allows for non-invasive visualization of 5-HT synthesis. Serotonin reuptake into presynaptic neurons occurs *via* a serotonin transporter (SERT). [^{123}I] nor- β -CIT, ^{11}C -DASB and [^{11}C](+)-McN-5652 are radioligands that bind specifically to SERTs. 5-HT_{1A} receptors are located on both presynaptic and postsynaptic neurons. ^{18}F -MPPF allows the visualization of 5-HT_{1A} receptors *in vivo*. Two different types of 5-HT receptors are expressed on postsynaptic neurons: 5-HT_{1A} and 5-HT_{2A}. ^{18}F -setoperone is a radioligand for mapping 5-HT₂ receptors.

find altered GABA_A receptor density in high-functioning adults with ASD using ^{18}F -flumazenil (^{18}F -FMZ) PET, region-dependent and sex-specific differences in GABA concentrations were indicated. Notably, they discovered a higher GABA concentration in the left dorsal-lateral PFC in the autistic group than in TD adults, which may underlie the hypo-activation of dorsal-lateral PFC during working memory tasks in adults with ASD [135]. Another possibility is that higher cortical GABA levels occur in compensation for primary defects in GABAergic signaling.

Glutamatergic System

Glutamate is the predominant excitatory neurotransmitter in the brain and plays vital roles in brain development and neural plasticity. Deficiency in *Shank 3* gene coding the postsynaptic scaffold protein located in glutamatergic neurons, has been associated with ASD [136]. A recent

study reported significantly higher metabotropic glutamate receptor 5 in the cerebellum and postcentral gyrus in ASD adults compared to those in the TD group, using ^{18}F -3-fluoro-5-[(pyridin-3-yl)ethynyl]benzotrile (^{18}F -FPEB) PET to measure metabotropic glutamate receptor 5 density [137]. The cerebellum is crucial to the control of action through the integration of sensory and motor signals necessary for skilled movement [138]. Morphological changes in the cerebellum of subjects with autism have been identified, such as changes in total cerebellar volume, altered Purkinje cell density, and abnormal deep cerebellar nuclei [138]. Changes of glutamate signaling in the cerebellum may contribute to abnormalities in these somatosensorimotor-cerebellar circuits, leading to the motor and cognitive deficits associated with autism. Intriguingly, positive correlation between [^{18}F]-FPEB binding and autistic symptomatology as measured by the autism behavior checklist has been found in the precuneus, a principal component of the DMN. Changes in glutamate signaling, leading to an excitatory/inhibitory imbalance, coupled with structural and functional abnormalities in the DMN, potentially impact the functioning of the DMN.

PET Imaging of Neuroinflammation

Increasing evidence has suggested involvement of the immune system in the pathophysiology of ASD. The ^{11}C -PBR28 is a radiotracer that is able to detect subtle changes of 18-kDa translocator protein (TSPO) expression [139]. The putative roles of TSPO include apoptosis, steroidogenesis, neuroinflammation, energy production, cell metabolism, and oxidative stress [140]. Changes in TSPO may reflect abnormalities in these processes. Using ^{11}C -PBR28 PET-MR, Zürcher *et al.* [141] reported significantly lower TSPO levels in young male adults with ASD compared to those of age- and sex-matched controls in multiple brain regions, including the precuneus/posterior cingulate cortex, insular cortex, and temporal, angular, and supramarginal gyri bilaterally. Decreased TSPO in ASD could reflect changes in glia, neurons, or endothelial cells. Additional research is warranted to elucidate the specific mechanism behind the abnormal TSPO expression in ASD.

Taken together, impaired serotonergic, dopaminergic, glutamatergic, and GABAergic systems are critically involved in shaping the disturbed neural circuitry of ASD. However, the specificity of such abnormalities remains to be elucidated, since similar alterations in neurotransmitter systems have also been shown in other psychiatric disorders, such as schizophrenia [107]. In addition, glucose metabolic abnormalities and neuroinflammation may contribute to the pathogenesis of autism. Thus, the onset and progression of ASD is a complex process that involves multiple mechanisms. Additional

research is warranted to identify the ASD-specific molecular basis and to further our understanding of the neural correlates of ASD.

Intervention-Related Neuroimaging Biomarkers

To date, psychological and behavioral interventions are still the predominant treatment for ASD. However, behavioral therapies are typically expensive and difficult to access, and can put substantial strain on families and caregivers. To provide on-demand, personalized interventions for ASD is urgently needed. Lately, technology-based interventions, such as wearable digital intervention and robot-assisted therapy, have shown potential to improve socialization in ASD and hold great promise for augmenting the current standard of care [142, 143]. However, effective pharmacological treatments for the core symptoms of ASD are still lacking. Oxytocin, a neuropeptide mediating social affiliation, is emerging as a promising medical therapy for ASD [144]. Neuroimaging techniques, such as resting-state MRI and PET have become important methods for measuring the therapeutic effect of oxytocin in patients with ASD [145–151] (Table 5). Using resting-state functional MRI, researchers found that oxytocin enhanced the functional connectivity of the DMN [152], and cortical-striatal circuits [153]. Specifically, 6-week intranasal administration of oxytocin enhanced the functional connectivity between the ACC and dorsal medial PFC in ASD patients, and significantly attenuated the impaired reciprocal social interactions [152]. Moreover, this functional connectivity enhancement was robustly correlated with symptom improvement. However, these findings cannot be extrapolated to female patients with ASD due to the unbalanced sex representation (all male participants). Another study focused on the effect of oxytocin on intrinsic functional connectivity in females [83] and found that oxytocin increased cortical-striatal connectivity and this was positively associated with autistic traits. Future work might include efforts to quantify how therapeutically effective treatments remediate topologically sub-optimal network configurations in ASD patients using graph theoretical measures.

Using 2'-methoxyphenyl-(N-2'-pyridinyl)-p-[^{18}F]fluoro-benzamidoethylpiperazine (^{18}F -MPPF) PET to assess 5-HT_{1A} receptors (Fig. 2), Lefevre *et al.* [154] investigated the therapeutic effect of oxytocin on the serotonergic system in ASD patients. In TD controls, they found an oxytocin-serotonin interaction which was absent in patients with ASD. Hirose *et al.* [155, 156] investigated the serotonergic modulation after long-term administration of oxytocin in ASD patients using (^{11}C)-3-amino-4-(2-[(demethylamino)methyl]phenylthio)benzotrile (^{11}C -

Table 5 Intervention-related neuroimaging studies.

Reference	Diagnosis	ASD age mean \pm SD, range	Medication	Major drug target(s)	Symptom treated in ASD	Therapeutic effect
Ajram <i>et al.</i> [145]	ASD (N=37)	33 years \pm 2.5	Riluzole	GABA and glutamate targets	Anxiety	\uparrow PFC inhibitory index in ASD; \downarrow PFC inhibitory in controls
Hegarty <i>et al.</i> [148]	ASD (N=13)	15-35 years	Propranolol vs. placebo	Beta-adrenergic antagonist	Attention deficit/hyperactivity disorder (ADHD) or anxiety	\downarrow Connectivity in the dorsal medial prefrontal cortex subnetwork of the DMN; \uparrow connectivity in the medial temporal lobe subnetwork
Alaerts <i>et al.</i> [149]	ASD (N=40)	Oxytocin: 24.76 years \pm 4.85; Placebo: 24.06 years \pm 5.54	Oxytocin vs. placebo	Resting-state functional connectivity between key regions of the central oxytocinergic system (amygdala, hippocampus, nucleus caudatus, nucleus accumbens, and hypothalamus).	ASD symptom	\downarrow Amygdala-hippocampal connectivity
Watanabe <i>et al.</i> [152]	High-functioning ASD (N = 20)	24-42 years	Oxytocin vs. placebo	Intrinsic functional connectivity in the medial PFC	Social reciprocity	\uparrow Functional connectivity between ACC and dorso-medial PFC
Chugani <i>et al.</i> [116]	ASD (N = 166)	2-6 years	Buspirone vs. placebo	5-HT _{1A} receptor	Restricted and repetitive behavior	\uparrow AMT SUV in basal ganglia, thalamus, cerebellum, and brainstem
Lefevre <i>et al.</i> [154]	ASD (N = 18)	34.3 years \pm 7.6	Oxytocin vs. placebo	5-HT _{1A} receptor	NA	No changes in MPPF binding potential or serum-free serotonin concentration
Fukai <i>et al.</i> [155]	ASD (N = 10)	23-41 years	Oxytocin vs. placebo	Serotonergic system	Emotional response to human faces	\uparrow ¹¹ C-DASB binding potential in the striatum; positive correlation with increased negative emotional response to human faces
Hirosawa <i>et al.</i> [156]	ASD (N = 10)	23-41 years	Oxytocin vs. placebo	Serotonergic system	ASD symptom	\uparrow ¹¹ C-DASB binding potential in the left inferior frontal gyrus extending to the left middle frontal gyrus

5-HT_{1A}: serotonin 1A receptor; ACC, anterior cingulate cortex; AMT, methyl-L-tryptophan; ¹¹C-DASB, (¹¹C)-3-amino-4-(2-[(demethylamino) methyl] phenylthio) benzonitrile; DMN, default mode network; GABA, gamma-aminobutyric acid; MPPF, 2'-methoxyphenyl-(N-2'-pyridinyl)-p-¹⁸F]fluoro-benzamidoethylpiperazine; PFC, prefrontal cortex; SUV, standard uptake value.

DASB) PET to measure SERT availability (Fig. 2). The authors found significantly elevated ^{11}C -DASB binding in regions including the left inferior frontal gyrus and striatum in patients with ASD following oxytocin administration. Given that oxytocin-based therapy can modulate the serotonergic system and enhance the functional connectivity in frontal-striatal neural circuits that are enriched in dopaminergic neurons [153, 157] in patients with ASD, further studies are needed to investigate the interaction of oxytocin with the dopaminergic system.

One study has investigated the therapeutic effect of deep brain stimulation for an ASD patient with self-injurious behaviors using ^{18}F -FDG PET [158]. The authors reported that the glucose metabolism in the occipital cortex as well as the prefrontal and frontal cortex was significantly decreased with symptomatic improvement 2 years after bilateral nucleus accumbens deep brain stimulation. Moreover, the reduction in glucose metabolism was associated with decreased volumes in these regions as revealed by volumetric MRI after deep brain stimulation. These results indicate that ASD patients with life-threatening self-injurious behaviors have organic lesions associated with structural and functional alterations, and such lesions can be modulated by deep brain stimulation to achieve symptomatic improvement, suggesting the therapeutic potential of nucleus accumbens-targeted deep brain stimulation for these patients.

Taken together, neuroimaging studies significantly increase our understanding of the treatment outcome in ASD at the circuit level, and offer objective biomarkers for the evaluation of novel therapies for ASD.

Conclusions and Future Perspectives

Accumulating evidence has suggested that ASD encompasses alterations of brain structural and functional connectivity, particularly in regions and networks implicated in social-cognition. Longitudinal neuroimaging studies have delineated atypical developmental trajectories of ASD that are associated with cascading neurobiological processes (Fig. 1). Meanwhile, impaired serotonergic, dopaminergic, glutamatergic, and GABAergic systems as well as neuroinflammation may be critically involved in the pathogenesis of ASD. Still, further research is warranted to explore how imaging biomarkers are related to the treatment effect, symptomology, and genetic variants of ASD.

While most neuroimaging findings show extensive variability [159], the progress of finding clinically-relevant biomarkers is likely to be facilitated by identifying homogeneous ASD subgroups based on neuroimaging features, referred to as neurosubtyping (for review, see

[160]). Future neurosubtyping approaches would benefit from leveraging findings from the larger literature of candidate biomarkers. Examining the totality of attributes in the context of each other is crucial for understanding the developmental course of individuals. Big data and data-driven methods may be promising approaches to decomposing the extensive heterogeneity in ASD [161]. Advanced analytical models that are tailored to capture the categorical and dimensional nature of ASD heterogeneity will be important to delineate biologically and clinically meaningful subgroups [162] and model complex growth- and time-related courses. In addition, the high comorbidity rate underscores the need for a trans-diagnostic framework for deepening our understanding of the heterogeneity within and beyond autism.

Future longitudinal studies covering younger patients may help identify the causative mechanisms and vulnerable developmental stages of ASD. Big data approaches coupled with data-driven methods will likely facilitate efforts to decompose the ASD heterogeneity. In parallel, large-scale, multi-center, multidisciplinary collaborations are increasingly important to elucidate neurophysiological underpinnings of ASD and facilitate the development of objective diagnostic biomarkers and ASD-targeted therapy. Future advances in imaging techniques and the development of new tracers may further our understanding of the pathophysiology and promote drug development by revealing novel mechanistic or therapeutic targets for ASD.

Acknowledgements This review was supported by grants from the National Key Research and the Development Program of China (2016YFA0100900) and the National Natural Science Foundation of China (81761148029, 81725009, 81425015, and 81900255).

Conflict of interest The authors claim that there are no conflicts of interest.

References

1. APA. Diagnostic and Statistical Manual of Mental Disorders. Fifth Edition. Washington, DC: American Psychiatric Association, 2013.
2. Baxter AJ, Brugha TS, Erskine HE, Scheurer RW, Vos T, Scott JG. The epidemiology and global burden of autism spectrum disorders. *Psychol Med* 2015, 45: 601–613.
3. Zhou H, Xu X, Yan W, Zou X, Wu L, Luo X. Prevalence of autism spectrum disorder in China: A nationwide multi-center population-based study among children aged 6 to 12 years. *Neurosci Bull* 2020, 36: 961–971.
4. Buescher AV, Cidav Z, Knapp M, Mandell DS. Costs of autism spectrum disorders in the United Kingdom and the United States. *JAMA Pediatr* 2014, 168: 721–728.
5. Hallmayer J, Cleveland S, Torres A, Phillips J, Cohen B, Torigoe T, *et al.* Genetic heritability and shared environmental factors among twin pairs with autism. *Arch Gen Psychiatry* 2011, 68: 1095–1102.

6. Sanders SJ, He X, Willsey AJ, Ercan-Sencicek AG, Samocha KE, Cicek AE, *et al.* Insights into autism spectrum disorder genomic architecture and biology from 71 risk loci. *Neuron* 2015, 87: 1215–1233.
7. Li C, Zhou H, Wang T, Long S, Du X, Xu X, *et al.* Performance of the autism spectrum rating scale and social responsiveness scale in identifying autism spectrum disorder among cases of intellectual disability. *Neurosci Bull* 2018, 34: 972–980.
8. Lord C, Elsabbagh M, Baird G, Veenstra-Vanderweele J. Autism spectrum disorder. *Lancet* 2018, 392: 508–520.
9. Weissleder R, Mahmood U. Molecular imaging. *Radiology* 2001, 219: 316–333.
10. James ML, Gambhir SS. A molecular imaging primer: modalities, imaging agents, and applications. *Physiol Rev* 2012, 92: 897–965.
11. Lerch JP, van der Kouwe AJ, Raznahan A, Paus T, Johansen-Berg H, Miller KL, *et al.* Studying neuroanatomy using MRI. *Nat Neurosci* 2017, 20: 314–326.
12. Logothetis NK, Pauls J, Augath M, Trinath T, Oeltermann A. Neurophysiological investigation of the basis of the fMRI signal. *Nature* 2001, 412: 150–157.
13. DeRamus TP, Kana RK. Anatomical likelihood estimation meta-analysis of grey and white matter anomalies in autism spectrum disorders. *Neuroimage Clin* 2015, 7: 525–536.
14. Liu J, Yao L, Zhang W, Xiao Y, Liu L, Gao X, *et al.* Gray matter abnormalities in pediatric autism spectrum disorder: a meta-analysis with signed differential mapping. *Eur Child Adolesc Psychiatry* 2017, 26: 933–945.
15. Schumann CM, Bloss CS, Barnes CC, Wideman GM, Carper RA, Akshoomoff N, *et al.* Longitudinal magnetic resonance imaging study of cortical development through early childhood in autism. *J Neurosci* 2010, 30: 4419–4427.
16. van Rooij D, Anagnostou E, Arango C, Auzias G, Behrmann M, Busatto GF, *et al.* Cortical and subcortical brain morphometry differences between patients with autism spectrum disorder and healthy individuals across the lifespan: results from the ENIGMA ASD working group. *Am J Psychiatry* 2018, 175: 359–369.
17. Hazlett HC, Poe M, Gerig G, Smith RG, Provenzale J, Ross A, *et al.* Magnetic resonance imaging and head circumference study of brain size in autism: birth through age 2 years. *Arch Gen Psychiatry* 2005, 62: 1366–1376.
18. Ashburner J, Friston KJ. Voxel-based morphometry—the methods. *Neuroimage* 2000, 11: 805–821.
19. Aron AR, Robbins TW, Poldrack RA. Inhibition and the right inferior frontal cortex: one decade on. *Trends Cogn Sci* 2014, 18: 177–185.
20. Ridderinkhof KR, Ullsperger M, Crone EA, Nieuwenhuis S. The role of the medial frontal cortex in cognitive control. *Science* 2004, 306: 443–447.
21. du Boisgucheneuc F, Levy R, Volle E, Seassau M, Duffau H, Kinkingnehun S, *et al.* Functions of the left superior frontal gyrus in humans: a lesion study. *Brain* 2006, 129: 3315–3328.
22. Hirshorn EA, Thompson-Schill SL. Role of the left inferior frontal gyrus in covert word retrieval: neural correlates of switching during verbal fluency. *Neuropsychologia* 2006, 44: 2547–2557.
23. Courchesne E, Campbell K, Solso S. Brain growth across the life span in autism: age-specific changes in anatomical pathology. *Brain Res* 2011, 1380: 138–145.
24. Courchesne E, Karns CM, Davis HR, Ziccardi R, Carper RA, Tigue ZD, *et al.* Unusual brain growth patterns in early life in patients with autistic disorder: an MRI study. *Neurology* 2001, 57: 245–254.
25. Carper RA, Courchesne E. Localized enlargement of the frontal cortex in early autism. *Biol Psychiatry* 2005, 57: 126–133.
26. Shen MD, Nordahl CW, Young GS, Wootton-Gorges SL, Lee A, Liston SE, *et al.* Early brain enlargement and elevated extra-axial fluid in infants who develop autism spectrum disorder. *Brain* 2013, 136: 2825–2835.
27. Wolff JJ, Gu H, Gerig G, Elison JT, Styner M, Gouttard S, *et al.* Differences in white matter fiber tract development present from 6 to 24 months in infants with autism. *Am J Psychiatry* 2012, 169: 589–600.
28. Solso S, Xu R, Proudfoot J, Hagler DJ Jr, Campbell K, Venkatraman V, *et al.* on tensor imaging provides evidence of possible axonal overconnectivity in frontal lobes in autism spectrum disorder toddlers. *Biol Psychiatry* 2016, 79: 676–684.
29. Hazlett HC, Gu H, Munsell BC, Kim SH, Styner M, Wolff JJ, *et al.* Early brain development in infants at high risk for autism spectrum disorder. *Nature* 2017, 542: 348–351.
30. Ohta H, Nordahl CW, Iosif AM, Lee A, Rogers S, Amaral DG. Increased surface area, but not cortical thickness, in a subset of young boys with autism spectrum disorder. *Autism Res* 2016, 9: 232–248.
31. Shen MD, Kim SH, McKinstry RC, Gu H, Hazlett HC, Nordahl CW, *et al.* Increased extra-axial cerebrospinal fluid in high-risk infants who later develop autism. *Biol Psychiatry* 2017, 82: 186–193.
32. Shen MD, Nordahl CW, Li DD, Lee A, Angkustsiri K, Emerson RW, *et al.* Extra-axial cerebrospinal fluid in high-risk and normal-risk children with autism aged 2–4 years: a case-control study. *Lancet Psychiatry* 2018, 5: 895–904.
33. Hazlett HC, Poe MD, Gerig G, Styner M, Chappell C, Smith RG, *et al.* Early brain overgrowth in autism associated with an increase in cortical surface area before age 2 years. *Arch Gen Psychiatry* 2011, 68: 467–476.
34. Martínez-Cerdeño V, Noctor SC, Kriegstein AR. The role of intermediate progenitor cells in the evolutionary expansion of the cerebral cortex. *Cereb Cortex* 2006, 16(Suppl 1): i152–161.
35. Lui JH, Hansen DV, Kriegstein AR. Development and evolution of the human neocortex. *Cell* 2011, 146: 18–36.
36. Rakic P. A small step for the cell, a giant leap for mankind: a hypothesis of neocortical expansion during evolution. *Trends Neurosci* 1995, 18: 383–388.
37. Marchetto MC, Belinson H, Tian Y, Freitas BC, Fu C, Vadodaria K, *et al.* Altered proliferation and networks in neural cells derived from idiopathic autistic individuals. *Mol Psychiatry* 2017, 22: 820–835.
38. Wang M, Wei PC, Lim CK, Gallina IS, Marshall S, Marchetto MC, *et al.* Increased neural progenitor proliferation in a hiPSC model of autism induces replication stress-associated genome instability. *Cell Stem Cell* 2020, 26(221–233): e226.
39. Mariani J, Coppola G, Zhang P, Abyzov A, Provini L, Tomasini L, *et al.* FOXP1-dependent dysregulation of GABA/glutamate neuron differentiation in autism spectrum disorders. *Cell* 2015, 162: 375–390.
40. Muhle RA, Reed HE, Stratigos KA, Veenstra-VanderWeele J. The emerging clinical neuroscience of autism spectrum disorder: a review. *JAMA Psychiatry* 2018, 75: 514–523.
41. Kohli JS, Kinnear MK, Martindale IA, Carper RA, Müller RA. Regionally decreased gyrification in middle-aged adults with autism spectrum disorders. *Neurology* 2019, 93: e1900–e1905.
42. Kohli JS, Kinnear MK, Fong CH, Fishman I, Carper RA, Müller RA. Local cortical gyrification is increased in children with autism spectrum disorders, but decreases rapidly in adolescents. *Cereb Cortex* 2019, 29: 2412–2423.
43. White T, Su S, Schmidt M, Kao CY, Sapiro G. The development of gyrification in childhood and adolescence. *Brain Cogn* 2010, 72: 36–45.

44. Van Essen DC. A tension-based theory of morphogenesis and compact wiring in the central nervous system. *Nature* 1997, 385: 313–318.
45. Reillo I, de Juan Romero C, García-Cabezas M, Borrell V. A role for intermediate radial glia in the tangential expansion of the mammalian cerebral cortex. *Cereb Cortex* 2011, 21: 1674–1694.
46. Postema MC, van Rooij D, Anagnostou E, Arango C, Auzias G, Behrmann M, *et al.* Altered structural brain asymmetry in autism spectrum disorder in a study of 54 datasets. *Nat Commun* 2019, 10: 4958.
47. Geschwind N, Galaburda AM. Cerebral lateralization. Biological mechanisms, associations, and pathology: II. A hypothesis and a program for research. *Arch Neurol* 1985, 42: 521–552.
48. Nielsen JA, Zielinski BA, Fletcher PT, Alexander AL, Lange N, Bigler ED, *et al.* Abnormal lateralization of functional connectivity between language and default mode regions in autism. *Mol Autism* 2014, 5: 8.
49. D’Mello AM, Crocetti D, Mostofsky SH, Stoodley CJ. Cerebellar gray matter and lobular volumes correlate with core autism symptoms. *Neuroimage Clin* 2015, 7: 631–639.
50. Pierce K, Courchesne E. Evidence for a cerebellar role in reduced exploration and stereotyped behavior in autism. *Biol Psychiatry* 2001, 49: 655–664.
51. Foster NE, Doyle-Thomas KA, Tryfon A, Ouimet T, Anagnostou E, Evans AC, *et al.* Structural gray matter differences during childhood development in autism spectrum disorder: a multi-metric approach. *Pediatr Neurol* 2015, 53: 350–359.
52. Wolff JJ, Gerig G, Lewis JD, Soda T, Styner MA, Vachet C, *et al.* Altered corpus callosum morphology associated with autism over the first 2 years of life. *Brain* 2015, 138: 2046–2058.
53. Haar S, Berman S, Behrmann M, Dinstein I. Anatomical Abnormalities in Autism?. *Cereb Cortex* 2016, 26: 1440–1452.
54. Nordahl CW, Iosif AM, Young GS, Perry LM, Dougherty R, Lee A, *et al.* Sex differences in the corpus callosum in preschool-aged children with autism spectrum disorder. *Mol Autism* 2015, 6: 26.
55. Schumann CM, Barnes CC, Lord C, Courchesne E. Amygdala enlargement in toddlers with autism related to severity of social and communication impairments. *Biol Psychiatry* 2009, 66: 942–949.
56. Qiu T, Chang C, Li Y, Qian L, Xiao CY, Xiao T, *et al.* Two years changes in the development of caudate nucleus are involved in restricted repetitive behaviors in 2-5-year-old children with autism spectrum disorder. *Dev Cogn Neurosci* 2016, 19: 137–143.
57. Wang SS, Kloth AD, Badura A. The cerebellum, sensitive periods, and autism. *Neuron* 2014, 83: 518–532.
58. Barnea-Goraly N, Frazier TW, Piacenza L, Minshew NJ, Keshavan MS, Reiss AL, *et al.* A preliminary longitudinal volumetric MRI study of amygdala and hippocampal volumes in autism. *Prog Neuropsychopharmacol Biol Psychiatry* 2014, 48: 124–128.
59. Pote I, Wang S, Sethna V, Blasi A, Daly E, Kuklisova-Murgasova M, *et al.* Familial risk of autism alters subcortical and cerebellar brain anatomy in infants and predicts the emergence of repetitive behaviors in early childhood. *Autism Res* 2019, 12: 614–627.
60. Zikopoulos B, Barbas H. Changes in prefrontal axons may disrupt the network in autism. *J Neurosci* 2010, 30: 14595–14609.
61. Lehtinen MK, Zappaterra MW, Chen X, Yang YJ, Hill AD, Lun M, *et al.* The cerebrospinal fluid provides a proliferative niche for neural progenitor cells. *Neuron* 2011, 69: 893–905.
62. Iliff JJ, Wang M, Liao Y, Plogg BA, Peng W, Gundersen GA, *et al.* A paravascular pathway facilitates CSF flow through the brain parenchyma and the clearance of interstitial solutes, including amyloid β . *Sci Transl Med* 2012, 4: 147ra111.
63. Mori S, Zhang J. Principles of diffusion tensor imaging and its applications to basic neuroscience research. *Neuron* 2006, 51: 527–539.
64. Sundaram SK, Kumar A, Makki MI, Behen ME, Chugani HT, Chugani DC. Diffusion tensor imaging of frontal lobe in autism spectrum disorder. *Cereb Cortex* 2008, 18: 2659–2665.
65. Langen M, Leemans A, Johnston P, Ecker C, Daly E, Murphy CM, *et al.* Fronto-striatal circuitry and inhibitory control in autism: findings from diffusion tensor imaging tractography. *Cortex* 2012, 48: 183–193.
66. Tau GZ, Peterson BS. Normal development of brain circuits. *Neuropsychopharmacology* 2010, 35: 147–168.
67. Andrews DS, Lee JK, Solomon M, Rogers SJ, Amaral DG, Nordahl CW. A diffusion-weighted imaging tract-based spatial statistics study of autism spectrum disorder in preschool-aged children. *J Neurodev Disord* 2019, 11: 32.
68. Catani M, Dell’Acqua F, Budisavljevic S, Howells H, Thiebaut de Schotten M, Froudist-Walsh S, *et al.* Frontal networks in adults with autism spectrum disorder. *Brain* 2016, 139: 616–630.
69. Supekar K, Kochalka J, Schaer M, Wakeman H, Qin S, Padmanabhan A, *et al.* Deficits in mesolimbic reward pathway underlie social interaction impairments in children with autism. *Brain* 2018, 141: 2795–2805.
70. Sparks BF, Friedman SD, Shaw DW, Aylward EH, Echelard D, Artru AA, *et al.* Brain structural abnormalities in young children with autism spectrum disorder. *Neurology* 2002, 59: 184–192.
71. Bedford SA, Park MTM, Devenyi GA, Tullo S, Germann J, Patel R, *et al.* Large-scale analyses of the relationship between sex, age and intelligence quotient heterogeneity and cortical morphology in autism spectrum disorder. *Mol Psychiatry* 2020, 25: 614–628.
72. Raichle ME. The restless brain: how intrinsic activity organizes brain function. *Philos Trans R Soc Lond B Biol Sci* 2015, 370: 20140172. <https://doi.org/10.1098/rstb.2014.0172>.
73. Smith SM, Vidaurre D, Beckmann CF, Glasser MF, Jenkinson M, Miller KL, *et al.* Functional connectomics from resting-state fMRI. *Trends Cogn Sci* 2013, 17: 666–682.
74. Uddin LQ, Supekar K, Lynch CJ, Khouzam A, Phillips J, Feinstein C, *et al.* Salience network-based classification and prediction of symptom severity in children with autism. *JAMA Psychiatry* 2013, 70: 869–879.
75. Abbott AE, Nair A, Keown CL, Datko M, Jahedi A, Fishman I, *et al.* Patterns of atypical functional connectivity and behavioral links in autism differ between default, salience, and executive networks. *Cereb Cortex* 2016, 26: 4034–4045.
76. Plitt M, Barnes KA, Wallace GL, Kenworthy L, Martin A. Resting-state functional connectivity predicts longitudinal change in autistic traits and adaptive functioning in autism. *Proc Natl Acad Sci U S A* 2015, 112: E6699–6706.
77. Elton A, Di Martino A, Hazlett HC, Gao W. Neural connectivity evidence for a categorical-dimensional hybrid model of autism spectrum disorder. *Biol Psychiatry* 2016, 80: 120–128.
78. Doyle-Thomas KA, Lee W, Foster NE, Tryfon A, Ouimet T, Hyde KL, *et al.* Atypical functional brain connectivity during rest in autism spectrum disorders. *Ann Neurol* 2015, 77: 866–876.
79. Holiga Š, Hipp JF, Chatham CH, Garces P, Spooren W, D’Arduy XL, *et al.* Patients with autism spectrum disorders display reproducible functional connectivity alterations. *Sci Transl Med* 2019, 11: eaat9223. doi: <https://doi.org/10.1126/scitranslmed.aat9223>.
80. Oldehinkel M, Mennes M, Marquand A, Charman T, Tillmann J, Ecker C, *et al.* Altered connectivity between cerebellum,

- visual, and sensory-motor networks in autism spectrum disorder: results from the EU-AIMS longitudinal European autism project. *Biol Psychiatry Cogn Neurosci Neuroimaging* 2019, 4: 260–270.
81. Uddin LQ. Salience processing and insular cortical function and dysfunction. *Nat Rev Neurosci* 2015, 16: 55–61.
 82. Buckner RL, Andrews-Hanna JR, Schacter DL. The brain's default network: anatomy, function, and relevance to disease. *Ann N Y Acad Sci* 2008, 1124: 1–38.
 83. Bethlehem RAI, Lombardo MV, Lai MC, Auyeung B, Crockford SK, Deakin J, *et al.* Intranasal oxytocin enhances intrinsic corticostriatal functional connectivity in women. *Transl Psychiatry* 2017, 7: e1099.
 84. Andrews-Hanna JR. The brain's default network and its adaptive role in internal mentation. *Neuroscientist* 2012, 18: 251–270.
 85. Yerys BE, Gordon EM, Abrams DN, Satterthwaite TD, Weinblatt R, Jankowski KF, *et al.* Default mode network segregation and social deficits in autism spectrum disorder: Evidence from non-medicated children. *Neuroimage Clin* 2015, 9: 223–232.
 86. Geschwind DH, Levitt P. Autism spectrum disorders: developmental disconnection syndromes. *Curr Opin Neurobiol* 2007, 17: 103–111.
 87. Broyd SJ, Demanuele C, Debener S, Helps SK, James CJ, Sonuga-Barke EJ. Default-mode brain dysfunction in mental disorders: a systematic review. *Neurosci Biobehav Rev* 2009, 33: 279–296.
 88. Courchesne E, Pierce K, Schumann CM, Redcay E, Buckwalter JA, Kennedy DP, *et al.* Mapping early brain development in autism. *Neuron* 2007, 56: 399–413.
 89. Seeley WW, Menon V, Schatzberg AF, Keller J, Glover GH, Kenna H, *et al.* Dissociable intrinsic connectivity networks for salience processing and executive control. *J Neurosci* 2007, 27: 2349–2356.
 90. Corbetta M, Shulman GL. Control of goal-directed and stimulus-driven attention in the brain. *Nat Rev Neurosci* 2002, 3: 201–215.
 91. Watanabe T, Rees G. Brain network dynamics in high-functioning individuals with autism. *Nat Commun* 2017, 8: 16048.
 92. Hahamy A, Behrmann M, Malach R. The idiosyncratic brain: distortion of spontaneous connectivity patterns in autism spectrum disorder. *Nat Neurosci* 2015, 18: 302–309.
 93. Dickie EW, Ameis SH, Shahab S, Calarco N, Smith DE, Miranda D, *et al.* Personalized intrinsic network topography mapping and functional connectivity deficits in autism spectrum disorder. *Biol Psychiatry* 2018, 84: 278–286.
 94. Shou XJ, Xu XJ, Zeng XZ, Liu Y, Yuan HS, Xing Y, *et al.* A volumetric and functional connectivity MRI study of brain arginine-vasopressin pathways in autistic children. *Neurosci Bull* 2017, 33: 130–142.
 95. Emerson RW, Adams C, Nishino T, Hazlett HC, Wolff JJ, Zwaigenbaum L, *et al.* Functional neuroimaging of high-risk 6-month-old infants predicts a diagnosis of autism at 24 months of age. *Sci Transl Med* 2017, 9: eaag2882. doi: <https://doi.org/10.1126/scitranslmed.aag2882>.
 96. Courchesne E, Pierce K. Why the frontal cortex in autism might be talking only to itself: local over-connectivity but long-distance disconnection. *Curr Opin Neurobiol* 2005, 15: 225–230.
 97. Hong SJ, Vos de Wael R, Bethlehem RAI, Lariviere S, Paquola C, Valk SL, *et al.* Atypical functional connectome hierarchy in autism. *Nat Commun* 2019, 10: 1022.
 98. Williams DS, Detre JA, Leigh JS, Koretsky AP. Magnetic resonance imaging of perfusion using spin inversion of arterial water. *Proc Natl Acad Sci U S A* 1992, 89: 212–216.
 99. Jann K, Hernandez LM, Beck-Pancer D, McCarron R, Smith RX, Dapretto M, *et al.* Altered resting perfusion and functional connectivity of default mode network in youth with autism spectrum disorder. *Brain Behav* 2015, 5: e00358.
 100. Peterson BS, Zargarian A, Peterson JB, Goh S, Sawardekar S, Williams SCR, *et al.* Hyperperfusion of Frontal White and Subcortical Gray Matter in Autism Spectrum Disorder. *Biol Psychiatry* 2019, 85: 584–595.
 101. Clark JB. N-acetyl aspartate: a marker for neuronal loss or mitochondrial dysfunction. *Dev Neurosci* 1998, 20: 271–276.
 102. Phelps ME. PET: the merging of biology and imaging into molecular imaging. *J Nucl Med* 2000, 41: 661–681.
 103. Phelps ME. Positron emission tomography provides molecular imaging of biological processes. *Proc Natl Acad Sci U S A* 2000, 97: 9226–9233.
 104. Laruelle M. Imaging synaptic neurotransmission with in vivo binding competition techniques: a critical review. *J Cereb Blood Flow Metab* 2000, 20: 423–451.
 105. Tian M, He X, Jin C, He X, Wu S, Zhou R, *et al.* Transpathology: molecular imaging-based pathology. *Eur J Nucl Med Mol Imaging* 2021, <https://doi.org/10.1007/s00259-021-05234-1>.
 106. Rahmim A, Zaidi H. PET versus SPECT: strengths, limitations and challenges. *Nucl Med Commun* 2008, 29: 193–207.
 107. Mitelman SA, Bralet MC, Mehmet Haznedar M, Hollander E, Shihabuddin L, Hazlett EA, *et al.* Positron emission tomography assessment of cerebral glucose metabolic rates in autism spectrum disorder and schizophrenia. *Brain Imaging Behav* 2018, 12: 532–546.
 108. Dichter GS. Functional magnetic resonance imaging of autism spectrum disorders. *Dialogues Clin Neurosci* 2012, 14: 319–351.
 109. Pfefferbaum A, Chandraud S, Pitel AL, Müller-Oehring E, Shankaranarayanan A, Alsop DC, *et al.* Cerebral blood flow in posterior cortical nodes of the default mode network decreases with task engagement but remains higher than in most brain regions. *Cereb Cortex* 2011, 21: 233–244.
 110. Davey CG, Pujol J, Harrison BJ. Mapping the self in the brain's default mode network. *Neuroimage* 2016, 132: 390–397.
 111. Mitelman SA, Buchsbaum MS, Young DS, Haznedar MM, Hollander E, Shihabuddin L, *et al.* Increased white matter metabolic rates in autism spectrum disorder and schizophrenia. *Brain Imaging Behav* 2018, 12: 1290–1305.
 112. Bullmore E, Sporns O. The economy of brain network organization. *Nat Rev Neurosci* 2012, 13: 336–349.
 113. Brooks JO 3rd, Wang PW, Bonner JC, Rosen AC, Hoblyn JC, Hill SJ, *et al.* Decreased prefrontal, anterior cingulate, insula, and ventral striatal metabolism in medication-free depressed outpatients with bipolar disorder. *J Psychiatr Res* 2009, 43: 181–188.
 114. Whitaker-Azmitia PM. Behavioral and cellular consequences of increasing serotonergic activity during brain development: a role in autism?. *Int J Dev Neurosci* 2005, 23: 75–83.
 115. Yang CJ, Tan HP, Du YJ. The developmental disruptions of serotonin signaling may involved in autism during early brain development. *Neuroscience* 2014, 267: 1–10.
 116. Chugani DC, Chugani HT, Wiznitzer M, Parikh S, Evans PA, Hansen RL, *et al.* Efficacy of low-dose buspirone for restricted and repetitive behavior in young children with autism spectrum disorder: a randomized trial. *J Pediatr* 2016, 170(45–53): e41–e44.
 117. Reddihough DS, Marraffa C, Mouti A, O'Sullivan M, Lee KJ, Orsini F, *et al.* Effect of fluoxetine on obsessive-compulsive behaviors in children and adolescents with autism spectrum disorders: a randomized clinical trial. *Jama* 2019, 322: 1561–1569.
 118. Chugani DC, Muzik O, Behen M, Rothermel R, Janisse JJ, Lee J, *et al.* Developmental changes in brain serotonin synthesis capacity in autistic and nonautistic children. *Ann Neurol* 1999, 45: 287–295.

119. Chugani DC, Muzik O, Rothermel R, Behen M, Chakraborty P, Mangner T, *et al.* Altered serotonin synthesis in the dentatohalamocortical pathway in autistic boys. *Ann Neurol* 1997, 42: 666–669.
120. Chandana SR, Behen ME, Juhász C, Muzik O, Rothermel RD, Mangner TJ, *et al.* Significance of abnormalities in developmental trajectory and asymmetry of cortical serotonin synthesis in autism. *Int J Dev Neurosci* 2005, 23: 171–182.
121. Beversdorf DQ, Nordgren RE, Bonab AA, Fischman AJ, Weise SB, Dougherty DD, *et al.* 5-HT₂ receptor distribution shown by [¹⁸F] setoperone PET in high-functioning autistic adults. *J Neuropsychiatry Clin Neurosci* 2012, 24: 191–197.
122. Coleman JA, Green EM, Gouaux E. X-ray structures and mechanism of the human serotonin transporter. *Nature* 2016, 532: 334–339.
123. Yonan AL, Alarcón M, Cheng R, Magnusson PK, Spence SJ, Palmer AA, *et al.* A genomewide screen of 345 families for autism-susceptibility loci. *Am J Hum Genet* 2003, 73: 886–897.
124. Makkonen I, Riikonen R, Kokki H, Airaksinen MM, Kuikka JT. Serotonin and dopamine transporter binding in children with autism determined by SPECT. *Dev Med Child Neurol* 2008, 50: 593–597.
125. Nakamura K, Sekine Y, Ouchi Y, Tsujii M, Yoshikawa E, Futatsubashi M, *et al.* Brain serotonin and dopamine transporter bindings in adults with high-functioning autism. *Arch Gen Psychiatry* 2010, 67: 59–68.
126. Murphy DG, Daly E, Schmitz N, Toal F, Murphy K, Curran S, *et al.* Cortical serotonin 5-HT_{2A} receptor binding and social communication in adults with Asperger's syndrome: an in vivo SPECT study. *Am J Psychiatry* 2006, 163: 934–936.
127. Chevallier C, Kohls G, Troiani V, Brodtkin ES, Schultz RT. The social motivation theory of autism. *Trends Cogn Sci* 2012, 16: 231–239.
128. Ernst M, Zametkin AJ, Matochik JA, Pascualvaca D, Cohen RM. Low medial prefrontal dopaminergic activity in autistic children. *Lancet* 1997, 350: 638.
129. Davidson RJ, Putnam KM, Larson CL. Dysfunction in the neural circuitry of emotion regulation—a possible prelude to violence. *Science* 2000, 289: 591–594.
130. Owens DF, Kriegstein AR. Is there more to GABA than synaptic inhibition?. *Nat Rev Neurosci* 2002, 3: 715–727.
131. Rubenstein JL, Merzenich MM. Model of autism: increased ratio of excitation/inhibition in key neural systems. *Genes Brain Behav* 2003, 2: 255–267.
132. Pizzarelli R, Cherubini E. Alterations of GABAergic signaling in autism spectrum disorders. *Neural Plast* 2011, 2011: 297153.
133. Mori T, Mori K, Fujii E, Toda Y, Miyazaki M, Harada M, *et al.* Evaluation of the GABAergic nervous system in autistic brain: (123)I-iomazenil SPECT study. *Brain Dev* 2012, 34: 648–654.
134. Fung LK, Flores RE, Gu M, Sun KL, James D, Schuck RK, *et al.* Thalamic and prefrontal GABA concentrations but not GABA(A) receptor densities are altered in high-functioning adults with autism spectrum disorder. *Mol Psychiatry* 2020, <https://doi.org/10.1038/s41380-020-0756-y>.
135. Luna B, Minshew NJ, Garver KE, Lazar NA, Thulborn KR, Eddy WF, *et al.* Neocortical system abnormalities in autism: an fMRI study of spatial working memory. *Neurology* 2002, 59: 834–840.
136. Leblond CS, Nava C, Polge A, Gauthier J, Hugué G, Lumbroso S, *et al.* Meta-analysis of SHANK mutations in autism spectrum disorders: a gradient of severity in cognitive impairments. *PLoS Genet* 2014, 10: e1004580.
137. Fatemi SH, Wong DF, Brašić JR, Kuwabara H, Mathur A, Folsom TD, *et al.* Metabotropic glutamate receptor 5 tracer [(18)F]-FPEB displays increased binding potential in postcentral gyrus and cerebellum of male individuals with autism: a pilot PET study. *Cerebellum Ataxias* 2018, 5: 3.
138. Fatemi SH, Aldinger KA, Ashwood P, Bauman ML, Blaha CD, Blatt GJ, *et al.* Consensus paper: pathological role of the cerebellum in autism. *Cerebellum* 2012, 11: 777–807.
139. Kreisler WC, Fujita M, Fujimura Y, Kimura N, Jenko KJ, Kannan P, *et al.* Comparison of [(11)C]-(R)-PK 11195 and [(11)C]PBR28, two radioligands for translocator protein (18 kDa) in human and monkey: Implications for positron emission tomographic imaging of this inflammation biomarker. *Neuroimage* 2010, 49: 2924–2932.
140. Notter T, Coughlin JM, Sawa A, Meyer U. Reconceptualization of translocator protein as a biomarker of neuroinflammation in psychiatry. *Mol Psychiatry* 2018, 23: 36–47.
141. Zürcher NR, Loggia ML, Mullett JE, Tseng C, Bhanot A, Richey L, *et al.* [(11)C]PBR28 MR-PET imaging reveals lower regional brain expression of translocator protein (TSPO) in young adult males with autism spectrum disorder. *Mol Psychiatry* 2020, <https://doi.org/10.1038/s41380-020-0682-z>.
142. Voss C, Schwartz J, Daniels J, Kline A, Haber N, Washington P, *et al.* Effect of wearable digital intervention for improving socialization in children with autism spectrum disorder: a randomized clinical trial. *JAMA Pediatr* 2019, 173: 446–454.
143. Scassellati B, Boccanfuso L, Huang CM, Mademtzzi M, Qin M, Salomons N, *et al.* Improving social skills in children with ASD using a long-term, in-home social robot. *Sci Robot* 2018, 3: eaat7544. <https://doi.org/10.1126/scirobotics.aat7544>.
144. Insel TR. The challenge of translation in social neuroscience: a review of oxytocin, vasopressin, and affiliative behavior. *Neuron* 2010, 65: 768–779.
145. Ajram LA, Horder J, Mendez MA, Galanopoulos A, Brennan LP, Wichers RH, *et al.* Shifting brain inhibitory balance and connectivity of the prefrontal cortex of adults with autism spectrum disorder. *Transl Psychiatry* 2017, 7: e1137.
146. Greene RK, Spanos M, Alderman C, Walsh E, Bizzell J, Mosner MG, *et al.* The effects of intranasal oxytocin on reward circuitry responses in children with autism spectrum disorder. *J Neurodev Disord* 2018, 10: 12.
147. Linke AC, Olson L, Gao Y, Fishman I, Müller RA. Psychotropic medication use in autism spectrum disorders may affect functional brain connectivity. *Biol Psychiatry Cogn Neurosci Neuroimaging* 2017, 2: 518–527.
148. Hegarty JP 2nd, Ferguson BJ, Zamzow RM, Rohowetz LJ, Johnson JD, Christ SE, *et al.* Beta-adrenergic antagonism modulates functional connectivity in the default mode network of individuals with and without autism spectrum disorder. *Brain Imaging Behav* 2017, 11: 1278–1289.
149. Alaerts K, Bernaerts S, Vanaudenaerde B, Daniels N, Wenderoth N. Amygdala-hippocampal connectivity is associated with endogenous levels of oxytocin and can be altered by exogenously administered oxytocin in adults with autism. *Biol Psychiatry Cogn Neurosci Neuroimaging* 2019, 4: 655–663.
150. Murdaugh DL, Maximo JO, Kana RK. Changes in intrinsic connectivity of the brain's reading network following intervention in children with autism. *Hum Brain Mapp* 2015, 36: 2965–2979.
151. Maximo JO, Murdaugh DL, O'Kelley S, Kana RK. Changes in intrinsic local connectivity after reading intervention in children with autism. *Brain Lang* 2017, 175: 11–17.
152. Watanabe T, Kuroda M, Kuwabara H, Aoki Y, Iwashiro N, Tatsunobu N, *et al.* Clinical and neural effects of six-week administration of oxytocin on core symptoms of autism. *Brain* 2015, 138: 3400–3412.
153. Gordon I, Vander Wyk BC, Bennett RH, Cordeaux C, Lucas MV, Eilbott JA, *et al.* Oxytocin enhances brain function in

- children with autism. *Proc Natl Acad Sci U S A* 2013, 110: 20953–20958.
154. Lefevre A, Mottolese R, Redouté J, Costes N, Le Bars D, Geoffroy MM, *et al.* Oxytocin fails to recruit serotonergic neurotransmission in the autistic brain. *Cereb Cortex* 2018, 28: 4169–4178.
155. Fukai M, Hirosawa T, Kikuchi M, Ouchi Y, Takahashi T, Yoshimura Y, *et al.* Oxytocin effects on emotional response to others' faces via serotonin system in autism: A pilot study. *Psychiatry Res Neuroimaging* 2017, 267: 45–50.
156. Hirosawa T, Kikuchi M, Ouchi Y, Takahashi T, Yoshimura Y, Kosaka H, *et al.* A pilot study of serotonergic modulation after long-term administration of oxytocin in autism spectrum disorder. *Autism Res* 2017, 10: 821–828.
157. Young LJ, Wang Z. The neurobiology of pair bonding. *Nat Neurosci* 2004, 7: 1048–1054.
158. Park HR, Kim IH, Kang H, Lee DS, Kim BN, Kim DG, *et al.* Nucleus accumbens deep brain stimulation for a patient with self-injurious behavior and autism spectrum disorder: functional and structural changes of the brain: report of a case and review of literature. *Acta Neurochir (Wien)* 2017, 159: 137–143.
159. King JB, Prigge MBD, King CK, Morgan J, Weathersby F, Fox JC, *et al.* Generalizability and reproducibility of functional connectivity in autism. *Mol Autism* 2019, 10: 27.
160. Hong SJ, Vogelstein JT, Gozzi A, Bernhardt BC, Yeo BTT, Milham MP, *et al.* Toward neurosubtypes in autism. *Biol Psychiatry* 2020, 88: 111–128.
161. Lombardo MV, Lai MC, Baron-Cohen S. Big data approaches to decomposing heterogeneity across the autism spectrum. *Mol Psychiatry* 2019, 24: 1435–1450.
162. Tang S, Sun N, Floris DL, Zhang X, Di Martino A, Yeo BTT. Reconciling dimensional and categorical models of autism heterogeneity: a brain connectomics and behavioral study. *Biol Psychiatry* 2020, 87: 1071–1082.
163. Courchesne E, Pramparo T, Gazestani VH, Lombardo MV, Pierce K, Lewis NE. The ASD Living Biology: from cell proliferation to clinical phenotype. *Mol Psychiatry* 2019, 24: 88–107.



RESEARCH HIGHLIGHT

STING-ing Pain: How Can Pro-inflammatory Signaling Attenuate Pain?

Wolfgang Liedtke^{1,2,3,4,5,6}

Received: 20 February 2021 / Accepted: 3 March 2021 / Published online: 9 April 2021
© The Author(s) 2021

Inflammation typically induces pain by producing pro-inflammatory mediators, but increasing evidence also indicates a role for inflammation in the resolution of pain by inducing anti-inflammatory and pro-resolution mediators [1, 2]. A recent *Nature* paper from Duke University, “STING controls nociception *via* type-I interferon signaling in sensory neurons”, is noteworthy in this respect [3].

In this paper, Donnelly *et al.* from Ru-Rong Ji’s lab report that activation of the STING (stimulator of interferon genes) signaling mechanism in nociceptive primary sensory neurons functions in an analgesic manner in naive and injured mice, using STING agonists, and applying sophisticated pain behavioral metrics to uninjured mice and mice with nerve constriction injury or a rigorous model of bone cancer pain. Their findings indicate that STING regulates steady-state nociception, which prompted the key discovery that analgesic STING signaling functions *via* type-I interferons (IFN- α or IFN- β). These findings, at the core of their new study, were derived from genetically-

engineered mice, using behavioral and electrophysiological measurements from dorsal root ganglion nociceptor neurons. Particularly important mouse lines for these mechanistic studies were type-I interferon-receptor knockout mice, including cell-specific knockout in nociceptor sensory neurons. In these animals, behavioral evidence of analgesia in response to a type-I interferon and the neurophysiologic correlates of nociceptor action potential formation and calcium currents were missing, suggesting autocrine signaling in the dorsal root ganglion.

Notably, both pro-nociceptive and anti-nociceptive inflammatory mediators can contribute to the ensemble of inflammation. While type-II interferon (IFN- γ) is a typical pro-inflammatory cytokine, type-I interferons (IFN- α and IFN- β) can be both pro-inflammatory and anti-inflammatory, depending on context. Previous studies have demonstrated anti-nociceptive actions of type-I interferons in the central nervous system [4]. Notably, STING is a strong inducer of type-I interferons in immune cells following infections or tissue injury [5, 6]. However, the role of STING in neurons, in particular primary sensory neurons, and in a larger context its role in pain have not been investigated.

The Donnelly *et al.* paper is a formidable piece of work because it elucidates a novel and unexpected mechanism of how interferon signaling is analgesic *via* STING. The new STING story from Dr. Ji’s lab stings the dogma of pro-inflammatory signaling being pro-algesic. Beyond its impact as a fundamentally new insight, its potential for translation into new analgesic treatments has to be recognized, also opening up several new avenues for further mechanistic insights.

The paper lays out a compelling, frequently not fully appreciated background and rationale, namely that pain is an instinct that, *via* its sentinel function, encodes avoidance

✉ Wolfgang Liedtke
wolfgangliedtke@icloud.com

¹ Department of Neurology, Duke University School of Medicine, Durham, NC 27710, USA
² Department of Anesthesiology, Duke University School of Medicine, Durham, NC 27710, USA
³ Department of Neurobiology, Duke University School of Medicine, Durham, NC 27710, USA
⁴ Duke Neurology Clinics for Headache, Head-Pain and Trigeminal Sensory Disorders, Durham, NC 27705, USA
⁵ Clinics for Innovative Pain Therapy, Department of Anesthesiology, Duke University, Raleigh, NC 27512, USA
⁶ Chair of Neurology, Global Scientific Development Council, Regeneron Pharmaceuticals, Tarrytown, NY 10591, USA

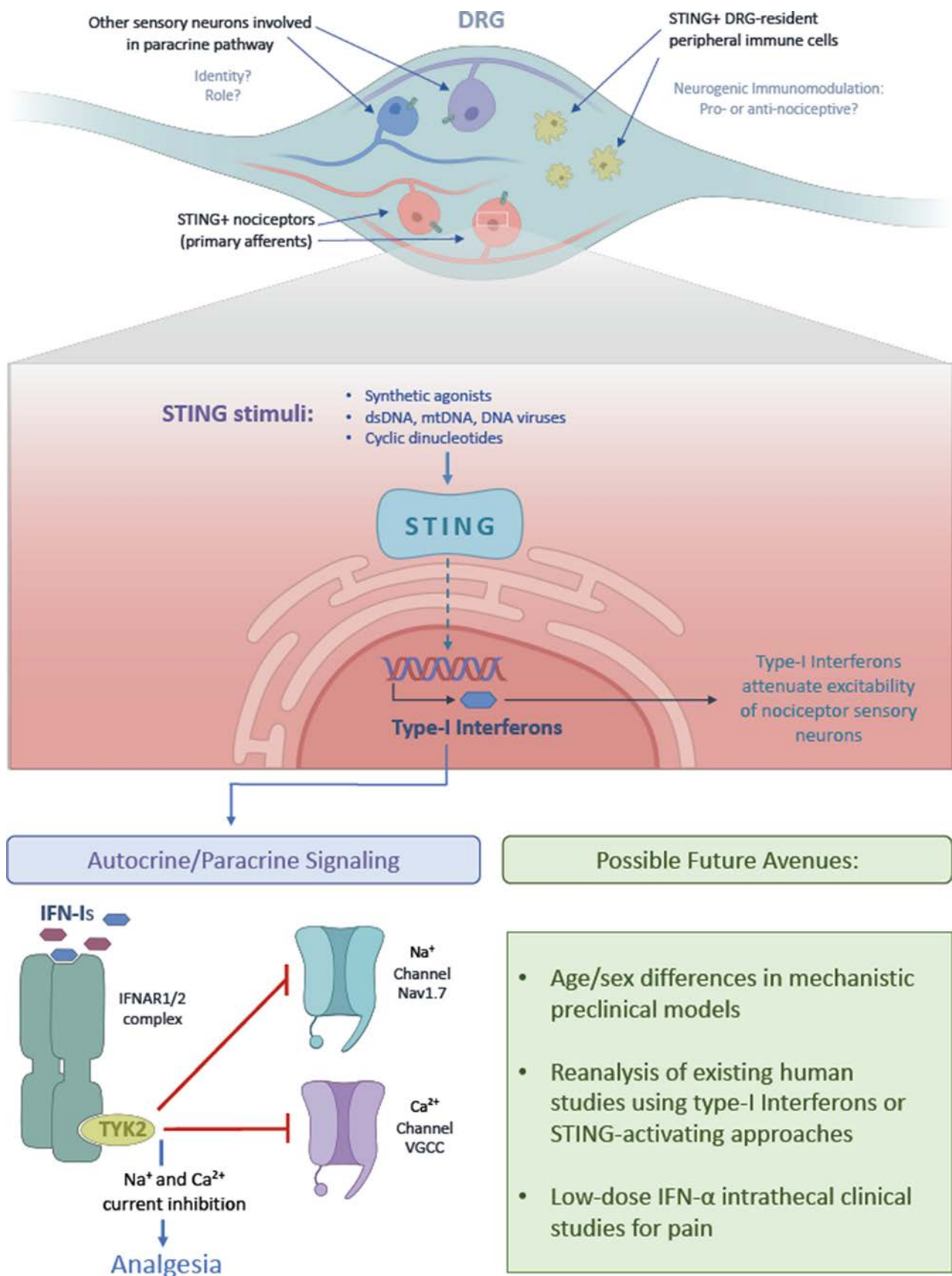


Fig. 1 Summary of concepts of the new STING paper [3] and future directions.

behaviors that protect the organism from potential danger, that neural encoding of pain preprograms the organism for future danger. In this vital system, as it subserves the physical integrity of the organism, primary nociceptor sensory neurons are centerfold because they function as neural integrators of the primary danger signal, modulated by inflammation, and coordinating unspecific defense and also more specific immune responses. So inflammation “increases the heat”, sensitizes these nociceptors, and represents a form of neural injury.

But now we know that it is not that simple, with profound implications. STING signaling, as part of the early inflammatory response, triggered by bacterial or viral infection as well as tissue injury, functions as a potent antinociceptive. Gain-of-function and loss-of-function studies of STING as presented by Donnelly *et al.* are deep and convincing. Gain-of-function of STING shows significant analgesic effects in naïve mice as well as in preclinical models of chemotherapy-induced painful polyneuropathy (CIPN), peripheral nerve constriction injury, and bone cancer pain. These favorable properties beget more advantageous features, namely independence of STING activation and the resulting analgesia from reward circuitry and lack of effect of the opioid receptor blocker naloxone.

To complement, the new results on loss-of-function of STING, both genetically-encoded and chemically-mediated, paint a clear picture of lowered pain thresholds, indicating hyperalgesia and overall increased pain sensitivity.

Both approaches unambiguously indict the primary sensory neurons, in particular nociceptors, in the dorsal root ganglion as a key cellular site of action for the observed behavioral and electrophysiological effects on nociception.

The work is primarily new, unexpected, and relevant for basic science as well as translational medical science, in the interdisciplinary arena of pain research - as one expects for a *Nature* paper. However, sections of the paper are outright elegant in approach. What impresses are the rescue experiments of STING activation in STING pan-nulls *versus* STING conditional knockout (cKO) mice, whereby selective STING activators were completely inert in pan-null mice, but showed delayed rescue of pain hypersensitivity in the cKO animals. This clarifies the role of sensory neuronal STING as critical for nociceptor function in the early pain response. Delayed analgesic effects of STING activators were present in mice that did not express STING in nociceptor neurons but elsewhere, so that the cellular site for these effects is now open for discovery.

STING enhances the expression and secretion of type-I interferons (IFN- α and IFN- β) by nociceptors which then signal in an autocrine/paracrine manner to interferon receptors, expressed by nociceptors. Importantly, this signaling critically involves TYK2 kinase, not PI3-kinase,

and not MAP-kinases. TYK2 kinase signaling, in turn, then attenuates the pro-nociceptive ion channel function of voltage-gated sodium channels, amongst them Nav1.7, that are essential for the generation of action potentials [7], and voltage-gated calcium channels that are critical for neurotransmitter release. The forceful exclamation marks of this impressive study are partial validation of the new pro-inflammatory yet analgesic STING mechanism in human DRG neurons, and skillfully-conducted studies in macaques, by primate pain researcher Dr. Mei Chuan Ko at Wake Forest University.

As we look forward, this leaves us where? There appears to be a clear and direct translational opportunity, which is to use low-dose type-I interferons (IFN- α or IFN- β , as used for adjuvant therapy of malignancy, in infections and autoimmune conditions) in chronic-refractory pain. One can consider the intrathecal route to avoid systemic effects, and apply low-dose interferon, perhaps the more widely used interferon- α , to patients with refractory CIPN or diabetic neuropathy pain. In addition, existing datasets and patients previously treated with low-dose IFN- α can be interrogated for whether this treatment led to diminished pain, in cases where there was pain before treatment. There appear to be 14 clinical studies referenced in clinicaltrials.gov. These trials were aiming for treatment of malignancies or chronic infections, not pain. In addition to trial application of IFN- α , STING agonists more recently used for adjuvant anti-malignancy treatments will be equally interesting, and whether treatment with them did diminish cancer/malignancy-associated pain (Fig. 1).

What might be a particularly interesting goal in the basic science arena is STING's effect on nociceptors, which will in turn influence immune cells. This begets the important question, how does feedback from immune cells modulate the analgesic effects of STING? In the case of immune-mediated attenuation of STING analgesic function, then STING's analgesic effects could be enhanced further by blocking (currently unknown) immune-mediated pro-algesic effects downstream of STING. Last but not least, the canonical “next” steps in the cookbook of pain research likely are already cooking: a more in-depth study of male/female sex differences [8], and how the new STING analgesic signaling plays out in young/old subjects?

Acknowledgements Illustration graphics were expertly provided by Ms Clara Sandu (Duke University).

Conflict of interest The author declares no conflict of interest.

Open Access This article is licensed under a Creative Commons Attribution 4.0 International License, which permits use, sharing, adaptation, distribution and reproduction in any medium or format, as long as you give appropriate credit to the original author(s) and the source, provide a link to the Creative Commons licence, and indicate

if changes were made. The images or other third party material in this article are included in the article's Creative Commons licence, unless indicated otherwise in a credit line to the material. If material is not included in the article's Creative Commons licence and your intended use is not permitted by statutory regulation or exceeds the permitted use, you will need to obtain permission directly from the copyright holder. To view a copy of this licence, visit <http://creativecommons.org/licenses/by/4.0/>.

References

1. Laumet G, Edralin JD, Dantzer R, Heijnen CJ, Kavelaars A. CD3(+) T cells are critical for the resolution of comorbid inflammatory pain and depression-like behavior. *Neurobiol Pain* 2020, 7: 100043.
2. Willemen HL, Eijkelkamp N, Garza Carbajal A, Wang H, Mack M, Zijlstra J. Monocytes/Macrophages control resolution of transient inflammatory pain. *J Pain* 2014, 15: 496–506.
3. Donnelly CR, Jiang C, Andriessen AS, Wang K, Wang Z, Ding H, *et al.* STING controls nociception via type I interferon signalling in sensory neurons. *Nature* 2021, 591(7849): 275–280.
4. Liu CC, Gao YJ, Luo H, Berta T, Xu ZZ, Ji RR, *et al.* Interferon alpha inhibits spinal cord synaptic and nociceptive transmission via neuronal-glia interactions. *Sci Rep* 2016, 6: 34356.
5. Le Naour J, Zitvogel L, Galluzzi L, Vacchelli E, Kroemer G. Trial watch: STING agonists in cancer therapy. *Oncoimmunology* 2020, 9: 1777624.
6. Landman SL, Ressing ME, van der Veen AG. Balancing STING in antimicrobial defense and autoinflammation. *Cytokine Growth Factor Rev* 2020, 55: 1–14.
7. Chang W, Berta T, Kim YH, Lee S, Lee SY, Ji RR. Expression and role of voltage-gated sodium channels in human dorsal root ganglion neurons with special focus on nav1.7, species differences, and regulation by paclitaxel. *Neurosci Bull* 2018, 34: 4–12.
8. Chen G, Luo X, Qadri MY, Berta T, Ji RR. Sex-dependent glial signaling in pathological pain: distinct roles of spinal microglia and astrocytes. *Neurosci Bull* 2018, 34: 98–108.



RESEARCH HIGHLIGHT

The Parabrachial Nucleus as a Key Regulator of Neuropathic Pain

Zilong Wang^{1,2} · Zhen-Zhong Xu³

Received: 30 December 2020 / Accepted: 2 January 2021 / Published online: 30 April 2021
© Center for Excellence in Brain Science and Intelligence Technology, CAS 2021

Neuropathic pain is a chronic pain caused by peripheral or central nervous system injury or diseases that affect the somatosensory nervous system. It is usually associated with abnormal sensations called dysesthesia and exaggerated pain from normally innocuous stimuli (allodynia) or noxious stimuli (hyperalgesia), and also aversive emotional responses [1, 2]. Neuropathic pain can be very difficult to treat, as classical analgesics like opioids produce inadequate pain relief and may cause tolerance and hyperalgesia, and even addiction after long-term use [3]. Thus, it is of critical importance to study the mechanisms of development, maintenance, and resolution of neuropathic pain. This study from Dr. Duan's research team at Zhejiang University reveals a critical regulatory mechanism for neuropathic pain [4].

The spinoparabrachial tract is an ascending pathway that transmits spinal pain signals to the parabrachial nucleus, which further projects to the amygdala and other brain regions [5]. Recent studies have shown that the lateral parabrachial nucleus (LPBN) receives nociceptive inputs

from projection neurons in the dorsal spinal cord [6, 7], as well as directly from the trigeminal ganglion [8]. However, the role of the LPBN in neuropathic pain is still elusive. Combining *in-vivo* calcium imaging, electrophysiological, optogenetic, and chemogenetic approaches, Sun *et al.* [4] demonstrated that the balance between glutamatergic and GABAergic LPBN neuronal activity modulates the initiation and maintenance of neuropathic pain. Furthermore, the GABAergic neurons in the LPBN gate control the sensitization of glutamatergic neurons that regulate the development and transmission of neuropathic pain (Fig. 1).

To determine whether LPBN neurons are activated by neuropathic pain, Sun *et al.* [4] first profiled neuronal activation using *c-Fos* mapping and found that a large population of glutamatergic neurons but not GABAergic neurons in the LPBN were activated after common peroneal nerve (CPN) ligation. Further *in-vivo* calcium imaging experiments, by fiber photometry and miniaturized microscopy, indicated that CPN ligation increased the sensitivity of glutamatergic neurons, but not GABAergic neurons, in the LPBN to pinch or mechanical stimulation. Moreover, Sun *et al.* [4] demonstrated that optogenetic activation of VgluT2 neurons or CaMKII α neurons, which represent approximately 90% of neurons in the LPBN, induced mechanical allodynia, thermal hyperalgesia, and place avoidance, mimicking neuropathic pain-like behaviors. On the other hand, optogenetic silencing of VgluT2 neurons or CaMKII α neurons in the LPBN not only inhibited the basal sensitivity to mechanical and thermal stimulation in sham mice, but also induced place preference and alleviated the mechanical allodynia and heat hyperalgesia in mice with neuropathic pain. These results indicate that glutamatergic neurons in the LPBN are crucial for both relaying physiological pain and transmitting neuropathic pain.

✉ Zilong Wang
wangzl6@sustech.edu.cn

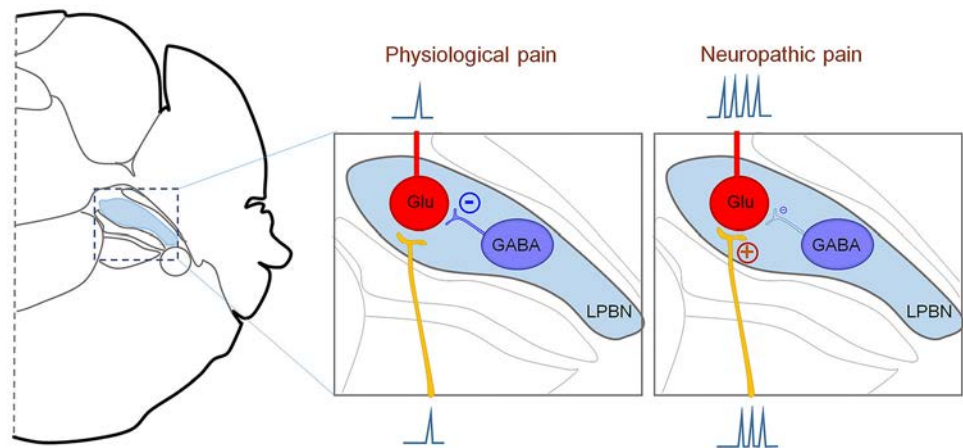
✉ Zhen-Zhong Xu
xuzz@zju.edu.cn

¹ Department of Anesthesiology, Center for Translational Pain Medicine, Duke University Medical Center, Durham, NC 27710, USA

² SUSTech Center for Pain Medicine, School of Medicine, Southern University of Science and Technology, Shenzhen 518055, China

³ Department of Neurobiology and Department of Anesthesiology of the First Affiliated Hospital, NHC and CAMS Key Laboratory of Medical Neurobiology, Zhejiang University School of Medicine, Hangzhou 310058, Zhejiang, China

Fig. 1 Glutamatergic neurons in the LPBN regulate both basal nociception and neuropathic pain. GABAergic neurons in the LPBN directly control the sensitization of glutamatergic neurons, which contribute to the development and maintenance of neuropathic pain.



Next, Sun *et al.* [4] illustrated that glutamatergic neurons in the LPBN receive direct monosynaptic innervation from local GABAergic neurons by using monosynaptic rabies virus tracing. They conducted elegant electrophysiological experiments to characterize the functional inhibitory synaptic inputs from GABAergic to glutamatergic neurons in the LPBN. Furthermore, they found that optogenetic activation of GABAergic neurons in the LPBN reversed the mechanical allodynia and heat hyperalgesia, and induced place preference in CPN-ligated mice, but not in sham-operated mice. Similarly, pharmacogenetic activation of GABAergic neurons in the LPBN had anti-allodynic effects in CPN-ligated mice, and these were blocked by the GABA_A receptor chloride channel blocker picrotoxin. Surprisingly, Sun *et al.* also showed that optogenetic inhibition of GABAergic neurons, which represent approximately 10% of the neurons in the LPBN, activated a large population of glutamatergic neurons in the LPBN and induced neuropathic pain-like symptoms. These data suggest that GABAergic LPBN neurons critically participate in the homeostasis of pain sensation in the LPBN circuit and gate neuropathic pain transmission *via* local inhibition of glutamatergic neurons (Fig. 1).

Sun *et al.* [4] took further steps to test the effects of persistent activation of glutamatergic or GABAergic neurons in the LPBN. Their results showed that prolonged activation of glutamatergic neurons in the LPBN by pharmacogenetic approaches produced mechanical allodynia and a conditioned place aversion response. Notably, the mechanical allodynia lasted at least one month after withdrawal the pharmacogenetic activator. These data indicated that prolonged activation of glutamatergic neurons in the LPBN is sufficient to induce neuropathic pain-like behaviors. Conversely, prolonged activation of GABAergic neurons in the LPBN during the first week totally prevented the development of neuropathic pain after CPN ligation.

Taken together, Sun *et al.* [4] used multiple approaches to comprehensively evaluate the roles of LPBN circuits in modulating physiological and neuropathic pain, including the transmission and processing of both the sensory and emotional components. Previous studies demonstrated that peripheral and central sensitization, mainly in the secondary order neurons in the spinal dorsal horn, play important roles in its development and maintenance. Here Sun *et al.* [4] present the first evidence that sensitization of the third-order neurons in the LPBN is also essential in its development, suggesting that the LPBN is a key regulator of neuropathic pain. This study also provides a new strategy for neuropathic pain treatment by targeting LPBN neurons and circuits.

The study from Sun *et al.* opens several future directions that will be helpful for better understanding the LPBN circuits in pain, especially in chronic pain. Recent studies have identified several subpopulations of LPBN neurons, such as that tachykinin receptor 1- and dynorphin-expressing neurons play important roles in pain transmission [7, 9]. Chiang *et al.* demonstrated that neurons in spatially segregated regions of the LPBN collateralize to distinct targets and that activation of distinct efferents gives rise to separate components of the nociceptive response [9]. But the manner of encoding the sensory modality information, such as the mechanical-, heat-, cold-, touch-, and pain-related emotional aspects by LPBN neurons is still poorly understood. More studies focusing on the identification of detailed subpopulations of glutamatergic and GABAergic neurons in the LPBN, and their respective functions are warranted. In addition, it has been demonstrated that the LPBN participates in both ascending and descending pain pathways. Neurons in the LPBN receive nociceptive inputs from the trigeminal ganglion, nodose ganglion, and spinal projection neurons [6, 8], then their outputs project predominantly to the periaqueductal gray and ventromedial hypothalamus, central amygdala (CeA), bed nucleus of the

stria terminalis (BNST), insular cortex, and medullary formation [8, 10, 11]. The LPBN neurons also receive inputs from several brain regions, such as the BNST and CeA [5, 12, 13], which are important for descending pain control. Future studies that aim to identify the upstream and downstream neuronal circuits that connect with LPBN neurons will be helpful to better understand the roles of LPBN neurons in pain modulation and provide new targets for chronic pain treatment.

Acknowledgements This Research Highlight was supported by Duke University Anesthesiology Research Funds and the National Natural Science Foundation of China (31771162).

References

1. Calvo M, Davies AJ, Hebert HL, Weir GA, Chesler EJ, Finnerup NB. The genetics of neuropathic pain from model organisms to clinical application. *Neuron* 2019, 104: 637–653.
2. Wu XB, He LN, Jiang BC, Wang X, Lu Y, Gao YJ. Increased CXCL13 and CXCR5 in anterior cingulate cortex contributes to neuropathic pain-related conditioned place aversion. *Neurosci Bull* 2019, 35: 613–623.
3. Finnerup NB, Attal N, Haroutounian S, McNicol E, Baron R, Dworkin RH, *et al.* Pharmacotherapy for neuropathic pain in adults: a systematic review and meta-analysis. *Lancet Neurol* 2015, 14: 162–173.
4. Sun L, Liu R, Guo F, Wen MQ, Ma XL, Li KY, *et al.* Parabrachial nucleus circuit governs neuropathic pain-like behavior. *Nat Commun* 2020, 11: 5974.
5. Chiang MC, Bowen A, Schier LA, Tupone D, Uddin O, Heinricher MM. Parabrachial complex: a hub for pain and aversion. *J Neurosci* 2019, 39: 8225–8230.
6. Choi S, Hachisuka J, Brett MA, Magee AR, Omori Y, Iqbal NU, *et al.* Parallel ascending spinal pathways for affective touch and pain. *Nature* 2020, 587: 258–263.
7. Deng J, Zhou H, Lin JK, Shen ZX, Chen WZ, Wang LH, *et al.* The parabrachial nucleus directly channels spinal nociceptive signals to the intralaminar thalamic nuclei, but not the amygdala. *Neuron* 2020, 107(909–923): e906.
8. Rodriguez E, Sakurai K, Xu J, Chen Y, Toda K, Zhao S, *et al.* A craniofacial-specific monosynaptic circuit enables heightened affective pain. *Nat Neurosci* 2017, 20: 1734–1743.
9. Chiang MC, Nguyen EK, Canto-Bustos M, Papale AE, Oswald AM, Ross SE. Divergent neural pathways emanating from the lateral parabrachial nucleus mediate distinct components of the pain response. *Neuron* 2020.
10. Palmiter RD. The parabrachial nucleus: CGRP neurons function as a general alarm. *Trends Neurosci* 2018, 41: 280–293.
11. Barik A, Thompson JH, Seltzer M, Ghitani N, Chesler AT. A brainstem-spinal circuit controlling nociceptive behavior. *Neuron* 2018, 100(1491–1503): e1493.
12. Roeder Z, Chen Q, Davis S, Carlson JD, Tupone D, Heinricher MM. Parabrachial complex links pain transmission to descending pain modulation. *Pain* 2016, 157: 2697–2708.
13. Raver C, Uddin O, Ji Y, Li Y, Cramer N, Jenne C, *et al.* An amygdalo-parabrachial pathway regulates pain perception and chronic pain. *J Neurosci* 2020, 40: 3424–3442.



RESEARCH HIGHLIGHT

Combination of Biomedical Techniques and Paradigms to Improve Prognostications for Disorders of Consciousness

Ming Song^{1,2,3} · Jianghong He⁴ · Yi Yang⁴ · Tianzi Jiang^{1,2,3,5,6,7,8}

Received: 24 June 2020 / Accepted: 5 July 2020 / Published online: 15 June 2021

© Center for Excellence in Brain Science and Intelligence Technology, Chinese Academy of Sciences 2021

For a long time, patients with disorders of consciousness (DoCs) have been considered to have a universally poor prognosis. However, along with the development of rehabilitation and nursing technology, the findings from recent clinical studies herald a philosophical shift: some DoC patients may have a better outcome than originally thought. A recent review suggests that >40% of DoC patients have the potential to achieve an improvement of consciousness level after specific follow-up [1]. Unfortunately, there is still no effective method to determine the

prognosis of DoC patients early. In the clinic, the prognosis for DoC remains restricted to symptom-based behavioral observations. Physicians and scientists have therefore been seeking accurate and objective biomarkers.

Recently, studies have proposed some novel techniques and paradigms for improving the prognosis for DoC [2–4]. Particularly, a paper published in *Nature* proposed to use the olfactory sniff response as a biomarker for consciousness [2]. The authors believed that the sniff response to different odorants can reflect situational understanding and/or learning, which is important to determine the severity of consciousness injury and predict the outcome for a DoC patient. Therefore, by measuring the DoC patients' sniff responses (i.e. nasal inhalation volume) to different odorants, the authors found that the nasal inhalation volume was significantly reduced in response to odorants in the patients in a minimally conscious state (MCS), while it was not influenced by odorants in patients in a vegetative state, i.e., a subcategory of DoC diagnosed as having worse consciousness than MCS. More importantly, the nasal sniff responses can accurately predict whether or not consciousness will be regained at the single-patient level. Since the nasal inhalation volume of patients was measured using a nasal cannula linked directly to a spirometer, this proposed technology can be deployed at the bedside in wards for a long time, and this could be an important tool for monitoring the dynamic fluctuations of a patient's consciousness level. In another study, Pan et al. instructed the DoC patients to perform an item-selection task (i.e. select a photograph or a number from two candidates) by using a EEG brain-computer interface, and then found that the patients who completed the task with high accuracy had a good outcome, including consciousness recovery or improved consciousness level [3]. In addition, Gui et al. adopted high-density EEG based on a language paradigm

✉ Tianzi Jiang
jiangtz@nlpr.ia.ac.cn

- ¹ National Laboratory of Pattern Recognition, Institute of Automation, The Chinese Academy of Sciences, Beijing 100190, China
- ² Brainnetome Center, Institute of Automation, The Chinese Academy of Sciences, Beijing 100190, China
- ³ University of Chinese Academy of Sciences, Beijing 100049, China
- ⁴ Department of Neurosurgery, Beijing Tiantan Hospital, Capital Medical University, Beijing 100070, China
- ⁵ Key Laboratory for Neuroinformation of the Ministry of Education, School of Life Science and Technology, University of Electronic Science and Technology of China, Chengdu 625014, China
- ⁶ CAS Center for Excellence in Brain Science and Intelligence Technology, Chinese Academy of Sciences, Beijing 100190, China
- ⁷ Key Laboratory for Neuroinformation of the Ministry of Education, School of Life Science and Technology, University of Electronic Science and Technology of China, Chengdu 625014, China
- ⁸ The Queensland Brain Institute, University of Queensland, Brisbane, QLD 4072, Australia

Table 1. Prognostic predictors for DoCs

Predictor name	Corresponding effects on prognosis
<i>Internal factors</i>	
Etiology	Traumatic brain injury tends to have a better outcome than a non-traumatic etiology
Age	Young adults are more likely to have a favorable outcome than older patients The effect of age on the prognosis of pediatric DoC patients is not clear
Duration of DoC	The longer the duration of DoC, the smaller the chance of consciousness recovery The long-term outcome cannot be considered as finite for DoC patients
Clinical diagnosis	MCS has a potentially more favorable outcome. Estimates of misdiagnosis among patients with DoC consistently approximate 40% It is argued that behavioral criteria for the application of DoC categories should be supplemented with brain-based criteria
Neurological examinations	Neural reflexes and behavioral responses (e.g., olfactory sniff responses) can predict the prognosis NSE and S-100B are predictive of outcome during acute brain injury. However, no biochemical marker exists for predicting the prognosis of prolonged DoC
Locations of brain lesions	Corpus callosal lesions, dorsolateral upper brainstem injury, or corona radiata injury can result in a worse prognosis
Signatures of residual brain function	
Brain activity in response to a stimulus	DoC patients who exhibit high-level responses to stimuli (including auditory/language, visual, noxious somatosensory, and thermal stimuli) often show clinical signs of recovery at long-term follow-up. Specific components in the ERP can be used as valuable prognostic factors, including MMN, P300, and N400. Perturbational complexity index from synchronous TMS and EEG is an attractive index for the prognosis of DoC patients
Brain activity following commands	The presence of near-normal activity following commands (e.g., motor, visuospatial or visual tasks) can be a marker for consciousness recovery
Brain activity during the resting state	EEG oscillations in the resting state can provide multiple information for prognosis of DoC, including the power of fluctuations (local synchronization), functional and effective connectivity (interactions between areas), and topological characteristics of the brain networks (complexity measures in networks) Using resting-state FDG PET, higher tracer uptake in the frontoparietal network, and stronger connections between brain areas in frontoparietal network and thalamic nuclei suggest a better prognosis for DoC Strong functional connectivity in the default mode network in resting-state fMRI may predict a better outcome. Near-normal spatio-temporal patterns in executive control, salience, sensorimotor, auditory, visual, and subcortical networks can predict a better prognosis. Anti-correlations between the default mode and executive control networks can be crucial to predicting better outcomes for DoC patients.
Sleep	Sleep patterns with more “complexes” (i.e., alternations between non-REM and REM, reappearance of sleep spindles) often suggest a good functional recovery. Near-normal circadian rhythms might indicate a good prognosis for DoC patients.
<i>External factors</i>	
Therapeutic interventions	Amantadine and tDCS are helpful for recovery from DoC. Novel treatment approaches have been proposed, but they await systematic assessment.
Rehabilitation and nursing	Education and perseverance can reduce complications and improve the chance of recovery.
Medical complications	Complication rates are high in DoC patients and negatively affect morbidity and mortality.

DoC, disorder of consciousness; ERP, event-related potential; MMN, mismatch negativity; TMS, transcranial magnetic stimulation; EEG, electroencephalogram; FDG PET, ¹⁸F-fluorodeoxyglucose PET; fMRI, functional MRI; REM, rapid eye movement sleep; NSE, neuron-specific enolase; S-100B, S100 calcium-binding protein B; tDCS, transcranial direct current stimulation.

that elicited rhythmic brain responses tracking the single-word, phrase, and sentence rhythms in speech, and found that the EEG features derived from both speech-tracking responses and the temporal dynamics of global brain states

predict the patients' outcomes [4]. In total, these recent studies have made promising progress and provided novel views on the prognostic factors for DoC.

Indeed, the DoCs are acquired brain injuries. DoC patients have impaired consciousness in common, but this can have many different causes and be associated with several neuropathological processes and different severity of damage. Therefore, a great many prognostic factors have been suggested to be related to a DoC patient's prognosis. Several reviews of these factors have been published in recent years [5–8]. In our own view, the prognostic factors can be classified as internal or external. Internal factors are associated with the patient's own condition, including etiology, age, duration of DoC, clinical diagnosis, location of brain injury, sleep characteristics, and residual brain activity patterns. External factors pertain to the direct external environment, including treatment and care, as well as the resulting medical complications and ethical decisions. To date, there are no effective therapeutic interventions to restore a DoC patient's consciousness; but recent studies suggest that some patients might benefit from therapeutic interventions, even years after the injury [9]. We summarize the internal and external prognostic factors and their effects on the prognosis for DoC in Table 1.

In summary, DoCs are heterogeneous mixtures of different diseases or injuries, and comprise a group of clinical syndromes in the continuum of diffuse and multifocal brain damage [10]. There is a real possibility that any prognostic factor when used alone either carries a risk of false prediction or encounters clinical scenarios where it cannot be applied. Therefore, on the one hand, researchers need to persistently explore novel ideas to identify new prognostic factors; on the other hand, it is even more necessary to integrate multiple verified prognostic factors to improve the accuracy of prognosis for

DoC patients and enhance clinical utility in different clinical scenarios.

Acknowledgements This Research Highlight was supported by the National Natural Science Foundation of China (31870984).

References

1. Song M, Yang Y, Yang ZY, Cui Y, Yu S, He JH. Prognostic models for prolonged disorders of consciousness: An integrative review. *Cell Mol Life Sci* 2020, 77: 3945–3961.
2. Arzi A, Rozenkrantz L, Gorodisky L, Rozenkrantz D, Holtzman Y, Ravia A, *et al.* Olfactory sniffing signals consciousness in unresponsive patients with brain injuries. *Nature* 2020, 581: 428–433.
3. Pan JH, Xie QY, Qin PM, Chen Y, He YB, Huang HY, *et al.* Prognosis for patients with cognitive motor dissociation identified by brain-computer interface. *Brain* 2020, 143: 1177–1189.
4. Gui P, Jiang YW, Zang D, Qi ZX, Tan JX, Tanigawa H, *et al.* Assessing the depth of language processing in patients with disorders of consciousness. *Nat Neurosci* 2020, 23: 761–770.
5. Kotchoubey B, Pavlov YG. A systematic review and meta-analysis of the relationship between brain data and the outcome in disorders of consciousness. *Front Neurol* 2018, 9: 315.
6. Estraneo A, Trojano L. Prognosis in disorders of consciousness. *Coma and Disorders of Consciousness*. Cham: Springer International Publishing, 2017: 17–36.
7. Zhao JZ. Disorders of consciousness in China. *Neurosci Bull* 2018, 34: 605–614.
8. Song M, Zhang YJ, Cui Y, Yang Y, Jiang TZ. Brain network studies in chronic disorders of consciousness: Advances and perspectives. *Neurosci Bull* 2018, 34: 592–604.
9. Xia X, Yang Y, Guo Y, Bai Y, Dang Y, Xu R, *et al.* Current status of neuromodulatory therapies for disorders of consciousness. *Neurosci Bull* 2018, 34: 615–625.
10. Bernat JL. Prognostic limitations of syndromic diagnosis in disorders of consciousness. *AJOB Neurosci* 2016, 7: 46–48.



RESEARCH HIGHLIGHT

Autologous Transplantation for Parkinson's Disease Patients: Feasibility and Challenge

Qi Zhang^{1,2} · Yanlin Wang¹ · Yukai Wang^{3,4,5,6} · Han Liu¹ · Huifang Sun^{1,2} · Zhuoya Wang¹ · Changhe Shi¹ · Jing Yang¹ · Yuming Xu¹

Received: 16 January 2021 / Accepted: 24 February 2021 / Published online: 27 May 2021

© Center for Excellence in Brain Science and Intelligence Technology, Chinese Academy of Sciences 2021

Parkinson's Disease (PD), second only to Alzheimer's disease, is a neurodegenerative disease, most commonly occurring in people over the age of 65 years and is mostly caused by loss of dopamine neurons [1]. Clinically, motor symptoms such as resting tremor, motor retardation, muscular rigidity, and disturbance of postural balance are the main symptoms, followed by non-motor symptoms such as cognitive impairment, autonomic nervous system dysfunction, depression, and sleep disorder [2]. In 2016, >6.1 million people were affected with PD globally, 2.4 times the number in 1990. The large number of affected people, coupled with the high mortality and disability rates, has placed a great burden on society [3]. Traditional treatment methods mainly include drugs and surgery and are supplemented by physical therapy. Drugs commonly used include levodopa, dopamine receptor agonists, and

monoamine oxidase B inhibitors. Surgical treatment mainly includes deep brain stimulation, focused ultrasound ablation, and placement of a levodopa infusion pump. However, medication or surgical treatment only controls the symptoms and not the progression of the disease [4]. New treatments are urgently needed.

A recent study demonstrated that the transplantation of autologous induced dopamine progenitor cells derived from pluripotent stem cells in a patient with PD [5]. The researchers transformed skin fibroblasts from the patient into induced pluripotent stem cells, differentiated them into dopamine precursor cells *in vitro*, performed a series of identification and related experiments, and finally completed a pilot study of autologous cell transplantation therapy [6]. The patient was a 69-year-old man with a 10-year history of PD. His symptoms of tremors and postural balance disorder were increasingly serious and levodopa and other drugs were ineffective. With the patient's informed consent and approval of the US Food and Drug Administration, he received personalized dopamine neural precursor cell autograft transplantation therapy. Before the clinical trial, neurologists performed neurological examinations and evaluations, followed by a stereotactic injection into the left putamen, and 6 months later, into the right putamen. CT was performed immediately after the injections and no bleeding was found. A series of detailed neurological examinations and evaluations were performed over 24 months after the injections, and graft survival was assessed by 18F-DOPA PET. After clinical evaluation, the patient had no adverse events or dyskinesias during follow-up. Scores on the MDS-UPDRS, part III (to assess parkinsonian motor signs), after overnight withdrawal of dopamine replacement therapy ("off") were 43 at 4 weeks after the first implantation and 33 at 24 months. The scores at the peak dose of dopamine

Qi Zhang and Yanlin Wang have contributed equally.

✉ Yuming Xu
xuyuming@zzu.edu.cn

- ¹ Department of Neurology, The First Affiliated Hospital of Zhengzhou University, Zhengzhou 450052, China
- ² Academy of Medical Sciences, Zhengzhou University, Zhengzhou 450052, China
- ³ State Key Laboratory of Stem Cell and Reproductive Biology, Institute of Zoology, Chinese Academy of Sciences, Beijing 100101, China
- ⁴ Institute for Stem Cell and Regeneration, Chinese Academy of Sciences, Beijing 100101, China
- ⁵ Department of National Stem Cell Resource Center, Institute of Zoology, Chinese Academy of Sciences, Beijing 100101, China
- ⁶ Beijing Institute for Stem Cell and Regenerative Medicine, Beijing 100101, China

replacement therapy (“on”) were 38 at the time of implantation, and 29 at 24 months. PDQ-39 scores (to assess parkinsonian disease-related quality of life; lower scores indicate better quality) were 62 at the time of implantation, and 2 at 24 months. Certainly, he did not follow the usual worsening trajectory of PD patients and showed some evidence of small improvements. The use of an autologous source rather than human embryonic stem cells or other allogeneic tissues has the major theoretical advantage of removing the need for immunosuppression. The results greatly encourage researchers in cell replacement therapy, and promote cell transplantation therapy to the clinical stage; this is a milestone of progress.

In the past few decades, cell transplantation therapy has been advancing. In 1998, Thomson reported embryonic stem cell lines from human blastocysts for the first time, and Kazutoshi reprogrammed human skin fibroblasts into induced pluripotent stem cells for the first time in 2007 [7], after which the development of human pluripotent stem cells entered a new era. PD researchers are also constantly exploring and promoting the clinical application of basic stem cell research. In 2011, Sonja differentiated embryonic stem cells into dopaminergic precursor cells through a novel method and greatly improved their quality. These cells were then transplanted into mouse, rat, and monkey models of PD. Eventually, they found that grafts can survive without forming teratomas, and the symptoms in animals improve to some extent after the transplants [8]. In 2017, Tetsuhiro transplanted dopaminergic neural precursor cells derived from induced pluripotent stem cells from healthy people and patients with PD into a monkey model of PD, and after two years of examination and evaluation, found that the transplanted cells were alive, the symptoms were improved, and some markers, including the *Dkl1* gene, may be used to predict the presence of donor cells in good condition [9]. Since then, many institutions have carried out clinical trials of dopaminergic neural precursor cells differentiated from human pluripotent stem cells in the treatment of PD.

Although we are optimistic that such research may bring hope for a cure of PD, the tumorigenicity, immunogenicity, and inherent heterogeneity of cells still pose many problems such as cell source, cell quality, injection method, and the number of transplanted cells, which directly or indirectly affect the efficacy of cell replacement therapy. Quality control is the lifeline of a cell product; how to manage cell transplantation in all kinds of clinical

experiments is an urgent problem that needs to be solved. Currently, in China, the issue of registration and approval regulations for clinical trials of similar drugs using stem cells is being explored. As Lindvall emphasized, we should take a rational, scientific, and rigorous approach to the therapeutic effects of clinical trials for PD and continue to optimize the transplantation program [10]. Many colleagues in China who are also doing this kind of work. Let’s work together to promote the project.

Acknowledgements This highlight article was supported by National Key R&D Program of China (2017YFA0105000), the National Natural Science Foundation of China (U1904207, 81530037, 91849115, and 82001973), the Provincial and Ministry of Health Construction Committee of Henan Province (SBGJ2020003017), and the Excellent Youth Foundation of Henan Health Commission.

Conflict of interest The authors claim that there are no conflicts of interest.

References

1. Li T, Le W. Biomarkers for Parkinson’s disease: How good are they? *Neurosci Bull* 2020, 36: 183–194.
2. Dong D, Xie J, Wang J. Neuroprotective effects of brain-gut peptides: a potential therapy for Parkinson’s disease. *Neurosci Bull* 2019, 35: 1085–1096.
3. Feigin VL, Nichols E, Alam T, Bannick MS, Beghi E, Blake N. Global, regional, and national burden of neurological disorders, 1990–2016: a systematic analysis for the Global Burden of Disease Study 2016. *Lancet Neurol* 2019, 18: 459–480.
4. Armstrong MJ, Okun MS. Diagnosis and treatment of Parkinson disease: a review. *JAMA* 2020, 323: 548–560.
5. Schweitzer JS, Song B, Herrington TM, Park TY, Lee N, Ko S, *et al.* Personalized iPSC-derived dopamine progenitor cells for Parkinson’s disease. *N Engl J Med* 2020, 382: 1926–1932.
6. Song B, Cha Y, Ko S, Jeon J, Lee N, Seo H, *et al.* Human autologous iPSC-derived dopaminergic progenitors restore motor function in Parkinson’s disease models. *J Clin Invest* 2020, 130: 904–920.
7. Takahashi K, Tanabe K, Ohnuki M, Narita M, Ichisaka T, Tomoda K, *et al.* Induction of pluripotent stem cells from adult human fibroblasts by defined factors. *Cell* 2007, 131: 861–872.
8. Kriks S, Shim JW, Piao J, Ganat YM, Wakeman DR, Xie Z, *et al.* Dopamine neurons derived from human ES cells efficiently engraft in animal models of Parkinson’s disease. *Nature* 2011, 480: 547–551.
9. Kikuchi T, Morizane A, Doi D, Magotani H, Onoe H, Hayashi T, *et al.* Human iPSC cell-derived dopaminergic neurons function in a primate Parkinson’s disease model. *Nature* 2017, 548: 592–596.
10. Lindvall O. Balancing expectations for success in stem cell-based clinical trials for Parkinson’s disease. *Cell Stem Cell* 2020, 27: 519–522.



RESEARCH HIGHLIGHT

Breakthrough in Structural and Functional Dissection of the Hypothalamo-Neurohypophysial System

Ying Wang¹ · Huamin Xu¹ · Xia Zhang¹

Received: 8 January 2021 / Accepted: 24 February 2021 / Published online: 28 April 2021
© Center for Excellence in Brain Science and Intelligence Technology, CAS 2021

The projections from hypothalamic magnocellular neuroendocrine cells (MNCs) to the posterior pituitary (PPi) are traditionally defined as the hypothalamo-neurohypophysial system (HNS), which releases oxytocin (OXT) and arginine vasopressin (AVP) into the blood stream to regulate peripheral function [1]. Recently, accumulating evidence has confirmed that OXT and AVP are not only involved in peripheral regulation [2], but also contribute to various central actions [3, 4], such as memory and social and stress-related behaviors [5]. However, peripherally released OXT and AVP rarely cross the blood-brain barrier and return to the central nervous system. So, whether and how they exert central effects remain to be elucidated. It is supposed that MNCs projecting to the PPi also have collaterals projecting centrally, and these might be responsible for the central actions of OXT and AVP. But there has been no cell-type-specific dissection of the hypothalamic MNC projections, due to the limited methods and techniques for imaging and manipulation. Recently, in *Neuron* [6], researchers at Zhejiang University and Huazhong University of Science and Technology in China report the skillful use of multiple viruses and advanced techniques to realize cell-type specific labeling and manipulation of hypothalamic MNCs. This is the first report of the three-dimensional reconstruction and cell-type specific functional dissection of the HNS in coordinating both peripheral and central actions, which provide technical references and new insights into the MNC-related mechanisms

underlying central behaviors and psychiatric diseases (Fig. 1).

Despite the pivotal importance of the HNS in neuroendocrine regulation, knowledge on its general structure is poor due to the limited labeling efficiency of traditional tracers and the low resolution of imaging techniques [7, 8]. To fully reconstruct the architecture of the HNS and selectively label the PPi-projecting MNC ensemble in Sprague-Dawley rats, the authors applied the advanced retrograde viral tracer Retro-GFP, which was injected into the PPi to selectively label the cell ensemble directly innervating the neurohypophysis as GFP⁺ cells. To assess the neuroendocrine nature of the labeled cells, Fluoro-Gold (FG) was injected intraperitoneally to label the neuroendocrine neurons as FG⁺ cells. And the results showed that 100% of the GFP⁺ cells in the hypothalamic supraoptic (SON) and paraventricular (PVN) nuclei were co-labeled with FG, which demonstrated that the labeled GFP⁺ cells were neuroendocrine neurons. Moreover, the authors used a well-established marker for parvocellular neuroendocrine cells (PNCs), thyrotropin-releasing hormone (TRH), to label the PNCs and found no co-localization of GFP⁺ and TRH⁺ cells in the PVN, which further identified the GFP⁺ cells as MNCs rather than PNCs [9]. Above all, the retrograde viral tracing with Retro-GFP proved to be a fine choice to label the HNS with higher labeling efficiency and specificity for the first time, and it is impressive that the authors cleverly used viral and immune markers to exclude the interference of non-neuroendocrine neurons and PNCs. Although this method has made advances, it is still not quite perfect. For example, all neurons in the SON project to the neurohypophysis [10], but only 60% of the FG⁺ cells in the SON were co-labeled with GFP. This result indicates that although Retro-GFP has higher efficiency, it still cannot achieve 100% labeling of PPi-projecting MNCs due

✉ Ying Wang
wangying_199110@163.com

¹ Institute of Brain Science and Disease, Qingdao University, Qingdao 266071, China

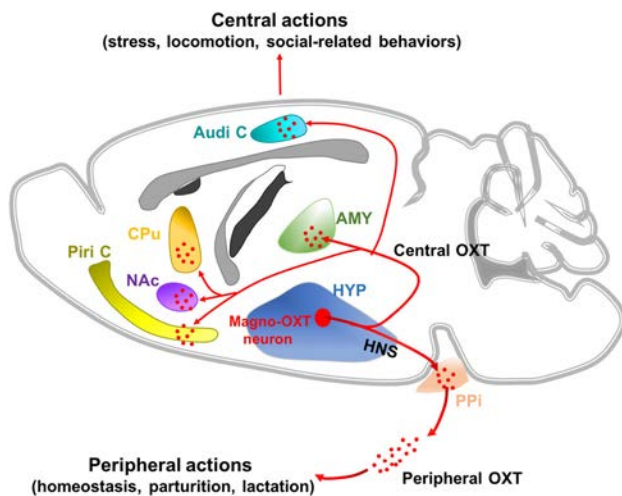


Fig. 1 Magnocellular oxytocin neurons coordinate both peripheral and central actions. The projections from hypothalamic magnocellular oxytocin cells (Magno-OXT neurons) to the posterior pituitary (PPI) were traditionally defined as the hypothalamo-neurohypophysial system (HNS); they release oxytocin (OXT) into the peripheral blood stream to regulate peripheral function. Magno-OXT neurons also project to extra-hypothalamic nuclei, including the amygdala (AMY), caudate-putamen (CPu), nucleus accumbens (NAc), piriform cortex (Piri C), and auditory cortex (Audi C), to regulate central function.

to defective viral infection and retrograde transport, which might affect the integrity of the HNS structure. Moreover, the method of labeling neuroendocrine neurons by intraperitoneally-injected FG is not generally acknowledged and its efficiency needs to be adequately verified.

Besides efficient viral tracers, advanced imaging techniques with higher resolution are also crucial for a clear visualization of the HNS. Then, with the above established method for selective labeling, the authors further used advanced fluorescent micro-optical sectioning tomography (fMOST) to make a 3D reconstruction of the HNS at high resolution. The 3D overview and measurement of the HNS showed that labeled MNCs were distributed in >8 hypothalamic nuclei, and they were divided into three MNC ensembles: a principal MNC nucleus with abundant GFP⁺ cells, an accessory MNC nucleus with densely-packed GFP⁺ cells, and a scattered MNC system with scattered GFP⁺ cells. However, it is noteworthy that GFP⁺ fibers were observed outside the hypothalamus, such as in the piriform cortex, amygdala, and nucleus accumbens, and they likely represent central collaterals of the PPI-projecting MNCs. Subsequently, the authors delineated the morphology of MNCs by single-cell reconstruction and provided more clear illustrations of the axons from the PPI-projecting MNCs. Moreover, the authors further designed two dual-viral strategies in both anterograde and retrograde directions, and verified that PPI-projecting MNCs really sent collaterals to extra-hypothalamic areas. In previous studies, knowledge of the general structure of the HNS was

poor, and MNCs were traditionally considered to send unipolar axons to the neurohypophysis [11]. Here, the authors inspiringly revealed central collaterals from the PPI-projecting MNCs for the first time, which is pivotal in revealing the previously unrecognized complexity of the HNS and provides structural evidence for PPI-projecting MNCs in coordinating both peripheral and central actions. Moreover, the reconstructed atlas needs continuing improvement with more data to summarize the collaterals of PPI-projecting MNCs from different hypothalamic subregions and distinguish their cell subsets in the future, which will benefit the functional dissection of MNC-related circuits.

After the structural imaging of MNC projections, the authors investigated their function in coordinating both peripheral and central actions. In this study, a majority of the PPI-projecting MNCs were shown to be magnocellular OXT (Magno-OXT) neurons through immunostaining with OXT antibody. Moreover, Magno-OXT neurons projected collaterals to multiple extra-hypothalamic regions, including the amygdala, caudate-putamen, and nucleus accumbens, reported for the first time in this study. Then, the authors generated an OXT-Cre rat line, and found that chemogenetic manipulation of Magno-OXT neurons coordinated both peripheral and central OXT-mediated actions. Particularly, the promotion of locomotion induced by chemogenetic activation of Magno-OXT neurons was reversed by infusing an OXT receptor antagonist into the caudate-putamen, further verifying the central release of OXT by Magno-OXT neurons. Although previous studies have already reported the role of central OXT in various social and stress-related behaviors, they did not specify the underlying related circuits. Here, the authors specifically demonstrated for the first time that Magno-OXT neurons release central OXT, and they are involved in the circuits mediating OXT-related central actions, breaking new ground in dissecting the oxytocinergic circuit mechanisms underlying OXT-related central behaviors and mental disorders. However, the wide distribution of PPI-projecting MNCs enhances the difficulty in area-specific labeling and manipulation of the Magno-OXT neuronal ensembles in different hypothalamic nuclei. Nevertheless, a dual-viral strategy by infusing Retro-DIO-Flp into the PPI and AAV-fDIO-hM3d/hM4d-EGFP into different hypothalamic nuclei in OXT-Cre rats might be a feasible method to overcome the difficulty. Moreover, other than OXT, MNCs also release other peptides, such as AVP, which has also been reported to be involved in central behaviors [12]. Therefore, future studies on the function of MNCs should also pay attention to Magno-AVP neurons or any other peptide-releasing magnocellular neurons. Although the functional dissection was not exhaustive, it at least offered technical references for future MNC-related studies.

In conclusion, this study not only provides advanced techniques and an efficient strategy for mapping the connectivity of the HNS, it also offers new insights for exploring the circuit mechanisms underlying MNC-related central behaviors and mental diseases, such as stress, autism, and anxiety-related disorders [13]. Although mapping of the HNS has been reported in earlier studies, the poor efficiency of traditional retrograde tracers and imaging instruments limited the structural dissection. Now, combing advanced retrograde viral tracers with high-resolution imaging fMOST, this study provides a full and clear reconstruction of the HNS architecture for the first time. Moreover, the authors first realized the specific labeling of Magno-OXT neurons in OXT-Cre rats, which is of great importance for further function dissection. Certainly, the present study is just the beginning for MNC-related circuit investigation and many valuable issues still need further research. First, MNCs are distributed in various hypothalamic nuclei, and it is important to segregate their anatomical and functional characteristics. Second, MNCs primarily release OXT and AVP, and it would be valuable to distinguish the roles of Magno-OXT neurons and Magno-AVP neurons in behaviors. Above all, this study used state-of-the-art techniques in the tracing and manipulation of MNCs, providing valuable references for further illumination of neuroendocrine networks.

Acknowledgments This Highlight was supported by the National Natural Science Foundation of China (81830035 and 82003729).

Conflict of interest The authors declare that they have no conflict of interest.

References

1. Hashimoto H, Matsuura T, Ueta Y. Fluorescent visualization of oxytocin in the hypothalamo-neurohypophysial system. *Front Neurosci* 2014, 8: 213.
2. Antunes-Rodrigues J, de Castro M, Elias LL, Valenca MM, McCann SM. Neuroendocrine control of body fluid metabolism. *Physiol Rev* 2004, 84: 169–208.
3. Raggenbass M. Vasopressin- and oxytocin-induced activity in the central nervous system: electrophysiological studies using in vitro systems. *Prog Neurobiol* 2001, 64: 307–326.
4. Hasan MT, Althammer F, Silva da Gouveia M, Goyon S, Eliava M, Lefevre A, *et al.* A fear memory engram and its plasticity in the hypothalamic oxytocin system. *Neuron* 2019, 103: 133–146 e138.
5. Meyer-Lindenberg A, Domes G, Kirsch P, Heinrichs M. Oxytocin and vasopressin in the human brain: social neuropeptides for translational medicine. *Nat Rev Neurosci* 2011, 12: 524–538.
6. Zhang B, Qiu L, Xiao W, Ni H, Chen L, Wang F. Reconstruction of the hypothalamo-neurohypophysial system and functional dissection of magnocellular oxytocin neurons in the brain. *Neuron* 2021, 109: 331–346. e7.
7. Taniguchi Y, Yoshida M, Ishikawa K, Suzuki M, Kurosumi K. The distribution of vasopressin- or oxytocin-neurons projecting to the posterior pituitary as revealed by a combination of retrograde transport of horseradish peroxidase and immunohistochemistry. *Arch Histol Cytol* 1988, 51: 83–89.
8. Fisher AW, Price PG, Burford GD, Lederis K. A 3-dimensional reconstruction of the hypothalamo-neurohypophysial system of the rat. The neurons projecting to the neuro/intermediate lobe and those containing vasopressin and somatostatin. *Cell Tissue Res* 1979, 204: 343–354.
9. Eliava M, Melchior M, Knobloch-Bollmann HS, Wahis J, da Silva Gouveia M, Tang Y, *et al.* A New population of parvocellular oxytocin neurons controlling magnocellular neuron activity and inflammatory pain processing. *Neuron* 2016, 89: 1291–1304.
10. Swanson LW, Sawchenko PE. Hypothalamic integration: organization of the paraventricular and supraoptic nuclei. *Annu Rev Neurosci* 1983, 6: 269–324.
11. Armstrong WE, Warach S, Hatton GI, McNeill TH. Subnuclei in the rat hypothalamic paraventricular nucleus: a cytoarchitectural, horseradish peroxidase and immunocytochemical analysis. *Neuroscience* 1980, 5: 1931–1958.
12. Brunnie C, Nave G, Camerer CF, Schosser S, Vogt B, Munte TF, *et al.* Vasopressin increases human risky cooperative behavior. *Proc Natl Acad Sci U S A* 2016, 113: 2051–2056.
13. Zhang R, Zhang HF, Han JS, Han SP. Genes related to oxytocin and arginine-vasopressin pathways: associations with autism spectrum disorders. *Neurosci Bull* 2017, 33: 238–246.

Brief Instructions to Authors

Neuroscience Bulletin (NB) aims to publish research advances in the field of neuroscience and promote exchange of scientific ideas within the community. The journal publishes original papers of various topics on neuroscience and focuses on potential disease implications on the nervous system. NB welcomes research contributions on molecular, cellular, or developmental neuroscience using multidisciplinary approaches and functional strategies.

Manuscript Submission

Manuscripts should be submitted through our online submission system, ScholarOne Manuscripts, at <http://mc03.manuscriptcentral.com/nsb> or <http://www.neurosci.cn>.

Manuscript file types that we accept for online submission include Word and WordPerfect. For Figure submission, we accept JPEG, TIFF, or AI files. Required items differ for each article type and are specified during the submission process.

The submitted manuscript should be accompanied with a signed “*Neuroscience Bulletin* copyright transfer statement and submission form”.

Manuscript Preparation

Original Article: An original article contains original research materials and presents compelling data on conceptual advances in any area of neuroscience. The total character count of all sections of the main text (including references and figure legends but excluding supplemental data) should not exceed 80,000, including spaces. Up to 8 figures and/or tables are allowed for the entire manuscript. The minimum requirement of a submitted research article is 40,000 characters in total (or 5000 words excluding the references) and at least 6 display items (figures and tables). The submitted manuscript should be a substantial novel research study in all aspects of neuroscience organizing a complete story with complex mechanisms elucidated using multiple techniques or approaches. NB also welcomes clinical research investigating the pathogenesis or diagnostic markers of a disease. Please note that for clinical trials, an Informed Consent should be provided as supplemental material and stated in the main text. NB no longer accepts clinical research that lack insightful mechanistic implications. References are limited to 100.

Review: Authoritative reviews contribute greatly to our journal and we are interested in comprehensive articles well-written to describe recent development in any field of neuroscience for a general audience. Authors are expected to cover controversies in the field and propose their own viewpoints in an unbiased and justifiable way. In particular, the scope of the review should not be dominated by the authors' own work. Review is usually 5,000 to 8,000 words in length (including an abstract of no more than 150 words, excluding the references and title) and 3–6 schematic illustrations are strongly encouraged. Reviews are often contributed by leaders in the field and solicited by the editors. The authors are encouraged to submit a letter of inquiry before the submission.

Insight: For Insight, the article should contain discussion on recent primary research literature similarly as Review. Yet, Insight is shorter in length (no more than 2,000 words, excluding the reference and title) and focuses on a narrower scope. It is possible

that in Insight authors advocate a position over a controversial issue or a speculative hypothesis. One schematic illustration is allowed to make the Insight more comprehensive. References are limited to 20.

Method: NB welcomes Method article on novel experimental techniques in any field of basic neuroscience. The Method can be written in the Research Article format yet the content should follow the criteria described below. The description of the method must be accompanied by its validation, its application to an important biological question, and results illustrating its performance in comparison to available approaches. The manuscript will be judged on its novelty, general interest, through assessments of methodological performance and comprehensive technical descriptions that facilitate immediate application. The detailed step-by-step procedure must be described in the form of flow charts for readers to comprehend easily. Additional annotation for key procedures and special treatments will be encouraged. In addition, please note that NB no longer accepts Method on neurosurgery pathway, surgical techniques, or any other clinical related technical studies.

Letter to the Editor: The Letter to the Editor reports a short but exciting finding in a particular field of neuroscience with high quality and of broad interest. The letter should be brief yet concise, and no specific subsections are required. No Materials and Methods section is needed, but any technical information which the authors think is important should be submitted as supplementary materials. The total words count should not exceed 2500 (exclude references and title) and the display items should be limited to 2. References are limited to 15. No abstract and subsections are needed.

Research Highlight: The Research Highlight describes recent research advances by articles published in NB or other journals. It highlights the main results of the research, emphasizes the significance and provides further discussion on the topic. The main text of a Research Highlight is up to 1,500 words (excluding references and title) with no more than 10 references and one or two figures. Research Highlights are usually by editor invitation, but submitted manuscript with high quality will also be considered. No abstract and subsections are needed.

Submitted manuscripts should be divided into the following sections:

(1) Title Page; (2) Abstract; (3) Introduction; (4) Materials and Methods; (5) Results; (6) Discussion; (7) Acknowledgements; (8) References; (9) Figures, legends, and tables; (10) Supplementary information.

Manuscript Revision

Upon peer-reviews, the authors may be asked to revise the manuscript. If the authors have substantial reasons to believe that their manuscript was treated unfairly, they may appeal for reconsideration. Revision should be completed within four (minor revision) or eight weeks (major revision). The authors should provide a cover letter and a point-to-point response for addressing the reviewers' comments. The editor will notify the corresponding author upon the acceptance of the manuscript. Accepted papers will be processed to advanced online publication as soon as possible.

Proofs

A PDF proof will be sent to the authors for them to correct last minute errors on the manuscript.

Page Charges

Page charges for the printed form are as follows: 500 CNY (80 USD) for each text page, 800 CNY (120 USD) for each page containing black-and-white figures, 1500 CNY (250 USD) for each page containing color figures. The corresponding author will receive an invoice on all the publication-related charges once the manuscript is accepted for publication and enters the editing process.

Make checks or money orders payable to:

Center for Excellence in Brain Science and Intelligence
Technology, Chinese Academy of Sciences
(中国科学院脑科学与智能技术卓越创新中心)

The bank account number is 4585 4835 7666,
Shanghai Jianguo West Road Subbranch, Bank of China
(中国银行上海市建国西路支行).

Address of Editorial Office of Neuroscience Bulletin:

319 YueYang Road, Room 612, Building 8, Shanghai 200031,
China.

Phone: +86-21-64232273; 64170853; 64032696;

E-mail: nsb@ion.ac.cn

<http://www.neurosci.cn>

(Updated January 2021)

Neuroscience Bulletin

Editors-in-Chief

Shumin Duan, Zhejiang University, Hangzhou, China
Ru-Rong Ji, Duke University, Durham, USA

Consulting Editors

Yizhang Chen, Second Military Medical University, Shanghai, China
Muming Poo, Center for Excellence in Brain Science and Intelligence Technology, CAS, Shanghai, China
Larry R. Squire, University of California, San Diego, USA
Charles F. Stevens, The Salk Institute, San Diego, USA
Xiongli Yang, Fudan University, Shanghai, China

Deputy Editors

Jiulin Du, Center for Excellence in Brain Science and Intelligence Technology, CAS, Shanghai, China
Zuoren Wang, Center for Excellence in Brain Science and Intelligence Technology, CAS, Shanghai, China

Executive Associate Editors

Iain C. Bruce, Zhejiang University, Hangzhou, China
Guangyin Xu, Institute of Neuroscience, Soochow University, Suzhou, China

Associate Editors

Shiqing Cai, Center for Excellence in Brain Science and Intelligence Technology, CAS, Shanghai, China
Zhong Chen, Zhejiang University, Hangzhou, China
Tianming Gao, South Medical University, Guangzhou, China
Yong Gu, Center for Excellence in Brain Science and Intelligence Technology, CAS, Shanghai, China
Shihui Han, Peking University, Beijing, China
Cheng He, Second Military Medical University, Shanghai, China
Tianzi Jiang, Institute of Automation, CAS, Beijing, China
Weidong Le, Dalian Medical University, Dalian, China
Tao Li, West China Hospital, Sichuan University, Chengdu, China
Chengyu Li, Center for Excellence in Brain Science and Intelligence Technology, CAS, Shanghai, China
Mengsheng Qiu, Hangzhou Normal University, Hangzhou, China
Fu-Dong Shi, St. Joseph's Hospital and Medical Center, Phoenix, USA
Yangang Sun, Center for Excellence in Brain Science and Intelligence Technology, CAS, Shanghai, China
You Wan, Peking University, Beijing, China
Jian-Zhi Wang, Huazhong University of Science and Technology, Wuhan, China
Yanjiang Wang, Daping Hospital, Third Military Medical University, Chongqing, China
Zheng Wang, Center for Excellence in Brain Science and Intelligence Technology, CAS, Shanghai, China
Longjun Wu, Mayo Clinic, Rochester, USA
Zhi-Ying Wu, Huashan Hospital, Shanghai Medical College, Fudan University, Shanghai, China
Tianle Xu, Shanghai Jiaotong University, Shanghai, China
Dai Zhang, Peking University, Beijing, China
Hanting Zhang, West Virginia University Health Sciences Center, Morgantown, USA
Chunjiu Zhong, Fudan University, Shanghai, China

Editorial Board

Philippe Ascher, Paris Diderot University, Paris, France
George Baillie, Institute of Cardiovascular and Medical Sciences, University of Glasgow, UK
Guo-Qiang Bi, University of Science and Technology of China, Hefei, China
Junli Cao, Xuzhou Medical College, Xuzhou, China
L. Judson Chandler, Medical University of South Carolina, USA
Jun Chen, The Fourth Military Medical University, Xi'an, China
Qing-Hui Chen, Michigan Technological University, Houghton, USA
Isaac M. Chiu, Harvard Medical School, Boston, USA
He Cui, Center for Excellence in Brain Science and Intelligence Technology, CAS, Shanghai, China
Yiru Fang, Shanghai Mental Health Center, Shanghai Jiaotong University School of Medicine, Shanghai, China
Richard S. Frackowiak, University of Lausanne, Lausanne, Switzerland
Tamás F. Freund, Institute of Experimental Medicine of the Hungarian Academy of Sciences, Budapest, Hungary
Yongjing Gao, Institute of Nautical Medicine, Nantong University, Nantong, China
Charles Gilbert, The Rockefeller University, New York, USA
Xiaosong Gu, Nantong University, Nantong, China

- Junhai Han**, Southeast University, Nanjing, China
Philip G. Haydon, Tufts University, Boston, USA
Joe Herbert, University of Cambridge, Cambridge, UK
Gregg E. Homanics, University of Pittsburgh, USA
Zhi-An Hu, Third Military Medical University, Chongqing, China
Kazuhide Inoue, Kyushu University, Fukuoka, Japan
Yong-Hua Ji, Shanghai University, Shanghai, China
Helmut Kettenmann, Max-Delbrück Center for Molecular Medicine, Berlin, Germany
O.A. Krishtal, Bogomoletz Institute of Physiology, Kiev, Ukraine
Robert H. LaMotte, Yale University School of Medicine, New Haven, USA
Pierre Lavenex, University of Fribourg, Fribourg, Switzerland
C. Justin Lee, Korea Institute of Science and Technology, Korea
Juan Lerma, Instituto de Neurociencias de Alicante, Alicante, Spain
Bao-Ming Li, Nanchang University, Nanchang, China
Wolfgang Liedtke, Duke University School of Medicine, Durham, USA
David J. Linden, Johns Hopkins University, Baltimore, USA
Stuart A. Lipton, Sanford-Burnham Medical Research Institute and University of California at San Diego, San Diego, USA
Jingyu Liu, Center for Excellence in Brain Science and Intelligence Technology, CAS, Shanghai, China
Tong Liu, Institute of Neuroscience, Soochow University, Suzhou, China
Lin Lu, Peking University Sixth Hospital, Beijing, China
Bridget Lumb, University of Bristol, Bristol, UK
Benyan Luo, Zhejiang University School of Medicine, China
Jian-Hong Luo, Zhejiang University School of Medicine, China
Zhen-Ge Luo, ShanghaiTech University, China
Lan Ma, Fudan University, Shanghai, China
Qiufu Ma, Dana-Farber Cancer Institute, Boston, USA
Qianhong Ma, Institute of Neuroscience, Soochow University, Suzhou, China
Robert C. Malenka, Stanford University, Stanford, USA
Manuel S. Malmierca, Universidad de Salamanca, Salamanca, Spain
John H.R. Maunsell, Harvard Medical School, Houston, USA
Earl K. Miller, Massachusetts Institute of Technology, Cambridge, USA
Enrico Mugnaini, Northwestern University, Feinberg School of Medicine, Chicago, USA
Vladimir Parpura, University of Alabama at Birmingham, Birmingham, USA
Jos Prickaerts, School for Mental Health and Neuroscience, Maastricht University, The Netherlands
Zilong Qiu, Center for Excellence in Brain Science and Intelligence Technology, CAS, Shanghai, China
Bruce R. Ransom, University of Washington, Seattle, USA
Tom E. Salt, University College London, London, UK
Joshua R. Sanes, Harvard University, Boston, USA
Michael N. Shadlen, Columbia University, New York, USA
Morgan Sheng, Genentech, Inc., South San Francisco, USA
Yousheng Shu, Fudan University, Shanghai, China
Sangram S. Sisodia, The University of Chicago, Chicago, USA
Peter Somogyi, University of Oxford, Oxford, UK
Feng-Yan Sun, Fudan University, Shanghai, China
Dick F. Swaab, Netherlands Institute for Neuroscience, Amsterdam, Netherlands
Keiji Tanaka, RIKEN Brain Science Institute, Tokyo, Japan
Xiaoqing Tang, University of South China, Hengyang, China
Yong Tang, Chengdu University of TCM, Chengdu, China
Makoto Tsuda, Kyushu University, Fukuoka, Japan
Alexej Verkhratsky, The University of Manchester, Manchester, UK
Steven R. Vincent, University of British Columbia, Vancouver, Canada
Guanghui Wang, Soochow University, Suzhou, China
Jian-Jun Wang, Nanjing University, Nanjing, China
Yun Wang, Neuroscience Research Institute, Peking University, Beijing, China
Xu-Chu Weng, South China Normal University, Guangzhou, China
William Wisden, Imperial College London, London, UK
Jun-Xia Xie, Qingdao University, Qingdao, China
Zhiqi Xiong, Center for Excellence in Brain Science and Intelligence Technology, CAS, Shanghai, China
Lin Xu, Kunming Institute of Zoology, CAS, Kunming, China
Ninglong Xu, Center for Excellence in Brain Science and Intelligence Technology, CAS, Shanghai, China
Xiao-Hong Xu, Center for Excellence in Brain Science and Intelligence Technology, CAS, Shanghai, China
Ying Xu, School of Pharmacy & Pharmaceutical Sciences, University at Buffalo, The State University of New York, USA
Yun Xu, Nanjing Drum Tower Hospital, Nanjing, China
Jun Yan, Center for Excellence in Brain Science and Intelligence Technology, CAS, Shanghai, China
Hui Yang, Center for Excellence in Brain Science and Intelligence Technology, CAS, Shanghai, China
Tianming Yang, Center for Excellence in Brain Science and Intelligence Technology, CAS, Shanghai, China
Haishan Yao, Center for Excellence in Brain Science and Intelligence Technology, CAS, Shanghai, China
Fengwei Yu, National University of Singapore, Singapore
Shanping Yu, Emory University School of Medicine, Atlanta, USA
Hong Zhang, The Second Affiliated Hospital of Zhejiang University School of Medicine, Hangzhou, China
Xiaohui Zhang, Beijing Normal University, Beijing, China
Xu Zhang, Institute of Neuroscience, CAS, Shanghai, China
Yong Zhang, Peking University, Beijing, China
Yu-Qiu Zhang, Fudan University, Shanghai, China
Zhi-Jun Zhang, Zhongda Hospital, Southeast University, Nanjing, China
Ping Zheng, Fudan University, Shanghai, China
Jiang-Ning Zhou, University of Science and Technology of China, Hefei, China
Jiawei Zhou, Center for Excellence in Brain Science and Intelligence Technology, CAS, Shanghai, China
Libin Zhou, Joint Laboratory for Brain Function and Health, Jinan University and The University of Hong Kong, Guangzhou, China
Richard E. Zigmond, Case Western Reserve University, Cleveland, USA
Yimin Zou, University of California-San Diego, USA

Neuroscience Bulletin

Copyright Information

For Authors

As soon as an article is accepted for publication, authors will be requested to assign copyright of the article (or to grant exclusive publication and dissemination rights) to the publisher (respective the owner if other than Springer Nature). This will ensure the widest possible protection and dissemination of information under copyright laws.

More information about copyright regulations for this journal is available at www.springer.com/12264

For Readers

While the advice and information in this journal is believed to be true and accurate at the date of its publication, neither the authors, the editors, nor the publisher can accept any legal responsibility for any errors or omissions that may have been made. The publisher makes no warranty, express or implied, with respect to the material contained herein.

All articles published in this journal are protected by copyright, which covers the exclusive rights to reproduce and distribute the article (e.g., as offprints), as well as all translation rights. No material published in this journal may be reproduced photographically or stored on microfilm, in electronic data bases, on video disks, etc., without first obtaining written permission from the publisher (respective the copyright owner if other than Springer Nature). The use of general descriptive names, trade names, trademarks, etc., in this publication, even if not specifically identified, does not imply that these names are not protected by the relevant laws and regulations.

Springer Nature has partnered with Copyright Clearance Center's RightsLink service to offer a variety of options for reusing Springer Nature content. For permission to reuse our content please locate the material that you wish to use on link.springer.com or on springerimages.com and click on the permissions link or go to copyright.com and enter the title of the publication that you wish to use. For assistance in placing a permission request, Copyright Clearance Center can be contacted directly via phone: +1-855-239-3415, fax: +1-978-646-8600, or e-mail: info@copyright.com

© Center for Excellence in Brain Science and Intelligence Technology, CAS 2021

Journal Website

www.springer.com/12264

For the actual version of record please always check the online version of the publication.

Subscription Information

Volume 37 (12 issues) will be published in 2021.

ISSN: 1673-7067 print
ISSN: 1995-8218 electronic

For information on subscription rates please contact Springer Nature Customer Service Center: customerservice@springernature.com

The Americas (North, South, Central America and the Caribbean)
Springer Nature Journal Fulfillment,
Harborside Plaza II,
200 Hudson Street, Jersey City,
NJ 07302, USA
Tel. 800-SPRINGER (777-4643);
212-460-1500 (outside
North America)

Outside the Americas

Springer Nature Customer Service
Center GmbH, Tiergartenstr. 15,
69121 Heidelberg, Germany
Tel.: +49-6221-345-4303

Advertisements

E-mail contact: advertising@springer.com or anzeigen@springer.com (Germany)

Disclaimer

Springer Nature publishes advertisements in this journal in reliance upon the responsibility of the advertiser to comply with all legal requirements relating to the marketing and sale of products or services advertised. Springer Nature and the editors are not responsible for claims made in the advertisements published in the journal. The appearance of advertisements in Springer Nature publications does not constitute endorsement, implied or intended, of the product advertised or the claims made for it by the advertiser.

Office of Publication

Springer Nature Singapore Pte Ltd.
152 Beach Road, #21-01/04
Gateway East, Singapore 189721,
Singapore



Impactor Factor

5.203

**2020 Journal Citation Reports: Q2
(CLARIVATE ANALYTICS, 2021)**

NEUROSCIENCE BULLETIN 神经科学通报 (Monthly)

Vol. 37 No. 7 July 15, 2021

Sponsored by: Center for Excellence in Brain Science and Intelligence Technology, Chinese Academy of Sciences
Chinese Neuroscience Society

Editors-in-Chief: Shunmin Duan, Ru-Rong Ji

Edited by: Editorial Board of *Neuroscience Bulletin*

319 Yueyang Road, Building 8, Room 612, Shanghai 200031, China

Phone: +86-21-64032273; 64170853; 64032696

E-mail: nsb@ion.ac.cn; <http://www.neurosci.cn>

Editors: Bin Wei, Fei Dong, Ting Lyu

Published by: Center for Excellence in Brain Science and Intelligence Technology, Chinese Academy of Sciences

Printed by: Shanghai Shengtong Times Printing Co.,Ltd (A6, No. 2888, Caolang Highway, Jinshan District, Shanghai)

Overseas Distributed by: Springer Nature

Home Distributed by: Local Post Offices

ISSN 1673-7067

CN 31-1975/R

Post Office Code Number: 4-608

Permit of Ad. Number: 3100420130051

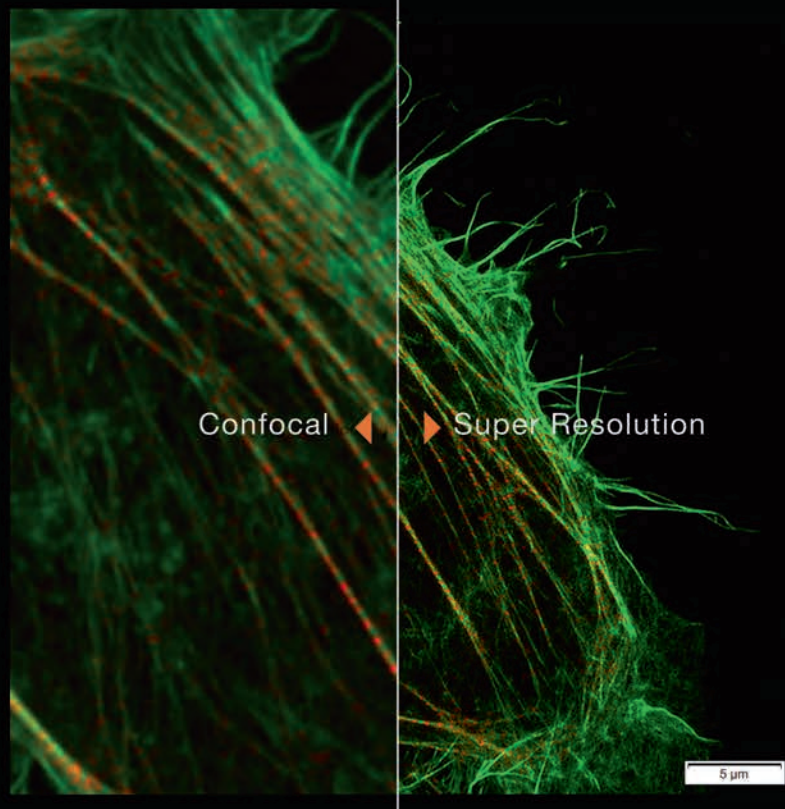
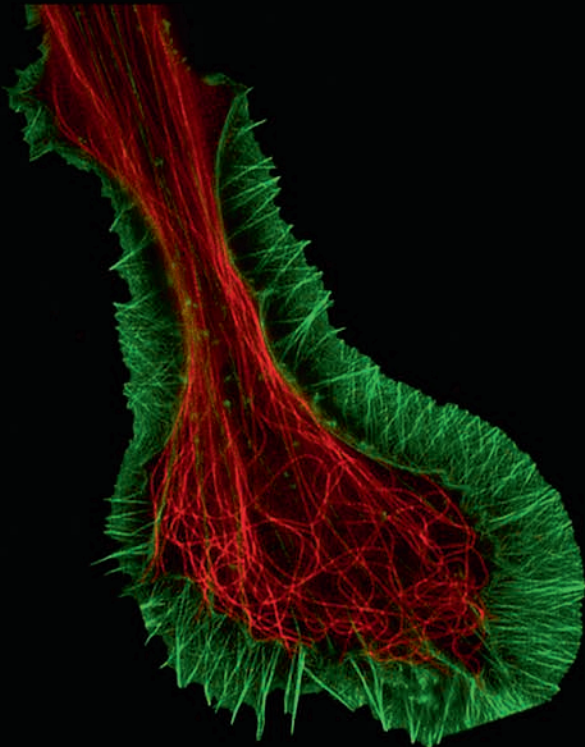
Price: ¥ 100.00

ISSN 1673-7067



兼顾分辨率和速度的

转盘共聚焦活细胞超分辨系统 **SpinSR10**



- 分辨率高达110nm的实时超分辨率成像
- 专有反卷积算法进一步提升图像质量
- 宽视野成像，速度高达 200fps
- 特色硅油物镜可以实现活细胞深层成像
- 宽场、共聚焦、超分辨率模式自由切换
- 功能强大的智能cellSens软件平台



奥林巴斯（北京）销售服务有限公司

北京朝阳区酒仙桥路10号恒通商务园B12C座2F (北京) 010-59756006
 上海市徐汇区淮海中路1010号嘉华中心11楼 (上海) 021-51582084
 广州市环市东路403号广州电子大厦16楼 (广州) 020-61227171

陕西省西安市新城区尚德路85号太平洋保险大厦8F

湖北省武汉市江岸区中山大道1628号武汉天地企业中心5号7楼701单元
 四川省成都市人民南路四段三号来福士广场T1-11楼
 辽宁省沈阳市沈河区友好街10号新地中心1号楼3501室

(西安) 029-87206108

(武汉) 027-82718838

(成都) 028-86703700

(沈阳) 024-23342084